Solar Thermal Thruster

Design of a Solar Thermal Propulsion System with Thermal Energy Storage

AE5822: Thesis Space

Stan Nuijten

Delft University of Technology

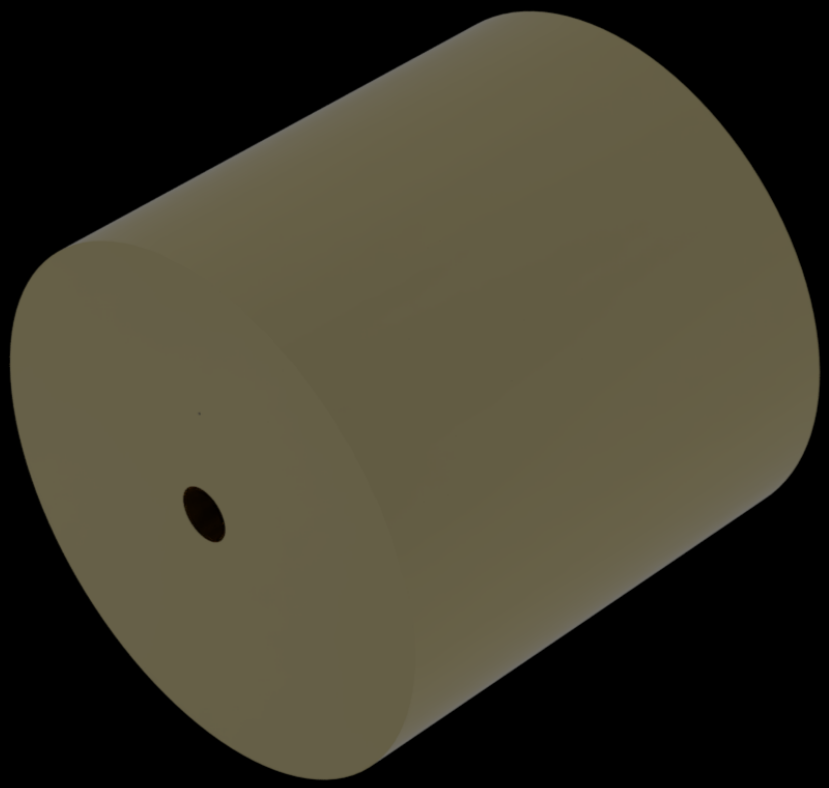

TU Delft

Solar Thermal Thruster

Design of a Solar Thermal Propulsion System with Thermal Energy Storage

by

Stan Nuijten

Responsible Supervisor:	Dr. A. Cervone
Daily Supervisor:	L. Dall' Osto
Project Duration:	February, 2025 - October, 2025
Faculty:	Faculty of Aerospace Engineering, Delft

TU Delft

Summary

This report discusses the design of a Solar Thermal Propulsion (STP) system for the Green SWaP mission. STP is a propulsion method that uses concentrated solar energy to heat a propellant and generate thrust. Absorbers transfer solar heat to the propellant through direct or indirect heating. The history of STP shows milestones such as inflatable concentrators and thermal energy storage (TES) for functioning during an eclipse.

Fundamental propulsion relations are discussed, along with real-world effects such as heat losses, viscous effects, and flow separation on the efficiency. Nozzle and absorber design strongly influence performance. Conical nozzles are often preferred for small systems, and refractory metals are often used for high-temperature components.

The design of the hydrogen propulsion system concept is based on the requirements for the Green SWaP mission. With a thrust of $1\,\mathrm{N}$, a specific impulse above $500\,\mathrm{s}$, and the ability to operate during eclipse being the most important.

A design option tree is created for heating methods, thermal energy storage, and nozzle shapes. A trade-off showed that a windowless cavity is the best heating method due to its simplicity, reliability, and sufficient performance. For TES, latent heat storage was selected for its high energy density and constant temperature, despite slightly lower reliability. A conical nozzle was chosen for effectiveness at low Reynolds numbers.

The preliminary design targets a chamber temperature of $3000\,\mathrm{K}$, a heat exchanger inlet at $5.0\,\mathrm{MPa}$ and $273.15\,\mathrm{K}$, assuming a wall temperature of $3100\,\mathrm{K}$. Rhenium is selected as the heat exchanger material for its high-temperature performance, ductility, and hydrogen compatibility. A spiral runner, multiple channels, and a porous medium concept are analysed, balancing turbulent flow, pressure drop, and required channel length.

The cavity absorbs concentrated solar radiation and converts it into thermal power, with graphite selected as the material due to its high absorptivity and high-temperature performance. Optimising the cavity shape maximises energy absorption and a uniform heat flux distribution.

The TES system stores energy to heat the propellant during eclipses, using boron for its high latent heat. The container is optimised to minimise surface area and thermal losses. The container thicknesses account for boron expansion, ensuring reliable performance.

The nozzle was sized to achieve sonic flow at the throat, with the lower-pressure concepts experiencing temporary propellant build-up due to chocked conditions. A higher specific impulse is possible with increased expansion.

Rhenium was selected as insulation for its high melting point and ductility. Using a porous foam layer reduces effective conductivity, reducing the insulation thickness. A low-emissivity from polished gold is used to lower the radiated power.

The analysis shows that high temperatures require significant insulation and significant solar input, motivating to lower the heat exchanger temperature for improved efficiency and feasibility.

The system is mathematically modelled using three differential control elements: a stationary control volume, a control volume with bulk motion, and a control surface. Heat transfer within solids is governed by conduction with latent and sensible energy terms, expressed in cylindrical coordinates.

The simulations are made based on the mathematical model. Convection is first simulated using CFD to compare the spiral runner and the multiple channels concept. The spiral runner achieved a slightly higher temperature and a lower pressure drop than the multiple channels concept, leading to its selection despite its larger size.

Conduction and radiation are simulated with a Python solver, using rotational symmetry. A 2D mesh of nodes with domain-specific properties is created. The solver applies central differences and harmonic conductivity averaging. The simulation results are used to iterate the design process and improve accuracy.

The final optimisation focuses on minimising TES material mass. By accounting for reduced thermal losses during eclipse conditions, the required TES mass, insulation thickness, and input power are decreased.

An experimental validation of the system is proposed. Materials, components, and the full system must be tested under operational conditions. High-temperature testing ensures that the thermal and mechanical properties of materials behave as expected. Hydrogen interactions at elevated temperatures must be validated to prevent degradation, leaks, and performance loss. Finally, system-level performance tests are required to determine actual mass flow, characteristic velocity, and thrust coefficient. This allows the identification of efficiencies and verification of system performance.

Contents

List of Figures

List of Tables

Nomenclature

Abbreviations

Abbreviation	Definition
AFRL	Air Force Research Laboratory
AFRPL	Air Force Rocket Propulsion Laboratory
CFD	Computational Fluid Dynamics
IPAPS	In-situ Propellant Acquisition and Processing System
ISUS	Integrated Solar Upper Stage
STP	Solar Thermal Propulsion
STUS	Solar Thermal Upper Stage
TES	Thermal Energy Storage
TDK	Two Dimensional Kinetics
TRL	Technology Readiness Level

Symbols

Symbol	Definition	Unit
A	Area	$[\mathrm{m}^2]$
A_{ap}	Aperture area	$[\mathrm{m}^2]$
A_{cav}	Cavity surface area	$[\mathrm{m}^2]$
$A_{cav,ins}$	Insulated cavity surface area	$[\mathrm{m}^2]$
A_{conc}	Concentrator area	$[\mathrm{m}^2]$
A_c	Channel cross-sectional area	$[\mathrm{m}^2]$
A_e	Nozzle exit area	$[\mathrm{m}^2]$
$A_{TES,ins}$	Insulated TES surface area	$[\mathrm{m}^2]$
$A_{TES,outer}$	Outer surface area of TES container	$[\mathrm{m}^2]$
A_s	Surface area for convection	$[\mathrm{m}^2]$
A_t	Nozzle throat area	$[\mathrm{m}^2]$
D	Channel diameter	$[\mathrm{m}]$
D_e	Nozzle exit diameter	$[\mathrm{m}]$
D_t	Throat diameter	$[\mathrm{m}]$
F	Thrust	$[\mathrm{N}]$
g_0	Gravitational acceleration at sea level	$[\mathrm{m\,s^{-2}}]$
H	Shannon entropy	[-]
H_{max}	Maximum Shannon entropy	[-]
I	Incident solar flux	$[\mathrm{W\,m^{-2}}]$
I_{sp}	Specific impulse	$[\mathrm{s}]$
k	Thermal conductivity / Turbulent kinetic energy	$[\mathrm{W\,m^{-1}\,K^{-1}}]$ / $[\mathrm{m^2\,s^{-2}}]$
k_{eff}	Effective thermal conductivity	$[\mathrm{W\,m^{-1}\,K^{-1}}]$
k_s	Thermal conductivity of solid material	$[\mathrm{W\,m^{-1}\,K^{-1}}]$
k_v	Thermal conductivity of void	$[\mathrm{W\,m^{-1}\,K^{-1}}]$
L	Channel length / characteristic length / Latent heat of fusion	$[\mathrm{m}]$ / $[\mathrm{J\,kg^{-1}}]$
L_{cav}	Cavity length	$[\mathrm{m}]$

Symbol	Definition	Unit
L_{cyl}	Cylinder length in cavity	[m]
L_{TES}	TES container length	[m]
$L_{thermal}$	Thermal entrance length	[m]
L_{total}	Total channel length	[m]
$\dot{m}$	Mass flow rate	[$\mathrm{kg\,s^{-1}}$]
$\dot{m}_{id}$	Ideal mass flow rate	[$\mathrm{kg\,s^{-1}}$]
m_{TES}	Mass of TES material	[kg]
M	Mach number / Molar mass of propellant	[-] / [$\mathrm{kg\,mol^{-1}}$]
$M_{channel}$	Mach number in heat exchanger channels	[-]
$\vec{n}$	Outward unit normal vector	[-]
NA	Numerical Aperture	[-]
Nu	Nusselt number	[-]
p	Pressure	[Pa]
p_a	Ambient pressure	[Pa]
p_c	Chamber pressure	[Pa]
p_e	Exit pressure	[Pa]
p_{in}	Inlet propellant pressure	[Pa]
q''	Heat flux vector	[$\mathrm{W\,m^{-2}}$]
q''_{cond}	Conduction heat flux at surface	[$\mathrm{W\,m^{-2}}$]
q''_{conv}	Convective heat flux at surface	[$\mathrm{W\,m^{-2}}$]
q''_{rad}	Radiative heat flux at surface	[$\mathrm{W\,m^{-2}}$]
$\dot{Q}_{abs}$	Absorbed power by cavity	[W]
$\dot{Q}_{in}$	Incident solar power	[W]
$\dot{Q}_{loss}$	Thermal power loss	[W]
$\dot{Q}_{p,req}$	Required thermal power to heat propellant	[W]
$\dot{Q}_{rad}$	Total radiated power	[W]
$\dot{Q}_{rad,cav}$	Radiated power from cavity	[W]
$\dot{Q}_{rad,outer}$	Radiated power from outer surfaces	[W]
Q_{TES}	Required energy stored in TES	[J]
$\vec{r}$	Position vector	[m]
R_{ap}	Aperture radius	[m]
R_{cav}	Cavity radius	[m]
R_{TES}	TES container radius	[m]
SF	Safety factor	[-]
t	Time	[s]
$t_{b,ec}$	Burn time during eclipse	[s]
t_{ec}	Eclipse duration	[s]
$t_{ins,cav}$	Insulation thickness around cavity	[m]
$t_{ins,TES}$	Insulation thickness around TES container	[m]
t_{TES}	TES container wall thickness	[m]
t_{wall}	Wall thickness	[m]
T	Temperature	[K]
T_a	Absorber temperature	[K]
T_c	Chamber temperature	[K]
T_{cav}	Cavity temperature	[K]
T_{in}	Inlet propellant temperature	[K]
$T_{min,TES}$	Minimum TES temperature	[K]
$T_{max,ins}$	Maximum insulation temperature	[K]
T_{wall}	Wall temperature	[K]
U	Uniformity score	[-]
$\vec{v}$	Velocity vector	[$\mathrm{m\,s^{-1}}$]
v	Propellant velocity	[$\mathrm{m\,s^{-1}}$]
v_e	Exhaust velocity	[$\mathrm{m\,s^{-1}}$]
v_{eq}	Equivalent velocity	[$\mathrm{m\,s^{-1}}$]

Symbol	Definition	Unit
V	Volume	[m^3]
V_{TES}	Volume of TES material	[m^3]
α	Absorptivity of cavity / absorber surface	[-]
ϵ	Turbulent dissipation rate	[$\mathrm{m}^2\,\mathrm{s}^{-3}$]
ϵ_a	Absorber emissivity	[-]
ϵ_p	Propellant emissivity	[-]
η_{abs}	Absorption efficiency	[-]
η_c	Collection efficiency	[-]
η_o	Optical efficiency	[-]
γ	Heat capacity ratio	[-]
Γ	Vandenkerckhove function	[-]
μ	Molecular dynamic viscosity	[$\mathrm{kg}\,\mathrm{m}^{-1}\,\mathrm{s}$]
μ_t	Turbulent dynamic viscosity	[$\mathrm{kg}\,\mathrm{m}^{-1}\,\mathrm{s}$]
ρ	Density	[$\mathrm{kg}\,\mathrm{m}^{-3}$]
σ	Stefan-Boltzmann constant	[$\mathrm{W}\,\mathrm{m}^{-2}\,\mathrm{K}^{-4}$]
$\sigma_{y0.2}$	Yield strength at 0.2% offset	[Pa]
ϕ	Porosity	[-]
θ	Angle	[rad]
θ_1	First cone angle of cavity	[rad]
θ_2	Second cone angle of cavity	[rad]
ξ_c	Heating quality factor	[-]
ξ_n	Nozzle flow quality factor	[-]

1

Introduction

With the number of spacecraft launches increasing each year, so does the search for more efficient and greener propulsion solutions. The downside of electrical propulsion systems is that even though they offer high specific impulses, the provided thrust is lower than chemical propulsion systems. For many mission applications that require a larger thrust, electrical propulsion is thus not feasible. The novel concept of Solar Thermal Propulsion (STP) is a potential solution that offers a higher specific impulse than chemical propulsion and a larger thrust than electrical propulsion. STP has been researched for some years already, but applications have been limited so far. The design of this thruster will show the feasibility of this technology and help implement it in future missions.

The Green SWaP mission aims to make space exploration more sustainable and implements STP for the secondary propulsion system. On board the spacecraft, water is split into hydrogen peroxide and hydrogen using solar energy, as hydrogen is a by-product of turning water into hydrogen peroxide. By doing this onboard, less volume is required for the propellant during launch, as hydrogen is a low-density propellant, and launching water requires significantly less volume. The hydrogen peroxide is used for the primary propulsion of the spacecraft, while the hydrogen is available for secondary propulsion.

This report focuses on the design of the STP system for the Green SWaP mission. With the mission being in a preliminary design phase, many requirements are not yet defined. The design of the STP system will thus focus on its own optimisation while not negatively impacting other systems and minimising the additional requirements for other systems.

First, a literature review will be performed to form a basis for the design process. A brief recap of the history of STP will be discussed, and outcomes of past publications will be used to make design choices for this propulsion system. Relevant fundamental relations will be identified that will be used during the design process.

Based on the literature review, multiple concepts will be generated, of which a selection will be made. Based on the selected concepts, a preliminary design will be made. To support the selection of the final concept, a thermofluidic analysis will be performed. This design will then be iterated and optimised to create the final design.

2

Literature Review

This chapter discusses a literature review on Solar Thermal Propulsion (STP) with the help of the review questions in section 2.1. STP is a type of propulsion based on solar energy. The solar radiation is concentrated and heats an absorber. The absorber then exchanges its heat with a propellant, which is expelled through a nozzle. A Schematic of an STP system is shown in Figure 2.1. First, the history of STP is reviewed in section 2.2. Then, the fundamental equations for rocket propulsion are discussed in section 2.3, followed by a review of the nozzle in section 2.4 and of the absorber in section 2.5. Finally, the conclusions that can be drawn from the literature review will be discussed in section 2.7.

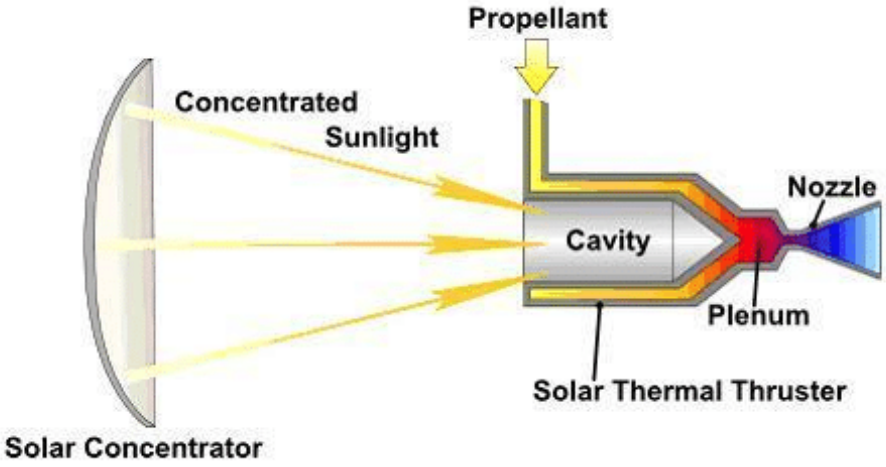

Figure 2.1: Schematic of a solar thermal propulsion system [1]

2.1. Review Questions

Review questions are used to determine what literature to review. For the history of STP, different designs will be compared with the help of the following questions:

1. *How has STP evolved over time?*
    1.1 *What were the key milestones in the development of STP?*
    1.2 *How did past attempts influence current designs?*
2. *What are the strengths and weaknesses of previous STP designs?*
    2.1 *How do different STP designs compare in terms of efficiency and feasibility?*
    2.2 *What are the major design limitations encountered in previous implementations?*

3. *What are the most advanced STP technologies currently available?*
    3.1 *What is the current TRL of various STP systems?*
    3.2 *How do state-of-the-art designs address the challenges of earlier models?*

To review the fundamental relations for rocket propulsion and the relations specific to STP, the following questions will be used:

4. *What are the fundamental relations governing rocket propulsion?*
    4.1 *What are the primary equations used to describe thrust, impulse, and efficiency?*
    4.2 *What role do thermodynamic and fluid dynamic principles play in propulsion analysis?*
5. *How do ideal and non-ideal performance estimations compare?*
    5.1 *What assumptions are made in ideal performance estimations, and how do they simplify calculations?*
    5.2 *What real-world effects (e.g., heat losses, flow separation, turbulence, friction forces) lead to deviations from ideal models?*

The different types of nozzles and nozzle materials will be reviewed with the following questions:

6. *How does the nozzle shape and material affect performance?*
    6.1 *How do different nozzle geometries influence exhaust flow and thrust?*
    6.2 *What materials are commonly used for space nozzles, and how do they withstand extreme temperatures?*
7. *What are the challenges of nozzles for STP?*
    7.1 *What are the main constraints in fabricating the nozzle?*
    7.2 *How do space environmental factors (vacuum, radiation, thermal cycling) impact long-term nozzle durability?*
    7.3 *How does the usage of hydrogen as a propellant affect the nozzle?*

Similarly, the different types of absorbers and absorber materials will be reviewed with the following questions:

8. *What are the different absorber designs used in STP systems?*
    8.1 *What types of absorbers are currently used in space propulsion systems?*
    8.2 *What are the advantages and disadvantages of each absorber design?*
    8.3 *How do the absorber designs interact with the collector?*
9. *How do material properties impact absorber efficiency?*
    9.1 *What are the key parameters for evaluating absorber performance?*
    9.2 *How do environmental factors influence the performance of the materials?*
    9.3 *How does the usage of hydrogen as a propellant affect the absorber performance?*

2.2. History

STP was mentioned for the first time by Krafft Ehricke in 1951 [2]. He envisioned a spacecraft that utilises inflatable sphere concentrators to heat hydrogen. The plastic concentrators would be mirrored on one side and transparent on the other, with the absorber being placed inside the sphere. The high energy efficiency of the system could be a solution to the high fuel consumption of chemical propulsion methods. This formulated concept has a TRL 2. Then in the 1960s, Electro-Optics Corporations performed research and development studies under contract for the Air Force Rocket Propulsion Laboratory (AFRPL) [3]. The goal was to determine the feasibility of an STP system with hydrogen as the propellant. Cold and hot flow studies were conducted, and the first STP thruster was successfully tested [4]. This resulted in a TRL 4. Specific impulses up to $680\,\mathrm{s}$ were reached during these tests. The

design contained the first electro-formed lightweight mirrored concentrator and was made from molybdenum. The absorber made from rhenium achieved temperatures up to $2300\,\mathrm{K}$. Despite the positive results, no additional funding was received to continue the efforts [5]. The main issue was the difficulty of integrating the large mirrors.

Rockwell Satellite Systems Division also performed conceptual design studies for the AFRPL, leading to the development of paired thrusters with off-axis concentrators in 1978 [6]. The concentrator and absorber were optically coupled, with the absorber being at the focus point of the concentrator. The concentrator consisted of an inflatable structure without rigid support, allowing it to deform easily. This made the design vulnerable to forces caused by accelerations or rotations.

In the 1980s, different absorber and thruster configurations and propellants were evaluated by the AFRPL and the windowless heat exchanger cavity absorber was selected for the development of a prototype [7]. Rocketdyne fabricated a ground test unit of the selected concept and tested it in 1984. The hardware consisted of a tubular rhenium heat absorber and a rhenium thruster as shown in Figure 2.2 [8]. The joining of rhenium components was researched because the fabricability of rhenium was relatively unknown. This research, combined with an advanced engine concept, led to the experimental investigation of the feasibility of the porous material absorption concept with a TRL 4. Rocketdyne designed, analysed, and fabricated the porous material absorber to investigate the thermohydraulics of the hydrogen flowing through the test bed. Analytic models estimated a $20\,\%$ higher specific impulse than for a windowless heat exchanger cavity solar absorber.

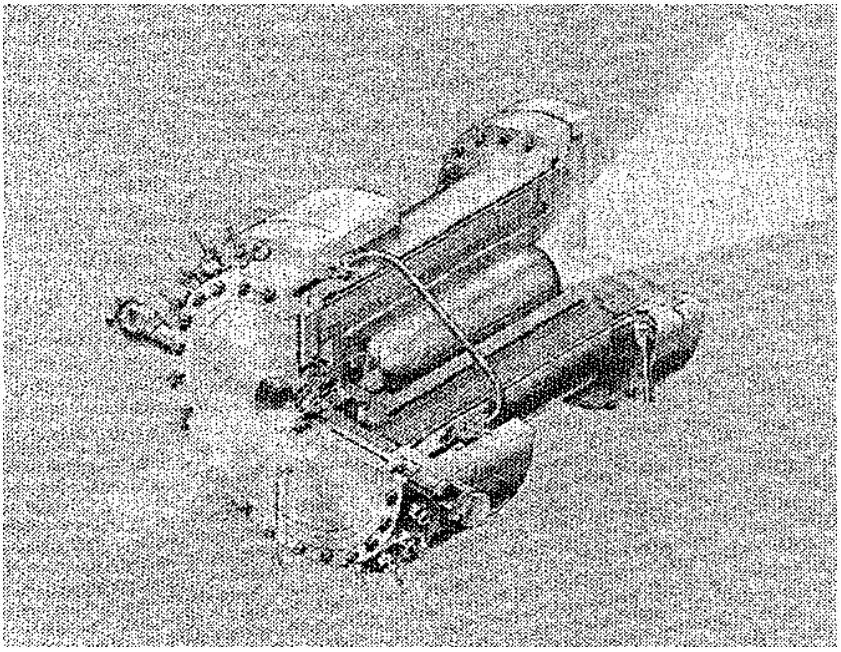

Figure 2.2: The rhenium ground test unit fabricated by Rocketdyne [8]

To better utilise the available resources onboard, the IPAPS proposed integrating a thermionic reactor to generate power [9]. The design could heat hydrogen to a temperature of $2200\,\mathrm{K}$, resulting in a specific impulse of $736\,\mathrm{s}$ and a thrust of $111\,\mathrm{N}$. This concept had a TRL 3. This, however, leads to the issue that less power is available during an eclipse. The ISUS program, sponsored by the AFRPL, addressed this issue by introducing the first sensible heat Thermal Energy Storage (TES) system [10]. Sensible heat was used to store the energy, making use of rhenium-coated graphite as the TES material. They worked on this concept from 1994 until 1998. This system allows the generation of power and provides thrust during an eclipse. This concept had a TRL 4.

Hydrogen occupies a large volume as a propellant due to its low density. To make more volume available for payload, the University of Alabama proposed a dual-fuel STP system in 1995 that can use ammonia and hydrogen [11]. Using ammonia increases the propellant mass but reduces the required

volume. This came at the cost of allowable payload mass due to the lower specific impulse reach with ammonia. However, by decreasing the size of the power system, the mass increase was compensated. This concept study had a TRL 3.

During the L'Garde Inflatable Antenna Experiment in 1996, an inflatable antenna was deployed successfully, resulting in a TRL 6 for the inflatable subsystem [12]. The antenna was a $14\,\mathrm{m}$ parabolic reflector as shown in Figure 2.3. Its surface accuracy was measured, and the damping characteristics were determined. The results of this mission are useful for inflatable concentrators.

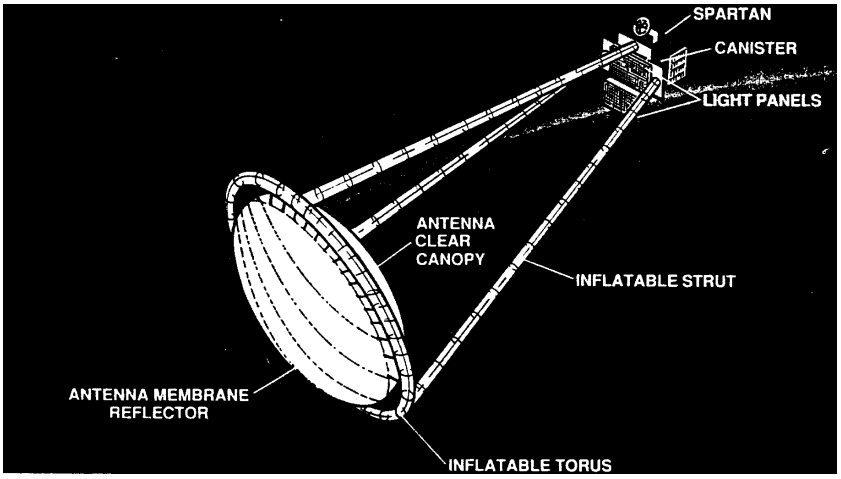

Figure 2.3: Sketch of the inflatable L'Garde Inflatable Antenna [12]

In 1996, NASA proposed, together with the United States Air Force, the Solar Thermal Upper Stage (STUS) [13]. STP was identified as the least complex and costly advanced propulsion concept. It was estimated that the development costs would be regained with two flights, making the concept competitive with Ariane stages. The concept used hydrogen as a propellant and contained two inflatable concentrators as shown in Figure 2.4.

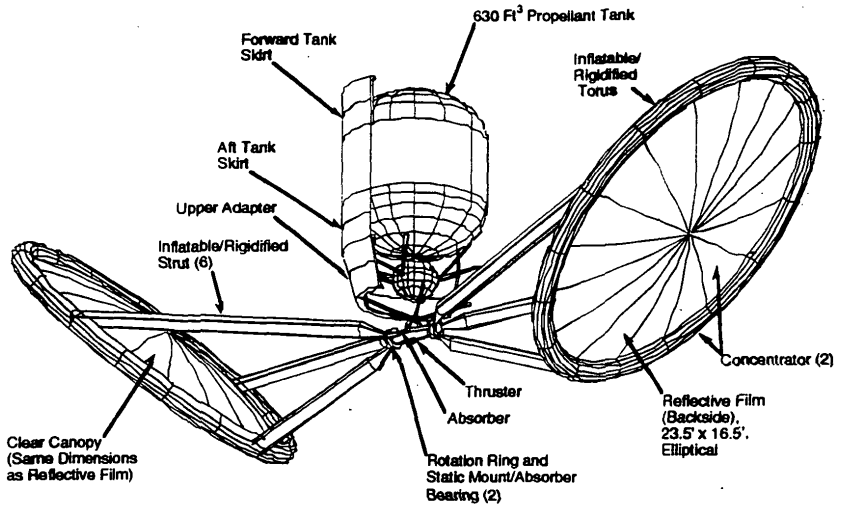

FIGURE 1. SOLAR THERMAL UPPER STAGE.

Figure 2.4: Sketch of the Solar Thermal Upper Stage concept [13]

During the following 4 years, NASA performed the Shooting Star Experiment to demonstrate the required technologies for the STUS on a smaller scale [14]. A secondary concentrator was proposed and an absorber with rhenium foam through which a propellant flows [15]. Graphite was used to in-

sulate the system. The Solar Orbit Transfer Vehicle program was meant for a flight test, but due to funding issues, no flight followed [16]. The program ended with a TRL 6.

From 1997 until 2000, Japan worked on the Japan Solar Upper Stage research program. Multiple thrusters made from single-crystal molybdenum, with a tungsten coating, and a carbon felt insulation, were tested, and a temperature of $2300\,\mathrm{K}$ was reached [17]. An opposed cavity design was also tested, but made from stainless steel to lower the testing costs [18]. The testing efforts led to a TRL 4.

The Integrated High Payoff Rocket Propulsion Technology program was set up as a collaboration between the government of the United States of America and the industry [19]. Their goal was to double the rocket propulsion capabilities in 10 years and demonstrate advanced technologies. In 2001, an inflatable concentrator with a sun tracking and focus control system was tested under space environment conditions, resulting in a TRL 6 [20]. The thruster developed for this program was made from tungsten.

The Surrey Space Centre researched STP for microsatellites from 2000 until 2006 [21]. Two receivers were tested, made from an intermetallic composite of boron nitride and titanium diboride, which functioned as a sensible TES system. These tests had a TRL 4. One of the receivers used a boron nitride particle bed, and the other used a spiral flow channel. Cracks and leaks were detected during the tests.

The research also led to the idea of using fibre optical cable to decouple the concentrator and thruster [22]. The decoupling of the thruster and concentrator would allow the absorber and thruster to be placed without compromising the efficiency of the concentrator. Flexible optical waveguide transmission lines can then transmit the concentrated solar radiation to one or multiple absorbers. Physical Sciences Inc., Boeing, and the Air Force Research Laboratory (AFRL) tested such a system in 2004 and 2005, giving this subsystem also a TRL 4 [23]. Results showed that an optical waveguide system increases the subsystem mass but decreases the launch mass due to increased optical train efficiency. The used experimental test setup is shown in Figure 2.5.

Figure 2.5: The experimental test set up with fibre optical cables [23]

The Hokkaido University analysed in 2009 the design of an STP system with a spiral cavity absorber made from heat-resistant steel [24]. In the same year, the AFRL reviewed different thrusters for a microsatellite [25]. STP was identified as a strong candidate, but further research and development were required. The research had a TRL 3.

Between 2011 and 2015, the University of Southern California worked on the proposal of an STP system with a latent heat TES system, as improved on previous sensible heat TES systems [26]. Boron and

silicon were determined to be the ideal candidates. Boron was identified as a high-performance far-term option, and silicon as a near-term solution. The research stopped at a TRL 4. In 2016, at Arizona State University, another American university, a concept was proposed for an STP system with water as a propellant [27]. The university analysed and experimented with the usage of a coating of carbon nanotubes to improve the absorption efficiency. Efficiencies of up to $99\,\%$ were achieved during the laboratory demonstrations, leading to a TRL 4 as well.

A different type of heat exchanger was proposed in 2014 by the National University of Defence in China [28]. The absorber contained multiple stacked plates made from molybdenum through which hydrogen flows, isolated with aluminium fibres. Until 2025, the research to simulate, optimise, and experiment continued [29] up to a TRL 4.

2.3. Fundamental Relations

The produced thrust by the STP system is in an ideal situation given by the following equation [30]:

$$F = \dot{m} \cdot v_{eq} \tag{2.1}$$

where F is the thrust in N, $\dot{m}$ is the mass flow in $\mathrm{kg\,s^{-1}}$, and v_{eq} is the equivalent velocity in $\mathrm{m\,s^{-1}}$.

An often-used performance parameter is the specific impulse, which measures how much impulse is produced per unit of propellant weight. When assuming a constant mass flow and exhaust velocity, the specific impulse is given by the following equation:

$$I_{sp} = \frac{v_{eq}}{g_0} \tag{2.2}$$

where I_{sp} is the specific impulse in s, and g_0 is the gravitational acceleration at sea level in $\mathrm{m\,s^{-2}}$.

When assuming a perfect expansion, the equivalent velocity is equal to the exhaust velocity. The exhaust velocity is given by the following equation:

$$v_e = \sqrt{\frac{2\gamma}{\gamma - 1} \cdot \frac{R_A}{M} \cdot T_c \cdot \left(1 - \left(\frac{p_e}{p_c}\right)^{\left(\frac{\gamma-1}{\gamma}\right)}\right)} \tag{2.3}$$

where v_e is the exhaust velocity in $\mathrm{m\,s^{-1}}$, γ is the dimensionless heat capacity ratio of the propellant, $R_A = 8.314 \times 10^3\,\mathrm{J\,mol^{-1}\,K^{-1}}$ is the universal gas constant, M is the molar mass of the propellant in $\mathrm{kg\,mol^{-1}}$, T_c is the chamber temperature in K, and p_e is the exhaust pressure in Pa. For diatomic hydrogen, the molar mass is $2.016 \times 10^{-3}\,\mathrm{kg\,mol^{-1}}$.

STP provides a thrust and specific impulse between the levels offered by chemical and ion propulsion as shown in Figure 2.6.

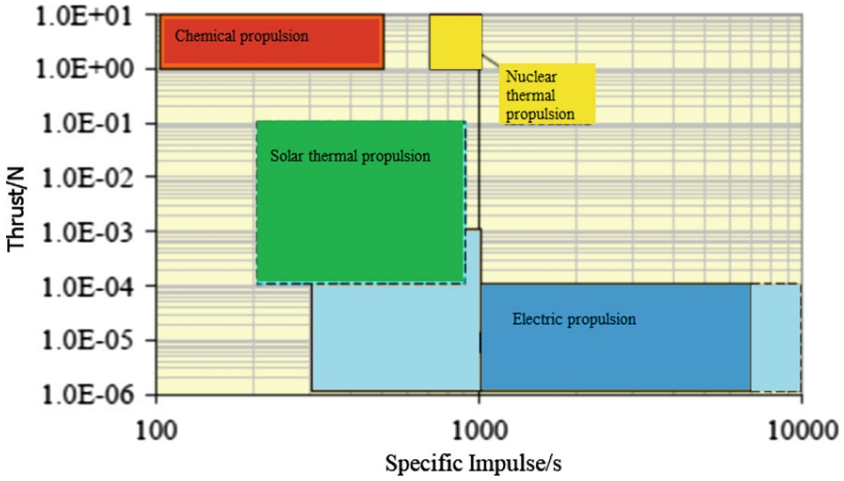

Figure 2.6: Thrust and specific impulse ranges of common propulsion methods [29]

The prediction is that when using hydrogen as the propellant, the specific impulse can reach $900\,\mathrm{s}$ [16].

The specific impulse measures the overall performance of a thruster, but it can be split into two different factors: the characteristic velocity and the thrust coefficient. The characteristic velocity measures the energy of the propellant, and the thrust coefficient measures how well this is converted into momentum. The characteristic velocity is given by the following equation:

$$c^* = \frac{p_c A_t}{\dot{m}} \tag{2.4}$$

where c^* is the characteristic velocity in $\mathrm{m\,s^{-1}}$, and A_t is the nozzle throat area in $\mathrm{m^2}$. For an ideal gas, the characteristic velocity can also be expressed as:□

$$c^* = \frac{1}{\Gamma}\sqrt{\frac{RT_c}{M}} \tag{2.5}$$

where $Gamma$ is the dimensionless Vandenkerckhove function defined as:

$$\Gamma = \sqrt{\gamma}\left(\frac{2}{\gamma+1}\right)^{\frac{\gamma+1}{2(\gamma-1)}} \tag{2.6}$$

The higher the characteristic velocity is, the higher the enthalpy of the propellant per unit mass. As no combustion happens in an STP thruster, the energy gained by the propellant is purely the net result of the absorbed solar irradiation and the thermal losses.

The thrust coefficient relates the chamber pressure to the thrust and is defined as:

$$C_F = \frac{F}{p_c A_t} \tag{2.7}$$

where C_F is the dimensionless thrust coefficient. For an ideal nozzle, the thrust coefficient is given by:

$$C_F = \sqrt{\frac{2\gamma^2}{\gamma-1}\left(\frac{2}{\gamma+1}\right)^{\frac{\gamma+1}{\gamma-1}}\left(1-\left(\frac{p_e}{p_c}\right)^{\frac{\gamma-1}{\gamma}}\right)} + \frac{(p_e-p_a)}{p_c}\frac{A_e}{A_t} \tag{2.8}$$

where p_a is the ambient pressure in Pa. It shows that for a perfectly expanded nozzle, the thrust coefficient is the largest.

Combining the parameters for the thermodynamic and aerodynamic performance results in the following equation for the thrust:

The thrust F can also be defined as:

$$F = \dot{m} \cdot c^* \cdot C_F \tag{2.9}$$

2.3.1. Heat transfer

To reach a high specific impulse, the propellant must absorb as much heat as possible. The resulting equilibrium temperature of the propellant is given by the following equation [31]:

$$T_p = \left(\frac{\eta_c \cdot C \cdot I}{\sigma \cdot \epsilon_p} \right)^{\frac{1}{4}} \tag{2.10}$$

where T_p is the propellant temperature in K, η_c is the dimensionless collection efficiency, C is the dimensionless concentration ratio of the concentrator, I is the incident energy in $\mathrm{W\,m^{-2}}$, $\sigma = 5.6704 \times 10^{-8}\,\mathrm{W\,m^{-2}\,K^{-4}}$ is the Stephan-Boltzmann constant, and ϵ_p is the dimensionless emissivity of the propellant. The collection efficiency is the ratio between the heat absorbed by the propellant and the incident energy. The equation relates the energy entering the propellant to the energy leaving it.

Not all energy goes into the propellant, as inefficiencies lead to the heating of other components. The resulting equilibrium temperature of the absorber is given by the following equation [31]:

$$T_a = \left(\frac{(\eta_o - \eta_c) \cdot C \cdot I}{\sigma \cdot \epsilon_a} \right)^{\frac{1}{4}} \tag{2.11}$$

where T_A is the absorber temperature in K, η_o is the dimensionless optical efficiency, and ϵ_a is the dimensionless emissivity of the absorber. The optical efficiency is the ratio between the heat absorbed by the absorber and the incident energy. The equation relates the energy entering the absorber to the energy leaving it.

For the heat transfer within the solid regions of the thruster, the energy transport equation is used [32]. When no internal energy is produced, the thermal conductivity is constant, and Fourier's law of conductivity is satisfied, the equation simplifies to:

$$\nabla^2 T = 0 \tag{2.12}$$

where T is the temperature of the solid in K. This steady-state Laplace equation describes how heat diffuses through the solid regions. It is used to determine the temperature distribution in the components and helps evaluate the thermal limits.

When using the finite element method, the energy balance equation is given by [29]:

$$[K]\{T\} = \{Q\} \tag{2.13}$$

where $[K]$ is the transfer matrix, T is the vector of nodal temperature, and Q is the vector of nodal heat flow rate. The transfer matrix $[K]$ contains the combined thermal properties of the material for the conduction within and the convection at the boundaries. The vector $\{Q\}$ contains the applied heat sources or sinks at each node, such as absorbed solar irradiation and radiation losses. Each element corresponds to the interaction between nodes. This allows the temperature distribution to be calculated for complex geometries. By solving the resulting system of equations, the temperature distribution of the thruster components can be determined.

To model the radiation heat transfer, the Discrete Ordinates model can be used. This model solves the radiative energy transfer along a set of directions to determine the energy exchange between surfaces

and media. This is especially useful for complex geometries where the thermal distribution is influenced by reflections and shadowing.

For the turbulence, the $k-\epsilon$ equation can be used to predict the effects without resolving all the small flow fluctuations [33]. It uses two additional transport variables: the turbulent kinetic energy k and the turbulent dissipation rate ϵ [34]:

$$\rho\frac{\partial k}{\partial t} = \frac{\partial}{\partial x_i}\left((\mu + \frac{\mu_t}{\epsilon_k})\frac{\partial k}{\partial x_i}\right) + G_k + G_b - \rho\epsilon - Y_M \tag{2.14}$$

where ρ is the density of the propellant in $\mathrm{kg\,m^{-3}}$, k is the turbulent kinetic energy generation term in $\mathrm{m^2\,s^{-2}}$, t is the time in s, μ is the molecular dynamic viscosity in $\mathrm{kg\,m^{-1}\,s}$, μ_t is the turbulent dynamic viscosity in $\mathrm{kg\,m^{-1}\,s}$, G_k is the contribution of the average velocity gradient to the turbulent kinetic energy generation term k in $\mathrm{m^2\,s^{-3}}$, G_b is the contribution of buoyancy to the turbulent kinetic energy generation term k in $\mathrm{m^2\,s^{-3}}$, ϵ is the dissipation rate of turbulent kinetic energy in $\mathrm{m^2\,s^{-3}}$, and Y_M is the contribution of the pulsating expansion of the compressible flow to the total dissipation rate in $\mathrm{m^2\,s^{-3}}$. The transport equation for k accounts for the production of turbulence by velocity gradients (G_k) and buoyancy effects (G_b), the dissipation of turbulent kinetic energy ($\rho\epsilon$), and compressibility effects (Y_M). The turbulent kinetic energy k represents the energy of the fluctuating velocity components of the flow, while ϵ represents how fast this energy is converted into heat due to viscous effects. A damping function is applied to reduce the turbulent viscosity if appropriate, such as near the walls.

2.3.2. Quality Factors

The real performance differs from the performance based on the ideal rocket theory. The assumptions are limitedly valid, resulting in losses due to thermodynamic and fluid dynamic effects such as heat transfer, non-axial flow, flow separation, and friction forces. These effects will be summarised by the discharge coefficient, heating quality and the nozzle flow quality. The subscript ”id” will be used to denote ideal values, and the subscript ”real” will be used to denote real values.

The discharge coefficient will be defined as:

$$C_d = \frac{\dot{m}_{real}}{\dot{m}_{id}} \tag{2.15}$$

where C_d is the dimensionless discharge coefficient. The discharge coefficient accounts for the reduction in mass flow due to viscous effects such as boundary layer formation.

The heating quality will be defined as:

$$\xi_c = \frac{c^*_{real}}{c^*_{id}} \tag{2.16}$$

where ξ_c is the dimensionless heating quality. The heating quality accounts for the energy losses, such as heat conduction to the chamber and nozzle walls.

The nozzle flow quality will be defined as:

$$\xi_n = \frac{C_{F,real}}{C_{F,id}} \tag{2.17}$$

where ξ_n is the dimensionless nozzle flow quality. The nozzle flow quality accounts for losses in direct momentum, such as turbulence and flow separation.

Combining Equation 2.9 with the quality factors results in the real thrust F_{real}:

$$F_{real} = C_d \cdot \xi_n \cdot \xi_c \cdot F_{id} \tag{2.18}$$

By separating the contributions to the differences in thrust, the predictions can be better validated. The quality factors have to be experimentally determined, but can be estimated with empirical relations.

2.4. Nozzle

The design of the nozzle affects all quality factors, making it important to select the right geometry and materials. It is a trade-off between performance, mass, size, manufacturability and cost. The nozzle converges to reach sonic conditions in the throat and then diverges to reach a high exhaust velocity. The shape of the nozzle influences how much the flow diverges, with a bell nozzle having the potential for the lowest flow divergence. Flow divergence is a radial momentum component that does not result in thrust. The radial momentum components of the nozzle exit cancel each other out due to the axial symmetry.

An ideal nozzle is a bell nozzle that expands until the exit pressure is equal to the ambient pressure. However, this results in a very long nozzle, making a truncated version often preferred. A simpler design is the conical nozzle with a constant divergence angle. These nozzles are relatively longer than bell nozzles for the same area ratio, but are easier to design and manufacture. Based on length, performance and mass, a divergence half angle of 15% is often used for conical nozzles [35]. This compromises between divergence losses and the length to reach an expansion ratio. Increasing the nozzle expansion ratio improves the specific impulse, but the increase becomes insignificant past 50:1 [29]. If the nozzle is over-expanded, the exit pressure is higher than the ambient pressure, resulting in a shock to compensate for the pressure difference. The effect of the nozzle expansion for the different nozzles is shown in Figure 2.7.

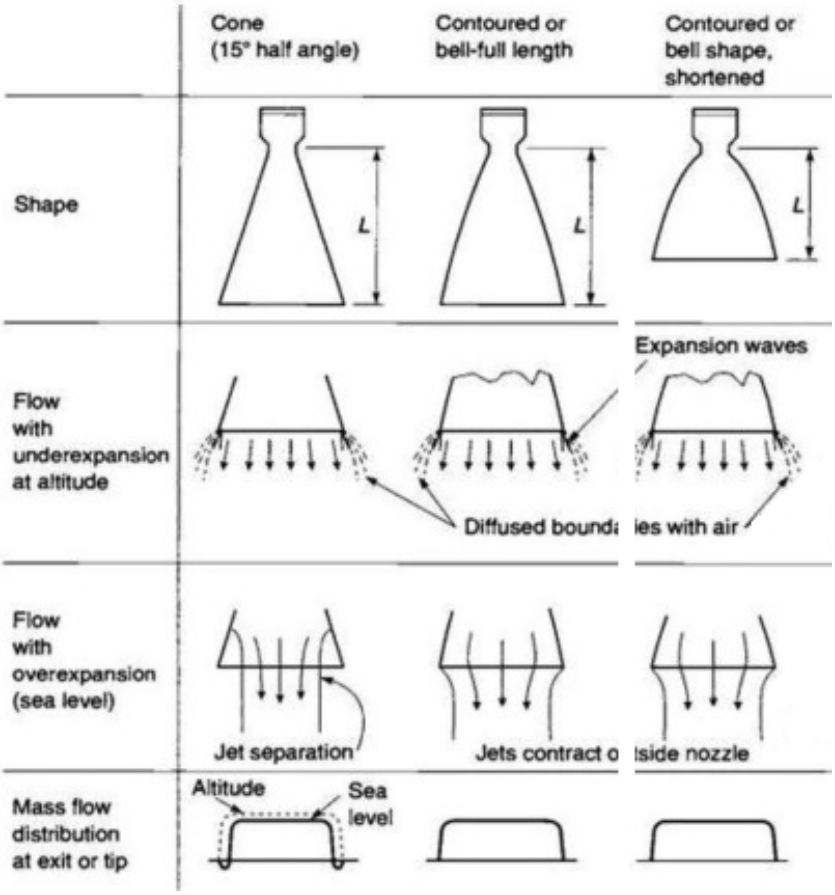

Figure 2.7: The effect of nozzle expansion for different nozzles [30]

For small nozzles, the viscous effects become more significant, especially for a lower Reynolds number. This makes it more difficult to determine the right bell curve, making the conical nozzle outperform the

bell nozzle when not properly designed [30]. For Reynold numbers below 2000, it is recommended not to use bell nozzles [36]. The performance differences are then small, thus manufacturing considerations become more important. Simulations also show that nozzle walls with a higher thermal conductivity, probably due to heat recirculation, result in a higher specific impulse [37]. The material considerations for the nozzle are discussed in section 2.6, because of the similar considerations as for the absorber, due to temperatures and the usage of hydrogen as the propellant.

How much specific impulse is exactly lost by chemical kinetics losses, divergence losses, and viscous losses can be determined with the Two Dimensional Kinetics (TDK) tool [38]. When minimising one loss, another can increase, resulting in a worse overall performance. This makes compromising between the losses important to optimise overall performance. An overview of different losses is shown in Figure 2.8.

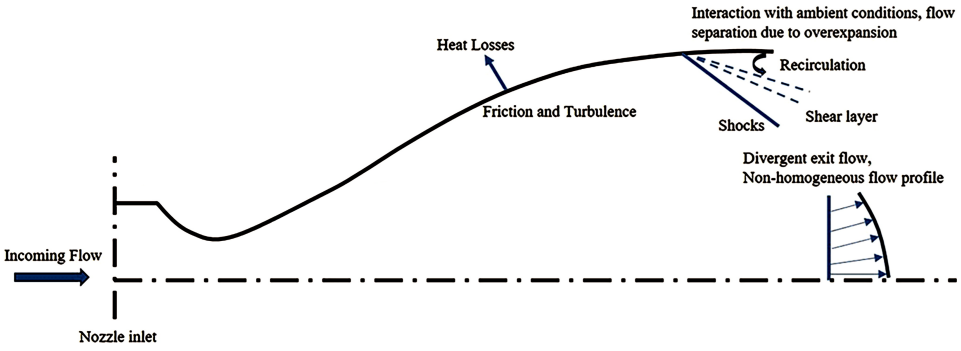

Figure 2.8: Different type of losses in a nozzle [39]

2.5. Absorber

The function of the absorber is to transform the solar irradiation that is received by the concentrator into thermal energy and transfer it to a propellant. The absorber heats directly or indirectly a propellant, which then flows through a Laval nozzle. The part of the absorber that exchanges the thermal energy with the propellant is called the heat exchanger. Radiation losses should be minimised for the maximum efficiency of the absorber. This can be done with insulation and low-emissivity coatings. If less energy is lost, less energy is required to achieve the same propellant temperature, resulting in a higher efficiency. Hydrogen provides the highest specific impulse due to its lower molar mass and is the best convective coolant for thruster components due to its high specific heat capacity. When placing a secondary concentrator inside the absorber, the propellant can be used to cool the concentrator as well [29]. A secondary concentrator can increase the solar flux even further, but unwanted absorption by it does increase its temperature more due to the higher concentrated energy. Some material considerations for the absorber are discussed in section 2.6, because of the similar considerations as for the nozzle, due to temperatures and the usage of hydrogen as the propellant.

2.5.1. Indirect Heating

Indirect heating means that there is a physical wall between the solar radiation and the propellant [40]. The windowless heat exchanger cavity concept is an example of indirect heating. The solar radiation is focused in a cavity, and a propellant then flows through its walls or on the other side of the wall. The propellant thus does not enter the cavity. The propellant cools the cavity walls and prevents them from overheating while the propellant temperature increases. The heated propellant then flows to the thruster. Examples are a spiral or tubes in the walls, or a porous medium through which the propellant flows. Often, a cavity is used, but a flat material is also possible.

A windowed heat exchanger cavity has a window through which the solar radiation enters. For this concept, the propellant does enter the cavity. Through the process of transpiration, the propellant enters the cavity and then flows to the thruster. The transpiration-cooled wall is heated by the solar irradiation. A disadvantage of indirect heating is that the allowable temperature of the wall material limits the maximum propellant temperature. This is because the propellant cannot achieve higher temperatures than the heat exchanger. Sketches of different indirect heating concepts are shown in Figure 2.9.

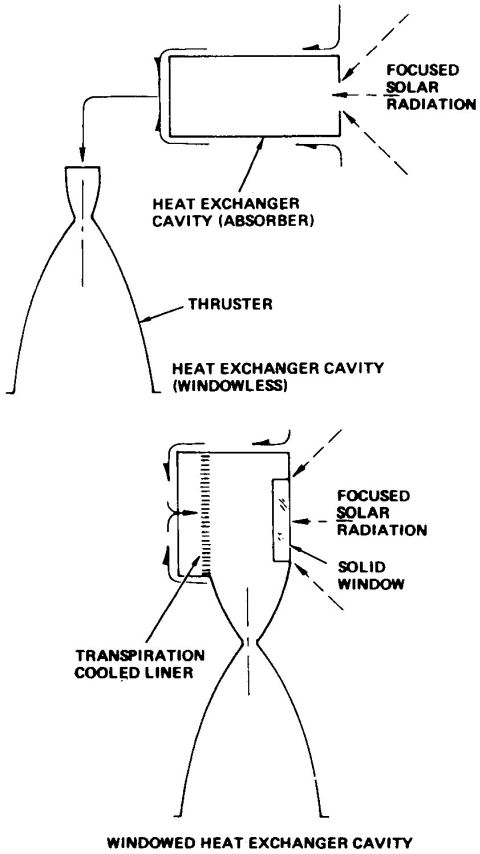

Figure 2.9: Indirect heating absorber concepts [40]

2.5.2. Direct Heating

Direct heating means that a propellant is heated by an added material that flows in the propellant and absorbs the solar radiation [40]. This so-called seedant absorbs the solar irradiation more easily than the transparent propellant. Because of the high combined surface area of the seedant, the heat easily transfers to the propellant. It is important that the seedant does not deposit on the window, as this decreases the solar radiation that enters the absorber. When the seedant is discharged through the nozzle, it lowers the specific impulse. It can also deposit on the collector and lower its performance.

To prevent this, a centrifugal force can be used to keep the seedant near the wall of the absorber. Due to its higher mass, it gets pushed to the outside, while propellant without seedant collects in the centre. The propellant can then flow through a hole on the longitudinal axis of the absorber with a sufficiently small diameter that prevents the seedant from entering the nozzle. This centrifugal force can be created by introducing a vortex flow in the absorber. When injecting a propellant tangentially, a vortex is created that causes the propellant to rotate around the longitudinal axis. If the seedant is small and has a large combined surface area, the heat transfers better to the propellant. However, its mass then also becomes lower, resulting in the seedant being forced outwards less. A larger and heavier seedant, on the other hand, is better separated from the propellant but has less surface area. An analysis of the windowed vortex flow concept showed that for efficient seedant discharge minimisation, particles are needed that are too large for efficient solar irradiation absorption.

Another concept uses a rotating bed to create the centrifugal force. The propellant then enters the absorber via the porous walls of the rotating cylinder. The rotating bed, however, requires a mechanism to rotate. Different mechanisms were compared, but no perfect solution exists as each option has its own advantages and disadvantages. An oversight of the advantages and disadvantages of each approach is shown in Figure 2.10. Sketches of the different discussed direct heating concepts are shown in Figure 2.11.

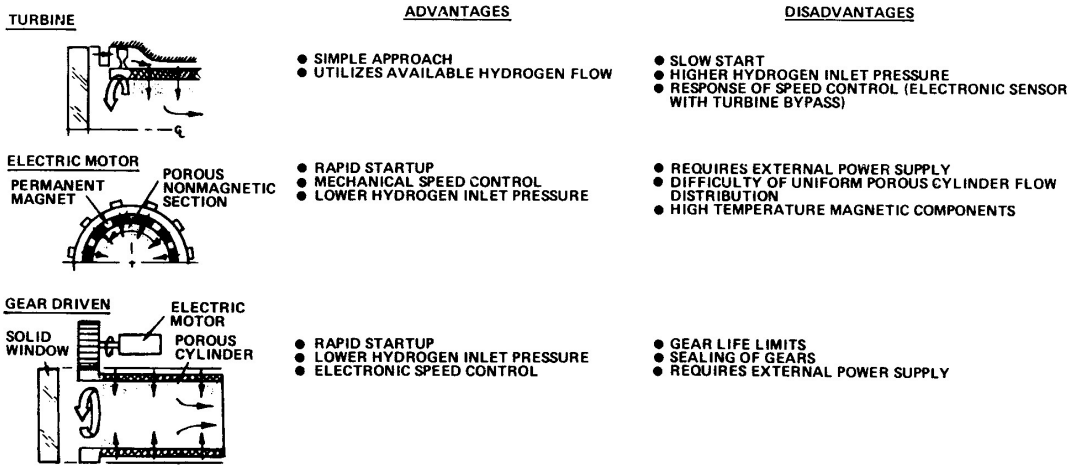

Figure 2.10: Advantages and disadvantages of different mechanisms for the rotating cylinder bed concept [40]

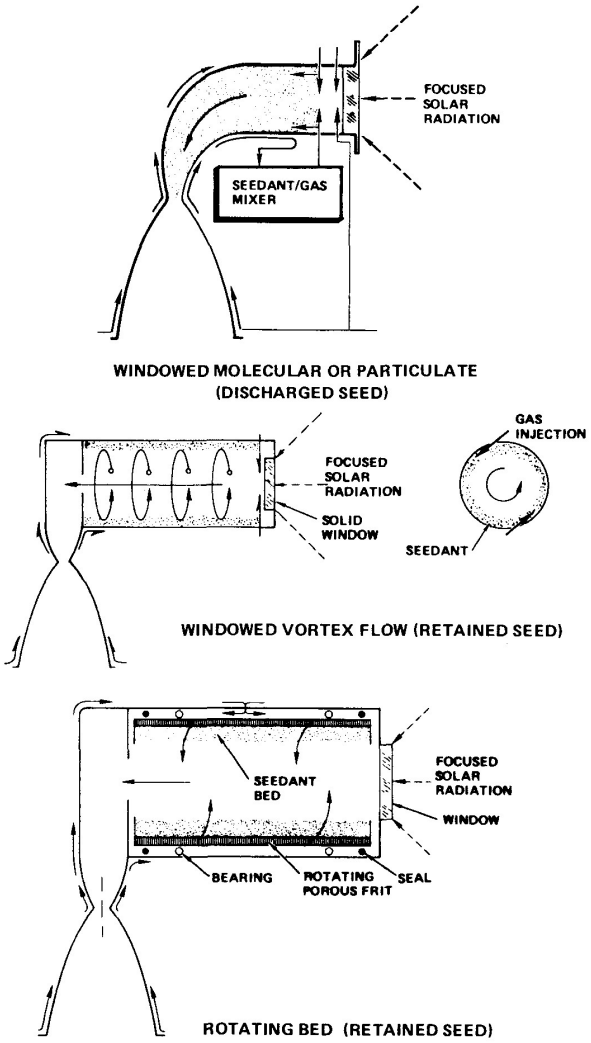

Figure 2.11: Direct heating absorber concepts [40]

2.5.3. State-of-the-Art

The spiral runner is the most used concept in previously proposed designs, but optimisation efforts still lead to a relatively low heat transfer efficiency [41]. To increase the temperature of the propellant further, a longer spiral is needed. Because this increases the size of the system, the losses also increase. A relatively long and heavy absorber is thus required to heat the propellant more.

A recently proposed absorber by the National University of Defence in China is based on the principle of transpiration cooling [29]. The design is based on technology used by the US Aerojet Corporation to cool the thrust chambers with hydrogen [42]. The propellant flows through small holes called control runners at a controlled rate. Based on the number of control runner and their length, the required mass flow can be achieved. These control runners are made in stacked plates with a larger thickness on the inside than on the outside. This results in a large surface area between the plates for heat transfer, called disperse runners. Between the disperse runners, the flow velocity is relatively low compared to the control runners. Because the propellant is most of the time in contact with the disperse runners, most of the heat exchange happens there.

After cooling the secondary concentrator in the centre, the propellant flows to the colder outside again. Via the discussed runners, the propellant then flows inwards again while being heated. This makes the design complex due to its flow path, but the hottest flow stays in the centre, reducing the thermal losses. Local overheating does not significantly influence the control runner, resulting in a stable mass flow and performance. The structure of the absorber is shown in Figure 2.12.

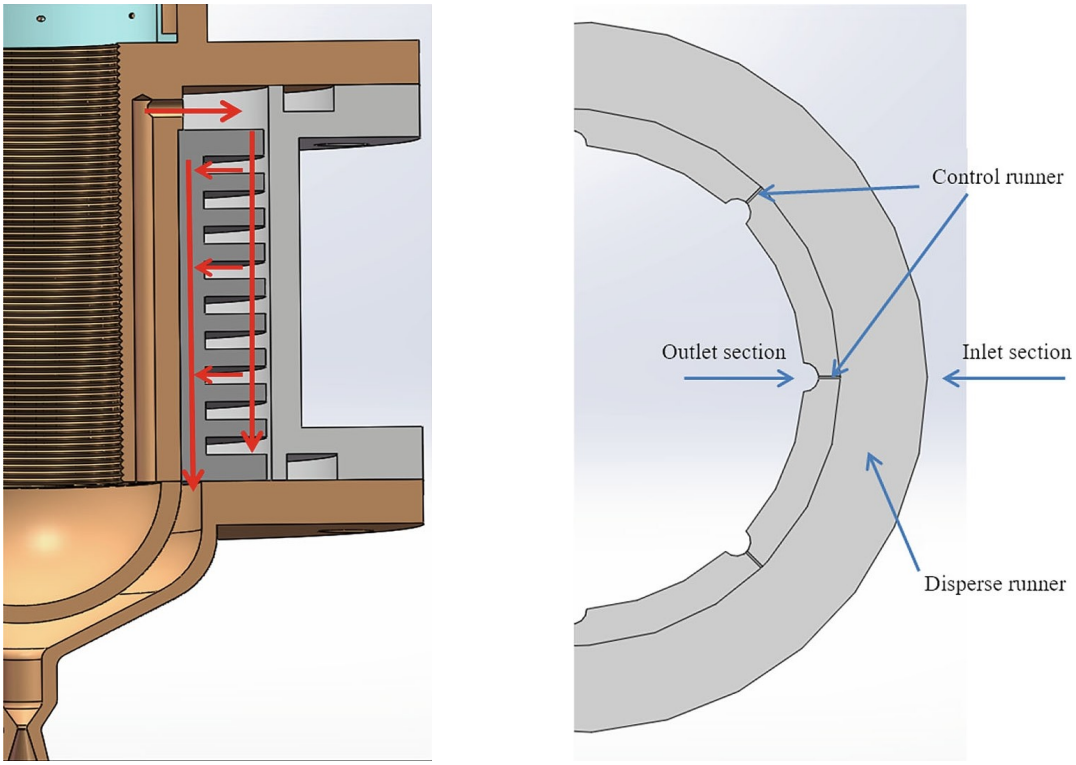

(a) Flow route of the propellant

(b) Names of the runners on the laminates

Figure 2.12: Structure of the laminated absorber [29]

To simulate the heat transfer in the runners, the symmetry of the plates was used to model the system. The symmetry of the absorber requires only part of the absorber to be modelled when using appropriate boundary conditions. The assigned boundary conditions at the symmetry planes control the propellant flow and the conduction in the plates. The model showed that the propellant temperature exceeds $2300\,\mathrm{K}$, which is close to the wall temperature of $2400\,\mathrm{K}$, demonstrating the high efficiency of the concept.

2.5.4. Thermal Energy Storage

The sun-pointing and thrusting direction can be decoupled when implementing a TES system. This does make the overall system more complicated, as insulation and thermal dams are required. Furthermore, the system weight increases due to the required material to store the thermal energy. Different kinds of TES are possible, such as sensible heat or phase change TES.

Sensible heat TES is the simplest design option, but has the lowest energy density. For sensible heat TES materials, it is important to have high specific heat, high melting point, high density, low-temperature expansion, and high thermal conductivity. Beryllia has a high energy density but is expensive and toxic. Refractory metals have high densities and melting points but a low heat capacity. Graphite is a relatively cheap option and easy to manufacture, but requires a non-reactive coating because it reacts with hydrogen. Boron carbide has a higher heat capacity than graphite but is more difficult to manufacture. Boron nitride has a similar performance to graphite but does not react with hydrogen.

For phase change TES materials, it is also important that the phase transition temperature is close to the operating temperature and that the heat of transition is high. Phase change TES materials can have issues such as structure bursting or void formation, but have a high energy density and can provide a constant temperature [16]. Silicon and boron have high heats of fusion and high melting temperatures [26]. Because they are elemental, these materials do not break down. Boron has the best performance but requires more research.

2.6. Structural Materials

The selection of the structural materials depends on the maximum temperatures to which they will be exposed. For temperatures above $1300\,\mathrm{K}$, refractory metals or alloys based on them are used due to their high heat resistance. A less resistant material can be used in combination with a protective coating for areas that do not become too hot. Protection against hydrogen erosion is necessary for temperatures above $3000\,\mathrm{K}$ because it then only dissociates significantly into atomic hydrogen [43].

At lower temperatures, the hydrogen can still affect the structure due to hydrogen embrittlement. Hydrogen atoms can enter the metal and collect in weak spots. This causes metals to lose ductility and increase the risk of fractures at stresses below their nominal strength [44]. How easily a material is affected by hydrogen embrittlement depends on temperature, stress, and material microstructure. High pressure increases penetration, and high temperatures increase hydrogen diffusion, but thermal stresses can promote cracking. A denser material makes it harder for the hydrogen atoms to penetrate. Low-permeable materials such as rhenium or low-permeable coatings protect against hydrogen embrittlement. Hydrogen embrittlement thus has to be taken into account carefully when selecting the structural materials, to ensure long-term reliability under high-pressure hydrogen flow.

Environmental factors also influence the materials when exposed [45]. Exposure to radiation in space can affect microstructures, possibly causing embrittlement over time. When the system is not in a perfect vacuum, reactions between the environmental gases and the materials can occur. Materials can, for example, oxidise due to oxygen and elevated temperatures. Thermal cycling due to periods of receiving solar irradiation and periods of eclipse can create fatigue. Therefore, testing in environmental conditions is crucial for ensuring reliability.

Rhenium does not lose ductility due to recrystallisation at high temperatures, but is more scarce than the refractory metals molybdenum and tungsten. It is possible to dope molybdenum to prevent unwanted recrystallisation by introducing intentional secondary recrystallisation [17]. When working with single-crystal molybdenum, a tungsten coating can be used to seal different parts.

2.7. Findings

This section discusses the answers to the review questions for the literature review and how these findings will be used. The first review question, with its sub-questions, was:

1. *How has STP evolved over time?*
    1.1 *What were the key milestones in the development of STP?*

1.2 *How did past attempts influence current designs?*

STP has evolved from early conceptual ideas in the 1950s, through ground-tested prototypes and feasibility studies in the 1960s–1980s, to more advanced designs incorporating secondary concentrators and thermal energy storage in the 1990s–2020s.

Key milestones include the first thruster tests, the deployment of inflatable concentrators, the inclusion of TES systems, and optical decoupling.

Based on the requirements for current designs, the outcomes of performed studies are used to select a concept, and newly developed technologies such as optical decoupling and TES systems are included if needed.

2. *What are the strengths and weaknesses of previous STP designs?*

    2.1 *How do different STP designs compare in terms of efficiency and feasibility?*

    2.2 *What are the major design limitations encountered in previous implementations?*

Previous STP designs show a range of efficiencies and feasibilities. Colder and simpler designs lead to more reliable systems, but at the cost of performance. More complex technologies can be implemented to improve the performance, but at the cost of reliability. Especially, the effects of the high heat can cause problems for different materials, such as the formation of cracks and leaks. Another limitation is the interaction with the high-temperature propellant.

3. *What are the most advanced STP technologies currently available?*

    3.1 *What is the current TRL of various STP systems?*

    3.2 *How do state-of-the-art designs address the challenges of earlier models?*

Many countries have researched or are researching STP, but the TRL is still limited to a TRL 6 for subsystems being tested in a relevant environment. The efficiencies of the concepts have improved over the years by making the heat exchangers more efficient and by reducing the thermal losses. The material studies performed helped improve the reliability of the designs due to the newly developed technologies.

The history of STP helps with trading off different concepts by better understanding their advantages and disadvantages. Furthermore, the research performed will help with making initial estimations for the system.

4. *What are the fundamental relations governing rocket propulsion?*

    4.1 *What are the primary equations used to describe thrust, impulse, and efficiency?*

    4.2 *What role do thermodynamic and fluid dynamic principles play in propulsion analysis?*

The most fundamental equations for thrust and specific impulse are Equation 2.1 and Equation 2.2 respectively. The performance of the system can be split into the characteristic velocity and the thrust coefficient, described by Equation 2.5 and Equation 2.8. The quality factors can be used to describe the different efficiencies of the system. The identified fundamental relations will help in understanding and modelling the system.

The thermodynamic and fluid dynamic principles are used to describe the heat transfer within the system and the performance. These principles are used to determine characteristics of the propulsion system.

5. *How do ideal and non-ideal performance estimations compare?*

    5.1 *What assumptions are made in ideal performance estimations, and how do they simplify calculations?*

    5.2 *What real-world effects (e.g., heat losses, flow separation, turbulence, friction forces) lead to deviations from ideal models?*

Real-world effects such as heat transfer, non-axial flow, flow separation, friction forces, etc., are ignored for ideal performance estimations but can be compensated for by applying correction factors. This will

help with designing a system with a thrust and specific impulse performance that complies with set requirements.

All real-world effects that result in energy not being converted into momentum that generates thrust lead to deviations from the ideal models.

6. *How does the nozzle shape and material affect performance?*
    - 6.1 *How do different nozzle geometries influence exhaust flow and thrust?*
    - 6.2 *What materials are commonly used for space nozzles, and how do they withstand extreme temperatures?*

The nozzle shape is important for the performance of the system. The shape influences the exhaust flow and how strongly real-world effects reduce the thrust. For smaller nozzles, conical shapes are often used. Viscosity strongly affects small nozzles, making it difficult to design an ideal bell curve. For smaller Reynolds numbers, the conical design can outperform the bell nozzle. After determining the flow characteristics, the appropriate shape can be selected.

For the nozzle material, refractory metals are often used, with some being more scarce than others. Rhenium is a great-performing material to withstand extreme temperatures, but it is an expensive option.

7. *What are the challenges of nozzles for STP?*
    - 7.1 *What are the main constraints in fabricating the nozzle?*
    - 7.2 *How do space environmental factors (vacuum, radiation, thermal cycling) impact long-term nozzle durability?*
    - 7.3 *How does the usage of hydrogen as a propellant affect the nozzle?*

Complex nozzle curves are more difficult to manufacture for small nozzles as the effects of deviations become more significant. Interaction with the environment can impact the reliability of the material due to reduced strength. Gases can react with the material, radiation can affect the microstructure, and thermal cycling can lead to fatigue. Hydrogen can penetrate the materials and make them brittle. When selecting a less dense material, it is important to protect the material against hydrogen embrittlement. A trade-off will be performed to determine the right material, based on the reviewed publications.

8. *What are the different absorber designs used in STP systems?*
    - 8.1 *What types of absorbers are currently used in space propulsion systems?*
    - 8.2 *What are the advantages and disadvantages of each absorber design?*
    - 8.3 *How do the absorber designs interact with the collector?*

Most proposed concepts make use of indirect heating of the propellant. A cavity in the absorber receives the concentrated solar radiation and transfers the heat to the propellant. It is possible to store thermal energy inside the system by implementing a sensible or phase change TES material. The selection of a TES material depends on many considerations such as performance, manufacturability and reliability. A spiral runner is often used due to its simplicity, but a recently proposed laminated heat exchanger shows an improved performance without compromising reliability. The reviewed publications will help determine the most suitable absorber concept and whether a TES material should be included.

Secondary contractors can have heat transfer with the heat exchanger, but the interaction with the primary concentrator is limited due to the spacing between the components, besides the transmission of solar irradiation.

9. *How do material properties impact absorber efficiency?*
    - 9.1 *What are the key parameters for evaluating absorber performance?*
    - 9.2 *How do environmental factors influence the performance of the materials?*
    - 9.3 *How does the usage of hydrogen as a propellant affect the absorber performance?*

The most important parameter of the absorber material is its conductivity. The materials should easily transfer the absorbed heat to the propellant. The absorber components that radiate should have a low emissivity to limit the thermal losses of the system and improve its efficiency. The considerations for the nozzle material also hold for the absorber.

3

Workflow

This chapter discusses the workflow of the report. First the main research questions are introduced. Then the following design process with intermediate phases are discussed, followed by the validation of the design.

3.1. Research questions

The goal of this report is to design the secondary propulsion system for the Green SWaP mission. This propulsion system is a based on the principle of STP. To tailor the design specifically for this mission, the following research question is defined:

1. *What is the most suitable STP system for the Green SWaP mission?*

This research question will be answered by using the information found during the literature review and create different design options. Then based on what is required for the propulsion system, the most suitable options are selected.

After creating a design, it has to be optimised for the Green SWaP mission, resulting in the following research question:

2. *How can the STP system be optimised for the Green SWaP mission?*

The optimisation goal will be defined, together with the optimisation process itself.

Finally, the design will have to be validated to ensure the reliability of the system and it meeting the requirements. This results in the following research question:

3. *How can the STP system be experimentally validated?*

This research question will be answered by first determining what needs to be validated and then how this can be done.

3.2. Phases

This section discuss the phases of the project, with the first phase being the performed literature review. Additional research questions are used for the phases to guide the process and answer the main research questions. The next step is to determine the requirements for the design based on the Green SWaP mission, this is done with the following dedicated research questions:

1. *What performance characteristics are required for the thruster?*
    1.1 *What is the required thrust of the thruster?*
    1.2 *What is the required minimum specific impulse of the thruster?*

2. *What functionalities are required for the thruster?*

Then, based on the literature review, different concepts will be created. A selection of these concepts is made, supported by the information found during the literature review and the requirements. To support the concept selection, the following research questions are used:

3. *What type of absorber is the most suitable for the mission?*
    - 3.1 *What type of heating is the most suitable for the mission?*
    - 3.2 *What type of thermal energy storage is the most suitable for the mission?*
4. *What nozzle is the most suitable for the mission?*
    - 4.1 *What nozzle shape is the most suitable for the mission?*
    - 4.2 *What protection against hydrogen is the most suitable for the mission?*

For the selection, a preliminary design phase follows. To guide the preliminary design phase, the following research questions will be used:

5. *What materials are the best option for the thruster?*
    - 5.1 *What material is the best option for the cavity?*
    - 5.2 *What material is the best option for the heat exchanger?*
    - 5.3 *What material is the best option for the nozzle?*
    - 5.4 *What material is the best option for the insulation?*
6. *What are the key parameters of the design?*

Then, a mathematical model will be created to analyse the design more accurately. Based on this model, the design will be simulated to have a better prediction of its performance. Based on the findings of the preliminary design phase and the simulation results, an improved design will be iterated. This design will be optimised to get to the final design. For this process, the following research questions are identified:

7. *What tools are the most suitable to analyse the design?*
    - 7.1 *What are the best ways to model the design?*
    - 7.2 *How can the models be used to optimise the design?*

The design will have to be experimentally validated. This validation is done with the following research questions:

8. *What are the goals of the experimental testing?*
    - 8.1 *What are the goals of testing the materials?*
    - 8.2 *What are the goals of testing the performance?*

The resulting workflow with different phases can be visualised and is shown in Figure 3.1.

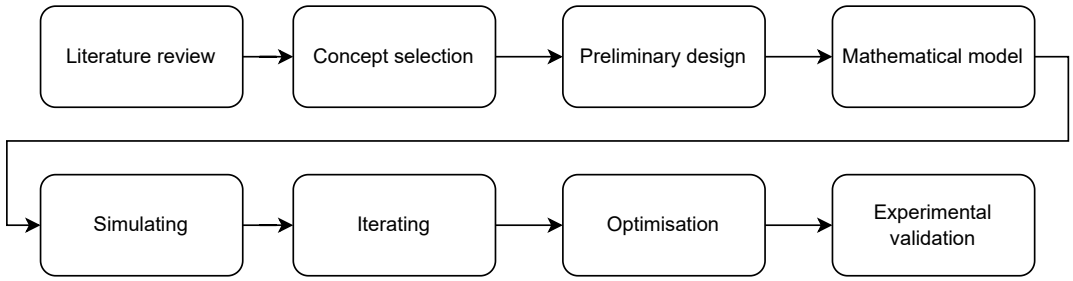

Figure 3.1: Workflow of the project

4

Concept selection

This chapter will discuss the selection of concepts that will be worked out in more detail. First, the requirements of the system will be discussed, which will be a combination of requirements provided by the GreenSWAP mission and those based on the literature review.

4.1. Requirements

To determine the requirements of the system, the following additional research questions are used:

1. *What performance characteristics are required for the thruster?*
    1.1 *What is the required thrust of the thruster?*
    1.2 *What is the required minimum specific impulse of the thruster?*
2. *What functionalities are required for the thruster?*

The requirements for the thruster are determined to ensure that the thruster's performance complies with what is required for the spacecraft. The given requirements are stated in Table 4.1.

Table 4.1: Given requirements for the propulsion system

ID	Type	Requirement Description
TRU-01	Thrust	The thrust generated by the propulsion system shall be $1.0\,\mathrm{N}$.
ISP-01	Specific impulse	The specific impulse of the propulsion system shall exceed TBD $500\,\mathrm{s}$
TES-01	Energy storage	Two propulsion systems shall be able to burn for $30\,\mathrm{min}$ during an eclipse with a $30\,\%$ margin.
PRE-01	Tank pressure	The propellant tank shall be able to store the propellant with a pressure of $5.0\,\mathrm{MPa}$.

When assuming an ideal system, Equation 2.1 and Equation 2.2 can be used in combination with requirement TRU-01 and ISP-01 to determine the mass flow. This results in $\dot{m}_{id} = 2.039 \times 10^{-4}\,\mathrm{kg\,s^{-1}}$. However, if a higher specific impulse is reached, the ideal mass flow becomes less.

When assuming an ideal expansion, the equivalent velocity equals the exit velocity, as there is no pressure thrust. When combining Equation 2.2 and Equation 2.3 with ISP-01, the chamber temperature can be determined. This results in $T_c = 848\,\mathrm{K}$. However, to account for real-life effects and losses, the heat exchanger will first be designed to heat the propellant to $3000\,\mathrm{K}$, as hydrogen dissociation becomes significant above this temperature. It is assumed that to achieve this temperature, the materials in contact with the hydrogen should reach a temperature of $3100\,\mathrm{K}$.

TES-01 is based on the worst-case scenario that at least one thruster can burn during an eclipse. The eclipse time is thus $t_{ec} = 30\,\mathrm{min}$. Based on the ideal mass flow, the TES system of a single thruster shall thus be able to heat $0.25\,\mathrm{kg}$ propellant.

When assuming there is no pressure drop between the tank and the thruster, the thrusters inlet pressure will be $5.0\,\mathrm{MPa}$. This pressure will be used for the inlet conditions of the heat exchanger.

The given requirements and the calculations lead to additional requirements for the system. These additional requirements are stated in Table 4.2.

Table 4.2: Requirements for the propulsion system

ID	Type	Requirement Description
TEM-01	Temperature	The heat exchanger shall heat the propellant to at least $848\,\mathrm{K}$.
MAT-01	Material	The heat exchanger material shall be able to withstand temperatures up to $3100\,\mathrm{K}$.
MAT-02	Material	The materials exposed to the propellant shall be able to withstand hydrogen embrittlement.

4.2. Design Option Tree

To select the concept or concepts for the propulsion system, the following research question will be used:

3. *What type of absorber is the most suitable for the mission?*
    - 3.1 *What type of heating is the most suitable for the mission?*
    - 3.2 *What type of thermal energy storage is the most suitable for the mission?*
4. *What nozzle is the most suitable for the mission?*
    - 4.1 *What nozzle shape is the most suitable for the mission?*
    - 4.2 *What protection against hydrogen is the most suitable for the mission?*

To select the concept or concepts for the propulsion system, a design option tree for the different components is first made. The design option tree is shown in Figure 4.1 and includes the heating method, TES, and nozzle shape.

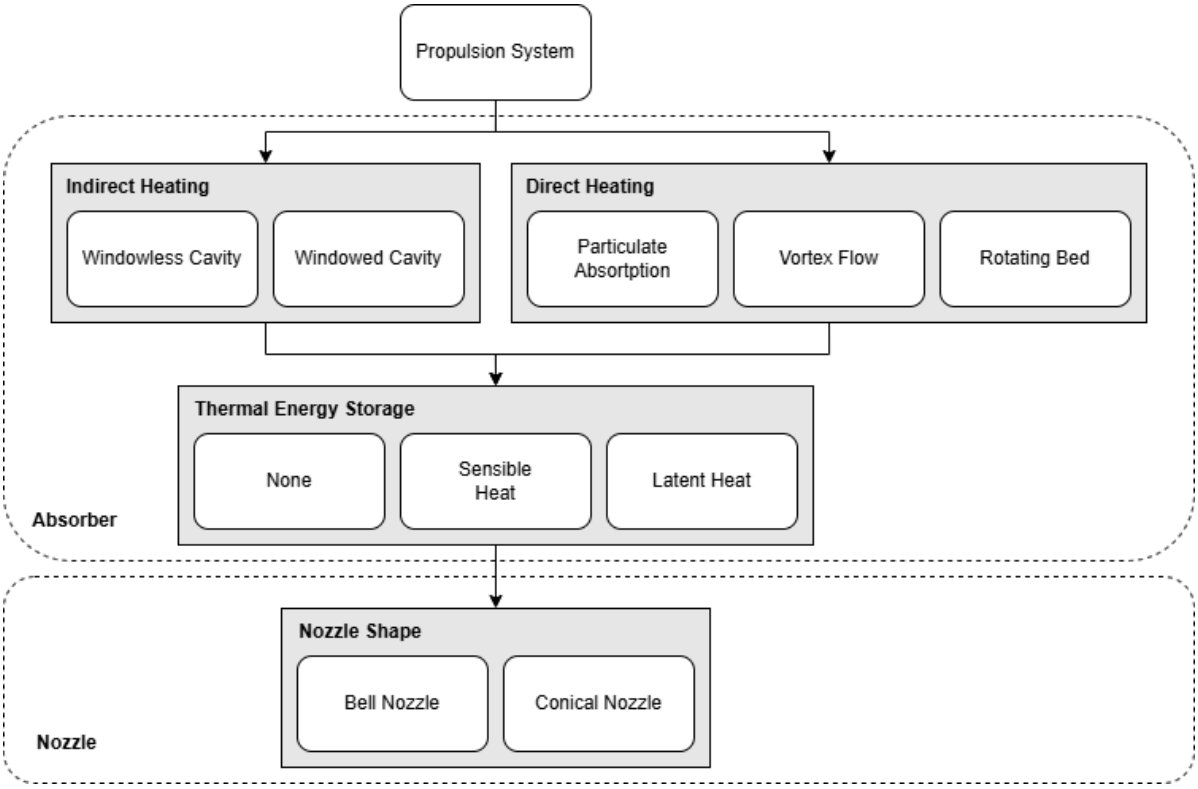

Figure 4.1: Design option tree for the propulsion system

4.3. Heating Method

In section 2.5, multiple direct and indirect heating methods were identified. The direct heating methods made use of a seedant that heats the propellant, and the indirect heating methods made use of a cavity that heats the propellant. Because the propulsion system is required to function while not receiving sunlight, direct sunlight will not be possible. However, to analyse the different concepts and compare them, this requirement will at first not be taken into account. To compare the achievable thrust and specific impulse, a study performed by Rocketdyne is used [40]. The results of this study are shown in Figure 4.2. It shows that to achieve a higher propellant temperature and thus a higher specific impulse, a direct heating method is required.

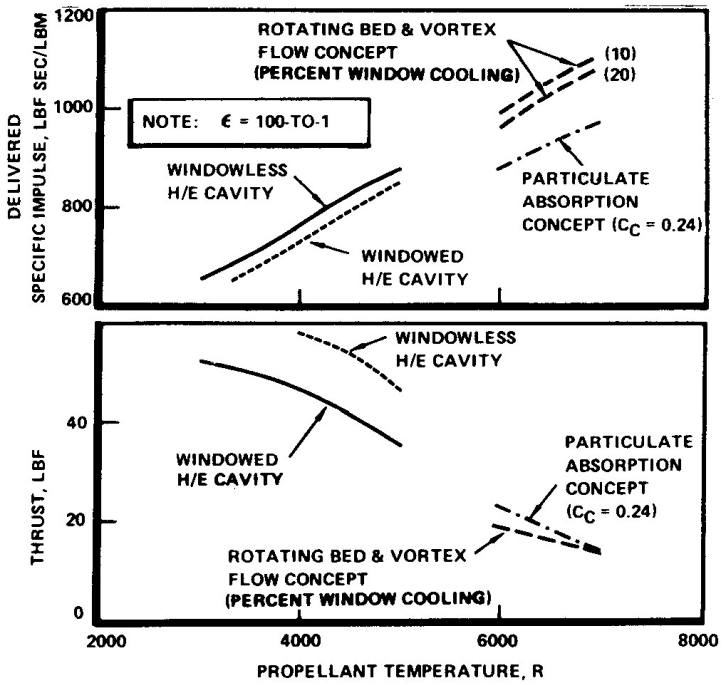

Figure 4.2: Performance comparison of absorber concepts [40]

The particulate absorption concept does not retain the seedant, leading to unwanted deposition and performance losses. The vortex flow and rotating bed concepts retain the seedant by introducing a centrifugal force, but are more complex. The required propellant temperature is close to the end of the specific impulse range of the indirect heating methods in the study. This means that an indirect method is not required to reach a sufficiently high propellant temperature. This relatively low temperature for an indirect heating method means that less surface area for the seedant is required to transfer the heat. Larger and heavier particles can thus be used to increase the centrifugal force and retain more seedant. However, a reduced centrifugal force at the beginning or end of a thrusting period can still lead to unwanted particle loss.

The windowed cavity concept and the direct heating concepts make use of a window to contain the propellant. To prevent the window from cracking, it should be cooled as it can typically withstand less heat than the structural material. When the seedant deposits on the window, local hotspots are formed, which can lead to cracks. Furthermore, the deposition results in less solar energy being available to heat the propellant. An overview of the advantages and disadvantages of the different concepts is given in Table 4.3.

Table 4.3: Advantages and disadvantages of heating method concepts

		Advantages	Disadvantages
Indirect heating	**Windowless cavity**	• Higher thrust than direct heating • Simplest design	• Lower specific impulse than direct heating
	Windowed cavity	• Higher thrust than direct heating	• Lower specific impulse than direct heating • Possible window cracking
Direct heating	**Particulate absorption**	• Higher specific impulse than indirect heating • High thermal efficiency	• Can only function while receiving sunlight • Reduced performance due to discharged particles • Particle deposition in nozzle throat or on window
	Vortex flow	• Higher specific impulse than indirect heating • High thermal efficiency	• Can only function while receiving sunlight • Particle size trade-off between heat transfer and particle loss • Possible particle loss and deposition • Complex flow dynamics
	Rotating bed	• Higher specific impulse than indirect heating • High thermal efficiency	• Can only function while receiving sunlight • Particle size trade-off between heat transfer and particle loss • Possible particle loss and deposition • Requires a mechanism for rotation

4.3.1. Trade-off

The advantages and disadvantages of the different heating methods are all related to performance and reliability. The more complex concepts are less reliable but offer better performance. A trade-off will thus be performed between these criteria.

In the trade-off table, the following colour scheme will be used to rate the different concepts for each criterion:

- Excellent (Marked with a 'G' for 'Green')
- Good (Marked with a 'L' for 'Lime')
- Average (Marked with a 'Y' for 'Yellow')
- Bad (Marked with an 'O' for 'Orange')
- Unacceptable (Marked with an 'R' for 'Red')

The highest rating "Excellent" will receive a score of 5 and the lowest rating "Unacceptable" will receive a score of 1. This rating and scoring system will be used for every trade-off.

Based on Figure 4.2, the performance scores are determined. Because the vortex flow concept and rotating bed concept have can reach a comparable high specific impulse and the same thrust, they receive a score of 5. Because the particulate absorption concept can reach a lower specific impulse than the other direct heating concepts, it receives a score of 4. The indirect heating concepts can reach an even lower specific impulse, with the windowless cavity providing a larger thrust than the windowed cavity. Due to their similar specific impulse but difference in thrust, the windowless cavity and the windowed cavity sore a 3 and 2 respectively.

The windowless cavity is the simplest and most reliable design, and receives a reliability score of 5. Because a window has the possibility to crack, the windowed cavity receives a score of 4. Then there

is a jump in reliability for the direct heating concept. To generate the centrifugal forces, the vortex flow and rotating bed concept are significantly more complex than the indirect heating concepts, resulting in a score of 2. Because not retaining the seedant in the particle absorption concept poses significant risks for the functioning of the heat exchanger itself, but also the nozzle, this concept receives a score of 1. The resulting trade-off table is shown in Table 4.4.

Table 4.4: Cavity concept trade-off

Criteria / Concepts	Performance	Reliability	Score
Windowless cavity	Y: 3	G: 5	4.0
Windowed cavity	O: 2	L: 4	3.0
Particulate absorption	L: 4	R: 1	2.5
Vortex flow	G: 5	O: 2	3.5
Rotating bed	G: 5	O: 2	3.5

The trade-off shows that the windowless cavity is the best option. It has an average performance, but the discussed study shows that it is sufficient for the required performance. This concept has a lot of heritage, as most proposed designs use this heating method due to its simplicity and reliability. To validate the outcome of the trade-off, a sensitivity analysis will be performed based on the positions when excluding a criterion.

When excluding the performance criterion, the windowless cavity concept wins with a score of 5.0 due to its high reliability. The windowed cavity with its score of 4.0 then scores higher than the vortex flow and rotating bed concept, which score a 2.0. The particulate absorption concept still scores the lowest with a 1.0.

When excluding the reliability criterion, the vortex flow and rotating bed now win due to their high performance, with a score of 5.0. The particulate absorption concept now gets the third position with a score of 4.0 instead of the last position. The windowless cavity gets the fourth position with a score of 3.0, and the windowed cavity gets the last position with a score of 2.0.

An overview of the positions per excluded criterion is given in Table 4.5.

Table 4.5: Sensitivity analysis of heating method concepts

Comparisons / Concepts	W/o performance	W/o reliability	Position
Windowless cavity	1	4	2.5
Windowed cavity	2	5	3.5
Particulate absorption	5	3	4.0
Vortex flow	3	1	2.0
Rotating bed	3	1	2.0

The sensitivity analysis shows that the vortex and rotating bed concepts have a better average position than the windowless cavity concept that won the trade-off. However, due to the requirement to function while not receiving sunlight, these two concepts are not feasible. The windowless cavity concept is therefore selected. A sketch of a windowless cavity is shown in Figure 4.3.

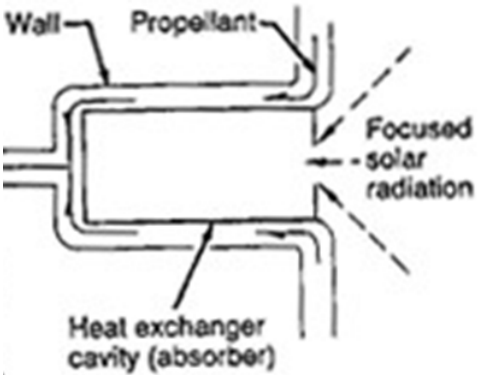

Figure 4.3: Sketch of the windowless cavity concept [40]

The cavity itself can have many shapes. Examples are conical cavities, cylindrical cavities, spherical cavities, or cavities that consist of a combination of these shapes. The cavity should absorb as much solar energy as possible, thus, the amount of light reflected out of the cavity should be minimised. Ray tracing is a suitable method to analyse the reflections within the cavity to determine the efficiency [46]. A conical shape results in the best absorption because less light is reflected back towards the source. However, the cylindrical cavity shape provides the best flux distribution. A good distribution prevents local heat spots. To compromise between these two qualities, a cylinder will be used with a cone on both circular sides. To improve the absorptivity of the cavity wall, the surface will be roughened [29]. This distributes the solar flux better, resulting in lower radiation losses. For the absorber cavity to act as a blackbody, the surface area of the cavity should be at least 50 times larger than the cavity opening [47].

There are also many ways in which the propellant can flow through the walls of the cavity. During the literature study, a complex laminated structure was discussed that demonstrated a high efficiency. Other options are a spiral tube along the cavity shape, multiple straight tubes in the walls, or a porous material in the wall. To determine how the system will be protected against hydrogen, it is important to know how the propellant will flow through the walls. If a porous material is selected, coating is not possible. Thus, the material needs to withstand the hydrogen itself. For runners through the wall, it is possible to be coated, but the high internal temperatures can still damage the material under the coating [47]. For the propellant flow, a trade-off between manufacturability and performance is needed. A thermofluidic analysis will be performed to support the trade-off of the propellant flow. This will be done for a concept with porous material, for a spiral runner, and for straight channels.

4.4. Thermal Energy Storage

TES allows the propulsion system to function when no sunlight is received. This improves operational flexibility at the cost of the added mass. When implementing a TES system, the sensible heat and latent heat concept can be selected. Sensible heat TES is a simpler and more reliable option, and latent heat TES is less reliable but offers a higher energy density. The phase change material requires a solid material to enclose it, but there is a risk of cracks forming in the case [26]. An overview of the advantages and disadvantages of the different concepts is given in Table 4.6.

Table 4.6: Advantages and disadvantages of thermal energy storage concepts

	Advantages	**Disadvantages**
None	• Simplest design • Lowest mass and volume	• Can only function while receiving sunlight
Sensible heat	• Can function while not receiving sunlight • Easy to implement	• Higher mass and volume • Possible unwanted chemical reactions
Latent heat	• Can function while not receiving sunlight • Highest energy density	• Highest mass and volume • Possible unwanted chemical reactions • Possible void formation or bursting

To compare the different concepts, a trade-off between performance, reliability, and mass will be performed.

4.4.1. Trade-off Result

Because the latent heat option function during an eclipse, and can maintain a constant temperature during the phase change, it has the best performance and receives a score of 5. The sensible heat option can also function during an eclipse, but not at a constant temperature and thus receives a score of 5. Because no TES system means no energy can be stored, its unacceptable performance scores a 1.

Excluding the TES system has the highest reliability as there are no components that can fail, resulting in a score of 5. Because sensible heat has a lower reliability due to possible unwanted chemical reactions with other materials, it receives a score of 4. Latent heat storage can besides possible unwanted chemical reactions, result in possible void formation and bursting. Because introducing space for the material to expand can mitigate this issue, it score is only reduced to a 3.

No TES system results in the lowest mass, and results in a score of 5. The latent heat option has a the highest possible energy storage density, and receives a score of 4. The sensible heat option has a lower possible energy storage density and score a 3.

The resulting trade-off table is shown in Table 4.7.

Table 4.7: TES concept trade-off

Criteria / Concepts	Performance	Reliability	Mass	Score
None	R: 1	G: 5	G: 5	3.7
Sensible heat	L: 4	L: 4	Y: 3	3.7
Latent heat	G: 5	Y: 3	L: 4	4.0

Based on the trade-off, the latent heat is the best option. It has a great performance due to its ability to deliver a constant temperature while not receiving sunlight. It has a lower reliability but was determined to be feasible [26]. Furthermore, its high energy density lowers the required mass. Because the scores are close to each other, a sensitivity analysis is performed based on the positions when excluding a criterion.

When excluding the performance criterion, the concept without a TES system wins due to its high reliability and low mass, with a score of 5.0. The sensible heat and latent heat score equally, resulting in a score of 3.5 for each one.

When excluding the reliability criterion, the latent heat option wins due to its excellent performance and a good mass with a score of 4.5. The sensible heat option scores a 3.5 due to the lower performance and higher mass than the latent heat concept. The option of no TES system scores a 3.0 due to its inability to function while not receiving sunlight.

When excluding the last criterion, mass, the sensible heat and latent heat concepts score equally a 4.0. The sensible heat option does not provide a constant temperature but has a higher reliability than the latent heat option. The option without a TES system loses with a score of 3.0. It has the highest reliability but the lowest performance.

An overview of the positions per excluded criterion is given in Table 4.8.

Table 4.8: Sensitivity analysis of TES concepts

Comparisons / Concepts	W/o performance	W/o reliability	W/o mass	Position
None	1	3	3	2.3
Sensible heat	2	2	1	1.7
Latent heat	2	1	1	1.3

The sensitivity analysis shows that the latent heat concept has the best average position when excluding the criteria. The difference compared to the trade-off is that the sensible heat option now scores better than no TES system, instead of scoring equally.

To maximise the amount of time that the system can function, it is important to minimise the losses of the system. To minimise the radiation losses, the system should be insulated. The losses are also minimised by having the hottest materials closest to the centre of the propulsion system. It is therefore decided to have the TES material directly around the cavity and the propellant flowing on the outside of the TES material for the most constant heat flow to the propellant. If the propellant flows between the cavity and TES material, the performance of the system would vary depending on whether sunlight is received or not. A sketch of the layout of the TES system is shown in Figure 4.4.

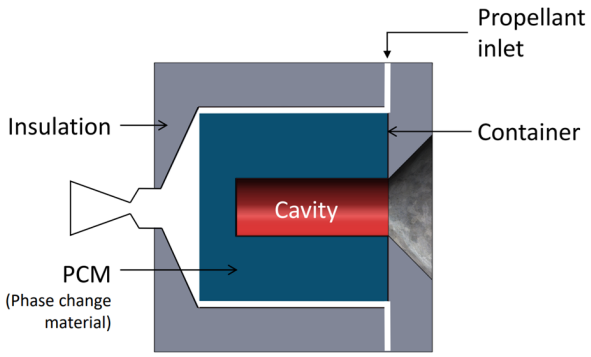

Figure 4.4: Sketch of the latent heat TES system concept [48]

4.5. Nozzle

The literature study showed that for small nozzles with lower Reynolds numbers, the conical nozzle is often de better choice. Most of the proposed concepts that were discussed in section 2.2 also contained a conical nozzle in their design. Furthermore, the simpler shape makes a conical nozzle easier to manufacture than a bell nozzle. Based on these findings, a conical nozzle will also be used for this design. For the nozzle shape, the main design parameters are the convergence half angle, divergence half angle, and throat diameter. A sketch of the nozzle concept is shown in Figure 4.5.

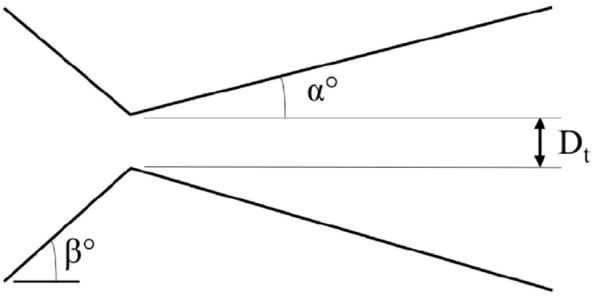

Figure 4.5: Sketch of the nozzle concept [49]

5

Preliminary Design

This chapter will discuss the preliminary design of the propulsion system. To guide the preliminary design phase, the following research questions are used:

5. *What materials are the best option for the thruster?*
    5.1 *What material is the best option for the cavity?*
    5.2 *What material is the best option for the heat exchanger?*
    5.3 *What material is the best option for the nozzle?*
    5.4 *What material is the best option for the insulation?*
6. *What are the key parameters of the design?*

Assumptions will be made to simplify the design process and decrease the dependencies between components. If a component has been designed, its characteristics can be used for the preliminary design of other components. If a component has not been designed, but its characteristics are required for the design of another component, the characteristics will be estimated.

First, the design of the absorber will be discussed, with the process for the heat exchanger in section 5.1, for the cavity in section 5.2, and for the TES system in section 5.3. Then, the design of the nozzle will be discussed in section 5.4, followed by the design of the insulation of the system in section 5.5. At the end of the chapter, the findings of the preliminary design phase will be discussed in section 5.6. These findings will be used for the design process of the final design.

All material properties are taken from Engineering Toolbox unless otherwise specified [1]. The maximum temperature of materials stated is the melting temperature, or if the material only evaporates, the evaporation temperature. As a safety factor, the allowed temperature of a component is $90\,\%$ of the maximum temperature.

5.1. Heat Exchanger

The function of the heat exchanger is to heat the hydrogen to the chamber temperature. The selected temperature that will be aimed to reach during the preliminary design process is a chamber temperature of $T_c = 3000\,\mathrm{K}$. The conditions at the beginning of the heat exchanger are an inlet pressure $p_{in} = 5.0\,\mathrm{MPa}$, and an inlet temperature $T_{in} = 273.15\,\mathrm{K}$. It is assumed that the walls in contact with the propellant have a constant temperature $T_{wall} = 3100\,\mathrm{K}$.

To select the material that will be used for the walls of the heat exchanger, a trade-off is performed. The materials that are compared were identified in chapter 2. For the wall material to maintain this high temperature while colder propellant flows past it, a high conductivity is beneficial. The temperature differences make the brittleness of the material also an important criterion, as brittleness can lead to

[1] URL: `https://www.engineeringtoolbox.com//` [cited 31/08/2025].

cracks. Due to the interaction with high-temperature propellant, the compatibility with hydrogen also needs to be included in the trade-off. An overview of the trade-off is shown in Table 5.1.

Table 5.1: Heat exchanger material trade-off

Criteria / Material	Max. Temp. [K]	Therm. Cond. [W/m/K]	Brittleness	Hydrogen Comp.	Score
Tungsten (W)	3687	182	2 (>1873 K)	2	3.5
K-doped W	3687	182	3 (>2773 K)	2	3.8
Rhenium	3448	48.6	5 (stays ductile)	5	4.0
Graphite	3773	168	1 (stays brittle)	1	3.0
Molybdenum (Mo)	2895	139	2 (>2200 K)	3	2.3
Ca+Mg-doped Mo	2895	139	3 (>2573 K)	3	2.5

A doped variant of tungsten and of molybdenum is included to show the difference in brittleness due to doping of the materials. Table 5.1 shows that rhenium is the most suitable material. Its melting temperature is not the highest, but it is above the operating temperature of the heat exchanger. Molybdenum has a melting temperature below the wall temperature $T_{wall} = 3100\,\mathrm{K}$, and is thus not feasible for the preliminary design. Rhenium has a lower thermal conductivity than the other options, but due to its compatibility with hydrogen and ductility, it has a higher reliability than the other options. This makes its overall score the highest.

When the temperature of the rhenium becomes closer to its melting temperature $T_m = 3448\,\mathrm{K}$, the strength of the material decreases [50]. Because the properties for a wall temperature $T_{wall} = 3100\,\mathrm{K}$ are not well documented, extrapolation will be used to determine the yield strength $\sigma_{y0.2}$. The used data from samples formed with hot isostatic pressure power metallurgy without heat treatment are shown in Table 5.2.

Table 5.2: Yield strength of rhenium $\sigma_{0.2}$ for samples formed with hot isostatic pressure power metallurgy without heat treatment at different temperatures [50]

Temperature [K]	Yield Strength [MPa]
1644	208.36
1644	211.19
1644	171.28
1644	173.14
1783	143.32
1783	137.59
1922	104.25
1922	101.12
2133	105.14
2200	87.63
2200	78.12
2200	67.42
2200	78.79
2367	71.02

Based on the samples, a non-linear regression model is fitted with the least squares method. The least squares method minimises the sum of squared residuals defined as:

$$S(\boldsymbol{\beta}) = \sum_{i=1}^{n} [y_i - f(x_i, \boldsymbol{\beta})]^2 \tag{5.1}$$

where $S(\boldsymbol{\beta})$ is the sum of squared residuals, y_i is the measured value at the i^{th} data point, x_i is the independent variable at the i^{th} data point, $\boldsymbol{\beta}$ is the vector of model parameters to be estimated, and $f(x_i, \boldsymbol{\beta})$ is the model function predicting y from x_i using parameters $\boldsymbol{\beta}$.

The model is a power-law equation with a yield strength $\sigma_{y0.2} = 0\,\mathrm{MPa}$ at the melting temperature $T_m = 3448\,\mathrm{K}$. The equation is of the following form:

$$\sigma_{y0.2} = a \left(1 - \frac{T}{T_m}\right)^b \tag{5.2}$$

Determining the best fit for the data results in the following parameter with a coefficient of determination of $R^2 = 0.8898$:

$$a = 8.515 \times 10^8, \quad b = 2.370 \quad \Longrightarrow \quad \sigma_{y0.2} = 8.515 \times 10^8 \left(1 - \frac{T}{T_m}\right)^{2.370} \tag{5.3}$$

The resulting extrapolated data with this equation is shown in Figure 5.1 and shows for the wall temperature $T_{wall} = 3100\,\mathrm{K}$ a yield strength $\sigma_{y0.2} = 3.712\,\mathrm{MPa}$.

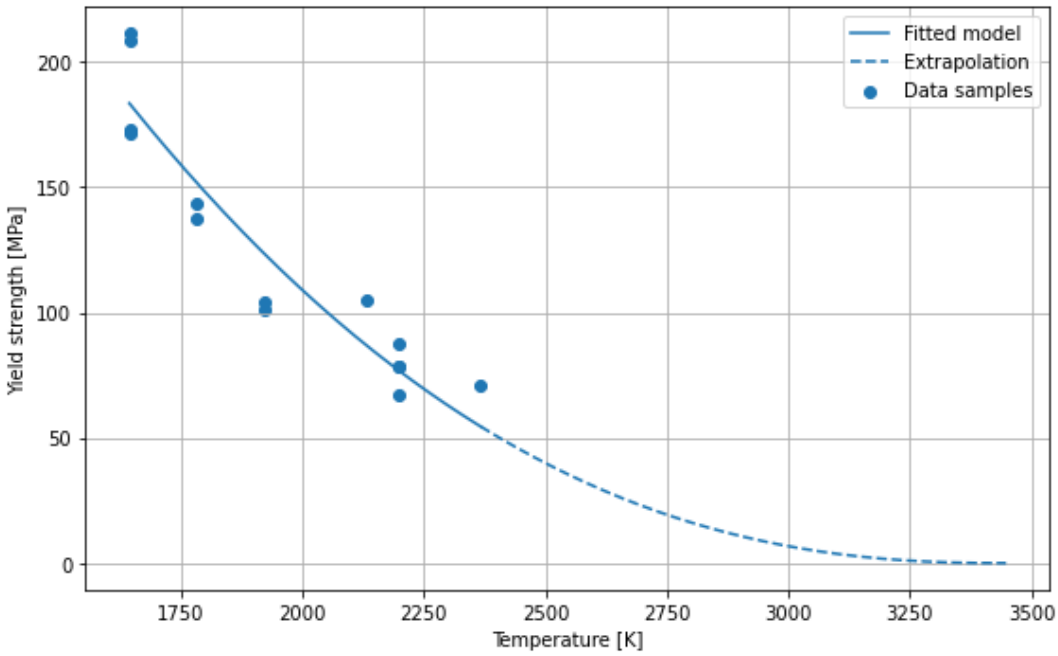

Figure 5.1: The non-linear regression model for the yield strength of rhenium $\sigma_{0.2}$, and the extrapolation

The amount of thermal power required to heat the propellant to the chamber temperature $T_c = 3000\,\mathrm{K}$ is given by the following equation:

$$\dot{Q}_{p,req} = \dot{m}\,\Delta H_p \tag{5.4}$$

where $\dot{Q}_{p,req}$ is the thermal power required to heat the propellant in W, ΔH_p is the change in specific enthalpy of the propellant in $\mathrm{J\,kg^{-1}}$. The specific enthalpy at a temperature can be determined with experimental data and depends on the pressure as well [51]. Based on this data, when assuming that the pressure of the propellant stays equal to the inlet pressure $p_{in} = 5.0\,\mathrm{MPa}$, the change in specific enthalpy between the inlet temperature $T_{in} = 273.15\,\mathrm{K}$ and the chamber temperature $T_c = 3000\,\mathrm{K}$ is found to be $\Delta H_p = 4.445 \times 10^7\,\mathrm{J\,kg^{-1}}$. Figure 5.2 shows the change in specific enthalpy over this

temperature range. The specific enthalpy changes insignificantly with the pressure for pressures below $P = 5.0\,\mathrm{MPa}$.

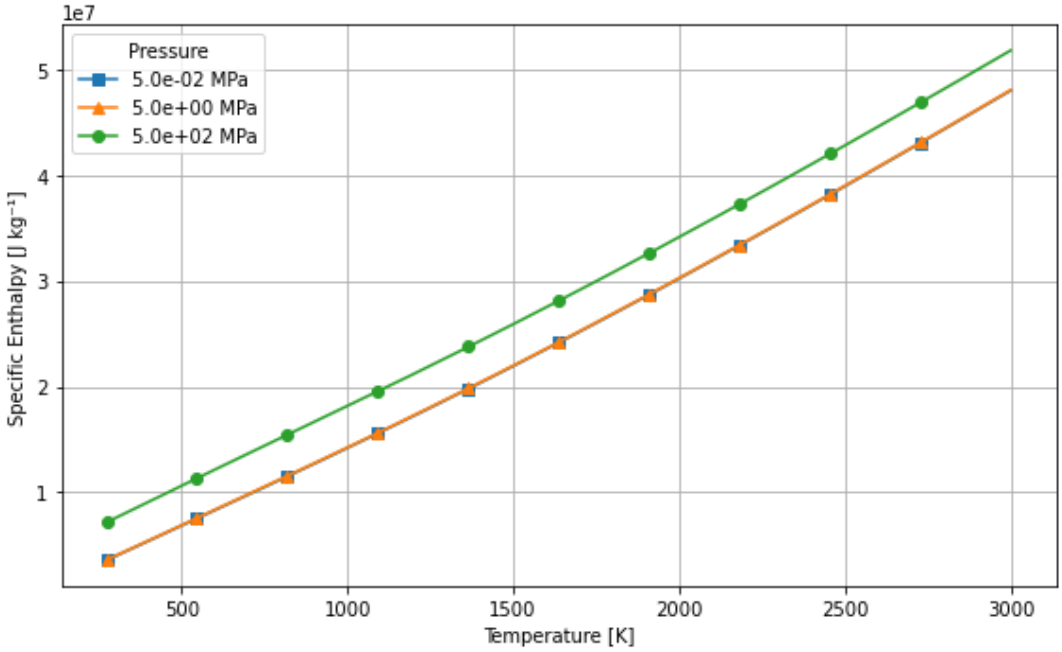

Figure 5.2: The change in specific enthalpy of hydrogen at different pressures

When using Equation 5.4, the change in specific enthalpy, combined with the mass flow of $\dot{m} = 2.039 \times 10^{-4}\,\mathrm{kg\,s^{-1}}$, results in a required power to heat the propellant of:

$$\begin{aligned}\dot{Q}_{p,req} &= \dot{m}\,\Delta H_p \\ &= 2.039 \times 10^{-4}\,\mathrm{kg\,s^{-1}} \times 4.445 \times 10^{7}\,\mathrm{J\,kg^{-1}} = 9063\,\mathrm{W}\end{aligned}$$

5.1.1. Spiral Runner

The first concept, the spiral runner, is a single channel that curves through the material surrounding the thruster. A sketch of the spiral runner is shown in Figure 5.3.

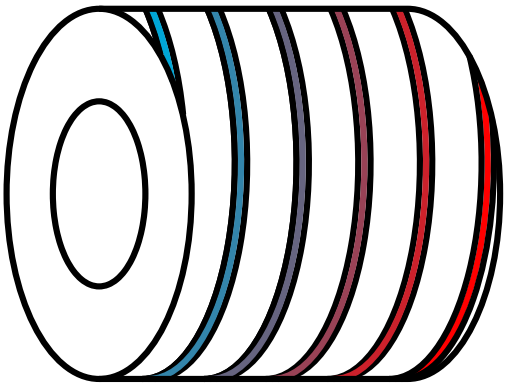

Figure 5.3: A sketch of the spiral channel

The power transferred between the runner wall and propellant due to convection is given by the following equation:

$$\dot{Q}_{p,trans} = h\, A_s\, \Delta T_{lm} \tag{5.5}$$

where $\dot{Q}_p$ is the thermal power transferred to the propellant in W, h is the coefficient of convective heat transfer in $\mathrm{W\,m^{-2}\,K^{-1}}$, A_s is the area of the convective surface in $\mathrm{m^2}$, and ΔT is the log-mean temperature difference in K.

When assuming a constant wall temperature, the log-mean temperature difference is defined as:

$$\Delta T_{lm} = \frac{T_c - T_{in}}{\ln \frac{T_{wall}-T_{in}}{T_{wall}-T_c}} \tag{5.6}$$

where T_{wall} is the wall temperature in K.

The coefficient of convective heat transfer describes how well heat is transferred due to fluid motion, and is given by the following equation:

$$h = \frac{Nu\, k}{L_c} \tag{5.7}$$

where Nu is the dimensionless Nusselt number, k is the thermal conductivity of the propellant in $\mathrm{W\,m^{-1}\,K^{-1}}$, and L_c is the characteristic length of the channel in m.

The Nusselt number describes the ratio between convective and conductive heat transfer. A Nusselt number of 1 means pure conduction, and a Nusselt number larger than 1 means that there is convective heat transfer as well. For the following equations, it is assumed that the propellant flows through a smooth and circular channel with a constant surface temperature and that the velocity profile is fully developed. The Nusselt number is dependent on the state of the flow. For a turbulent flow and part of the transition region, a Gnielinski correlation can be used to determine the Nusselt number:

$$Nu = \frac{\frac{f}{8}\,(Re - 1000)\,Pr}{1 + 12.7\left(\frac{f}{8}\right)^{\left(\frac{1}{2}\right)}\left(Pr^{\left(\frac{2}{3}\right)} - 1\right)} \tag{5.8}$$

where f is the dimensionless friction factor, and Pr is the dimensionless Prandtl number. This correlation is valid for $0.5 \lesssim Pr \lesssim 2000$ and $3000 \lesssim Re \lesssim 5 \times 10^6$.

For a laminar flow with a fully developed thermal profile, the Nusselt number is approximately $Nu = 3.66$. However, in the thermal entrance region, the Nusselt number is higher. When the thermal boundary layer is not fully developed, the temperature gradient near the wall is higher. This effect is covered by the following equation for the average Nusselt number in the channel:

$$\overline{Nu} = 3.66 + \frac{0.0668\,\frac{D}{L}\,Re\,Pr}{1 + 0.04\,\left(\frac{D}{L}\,Re\,Pr\right)^{\left(\frac{2}{3}\right)}} \tag{5.9}$$

where $\overline{Nu}$ is the dimensionless average Nusselt number, D is the diameter of the channel in m, and L is the length of the channel in m. For $L \to \infty$, the Nusselt number approaches $Nu = 3.66$. The length of the thermal entrance region can be determined with the following equation:

$$L_{thermal} = 0.05\, Re\, Pr \tag{5.10}$$

where $L_{thermal}$ is the length of the thermal entrance region in m.

The Reynolds number is given by the following equation:

$$Re = \frac{\rho\, v\, L_c}{\mu} \tag{5.11}$$

where ρ is the density of the propellant in $\mathrm{kg\,m^{-3}}$, v is the velocity of the propellant in $\mathrm{m\,s^{-1}}$, and μ is the dynamic viscosity of the propellant in $\mathrm{Pa\,s}$. This equation can be rewritten:

$$\rho\, v = \frac{\dot{m}}{A_c} \quad \Longrightarrow \quad Re = \frac{\left(\frac{\dot{m}}{A_c}\right) L_c}{\mu} \tag{5.12}$$

where A_c is the cross-sectional area in $\mathrm{m^2}$. The dynamic viscosity depends on the temperature and pressure [51]. Figure 5.4 shows the dynamic viscosity in the temperature range from the inlet temperature $T_{in} = 273.15\,\mathrm{K}$ until the chamber temperature $T_c = 3000\,\mathrm{K}$ for different pressures. For pressures below $5.0\,\mathrm{MPa}$, the dynamic viscosity changes insignificantly with the pressure.

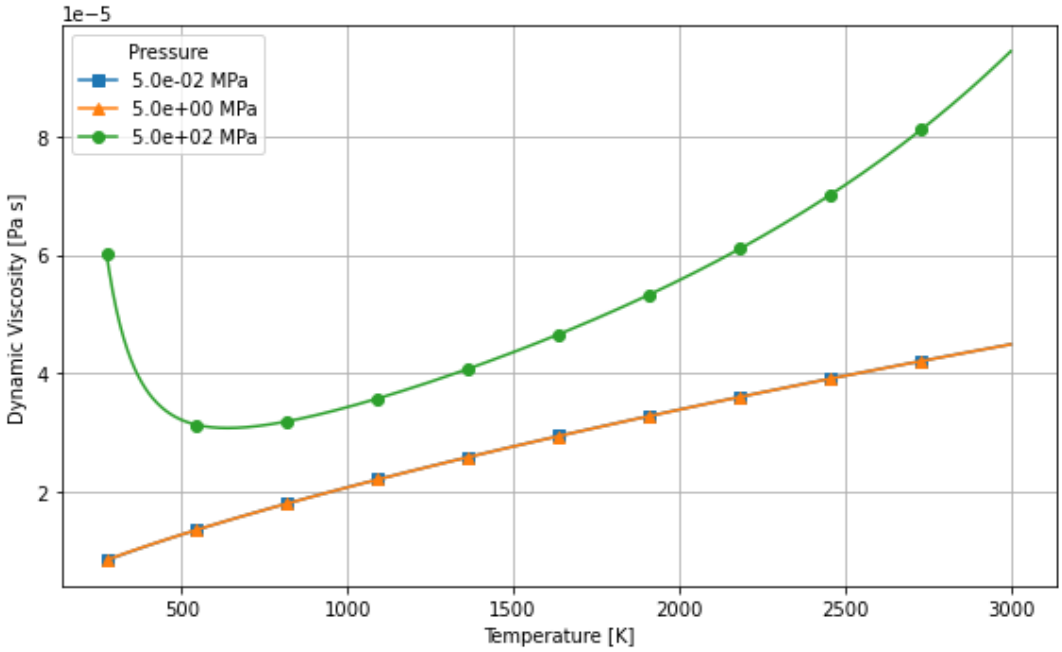

Figure 5.4: The dynamic viscosity of hydrogen at different pressures

Due to the significant difference in dynamic viscosity over the temperature range, the flow can transition from turbulent to laminar. The flow is laminar for Reynolds numbers $Re \lesssim 2300$, in transition for $2300 \lesssim Re \lesssim 4000$, and turbulent for $Re \gtrsim 4000$. For Reynolds numbers in the range $2300 \lesssim Re \lesssim 3000$, neither Equation 5.8 or Equation 5.9 are valid. Linear interpolation between the limits of these equations will be used to determine the Nusselt numbers in this range. However, Equation 5.9 gives the average Nusselt number and not the local Nusselt number at location x along the length of the channel. An equation for the local Nusselt number can be derived based on the equation for the average Nusselt number:

$$\overline{Nu}(x) = \frac{1}{x}\int Nu(x)dx \quad \Longrightarrow \quad Nu(x) = \frac{d}{dx}\left(x\,\overline{Nu}(x)\right) \tag{5.13}$$

$$Nu(x) = 3.66 + \frac{0.0688\,0.04\,\frac{2}{3}\left(\frac{D}{x}\,Pr\,Re\right)^{\left(\frac{5}{3}\right)}}{\left(1 + 0.04\left(\frac{D}{x}\,Re\,Pr\right)^{\left(\frac{2}{3}\right)}\right)^2} \tag{5.14}$$

For a turbulent flow and part of the transition region, the following equation will be used to determine the friction factor:

$$f = \frac{1}{(0.790 \ln Re - 1.64)^2} \tag{5.15}$$

This equation is valid for the same range of Reynolds numbers $3000 \lesssim Re \lesssim 5 \times 10^6$ as Equation 5.8. For a laminar flow, the following equation for the friction factor will be used:

$$f = \frac{64}{Re} \tag{5.16}$$

For Reynolds numbers in the range $2300 \lesssim Re \lesssim 3000$, linear interpolation will be used to determine the friction factors in this range.

The pressure drop is given by the following equation:

$$\Delta P = f \frac{\rho v^2}{2} \frac{L}{D} \tag{5.17}$$

For each equation, the properties should be determined at the mean temperature. However, due to the large change in propellant temperature through the channel, there will also be a significant change in these properties. For improved accuracy, the required channel length will be determined for which the transferred thermal power equals the required thermal power per small temperature increment. At the mean temperature and mean pressure of that segment, the properties of the fluid are determined. A sketch of such a segment is shown in Figure 5.5.

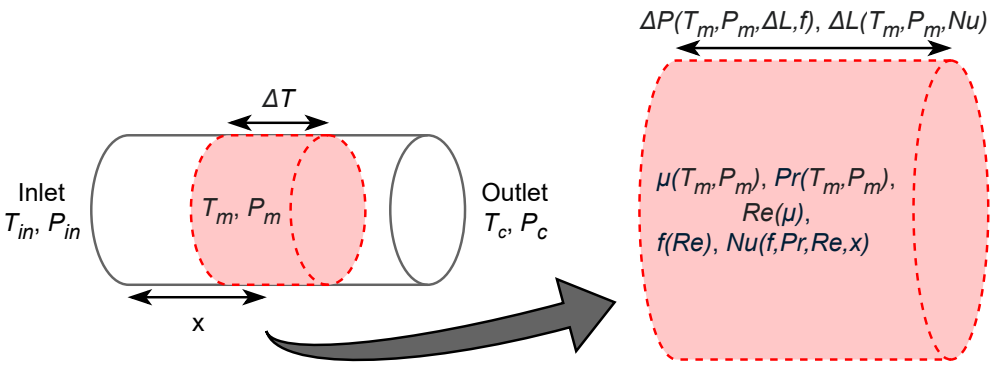

Figure 5.5: A channel segment required for a small temperature increment

The mean pressure of a segment depends on the pressure drop over that segment. The pressure drop itself, however, depends on the length of the segment and the properties at the mean pressure of the segment. The required length for the temperature increment of the segment depends on the properties at the mean pressure of the segment as well. Due to this circular dependency, an initial estimation is made for the pressure drop of the segment. This estimated pressure drop is then used to determine the mean pressure and the corresponding properties at that pressure. The required length for the temperature increment of the segment can then be calculated and used to determine the actual pressure drop. This pressure drop can then be used as the new estimate when recalculating the segment. This process is repeated until the estimated and actual pressure drop results have converged.

Because Equation 5.14 is used to determine the Nusselt number for a laminar flow or the interpolated Reynolds number range, the mean position along the channel is also required. An estimation for the length of the segment is thus also needed. Based on the Nusselt number, the actual required length for the temperature increment is then determined. This length is then used as well for the new estimated length until the results converge. When both the pressure drop estimate and the segment length estimate have converged, the same process will be used for the next temperature increment until the chamber temperature is reached. A flow chart of the process to determine the required channel length for a specific chamber pressure is shown in Figure 5.6,

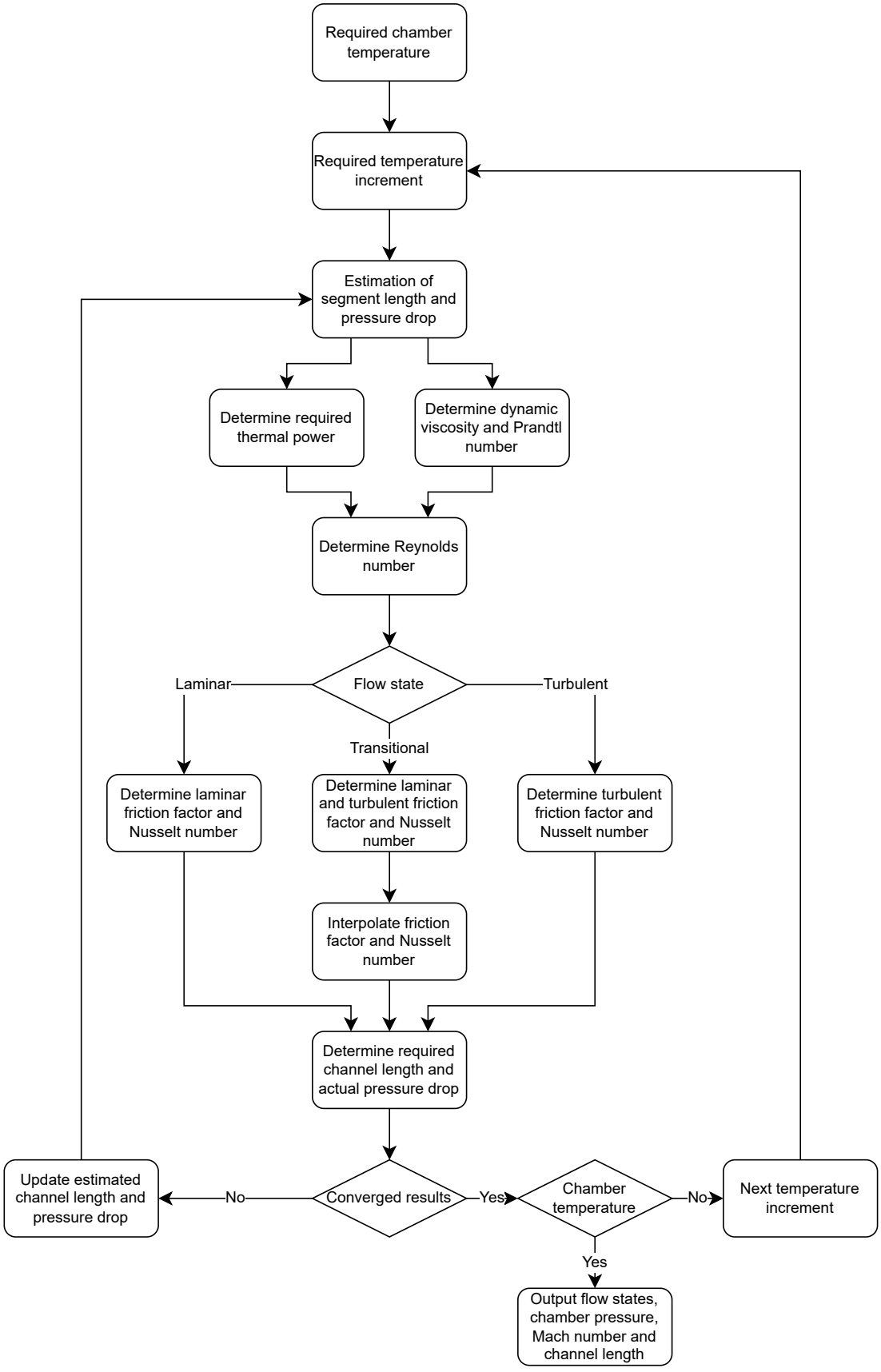

Figure 5.6: A flow chart of the segment-based required channel length determination

The script based on this flow chart and all relevant functions used to determine the required channel length are shown in Listing A. The results for the total required length of the channel per diameter of a circular channel are shown in Figure 5.7.

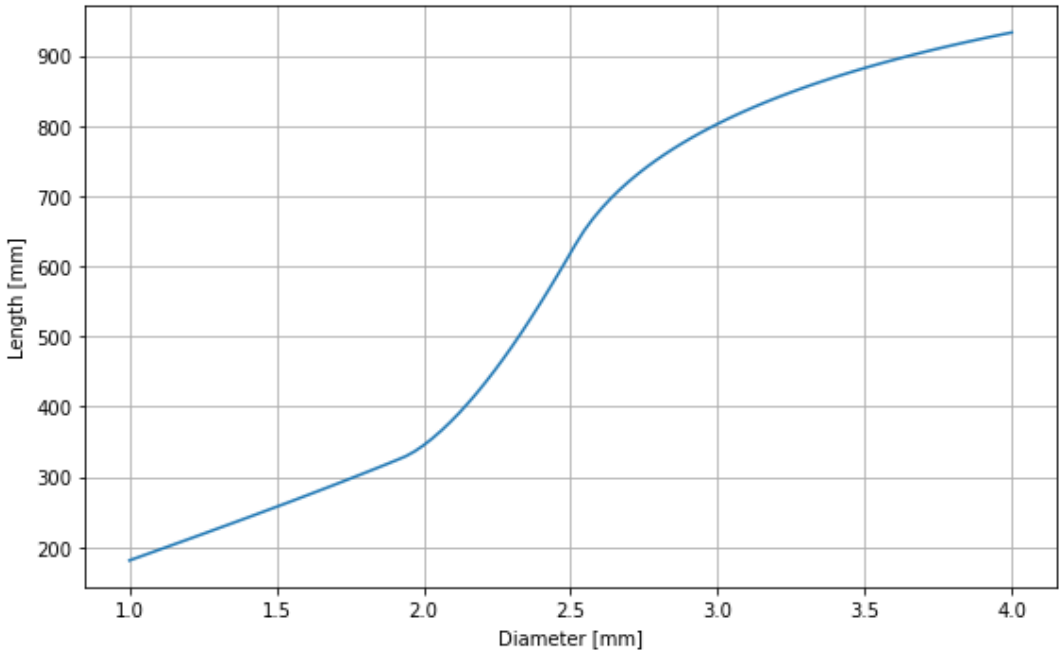

Figure 5.7: The total required length of the channel per diameter of a circular channel

This figure shows that for increasing diameter, the required length of the channel increases more steeply once the flow in part of the channel is in the transition region. Once the flow in part of the channel becomes laminar, the required length of the channel increases less steeply again. The percentage of the length of the channel in each flow state is shown in Figure 5.8.

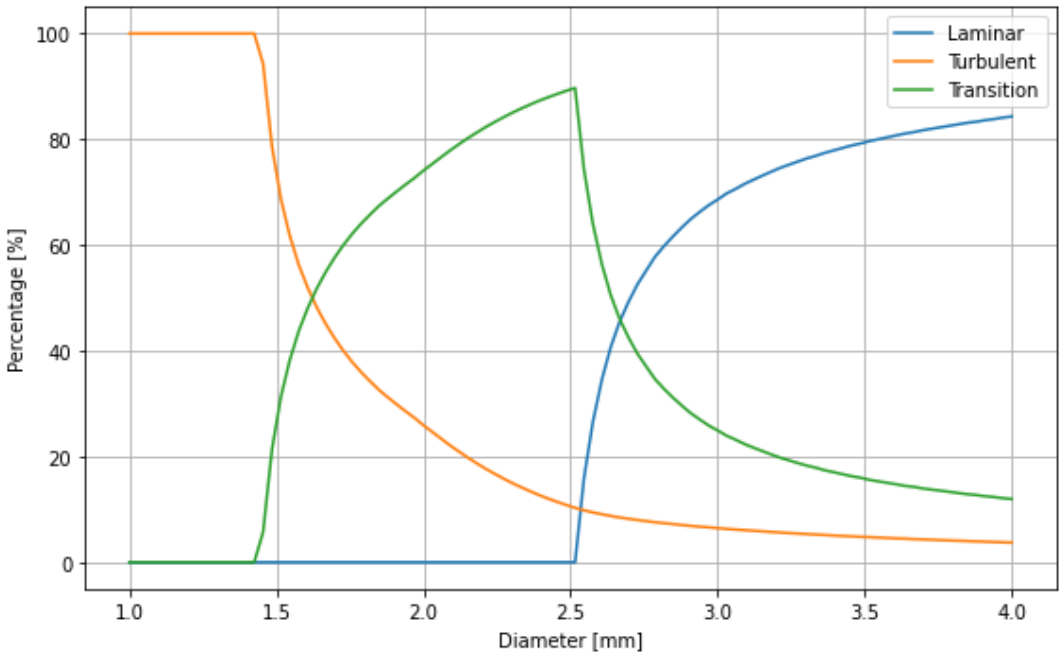

Figure 5.8: The percentage of the length of the channel in each flow state

Figure 5.7 shows that the power transfer is the most efficient for a turbulent flow. For a smaller diameter, a relatively larger part of the flow is close to the hot wall of the channel. This reduces the required length of the channel. However, a small diameter also increases the pressure drop, leading to a lower specific impulse. The chamber pressure at the end of the channel for each diameter is shown in Figure 5.9. To balance between pressure drop and channel length, the diameter for which the flow in the whole channel is turbulent will be selected. For a single channel, this is at a diameter of $D = 1.447\,\mathrm{mm}$ and a resulting length of $L = 248.8\,\mathrm{mm}$. At this diameter and length, the pressure drop is $\Delta P = 9.884 \times 10^{-2}\,\mathrm{MPa}$, resulting in a chamber pressure of $p_c = 4.901\,\mathrm{MPa}$ at the end of the channel.

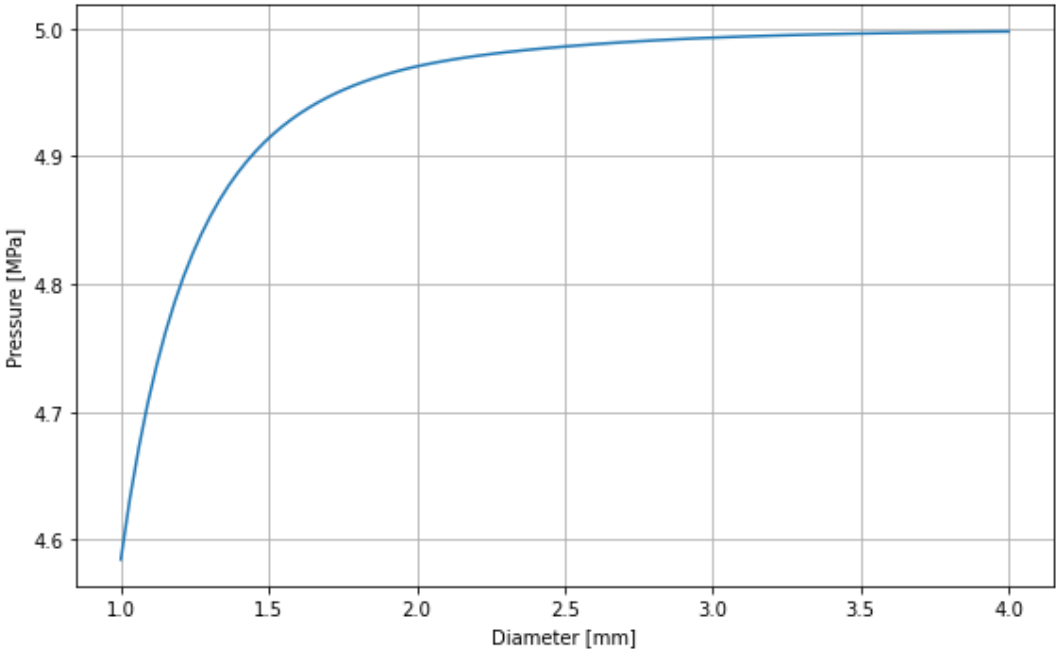

Figure 5.9: The chamber pressure at the end of the channel per diameter

The Mach number is given by the following equation:

$$M = \frac{v}{a} \tag{5.18}$$

where a is the local speed of sound in the propellant in $\mathrm{m\,s^{-1}}$. The following equation is used for the local speed of sound:

$$a = \sqrt{\gamma R T} \tag{5.19}$$

Equation 5.18 can be rewritten:

$$v = \frac{\dot{m}}{A_c\,\rho} \quad \Longrightarrow \quad M = \frac{\left(\frac{\dot{m}}{A_c\,\rho}\right)}{a} \tag{5.20}$$

The Mach number at the end of the channel for each diameter is shown in Figure 5.10. For a single channel with a diameter of $D = 1.447\,\mathrm{mm}$, the Mach number at the end of the channel is $M_{channel} = 0.079$.

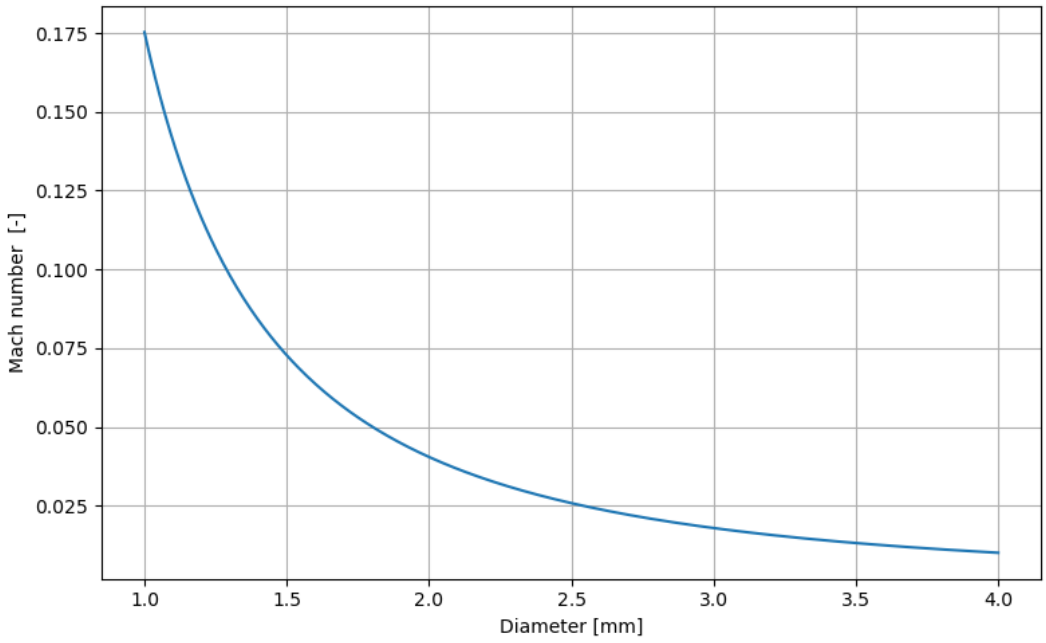

Figure 5.10: The Mach number at the end of the channel per diameter

The required thickness of the spiral runner will be determined for the hoop stress. The hoop stress is given by the following equation:

$$\sigma_\theta = \frac{p\,D}{2\,t_{wall}}\,SF \tag{5.21}$$

where σ_θ is the hoop stress in Pa, t_{wall} is the wall thickness in m, and SF the dimensionless safety factor.

The maximum allowable hoop stress is taken to be the yield strength of the material. Because the yield strength is determined with extrapolated data, a safety factor of $SF = 1.5$ is used. With the highest pressure in the heat exchanger $p_{in} = 5.0\,\mathrm{MPa}$, the diameter $D = 1.447\,\mathrm{mm}$, the yield strength $\sigma_{y0.2} = 3.712\,\mathrm{MPa}$ at the highest temperature $T_{wall} = 3100\,\mathrm{K}$, Equation 5.21 can be solved for the wall thickness t_{wall}. This is the minimum thickness of the material through which the channel goes:

$$\begin{aligned} t_{wall} &= \frac{p\,D}{2\,\sigma_\theta}\,SF \\ &= \frac{5.0\times10^{6}\,\mathrm{Pa}\times1.447\times10^{-3}\,\mathrm{m}}{2\times3.712\times10^{6}\,\mathrm{Pa}}\times1.5 = 1.462\times10^{-3}\,\mathrm{m} \end{aligned}$$

An overview of the dimensions of the spiral runner and the resulting conditions at the end of the channel is given in Table 5.3. Note that the determined pressure drop is due to the friction in the channel. Additional pressure drop due to bends is not included.

Table 5.3: Dimensions and end conditions of the spiral runner

Variable	Value
A_c	$1.640\,\mathrm{mm}$
L	$248.8\,\mathrm{mm}$
p_c	$4.901\,\mathrm{MPa}$
$M_{channels}$	0.079
t_{wall}	$1.462\,\mathrm{mm}$

5.1.2. Multiple Channels

The second concept is multiple straight channels on the outside of the thruster to require less length. A sketch of the multiple channels is shown in Figure 5.11.

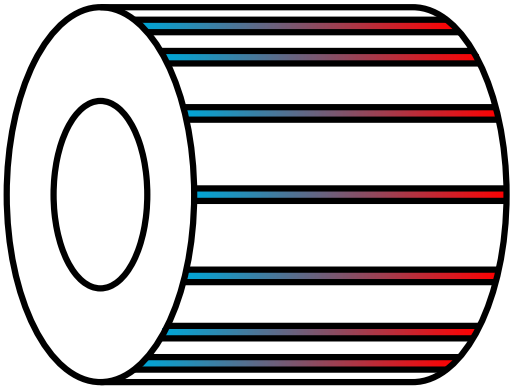

Figure 5.11: A sketch of the multiple channels

When using multiple channels, the mass flow per channel decreases. This lower mass flow requires a smaller diameter to keep the flow turbulent, and a shorter length to transfer sufficient thermal power. The number of channels will be increased while the flow stays subsonic and the pressure drop does not exceed the inlet pressure.

When increasing the number of channels while keeping the complete flow turbulent, a maximum number of channels of $N = 4$ is found. The percentage of the length of the channel in each flow state for this number of channels is shown in Figure 5.12, the chamber pressure is shown in Figure 5.13, and the Mach number at the end of the channels per diameter is shown in Figure 5.14.

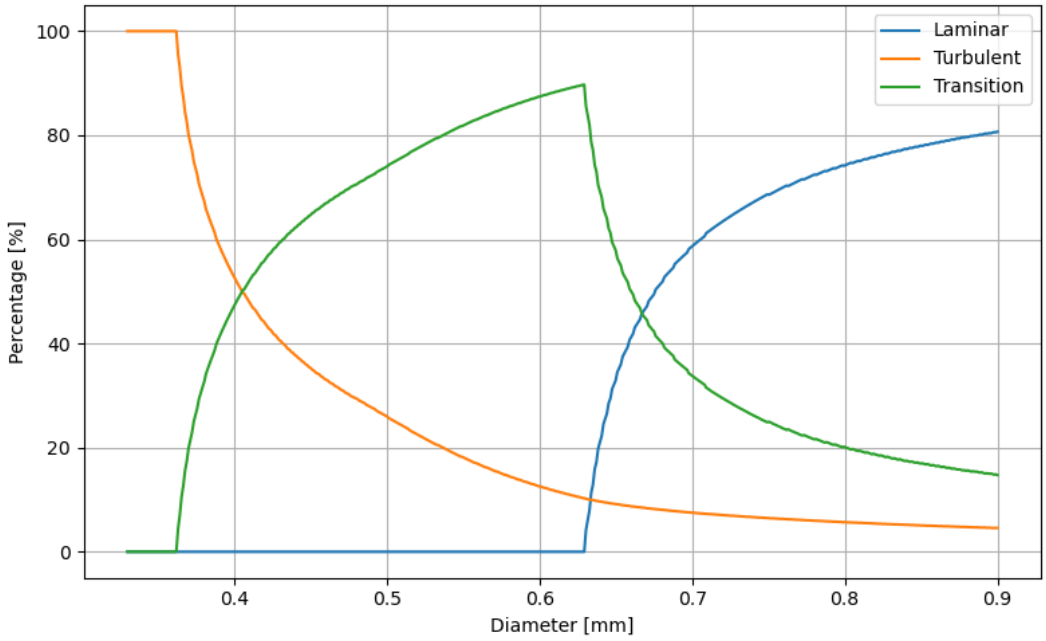

Figure 5.12: The percentage of the length of the channel in each flow state for $N = 4$ channels

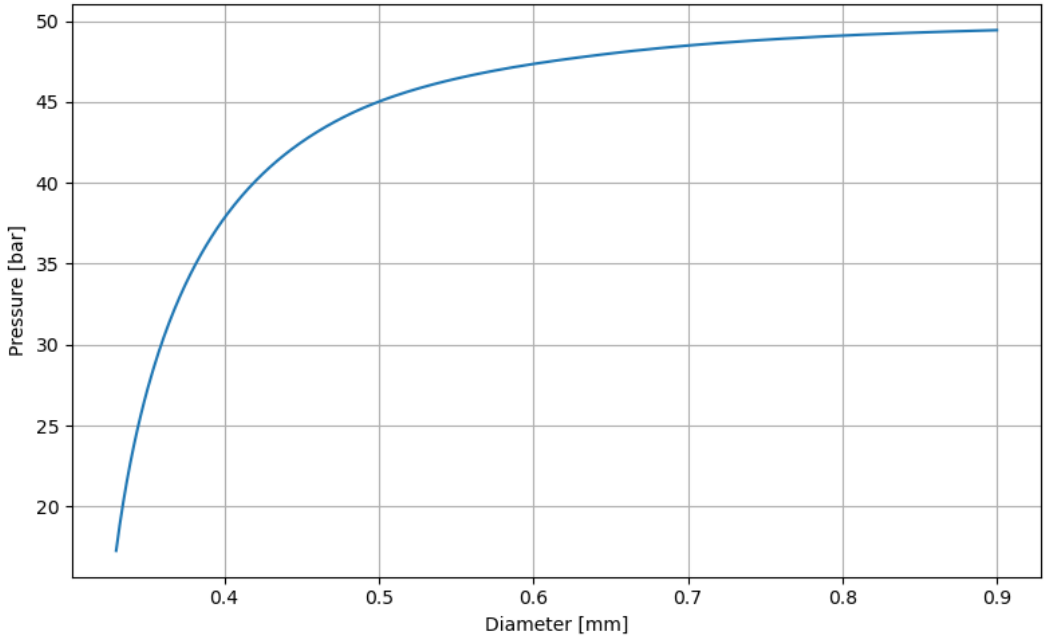

Figure 5.13: The chamber pressure at the end of the channels per diameter

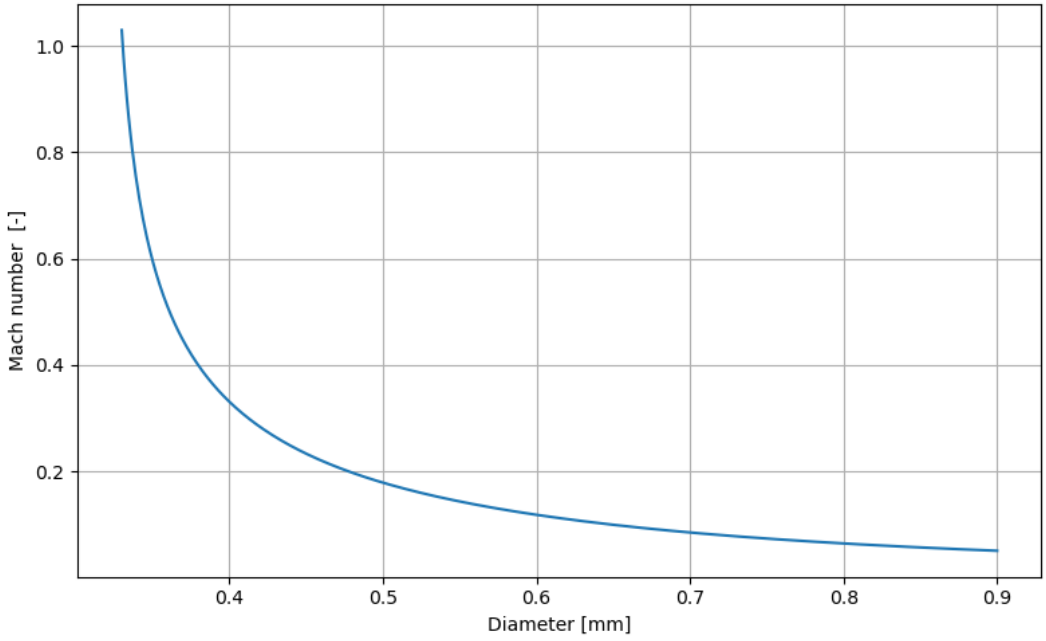

Figure 5.14: The Mach number at the end of the channels for $N = 4$ channels

For $N = 4$ channels, the maximum diameter for which the complete flow stays turbulent is found to be $D = 3.618 \times 10^{-1}\,\mathrm{mm}$. At this diameter, the chamber pressure at the end of the channels is $p_c = 3.074\,\mathrm{MPa}$, and the Mach number is $M_{channel} = 0.500$.

Figure 5.15 shows the required total length for each channel per diameter. For the selected diameter, a total required length of $L = 62.23\,\mathrm{mm}$ for each channel is found.

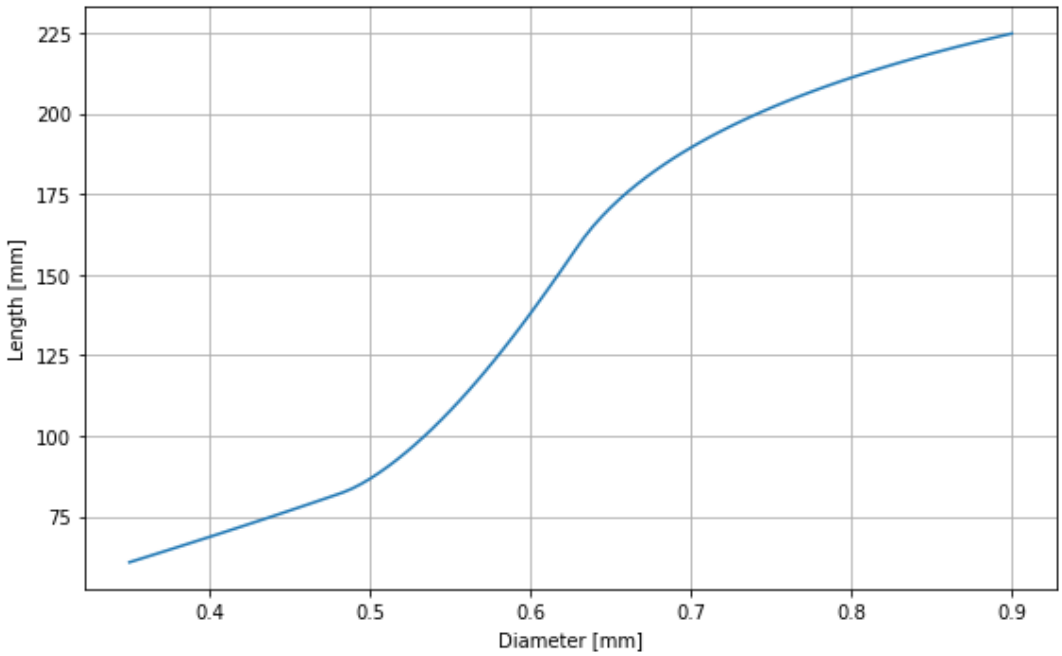

Figure 5.15: The total required length for each channel per diameter for $N = 4$ channels

Using the same conditions as for the spiral runner, but with the adjusted diameter of the 4 channels, the wall thickness can be determined:

$$t_{wall} = \frac{p\,D}{2\,\sigma_\theta}\,SF$$
$$= \frac{5.0 \times 10^6\,\mathrm{Pa} \times 3.618 \times 10^{-4}\,\mathrm{m}}{2 \times 3.712 \times 10^6\,\mathrm{Pa}} \times 1.5 = 3.655 \times 10^{-4}\,\mathrm{m}$$

An overview of the dimensions of the channels and the resulting conditions at the end of the channels is given in Table 5.4. The determined pressure drop is again only due to the friction in the channels.

Table 5.4: Dimensions and end conditions per channel

Variable	Value
N	4
A_c	$1.028 \times 10^{-1}\,\mathrm{mm}^2$
L	$62.23\,\mathrm{mm}$
p_c	$3.074\,\mathrm{MPa}$
$M_{channels}$	0.500
t_{wall}	$3.655 \times 10^{-1}\,\mathrm{mm}$

5.1.3. Porous Medium

The porous medium is placed as a layer around the cylindrical side of the TES container. A sketch of the porous medium is shown in Figure 5.16.

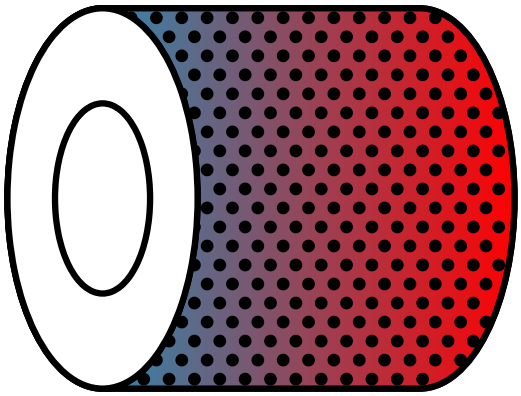

Figure 5.16: A sketch of the porous medium

For a porous medium, the power transferred between the medium and propellant due to convection is often based on a volumetric instead of a surface-based convective heat transfer coefficient:

$$\dot{Q}_{p,trans} = h_v \, V \, \Delta T_{lm} \tag{5.22}$$

where h_v is the dimensionless volumetric convective heat transfer coefficient, and V is the volume of the porous medium in m^3. The volumetric convective heat transfer coefficient can be determined with:

$$h_v = a_s \, h \tag{5.23}$$

where a_s is the specific surface area in $\mathrm{m}^2\,\mathrm{m}^{-3}$. To compare the effectiveness of the flow through the porous medium, the same surface area per propellant volume will be used as for the multiple channels concept. This is because the multiple channels concept also has a higher specific surface area due to the small tubes. The surface area of the channels is:

$$A_s = \pi \, D \, L \tag{5.24}$$

The volume of the channels is:

$$V = \frac{\pi}{4} \, D^2 \, L \tag{5.25}$$

The specific surface area for the channels is:

$$a_s = \frac{A_s}{V} \tag{5.26}$$

Substituting Equation 5.24 and Equation 5.24 in Equation 5.26 results in:

$$a_s = \frac{(\pi \, D \, L)}{\left(\frac{\pi}{4} \, D^2 \, L\right)} = \frac{4}{D} \tag{5.27}$$

For the determined $D = 0.3618\,\mathrm{mm}$, the specific surface area of the channels becomes:

$$\begin{aligned} a_s &= \frac{4}{D} \\ &= \frac{4}{3.618 \times 10^{-4}\,\mathrm{m}} = 1.106 \times 10^4\,\mathrm{m}^2\,\mathrm{m}^{-3} \end{aligned}$$

For the porous medium, the required volume also includes the volume occupied by the solid material. This ratio is called the porosity and is defined as:

$$\phi = \frac{V_{void}}{V_{total}} = 1 - \frac{V_{solid}}{V_{total}} \tag{5.28}$$

where ϕ is the dimensionless porosity, V_{void} is the volume of the void in the porous medium in m^3, V_{total} is the total volume of the porous medium in m^3, and V_{solid} is the volume of the solid material in the porous medium in m^3. To keep the constant surface temperature assumption valid, a low porosity is selected. With a lower porosity, the thermal conductivity is higher, making it easier for the porous medium to maintain its temperature when the cooler propellant flows through it. A face-centred cubic packing has the lowest possible porosity for packed spheres [52]. Using this packing results in a porosity of:

$$\phi = 1 - \frac{\pi}{3\sqrt{2}} \approx 0.260 \tag{5.29}$$

Substituting Equation 5.28 in Equation 5.26 results in the following specific surface area for the porous medium:

$$a_s = \frac{A_s}{V_{total}} = \frac{A_s}{V_{void}}\,\phi \tag{5.30}$$

$$\begin{aligned} a_s &= \frac{A_s}{V_{void}}\,\phi \\ &= 1.106 \times 10^4\,\mathrm{m}^2\,\mathrm{m}^{-3} \times 0.260 = 2.869 \times 10^3\,\mathrm{m}^2\,\mathrm{m}^{-3} \end{aligned}$$

While the propellant flows through the porous medium, the interstitial characteristics are difficult to determine due to the change in local conditions. To determine the average Reynolds number, the average interstitial velocity will be used. The average velocity inside the porous medium is the product of the superficial velocity and porosity, due to the reduced cross-sectional area. For packed spheres, the characteristic length is taken to be the particle diameter. The surface area of a single particle is given by the following equation:

$$A_p = \pi\, d_p^2 \tag{5.31}$$

where A_p is the surface area of a single particle in m^2, and d_p is the diameter of a single particle in m.

The volume of a single particle is given by the following equation:

$$V_p = \frac{\pi}{6}\, d_p^3 \tag{5.32}$$

where V_p is the volume of a single particle in m^3.

Rewriting Equation 5.28 and substituting it in Equation 5.26 results in the following equation:

$$a_s = \frac{A_s}{\frac{V_{solid}}{1-\phi}} = \frac{(1-\phi)\,A_s}{V_{solid}} \tag{5.33}$$

When substituting with the specific area of a single particle, this becomes:

$$a_s = \frac{(1-\phi)\,A_p}{V_p} = \frac{(1-\phi)\,\left(\pi\, d_p^2\right)}{\left(\frac{\pi}{6}\, d_p^3\right)} = \frac{6\,(1-\phi)}{d_p} \tag{5.34}$$

Solving this equation for the diameter of a single particle results in the particle diameter:

$$d_p = \frac{6\,(1-\phi)}{d_p}$$
$$= \frac{6\,(1-0.260)}{2.869 \times 10^3\,\mathrm{m^2\,m^{-3}}} = 1.548 \times 10^{-3}\,\mathrm{m}$$

The change in local conditions in the porous medium can lead to local laminar flow even if the average flow is turbulent. A Gnielinski correlation for ball beds is therefore used for the Nusselt number that combines a correlation for laminar flow and a correlation for turbulent flow [53]:

$$Nu_{lam} = 0.664\,Re^{0.5}\,Pr^{\left(\frac{1}{3}\right)} \tag{5.35}$$

$$Nu_{turb} = \frac{0.037\,Re^{0.8}\,Pr}{1 + 2.443\,Re^{-0.1}\left(Pr^{\left(\frac{2}{3}\right)} - 1\right)} \tag{5.36}$$

$$Nu = 2 + \left(Nu_{lam}^2 + Nu_{turb}^2\right)^{\left(\frac{1}{2}\right)} \tag{5.37}$$

To determine the pressure drop inside the porous medium, the Ergun equation will be used:

$$\Delta P = L\left(\frac{150\,(1-\phi)^2\,\mu\,v_s}{\phi^3\,d_p^2} + \frac{1.75\,(1-\phi)\,\rho\,v_s^2}{\phi^3\,d_p}\right) \tag{5.38}$$

To determine the dimensions of the porous medium, the same method will be used as in subsection 5.1.1, but with the equations relevant for the porous medium. The required length of the porous medium will be determined for a specific cross-sectional area per segment instead of its diameter. The percentage of the length of the porous medium in each flow state is shown in Figure 5.17.

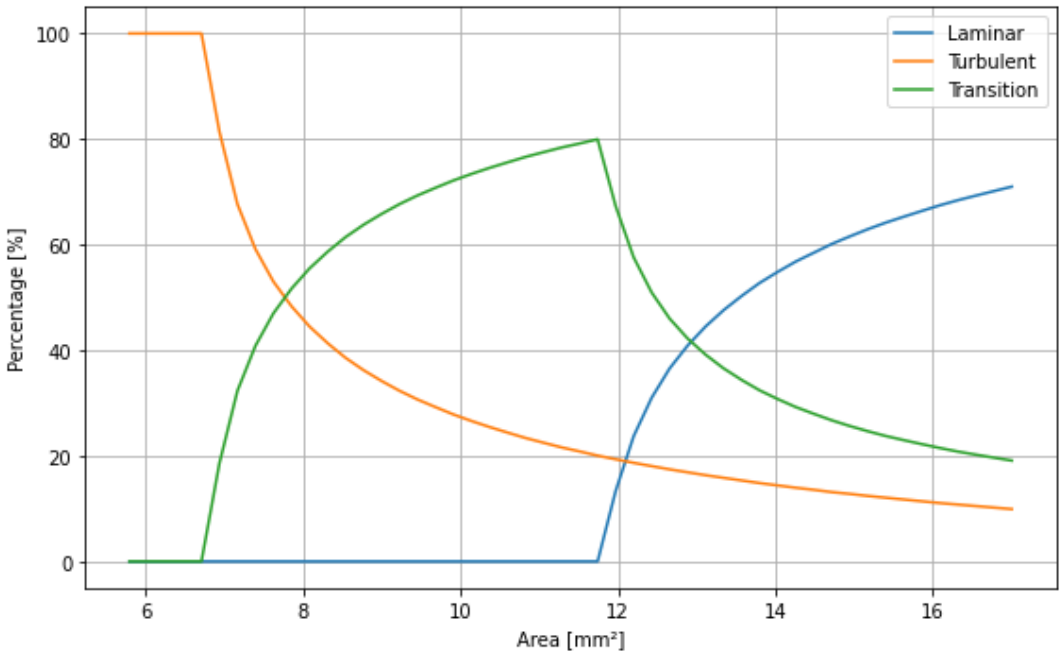

Figure 5.17: The percentage of the length of the porous medium in each flow state

The maximum cross-sectional area for which the average flow per segment for each segment stays turbulent is found to be $A_c = 6.7814\,\mathrm{mm^2}$. This cross-sectional requires the porous medium to have a

length of $19.36\,\mathrm{mm}$. At this cross-sectional area, the chamber pressure at the end of the porous medium is $p_c = 3.022\,\mathrm{MPa}$, and the Mach number is $M_{channel} = 0.118$.

The porous medium requires a container that is located around the TES container. Therefore, the hoop stress for the porous medium container depends on the radius of the TES container. The sizing of the thickness of the porous medium container will thus be done when the sizing of the porous medium container is done. An overview of the dimensions of the porous medium and the resulting conditions at the end of the porous medium is given in Table 5.5.

Table 5.5: Dimensions and end conditions of the porous medium

Variable	Value
d_p	$1.548\,\mathrm{mm}$
A_c	$6.781\,\mathrm{mm}^2$
L	$19.36\,\mathrm{mm}$
p_c	$3.022\,\mathrm{MPa}$
M	0.118

5.1.4. Assumptions

Multiple assumptions have been stated where relevant for the design process. The key assumptions for the heat exchanger are:

- The wall temperature is assumed constant at $T_{wall} = 3100\,\mathrm{K}$.
  Validity: This simplifies the design process, but the effect of wall-cooling is analysed later.
- Propellant properties are taken at the mean temperature and pressure.
  Validity: The channels are divided into short segments with small temperature gradients.
- The correlations for the Nusselt number are valid.
  Validity: Based on the type of channel and the state of the flow, different equations are used to determine the Nusselt number.
- Radiation heat transfer between the hot wall and hydrogen is neglected.
  Validity: Convective heat transfer dominates the heat transfer process.
- No dissociation of hydrogen occurs in the heat exchanger.
  Validity: At the expected temperature $T < 3000\,\mathrm{K}$, hydrogen remains stable.
- Structural analysis assumes a uniform stress distribution across the channel wall.
  Validity: For thin-walled cylindrical channels, hoop stress dominates.
- Steady-state operation is assumed.
  Validity: This is valid after the system has reached operating conditions.

5.2. Cavity

The function of the cavity is to absorb the solar radiation and transform it into thermal power. Because the cavity is not in contact with the propellant, the hydrogen compatibility is not relevant. However, for the cavity material, the absorptivity is important. Adjusting the last criterion in Table 5.1 results in a trade-off table for the cavity material as shown in Table 5.6.

Table 5.6: Cavity material trade-off

Criteria / Material	Max. Temp. [K]	Therm. Cond. [W/m/K]	Brittleness	Absorptivity	Score
Tungsten (W)	3687	182	2 (>1873 K)	0.4–0.45	3.5
K-doped W	3687	182	3 (>2773 K)	0.4–0.45	3.8
Rhenium	3448	48.6	5 (stays ductile)	0.55–0.6	3.5
Graphite	3773	168	1 (stays brittle)	0.85–0.95	4.0
Molybdenum (Mo)	2895	139	2 (>2200 K)	0.55–0.6	3.0
Ca+Mg-doped Mo	2895	139	3 (>2573 K)	0.55–0.6	3.3

Table 5.6 shows that graphite, even though it has high brittleness, is the best option due to its great performance in the other criteria.

The solar radiation that is concentrated should, per orbit, be larger than the energy required to heat the propellant and the energy that is lost. The power that is lost consists of losses in the optical fibre cable, not absorbed solar rays, and radiation losses. The radiation losses are given by the following equation:

$$\dot{Q}_{rad} = \varepsilon \, \sigma \, A \left(T_{sur}^4 - T_{amb} \right) \tag{5.39}$$

where $\dot{Q}_{rad}$ is radiated power in W, ε is the dimensionless emissivity of the radiating surface, $\sigma = 5.6704 \times 10^{-8} \, \mathrm{W\,m^{-2}\,K^{-4}}$ is the Stefan-Boltzmann constant, A is the radiating surface area in $\mathrm{m^2}$, T_{sur} is the radiating surface temperature in K, and T_{amb} is the ambient temperature in K. It is assumed that the ambient temperature is $T_{amb} = 0 \, \mathrm{K}$.

The absorber cavity radiates a lot due to the high temperature of the surface that absorbs the solar power. The radiation that is lost is the radiation that leaves the cavity. Most of the radiation inside the cavity is absorbed by the other cavity walls again. Thus, the radiation surface area of the lost radiation is the area of the aperture. To minimise the losses, the inlet of the cavity will be the size of the fibre optical cable, plus a margin to prevent conduction to the fibre optical cable. Because the design of the fibre optical cables is out of the scope of this report, the characteristics will be based on the design from Physical Sciences Inc., Boeing, and the AFRL as discussed in section 2.2 [23]. The radius of the aperture in this design is $R_{ap} = 10 \, \mathrm{mm}$, and the numerical aperture is $NA = 0.48$.

As discussed in section 4.3, the cavity will be composed of a cylinder with a cone on each circular side. The smaller the inlet is, the fewer rays can escape from the cavity, and every additional hit of a ray inside the cavity results in more absorbed solar power. A fraction $alpha$ of a hit's energy is absorbed, and a fraction $(1 - \alpha)$ is reflected with each wall hit. The probability of a ray hitting a cavity wall again is $\frac{A_{cav}}{A_{ap}+A_{cav}}$. The absorbed energy during the n^{th} hit becomes:

$$Q_{abs,n} = \alpha \, Q_{in} \left((1 - \alpha) \frac{A_{cav}}{A_{ap} + A_{cav}} \right)^{n-1} \tag{5.40}$$

Summing the absorbed energy of every hit results in the total energy power by the cavity:

$$Q_{abs} = \alpha \, Q_{in} \sum_{n=1}^{\infty} \left((1 - \alpha) \frac{A_{cav}}{A_{ap} + A_{cav}} \right)^{n-1} = \alpha \, Q_{in} \sum_{n=0}^{\infty} \left((1 - \alpha) \frac{A_{cav}}{A_{ap} + A_{cav}} \right)^{n} \tag{5.41}$$

This is a geometric series of the form:

$$\sum_{n=0}^{\infty} r^n = \frac{1}{1 - r} \tag{5.42}$$

where r is defined as:

$$r = (1 - \alpha) \frac{A_{cav}}{A_{ap} + A_{cav}} \tag{5.43}$$

The total absorbed power thus becomes:

$$\dot{Q}_{abs} = \frac{\alpha}{1 - (1 - \alpha) \frac{A_{cav}}{A_{ap} + A_{cav}}} \dot{Q}_{in} \tag{5.44}$$

Equation 5.44 shows that for a sufficiently larger cavity surface area A_{cav} than aperture area A_{ap}, the cavity acts as a black body. It is based on the assumption that all areas have the same probability of being hit by solar radiation. However, the actual probability depends on the shape of the cavity. When filling the absorptivity of $\alpha = 0.84$ into Equation 5.44, it is found that for a ratio between the aperture area and surface area of $\frac{A_{cav}}{A_{ap}} = 18$, the percentage of the solar power going into the cavity being absorbed is $99.0\,\%$:

$$\begin{aligned} \dot{Q}_{abs} &= \frac{\alpha}{1 - (1 - \alpha) \frac{A_{cav}}{A_{ap} + A_{cav}}} \dot{Q}_{in} \\ \dot{Q}_{abs} &= \frac{0.84}{1 - (1 - 0.84) \frac{18}{1+18}} \dot{Q}_{in} \qquad = 0.990\, \dot{Q}_{in} \end{aligned}$$

Local hotspots inside the cavity induce extra thermal stress and can lead to damage. To prevent thermal degradation of the cavity, the shape will be optimised for the most uniform distribution of the absorbed solar power. A sketch of a 2D representation of the shape is shown in Figure 5.18.

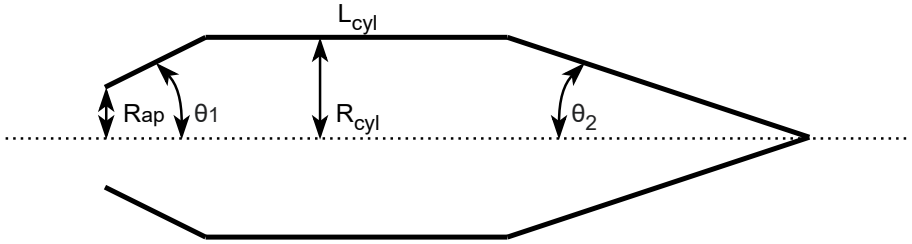

Figure 5.18: A sketch of the cavity shape

To optimise the shape of the cavity, the following design variables are identified:

- θ_1
- θ_2
- $\frac{L_{cyl}}{R_{cyl}}$

The aperture radius $R_{ap} = 10\,\mathrm{mm}$, results in the following aperture area:

$$\begin{aligned} A_{ap} &= \pi\, R_{ap}^2 \\ &= \pi\, (1.000 \times 10^{-2}\,\mathrm{m})^2 = 3.142 \times 10^{-4}\,\mathrm{m}^2 \end{aligned}$$

The size of the cavity is then determined based on the ratio $\frac{A_{cav}}{A_{ap}} = 18$ and the aperture area $A_{ap} = 314.2\,\mathrm{mm}^2$. This results in a cavity area of:

$$\begin{aligned} A_{cav} &= \frac{A_{cav}}{A_{ap}} A_{ap} \\ &= 18 \times 3.142 \times 10^{-4}\,\mathrm{m}^2 = 5.655 \times 10^{-3}\,\mathrm{m}^2 \end{aligned}$$

For a given set of design variables and the required areas $A_{ap} = 314.2\,\mathrm{mm}^2$ and $A_{cav} = 5655\,\mathrm{mm}^2$, only one solution for the shape and size exists.

The solar power entering the cavity will be modelled as a point source in the aperture on the longitudinal axis. The half angle of the source is given by the following equation [54]:

$$\theta_{source} = \sin\left(\frac{NA}{n}\right)^{-1} \tag{5.45}$$

where θ_{source} is the half angle of the source, and n is the dimensionless refractive index of the medium. Because the refractive index in a vacuum is $n = 1$, the half-angle of the source becomes:

$$\begin{aligned} \theta_{source} &= \sin\left(\frac{NA}{n}\right)^{-1} \\ &= \sin\left(\frac{0.48}{1}\right)^{-1} = 0.501\,\mathrm{rad} \end{aligned}$$

The rays leave the source and enter the cavity with a Lambertian distributed spacing and an equal amount of energy per ray [54]. Using parametric line intersection, it is determined if a ray hits a wall segment and where the hit occurs. Then, using the law of reflection, the direction of the reflected ray is determined. Hits will be modelled until more than $99.9\,\%$ of the ray's initial energy is absorbed. This allows determining if $99.0\,\%$ of the solar power entering the cavity is absorbed. Dividing a segment's received power by the area it represents in 3D results in the heat flux of the segment $\dot{q}$.

The optimisation goal will be the highest uniformity score. For the uniformity score, the heat flux per segment will be normalised by the maximum possible heat flux to get the probability of a segment receiving solar power:

$$p_i = \frac{\dot{q}_i}{\sum_{j=1}^{n} \dot{q}_j} \tag{5.46}$$

Based on this probability, the Shannon entropy is determined with the following equation [55]:

$$H = -\sum_{i:p_i>0}^{n} p_i \log(p_i) \tag{5.47}$$

The maximum possible entropy is given by the following equation:

$$H_{max} = \log(n) \tag{5.48}$$

Normalising the Shannon entropy by the maximum entropy results in the uniformity score, as it allows comparing cavities with a different number of segments:

$$U = \frac{H}{H_{max}} \tag{5.49}$$

This results in a score between 0 and 1, with a score of 1 being perfect uniformity.

Figure 5.19 shows the uniformity score for an area ratio of $\frac{A_{cav}}{A_{ap}} = 18$ and varying design parameters.

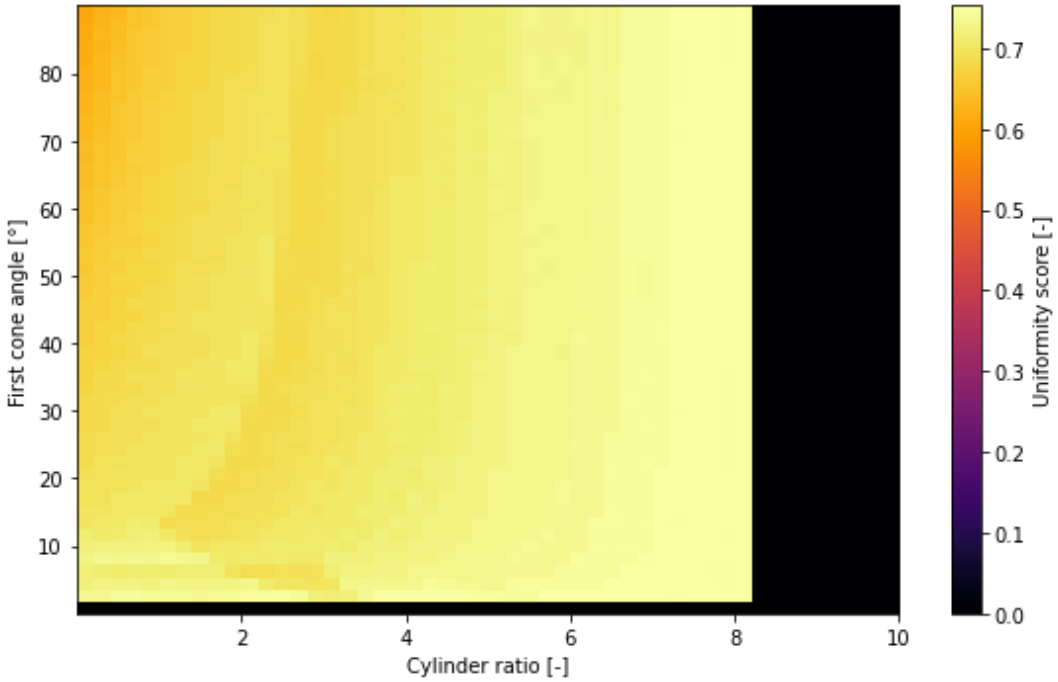

(a) A constant second cone angle $\theta_2 = 45^\circ$

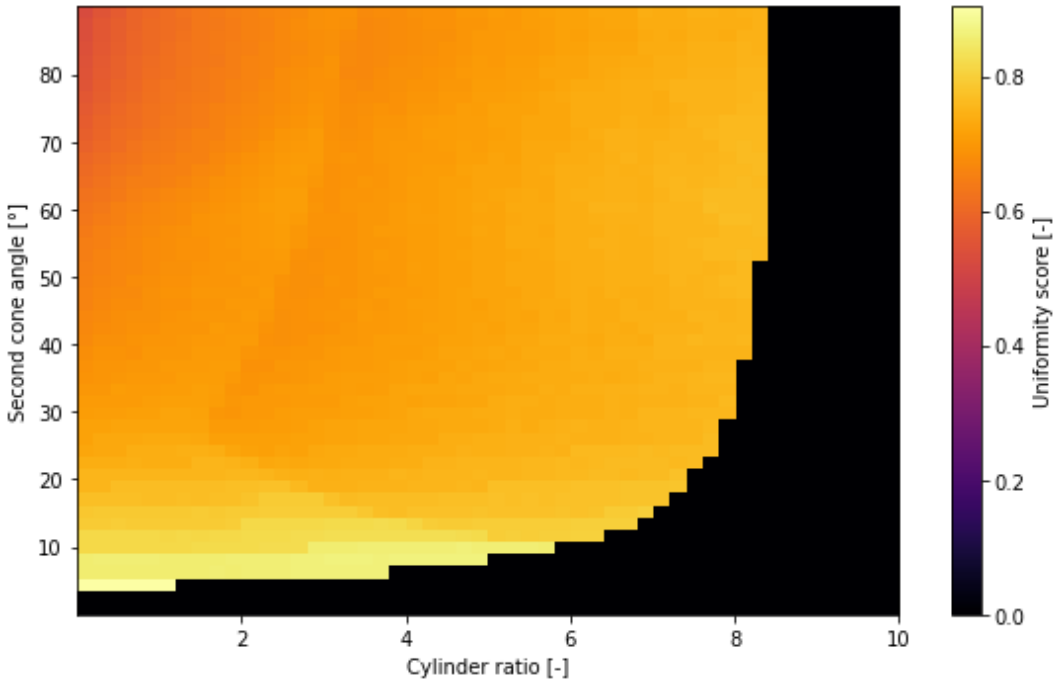

(b) A constant first cone angle $\theta_1 = 45^\circ$

Figure 5.19: The uniformity score for an area ratio of $\frac{A_{cav}}{A_{ap}} = 18$ and varying design parameters

Because many local optima exist, a differential evolution algorithm is used. The uniformity score is determined for different sets of design variables, and based on the scores per set, each set of design variables is mutated. If a mutated set scores better than the original set, it replaces the original set. If the original set scores better, it is kept. This results in a new generation of sets of design variables. Based on the scores of the new generation, the sets are mutated again. This process continues until the scores within a generation converge and the optimum cavity design is found. A flow chart of this

process is shown in Figure 5.20.

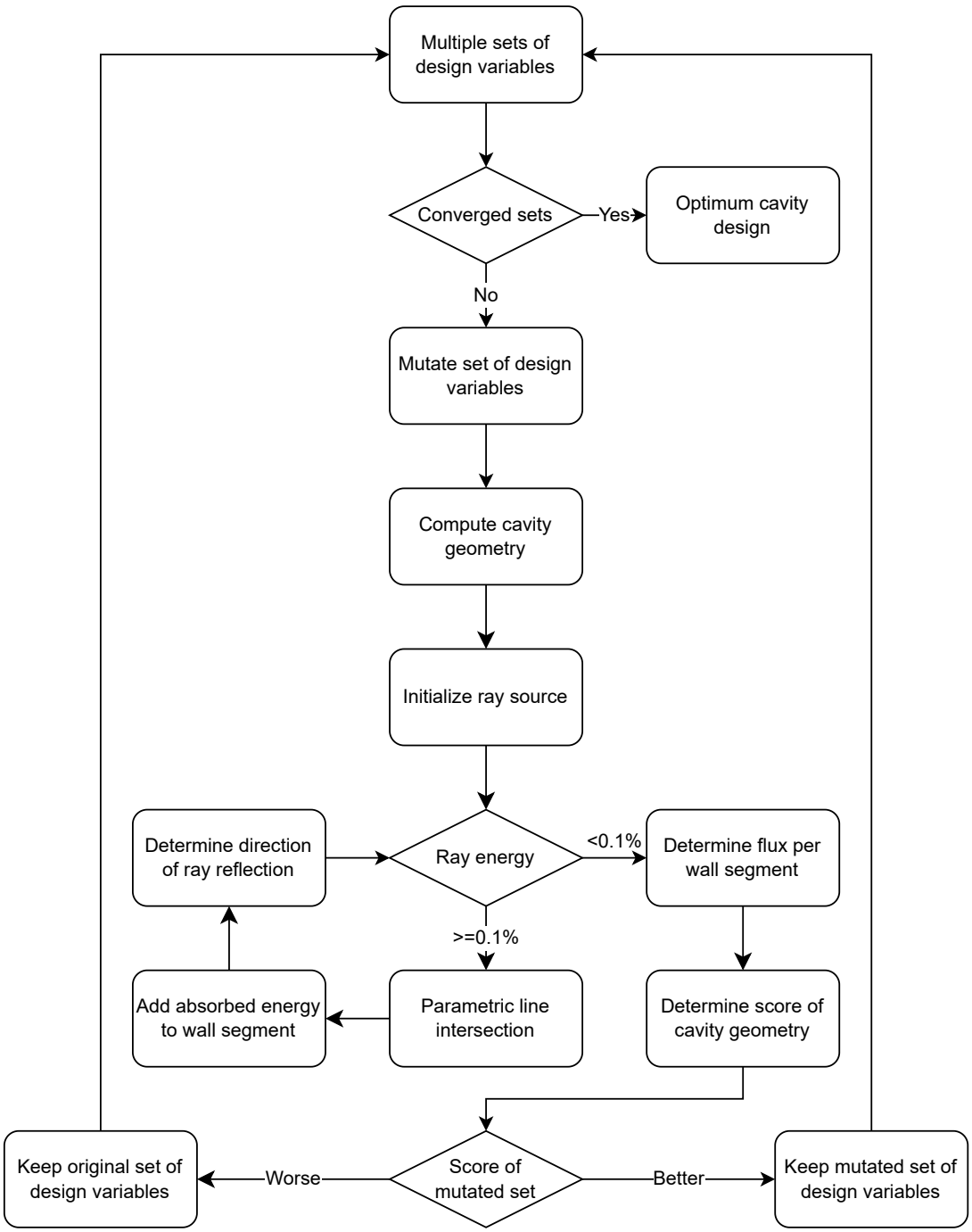

Figure 5.20: A flow chart of the optimum cavity design determination

The script based on this flow chart and all relevant functions used to determine the optimum cavity design are shown in Listing A.

Using the differential evolution algorithm, the optimum cavity design with a uniformity score of $8.691 \times$

10^{-1} is found. For this cavity, the cone angles are $\theta_1 = 12.86°$ and $\theta_2 = 7.843°$, and the cylinder ratio is $\frac{L_{cyl}}{R_{cyl}} = 4.853$. This results in a cylinder with radius $R_{cyl} = 10.22\,\mathrm{mm}$, and a total length $L_{total} = 124.8\,\mathrm{mm}$. Figure 5.21 shows the uniformity of the heat flux distribution of this design.

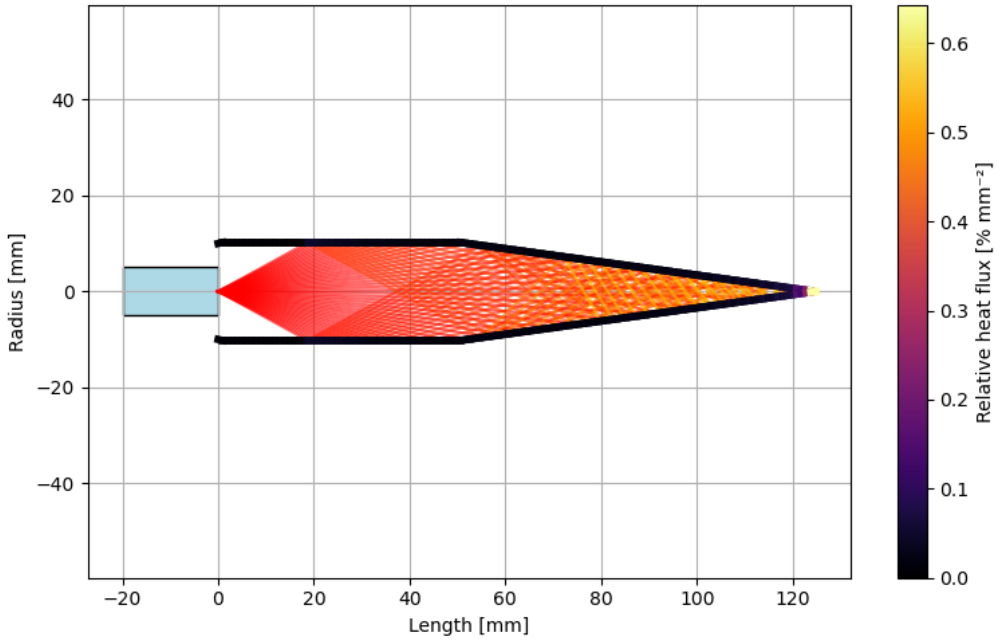

Figure 5.21: The uniformity of the heat flux distribution for the optimum cavity design

Due to the large aspect ratio of this design, the probability of a wall segment being hit is significantly larger during the first reflections. This results in an absorption of $\eta_{abs} = 99.9\,\%$, and thus larger than Equation 5.44 estimates. The effects of a smaller cavity will be discussed later, when optimising the overall system.

Equation 5.21 shows that the diameter of the cylinder should be determined with the widest part of the cavity shape $R_{cyl} = 10.22\,\mathrm{mm}$. The strength of the graphite depends on the temperature as well. At extreme temperatures, its strength increases due to the reduced formation of microcracking [56]. Figure 5.22 shows the change in material strength for different grades of graphite.

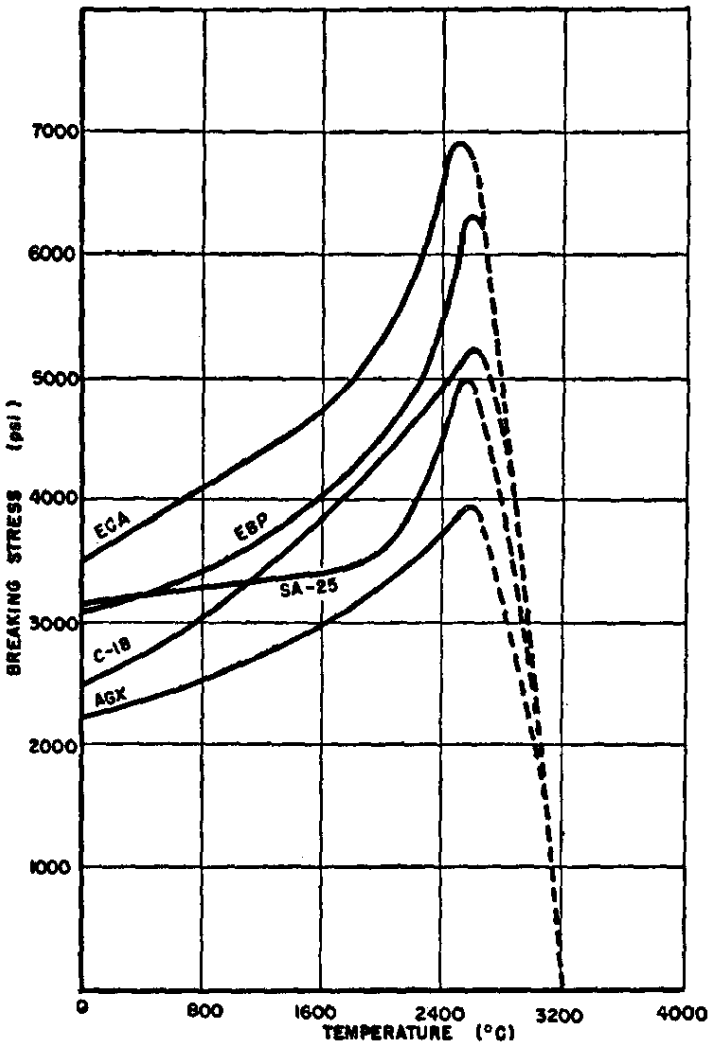

Figure 5.22: The strength of different grades of graphite for different temperatures [56]

The cavity is hotter than the heat exchanger when the system heats up with solar radiation. This means that the graphite has to withstand temperatures higher than the wall temperature of the heat exchanger $T_{wall} = 3100\,\mathrm{K}$. For the preliminary design, it will be estimated that the cavity temperature is $10\,\%$ higher than the heat exchanger. Figure 5.22 shows that at this cavity temperature $T_{cav} = 3410\,\mathrm{K}$, the maximum allowable stress is $6.9\,\mathrm{MPa}$. Because this stress is based on experimental data and not an extrapolation of experimental data, a safety factor of $SF = 1.2$ is used. When assuming that the cavity material experiences the maximum pressure $p_{in} = 5.0\,\mathrm{MPa}$, Equation 5.21 and a safety factor of $20\,\%$ results then in a cavity wall thickness:

$$\begin{aligned} t_{cav} &= \frac{p\,D}{2\,\sigma_\theta}\,SF \\ &= \frac{5.0 \times 10^6\,\mathrm{Pa} \times 1.022 \times 10^{-2}\,\mathrm{m}}{2 \times 6.9 \times 10^6\,\mathrm{Pa}} \times 1.2 = 8.889\,\mathrm{mm} \end{aligned}$$

This thickness results in a cavity radius $R_{cav} = 19.11\,\mathrm{mm}$, and a cavity length $L_{cav} = 133.7\,\mathrm{mm}$. Note that if the heat exchanger imposes pressure on the inside of the system, this will be distributed over the heat exchanger, TES container and the cavity material. A model of the preliminary cavity design, including a section view, is shown in Figure 5.23.

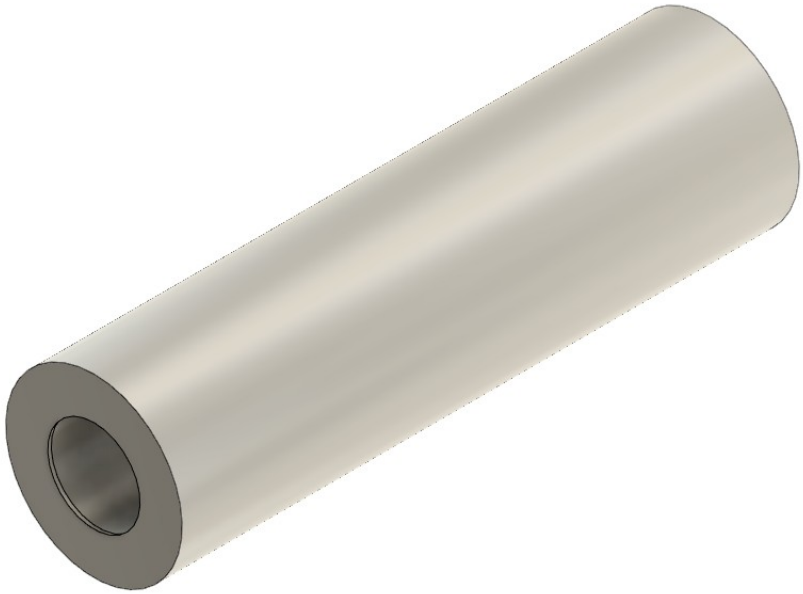

(a) An isometric view

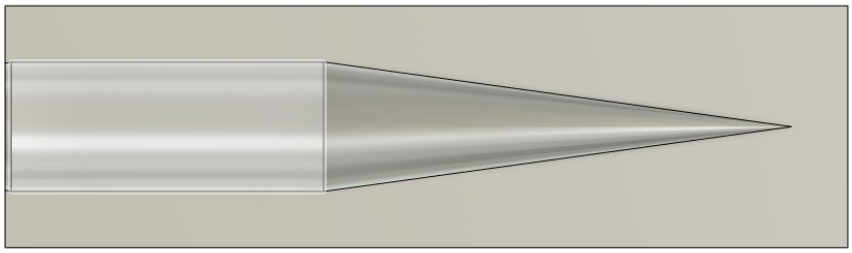

(b) A section view

Figure 5.23: A model of the preliminary cavity design

5.2.1. Assumptions

Multiple assumptions have been stated where relevant for the design process. The key assumptions for the cavity are:

- The cavity temperature is assumed to be $10\,\%$ higher than the heat exchanger wall temperature.
  Validity: This preliminary estimate accounts for an increased temperature without requiring detailed thermal modelling.
- Solar radiation enters the cavity with a Lambertian distribution.
  Validity: The Lambertian distribution approximates the distribution of rays leaving the optical fibre cable.
- Radiation losses are only considered through the aperture; internal re-radiation is neglected.
  Validity: Most radiation is absorbed by cavity walls, thus only the aperture contributes significantly to net radiative loss.
- Hoop stress in the cavity wall is calculated assuming a uniform pressure distribution.

Validity: Pressure gradients are negligible along the cavity length.

- The solar input is modelled as a point source on the cavity axis.
  Validity: The Lambertian distribution covers the effect due to radial differences in the source.

5.3. Thermal Energy Storage

Because the propellant is flowing on the outside of the container, the container walls are also the heat exchanger walls and thus made from rhenium. However, [26] showed that a $0.5\,\mathrm{mm}$ boron nitride liner on the inside of the container is necessary to prevent a reaction between the rhenium and boron. Sealing the container allows the build-up of vapour pressure, preventing further dissociation of the boron nitride [57].

The amount of energy the system needs to store depends on how much energy is needed to heat the propellant while not receiving sunlight. The required mass for this can be determined with the following equation:

$$m_{TES} = \frac{t_{b,ec}\,\dot{Q}_p + t_{ec}\,\dot{Q}_{loss}}{L} \tag{5.50}$$

where m_{TES} is the mass of the TES material in kg, $t_{b,ec}$ is the burn time during eclipse in s, t_{ec} is the eclipse time in s, $\dot{Q}_{loss}$ is the thermal power losses in W, and L is the latent heat of fusion in $\mathrm{J\,kg^{-1}}$. This does not include the mass required to contain the material. Because the thermal losses are not known during the preliminary design phase, the required TES material mass will be based on only the energy required to heat the propellant. For the mass flow of the preliminary design, requirement TES-01 resulted in $0.25\,\mathrm{kg}$ of propellant that needs to be heated during an eclipse.

It was determined that for the mass flow of $\dot{m} = 2.039 \times 10^{-4}\,\mathrm{kg\,s^{-1}}$, the required power to heat the propellant to a chamber temperature of $T_c = 3000\,\mathrm{K}$ is $\dot{Q}_{p,req} = 9063\,\mathrm{W}$. Thus to heat $0.25\,\mathrm{kg}$ of propellant to a temperature of $3000\,\mathrm{K}$, the required energy is $Q_{TES} = 1.111 \times 10^6\,\mathrm{J}$.

In subsection 2.5.4, it was identified that Boron is the best-performing option for latent heat TES. For the preliminary design, its latent heat of melting of $4.644 \times 10^6\,\mathrm{J\,kg^{-1}}$ is used to estimate the required mass for the propulsion system to function during an eclipse. When assuming that only latent heat is used to heat the propellant, this results in a required mass of the TES material of $m_{TES} = 2.393\,\mathrm{kg}$ to store sufficient thermal energy.

subsection 2.5.4 also discussed that a $20\,\%$ void in the container reduces the stresses when the boron expands when becoming liquid, preventing the formation of cracks and leaks. Boron has a density of $2340\,\mathrm{kg\,m^{-3}}$. This results in a volume of $1.022 \times 10^6\,\mathrm{mm^3}$ Boron and, including the void, a total volume of $V_{TES} = 1.278 \times 10^6\,\mathrm{mm^3}$.

For the preliminary design, a thin wall is assumed. The effect of the thickness of the container on the volume of TES material will be considered for the final design. To minimise the radiation losses of the propulsion system, the TES container will be placed around the cavity such that its surface area is minimised. Based on this design choice, equations can be set up for the geometry of the TES system. If the cavity is shorter than the container, the cavity introduces a cylindrical hole in the container with a length of L_{cav} and a radius of R_{cav}. The TES material has a cylindrical shape as well, with a length of L_{TES} and a radius of R_{TES}. The volume of the TES material is then the total volume minus the cavity volume:

$$V_{TES} = \underbrace{\pi\,R_{TES}^2\,L_{TES}}_{\text{outer cylinder volume}} - \underbrace{\pi\,R_{cav}^2\,L_{cav}}_{\text{cavity volume}} \tag{5.51}$$

The surface area of the TES container is to be minimised to reduce the outflow of thermal energy from the TES container:

$$A_{sur} = \underbrace{2\,\pi\,R_{TES}^2}_{\text{two circular faces}} + \underbrace{2\,\pi\,R_{cav}\,L_{cav}}_{\text{inner cylindrical face}} + \underbrace{2\,\pi\,R_{TES}\,L_{TES}}_{\text{outer cylindrical face}} \tag{5.52}$$

Rearranging Equation 5.51 results in:

$$L_{TES} = \frac{V_{TES} + \pi\, R_{cav}^2\, L_{cav}}{\pi\, R_{TES}^2} \tag{5.53}$$

Substituting Equation 5.53 into Equation 5.52:

$$A_{sur} = 2\,\pi\, R_{TES}^2 + 2\,\pi\, R_{cav}\, L_{cav} + 2\,\pi\, R_{TES} \left(\frac{V_{TES} + \pi\, R_{cav}^2\, L_{cav}}{\pi\, R_{TES}^2} \right) \tag{5.54}$$

The only unknown in this equation is the TES container radius R_{TES}. Equation 5.54 can be differentiated to find the minimum:

$$\begin{aligned} \frac{dA_{sur}}{dR_{TES}} &= \frac{d}{dR_{TES}} \left(2\,\pi\, R_{TES}^2\right) + \frac{d}{dR_{TES}} \left(2\,\pi\, R_{cav}\, L_{cav}\right) + \frac{d}{dR_{TES}} \left(\frac{2\,(V_{TES} + \pi\, R_{cav}^2\, L_{cav})}{R_{TES}} \right) \\ &= 4\,\pi\, R_{TES} + 0 - \frac{2\,(V_{TES} + \pi\, R_{cav}^2\, L_{cav})}{R_{TES}^2} \\ &= 4\,\pi\, R_{TES} - \frac{2\,(V_{TES} + \pi\, R_{cav}^2\, L_{cav})}{R_{TES}^2} \end{aligned} \tag{5.55}$$

Setting the derivative equal to $\frac{dA}{dR_{TES}} = 0$ and solving for the TES container radius R_{TES} results in:

$$\begin{aligned} \frac{dA_{sur}}{dR_{TES}} = 0 \quad \Longrightarrow \\ 4\,\pi\, R_{TES} - \frac{2\,(V_{TES} + \pi\, R_{cav}^2\, L_{cav})}{R_{TES}^2} = 0 \end{aligned} \tag{5.56}$$

This equation can be solved algebraically to determine the optimal value of the TES container radius R_{TES}:

$$\begin{aligned} 4\,\pi\, R_{TES} - \frac{2\,(V_{TES} + \pi\, R_{cav}^2\, L_{cav})}{R_{TES}^2} &= 0 \\ 4\,\pi\, R_{TES} - \frac{2\,(1.278 \times 10^{-3}\,\mathrm{m}^3 + \pi\,(1.911 \times 10^{-2}\,\mathrm{m})^2\, 1.337 \times 10^{-1}\,\mathrm{m})}{R_{TES}^2} &= 0 \quad \Longrightarrow \\ R_{TES} &= 6.107 \times 10^{-2}\,\mathrm{m} \end{aligned}$$

Once the TES container radius $R_{TES} = 61.07\,\mathrm{mm}$ is known, the TES container length L_{TES} is determined with Equation 5.53:

$$\begin{aligned} L_{TES} &= \frac{V_{TES} + \pi\, R_{cav}^2\, L_{cav}}{\pi\, R_{TES}^2} \\ &= \frac{1.278 \times 10^{-3}\,\mathrm{m}^3 + \pi\,(1.911 \times 10^{-2}\,\mathrm{m})^2\, 1.337 \times 10^{-1}\,\mathrm{m}}{\pi\,(6.107 \times 10^{-2}\,\mathrm{m})^2} = 1.221 \times 10^{-1}\,\mathrm{m} \end{aligned}$$

Because the cavity length $L_{TES} = 122.1\,\mathrm{mm}$ is longer than the determined TES container length, the volume that is removed to get the TES container volume V_{TES} is based on the TES container length L_{TES} instead of the cavity length L_{cav}:

$$V_{TES} = \underbrace{\pi\, R_{TES}^2\, L_{TES}}_{\text{outer cylinder volume}} - \underbrace{\pi\, R_{cav}^2\, L_{TES}}_{\text{cavity volume}} \tag{5.57}$$

The surface area of the TES container to be minimised then becomes:

$$A_{sur} = \underbrace{2\,\pi\,R_{TES}\,L_{TES}}_{\text{outer cylindrical face}} + \underbrace{2\,\pi\,R_{cav}\,L_{TES}}_{\text{inner cylindrical face}} + \underbrace{2\,\pi\,(R_{TES}^2 - R_{cav}^2)}_{\text{two annular circular faces}} \tag{5.58}$$

Rearranging Equation 5.57 results in:

$$L_{TES} = \frac{V_{TES}}{\pi\,(R_{TES}^2 - R_{cav}^2)} \tag{5.59}$$

Substituting Equation 5.59 into Equation 5.58:

$$A_{sur} = 2\,\pi\,(R_{TES} + R_{cav})\,\frac{V_{TES}}{\pi\,(R_{TES}^2 - R_{cav}^2)} + 2\,\pi\,(R_{TES}^2 - R_{cav}^2) \tag{5.60}$$

Now differentiate with respect to the container radius R_{TES}:

$$\begin{aligned}\frac{dA_{sur}}{dR_{TES}} &= \frac{d}{dR_{TES}}\left(\frac{2\,V_{TES}\,(R_{TES} + R_{cav})}{R_{TES}^2 - R_{cav}^2}\right) + \frac{d}{dR_{TES}}\left(2\,\pi\,(R_{TES}^2 - R_{cav}^2)\right) \\ &= \frac{2\,V_{TES}\,(R_{TES}^2 - R_{cav}^2)\cdot 1 - 2\,V_{TES}\,(R_{TES} + R_{cav})\cdot(2\,R_{TES})}{(R_{TES}^2 - R_{cav}^2)^2} + 4\,\pi\,R_{TES} \\ &= \frac{2\,V_{TES}}{R_{TES}^2 - R_{cav}^2} - \frac{4\,V_{TES}\,R_{TES}\,(R_{TES} + R_{cav})}{(R_{TES}^2 - R_{cav}^2)^2} + 4\,\pi\,R_{TES}\end{aligned} \tag{5.61}$$

Setting the derivative equal to $\frac{dA}{dR_{TES}} = 0$ results in:

$$\begin{gathered}\frac{dA_{sur}}{dR_{TES}} = 0 \quad \Longrightarrow \\ \frac{2\,V_{TES}}{R_{TES}^2 - R_{cav}^2} - \frac{4\,V_{TES}\,R_{TES}\,(R_{TES} + R_{cav})}{(R_{TES}^2 - R_{cav}^2)^2} + 4\,\pi\,R_{TES} = 0\end{gathered} \tag{5.62}$$

Solving this equation for the positive root results in the TES container radius R_{TES}:

$$\begin{gathered}\frac{2\,V_{TES}}{R_{TES}^2 - R_{cav}^2} - \frac{4\,V_{TES}\,R_{TES}\,(R_{TES} + R_{cav})}{(R_{TES}^2 - R_{cav}^2)^2} + 4\,\pi\,R_{TES} = 0 \\ \frac{2\times 1.278\times 10^{-3}\,\mathrm{m}^3}{R_{TES}^2 - (1.911\times 10^{-2}\,\mathrm{m})^2} - \frac{4\times 1.278\times 10^{-3}\,\mathrm{m}^3\,R_{TES}\,(R_{TES} + 1.911\times 10^{-2}\,\mathrm{m})}{(R_{TES}^2 - (1.911\times 10^{-2}\,\mathrm{m})^2)^2} + 4\,\pi\,R_{TES} = 0 \quad \Longrightarrow\end{gathered}$$

$$R_{TES} = 7.219\times 10^{-2}\,\mathrm{m}$$

With the radius $R_{TES} = 72.19\,\mathrm{mm}$ known, the TES container length L_{TES} is determined with Equation 5.59:

$$\begin{aligned}L_{TES} &= \frac{V_{TES}}{\pi\,(R_{TES}^2 - R_{cav}^2)} \\ &= \frac{1.278\times 10^{-3}\,\mathrm{m}^3}{\pi\,((7.219\times 10^{-2}\,\mathrm{m})^2 - (1.911\times 10^{-2}\,\mathrm{m})^2)} = 8.394\times 10^{-2}\,\mathrm{m}\end{aligned}$$

With the radius of the TES container $R_{TES} = 72.19\,\mathrm{mm}$, the wall thickness of the porous medium t_{wall} can be determined as the inner wall of the porous medium is the outer wall of the TES container. Solving Equation 5.21 with the found radius and the same conditions as the spiral runner and multiple

channels, results in a required wall thickness $t_{wall} = 145.9\,\mathrm{mm}$. The benefit of the porous medium is that the cross-sectional area required for the flow of propellant can be placed thinly around the TES container. However, the required wall thickness makes this heat exchanger concept wider than the other concepts. The same length as the porous medium can be achieved by spiralling the channels, and the pressure drop and Mach number of the spiral runner are lower. Based on this performance, it is decided to continue only with the spiral runner and multiple channels concepts. Because the TES container length $L_{TES} = 83.94\,\mathrm{mm}$ is $34.89\,\%$ larger than the length of a channel for the multiple channels design $L = 62.23\,\mathrm{mm}$, a $34.89\,\%$ longer spiral channel will be used to compare the designs during the fluidic analysis:

$$L = 1.3489 \times 2.488 \times 10^{-1}\,\mathrm{m} = 3.356 \times 10^{-1}\,\mathrm{m}$$

By using a spiral channel with a length of $L = 335.6\,\mathrm{mm}$, the relative pressure drop en temperature gain of the concepts can be compared.

For the simplicity of the preliminary design, the thickness of the TES container t_{TES} will be the same for the whole container. To be conservative, the largest wall thickness of the spiral runner concept $t_{wall} = 1.462\,\mathrm{mm}$ and the additional boron nitride liner of $0.5\,\mathrm{mm}$ is used, resulting in the TES container thickness $t_{TES} = 1.962\,\mathrm{mm}$.

A model of the spiral channel in the TES container wall, including a section view, is shown in Figure 5.24. The container is transparent in the model to show the channel.

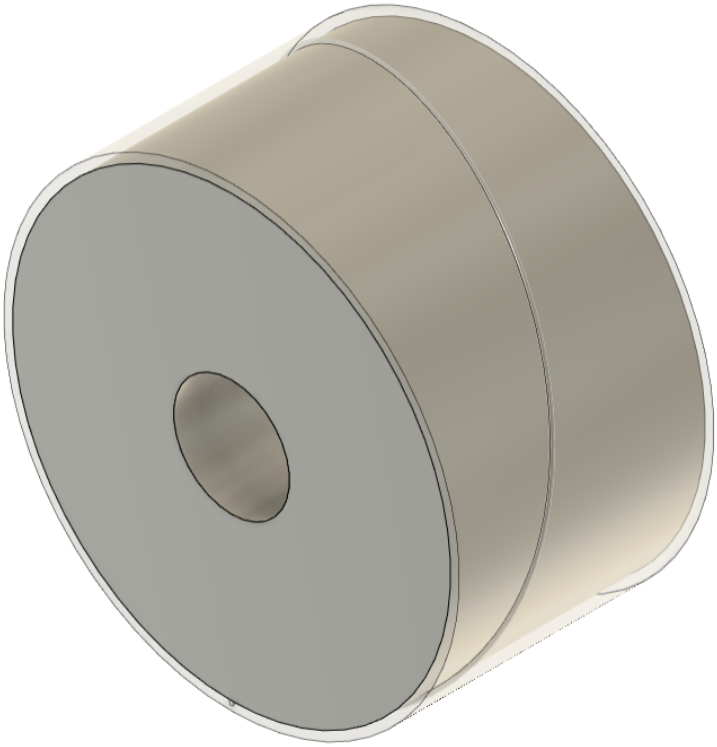

(a) An isometric view

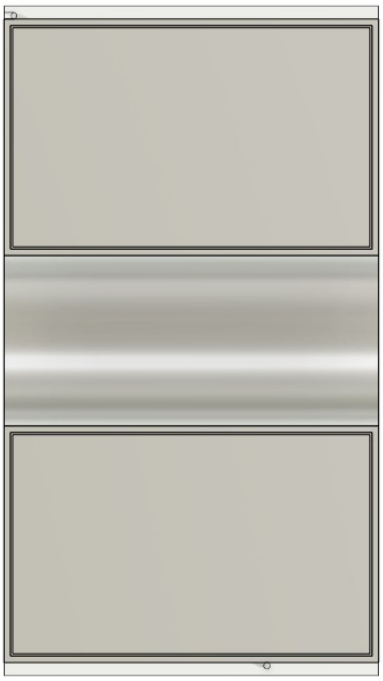

(b) A section view

Figure 5.24: A model of the preliminary design of the TES system with the spiral runner

A model of the multiple channels in the TES container wall, including a section view, is shown in Figure 5.25. The container is transparent in the model to show the channels.

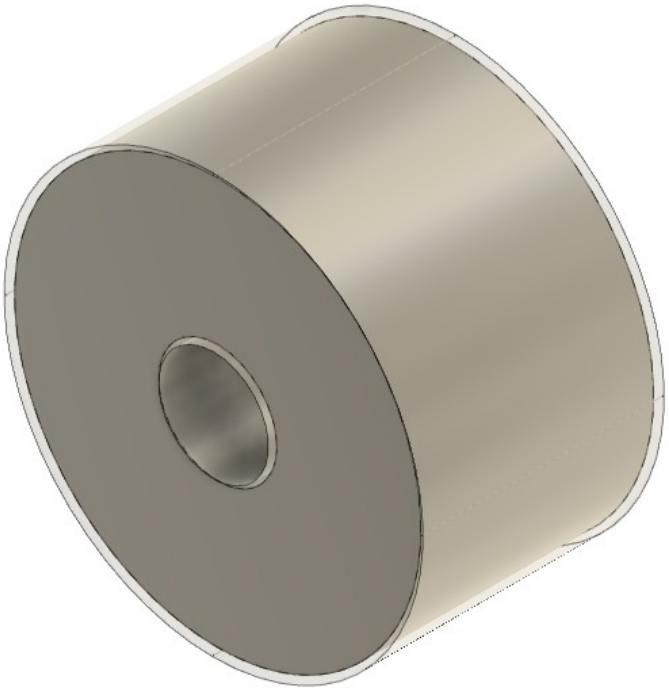

(a) An isometric view

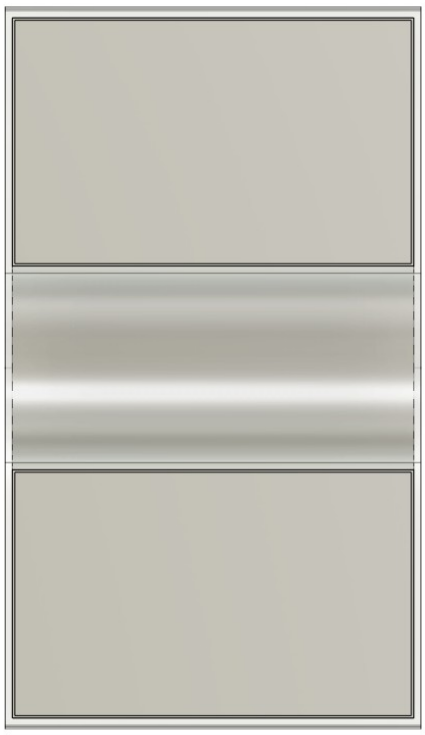

(b) A section view

Figure 5.25: A model of the preliminary design of the TES system with the multiple channels

Because the melting temperature of Boron is $2349\,\mathrm{K}$, the material will not be able to heat the propel-

lant to a chamber temperature of $T_c = 3000\,\mathrm{K}$ during an eclipse when depending only on its latent heat of melting. If the TES material in the final design is also not capable of heating the propellant to a temperature of $3000\,\mathrm{K}$, the mass has to increase to compensate for the lower equivalent velocity. Equation 2.3 shows that for a perfect expanded nozzle, the equivalent velocity changes with the square root of the chamber temperature T_c. Equation 2.1 shows that for a constant thrust, the relation between the chamber temperature T_c and mass flow $\dot{m}$ becomes:

$$T_c \propto \frac{1}{\dot{m}^2} \tag{5.63}$$

Figure 5.2 shows that the change in specific enthalpy is almost linearly dependent on the change in propellant temperature. Combining Equation 5.4 with Equation 5.63 results in the following relation:

$$\dot{Q}_{req} \propto \sqrt{T_c} \tag{5.64}$$

Thus, for a lower propellant temperature and a constant thrust, less energy needs to be stored. Furthermore, the sensible heat of the propulsion system can also be used to heat the propellant.

5.3.1. Assumptions

Multiple assumptions have been stated where relevant for the TES system design process. The key assumptions for the TES system are:

- Only the latent heat of fusion is considered for energy storage calculations.
  Validity: The latent heat dominates the energy storage, and by not including the sensible heat, the estimated required material is conservative.
- A $20\,\%$ void is included in the TES container.
  Validity: The void accommodates expansion of molten boron, preventing stress-induced cracking.
- The TES material is assumed to reach and remain at a uniform temperature.
  Validity: Pure boron has a small melting range, and during the melting process, this temperature is maintained.

5.4. Nozzle

The same nozzle will be designed for each heat exchanger concept and adjusted later for the selected concept. The throat should reach sonic conditions for each concept. This critical throat area is given by the following equation:

$$A_t = \frac{\dot{m}\sqrt{\frac{R_A}{M}\,T_c}}{\Gamma\,p_c} \tag{5.65}$$

Equation 5.65 shows that the only parameter that is different for each concept and influences the critical throat area A_t is the chamber pressure p_c. The throat area will be based on the chamber pressure of the single spiral runner $p_c = 4.901 \times 10^6\,\mathrm{Pa}$, as this is the lowest pressure. For the lower pressures, the flow chokes and the mass flow in the nozzle becomes lower than the mass flow in the chamber. This results in a build-up of propellant and pressure inside the chamber. This increasing pressure allows the mass flow in the nozzle to increase as the critical throat area decreases with increasing pressure. When the inflow of propellant stops, the thruster continues until the build-up has left the nozzle as well.

At a chamber temperature of $T_c = 3000\,\mathrm{K}$ and a chamber pressure of $p_c = 4.901 \times 10^6\,\mathrm{Pa}$, the dimensionless specific heat capacity ratio of the propellant is $\gamma = 1.289$ [51]. With this specific heat capacity ratio, the Vandenkerkhove function shown in Equation 2.6 becomes:

$$\Gamma = \sqrt{\gamma}\left(\frac{2}{\gamma+1}\right)^{\frac{\gamma+1}{2(\gamma-1)}}$$
$$= \sqrt{1.289}\left(\frac{2}{1.289+1}\right)^{\frac{1.289+1}{2(1.289-1)}} = 6.653\times10^{-1}$$

Using Equation 5.65, the critical throat area thus A_t becomes:

$$A_t = \frac{\dot{m}\sqrt{\frac{R}{M}T_c}}{\Gamma\, p_c}$$
$$= \frac{2.039\times10^{-4}\,\mathrm{kg\,s^{-1}}\sqrt{\frac{8.314\,\mathrm{J\,mol^{-1}\,K^{-1}}}{2.016\times10^{-3}\,\mathrm{kg\,mol^{-1}}}3000\,\mathrm{K}}}{6.6527\times10^{-1}\ \times\ 4.901\times10^{6}\,\mathrm{Pa}} = 2.200\times10^{-7}\,\mathrm{m^2}$$

This critical throat area of $A_t = 2.200\times10^{-1}\,\mathrm{mm^2}$, results thus in a throat diameter of $D_t = 5.292\times10^{-1}\,\mathrm{mm}$.

The minimum required expansion ratio will be determined for the choked mass flow of the porous medium, as this concept has the lowest chamber pressure $p_c = 3.022\times10^{6}\,\mathrm{Pa}$. Equation 5.65 shows that for a throat area of $A_t = 2.200\times10^{-1}\,\mathrm{mm^2}$, the maximum mass flow in the nozzle becomes:

$$\dot{m} = \frac{A_t\,\Gamma\,p_c}{\sqrt{\frac{R}{M}T_c}}$$
$$\dot{m} = \frac{2.200\times10^{-7}\,\mathrm{m^2}\ \times\ 6.6527\times10^{-1}\ \times\ 3.022\times10^{6}\,\mathrm{Pa}}{\sqrt{\frac{8.314\,\mathrm{J\,mol^{-1}\,K^{-1}}}{2.016\times10^{-3}\,\mathrm{kg\,mol^{-1}}}3000\,\mathrm{K}}} \quad\Longrightarrow$$

$$\dot{m} = 1.257\times10^{-4}\,\mathrm{kg\,s^{-1}}$$

So far, it has been assumed that there is perfect expansion, resulting in $v_{eq} = v_e$. However, when there is an exit pressure greater than the ambient pressure, the thrust contains a pressure component. The thrust generated by the propulsion system then has two components, a momentum thrust and a pressure thrust. This results in the following equation:

$$F = \dot{m}\,v_e + (p_e - p_a)A_e \tag{5.66}$$

where $p_a = 0\,\mathrm{Pa}$ is the ambient pressure. The exit area A_e is the product of the expansion ratio and the throat area A_t. The relation between the expansion ratio and the pressure ratio is given by the following equation:

$$\frac{A_e}{A_t} = \frac{\Gamma}{\sqrt{\frac{2\gamma}{\gamma-1}\left(\frac{p_e}{p_c}\right)^{\left(\frac{2}{\gamma}\right)}\left(1-\left(\frac{p_e}{p_c}\right)^{\left(\frac{\gamma-1}{\gamma}\right)}\right)}} \tag{5.67}$$

The only remaining unknowns are the exit area A_e and the exit pressure p_e. Based on the characteristics of the fluid and the conditions of the choked flow at the chamber temperature $T_c = 3000\,\mathrm{K}$ and the chamber pressure $p_c = 3.022\times10^{6}\,\mathrm{Pa}$, the expansion ratio is then found for which TRU-01 is satisfied and the thrust is $F = 1.0\,\mathrm{N}$. Because this method does not bound the expansion ratio and only ensures

the thrust for the set mass flow is $F = 1.0\,\mathrm{N}$ as required by TRU-01, this method can result in a very large expansion ratio or a very low expansion ratio.

Solving this set of equations for the preliminary design results in an expansion ratio of $\frac{A_e}{A_t} = 2.479$. This nozzle design would result in a low specific impulse because only a small amount of pressure is converted into momentum. As the expansion ratio is extremely low, a higher specific impulse can be reached by increasing the expansion ratio. The higher expansion ratio can then be combined with a reduced mass flow to get a thrust of $1.0\,\mathrm{N}$ and ensure that requirement TRU-01 is still met. This will be done during the iteration phase.

A model of the preliminary nozzle design, including a section view, is shown in Figure 5.26.

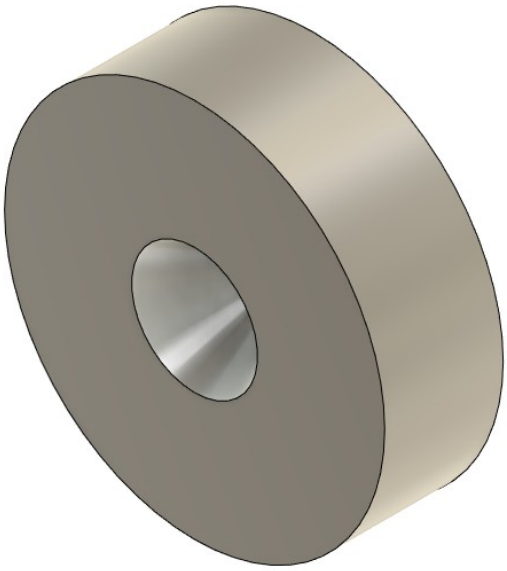

(a) An isometric view

(b) A section view

Figure 5.26: A model of the preliminary nozzle design

5.4.1. Assumptions

Multiple assumptions have been made for the nozzle design. The key assumptions for the preliminary nozzle are:

- The flow at the throat reaches sonic conditions.
  Validity: The nozzle is designed with a throat based on the critical area equation, ensuring choked flow under all considered chamber pressures.

- The nozzle operates in steady-state conditions.
  Validity: The propulsion system is assumed to have reached operating conditions, so transient effects are negligible.
- The propellant behaves as an ideal gas with a constant specific heat ratio.
  Validity: At the chamber temperature and pressure, the propellant behaves as an ideal gas.
- The ambient pressure is zero.
  Validity: The nozzle operates in space, where ambient pressure is effectively zero.
- Viscous and boundary layer effects are neglected for initial expansion calculations.
  Validity: The conical nozzle shape is selected to prevent large losses due to inefficient expansion shapes.

5.5. Insulation

For the system to stabilise at its design temperature, the emitted radiation needs to be equal to the received radiation at this temperature according to the conservation of energy. The emitted radiation power is given by the Equation 5.39 and shows that the high temperature of the cavity $T_{cav} = 3410\,\mathrm{K}$ and of the heat exchanger $T_{wall} = 3100\,\mathrm{K}$ result in a lot of emitted radiation.

To reduce the outer temperature and thus the emitted radiation, a low-conducting insulation layer will be added. The high thermal resistance of this insulation layer will allow to have a colder outer surface temperature while maintaining the hotter heat exchanger temperature $T_{wall} = 3100\,\mathrm{K}$. On the outside of the insulation, a layer of material with a low emissivity will be used to lower the emitted radiation further. A trade-off for the material of the low-emissivity coating is shown in Table 5.7.

Table 5.7: Low-emissivity coating material trade-off

Criteria / Material	Emissivity (polished)	Max. Temp. [K]	Score
Silver (Ag)	0.025	1234	3.5
Gold (Au)	0.030	1336	4.0
Copper (Cu)	0.038	1357	3.5

Table 5.7 shows that gold is the most suitable candidate as it balances between emissivity and the maximum temperature.

It is assumed that the insulation layer is a thin wall that does not affect the surface area. Furthermore, the additional material through which the propellant flows is not taken into account. Only the dimensions of the cavity and the TES container are considered for the preliminary design. The inner surface of the cavity $A_{cav} = 5655\,\mathrm{mm}^2$ was determined in section 5.2. The outer surface area of the cavity material is given by the following equation:

$$A_{cav,outer} = \underbrace{\pi\left(R_{cav}^2 - R_{ap}^2\right)}_{\text{annular circular face}} + \underbrace{\pi R_{cav}^2}_{\text{circular face}} + \underbrace{2\,\pi R_{cav}\,\left(L_{cav} - L_{TES}\right)}_{\text{cylindrical face}} \tag{5.68}$$

$$\begin{aligned} A_{cav,outer} &= \pi\left((1.911\times10^{-2}\,\mathrm{m})^2 - (1.0\times10^{-2}\,\mathrm{m})^2\right) + \pi\,(1.911\times10^{-2}\,\mathrm{m})^2 \\ &\quad + 2\,\pi\,(1.911\times10^{-2}\,\mathrm{m})\,(1.337\times10^{-1}\,\mathrm{m} - 8.394\times10^{-2}\,\mathrm{m}) \quad \Longrightarrow \\ &= 7.953\times10^{-3}\,\mathrm{m}^2 \end{aligned}$$

The outer surface area of the TES container is given by the following equation:

$$A_{TES,outer} = \underbrace{2\,\pi\,\left(R_{TES}^2 - R_{cav}^2\right)}_{\text{annular circular faces}} + \underbrace{2\,\pi\,R_{TES}\,L_{TES}}_{\text{cylindrical face}} \tag{5.69}$$

$$\begin{aligned} A_{TES,outer} &= 2\,\pi\,((7.219\times10^{-2}\,\mathrm{m})^2 - (1.911\times10^{-2}\,\mathrm{m})^2) + 2\,\pi\,(7.219\times10^{-2}\,\mathrm{m})\,(8.394\times10^{-2}\,\mathrm{m}) \\ &= 6.852\times10^{-2}\,\mathrm{m}^2 \end{aligned}$$

This thus results in an outer surface area of the cavity material of $A_{cav,outer} = 7953\,\mathrm{mm}^2$, and an outer surface area of the TES container $A_{TES,outer} = 6.852\times10^{4}\,\mathrm{mm}^2$.

When assuming that the low-emissivity layer has a temperature that is $10\,\%$ lower than the melting temperature, it results in an outer surface temperature of $T_{outer} = 1202\,\mathrm{K}$. Then, solving Equation 5.39 with the found surface areas and the outer surface temperature for the radiated power, results in the radiated power by the outer surface:

$$\begin{aligned} \dot{Q}_{rad,outer} &= \varepsilon\,\sigma\left(A_{TES,outer} + A_{cav,outer}\right)\left(T_{outer}^4 - T_{amb}^4\right) \\ &= 0.030\ \times\ 5.670\times10^{-8}\,\mathrm{W\,m^{-2}\,K^{-4}}\times \\ &\quad \left(6.852\times10^{-2}\,\mathrm{m}^2 + 7.953\times10^{-3}\,\mathrm{m}^2\right)\ \times\ \left(1202\,\mathrm{K}^4 - 0\,\mathrm{K}^4\right) = 271.6\,\mathrm{W} \end{aligned} \tag{5.70}$$

The inner cavity material also emits radiation, but this is partially absorbed by the cavity itself again. This radiation follows a similar path to that of the received radiation from the optical cable. The difference is that the emitted radiation can leave via the aperture area without needing to reflect via a wall segment first. The probability of a ray leaving the cavity is $\frac{A_{ap}}{A_{ap}+A_{cav}}$. The radiated energy of the n^{th} rays becomes:

$$Q_{rad,n} = Q_{emit}\,\frac{A_{ap}}{A_{ap}+A_{cav}}\left((1-\alpha)\,\frac{A_{cav}}{A_{ap}+A_{cav}}\right)^{n-1} \tag{5.71}$$

Summing the radiated energy of all rays results in the total energy radiated by the cavity:

$$\begin{aligned} Q_{rad,cav} &= Q_{emit}\,\frac{A_{ap}}{A_{ap}+A_{cav}}\sum_{n=1}^{\infty}\left((1-\alpha)\,\frac{A_{cav}}{A_{ap}+A_{cav}}\right)^{n-1} \\ &= Q_{emit}\,\frac{A_{ap}}{A_{ap}+A_{cav}}\sum_{n=0}^{\infty}\left((1-\alpha)\,\frac{A_{cav}}{A_{ap}+A_{cav}}\right)^{n} \end{aligned} \tag{5.72}$$

This is a geometric series of the form:

$$\sum_{n=0}^{\infty} r^n = \frac{1}{1-r} \tag{5.73}$$

where r is defined as:

$$r = (1-\alpha)\,\frac{A_{cav}}{A_{ap}+A_{cav}} \tag{5.74}$$

The total radiated power thus becomes:

$$\dot{Q}_{rad,cav} = \frac{\frac{A_{ap}}{A_{ap}+A_{cav}}}{1-(1-\alpha)\,\frac{A_{cav}}{A_{ap}+A_{cav}}}\,\dot{Q}_{emit} = \frac{A_{ap}}{A_{ap}+\alpha\,A_{cav}}\,\dot{Q}_{emit} \tag{5.75}$$

Solving this equation results in the radiated power from the cavity:

$$\begin{aligned} \dot{Q}_{rad,cav} &= \frac{A_{ap}}{A_{ap}+\alpha\,A_{cav}}\,\dot{Q}_{emit} \\ \dot{Q}_{rad,cav} &= \frac{3.142\times10^{-4}\,\mathrm{m}^2}{3.142\times10^{-4}\,\mathrm{m}^2 + 0.84\times5.655\times10^{-3}\,\mathrm{m}^2}\,\dot{Q}_{emit} = 2179\,\mathrm{W} \end{aligned}$$

The total radiated power of the system thus becomes:

$$\dot{Q}_{rad} = \dot{Q}_{rad,cav} + \dot{Q}_{rad,outer} \tag{5.76}$$

$$\dot{Q}_{rad} = 2179\,\mathrm{W} + 271.6\,\mathrm{W} = 2450\,\mathrm{W}$$

For the total radiated power $Q_{rad} = 2450\,\mathrm{W}$ an equal power $\dot{Q}_{abs} = 2450\,\mathrm{W}$ is needed for the system to maintain its temperature. Based on the absorptivity of $99.9\,\%$ of the cavity, the solar power entering the cavity should thus be:

$$\dot{Q}_{abs} = \eta_{abs}\,\dot{Q}_{in} \tag{5.77}$$

$$\dot{Q}_{in} = \frac{2450\,\mathrm{W}}{0.999} = 2452\,\mathrm{W}$$

An optical train efficiency of $\eta_{opt} = 57.5\,\%$ is assumed [23]. For a solar irradiation of $G = 1361\,\mathrm{W\,m^{-2}}$ at 1 AU from the sun, a concentrator is thus needed with an area of:

$$A_{conc} = \frac{\dot{Q}_{in}}{\eta_{opt}\,G} \tag{5.78}$$

$$= \frac{\dot{Q}_{in}}{\eta_{opt}\,G}$$
$$= \frac{2452\,\mathrm{W}}{0.575 \times 1361\,\mathrm{W\,m^{-2}}} = 3.133\,\mathrm{m^2}$$

The insulation layer will be made of a high-temperature resistant material because the inner surface of the insulation layer will have the same temperature as the cavity $T_{cav} = 3410\,\mathrm{K}$ or the heat exchanger $T_{wall} = 3100\,\mathrm{K}$. Table 5.8 shows a trade-off for the insulation material.

Table 5.8: Insulation material trade-off

Criteria / Material	Max. Temp. [K]	Therm. Cond. [W/m/K]	Brittleness	Score
Tungsten (W)	3687	182	2 (>1873 K)	2.7
K-doped W	3687	182	3 (>2773 K)	3.0
Rhenium	3448	48.6	5 (stays ductile)	3.7
Graphite	3773	168	1 (stays brittle)	3.7
Molybdenum (Mo)	2895	139	2 (>2200 K)	2.3
Ca+Mg-doped Mo	2895	139	3 (>2573 K)	2.7

Table 5.8 shows that rhenium and graphite have the same score. Due to the unacceptable score of graphite for the criterion brittleness, rhenium will be chosen as the insulation material.

The insulation layer allows the system to have a lower outer surface temperature than the inside. For the system temperatures to be stable, the radiated power by a surface area should be equal to the power conducted through the insulation to the surface area. The conduction through a material in one dimension is given by the following equation:

$$\dot{Q}_{cond} = \frac{k\,A\,\Delta T}{t} \tag{5.79}$$

To reduce the mass and thickness of the material needed to insulate the system, a foam variant of the insulation material will be used to reduce its conductivity. The Maxwell-Eucken equation gives the effective conductivity of a porous medium:

$$k_{eff} = k_s \frac{2k_s + k_v - 2\phi(k_s - k_v)}{2k_s + k_v + \phi(k_s - k_v)} \tag{5.80}$$

If the void does not conduct heat, the equation simplifies to:

$$k_{eff} = k_s \frac{2(1-\phi)}{2+\phi} \tag{5.81}$$

When assuming a porosity of $phi = 99\,\%$, and with the thermal conductivity of rhenium $k_s = 48.6\,\mathrm{W\,m^{-1}\,K^{-1}}$, this results in an effective conductivity:

$$\begin{aligned} k_{eff} &= k_s \frac{2(1-\phi)}{2+\phi} \\ &= (48.6\,\mathrm{W\,m^{-1}\,K^{-1}}) \frac{2\,(1-0.99)}{2+0.99} \\ &= 3.251 \times 10^{-1}\,\mathrm{W\,m^{-1}\,K^{-1}} \end{aligned}$$

Equation 5.79 can then be solved to determine the insulation thickness for the cavity material $t_{ins,cav}$ and the insulation thickness for the TES container $t_{ins,TES}$. This gives a thickness of $t_{ins,cav} = 202.1\,\mathrm{mm}$ and $t_{ins,TES} = 173.8\,\mathrm{mm}$ respectively, which increases the size of the system by an order of magnitude.

5.5.1. Assumptions

Multiple assumptions have been stated for the insulation design. The key assumptions for the insulation are:

- The insulation layer is assumed to be a thin wall that does not affect the overall surface area.
  Validity: The effect of the increased surface area is included later.
- Radiation from the cavity inner surface is partially absorbed internally before escaping.
  Validity: The probability model approximates internal absorption based on area ratios and absorptivity.
- The outer surface of the insulation has a temperature 10% below the melting temperature of the coating.
  Validity: The constant temperature simplifies the thermal analysis while applying a safety factor.
- Heat transfer through the insulation is assumed one-dimensional.
  Validity: The assumption is conservative as the actual insulation volume is relatively larger on the outside of the system.
- Steady-state thermal conditions are assumed.
  Validity: The system is expected to reach thermal equilibrium.

5.6. Findings

The cavity area A_{cav} can be reduced further due to the higher absorption efficiency than estimated. This will mainly affect the cavity length L_{cav} because the cavity radius R_{cav} will be dominated by the required aperture radius R_{ap} instead of the cylinder radius R_{cyl}. The strength of the graphite is also strongly reduced at $T_{cav} = 3410\,\mathrm{K}$, which increases the required thickness.

The same effect was also seen for the rhenium, where the uncertainty was even larger, requiring a larger safety factor. The effect of the thickness of the container on the TES material volume will increase the required volume. Furthermore, accounting for the radiation losses will increase the required volume as

well. The TES container sizing was done for a minimal surface area, but will, in the next iteration, be done to minimise radiation losses. Also, the reduced conductivity of the TES material when melted can increase the temperature of the cavity T_{cav} and, when burning for a longer period, limit the heat flow to the propellant.

The chamber temperature of $T_c = 3000\,\mathrm{K}$ combined with the set mass flow resulted in an extremely low expansion ratio. The specific impulse I_{sp} of the system, and thus its efficiency, can be improved by increasing the expansion ratio. The propellant mass flow can then be reduced to have a thrust of $F = 1.0\,\mathrm{N}$ and still meet requirement TRU-01.

The high temperatures also resulted in large thermal losses, requiring a high TES material mass. Only the area of the solar concentrator has been determined, but the high input power required to maintain such a temperature would increase the mass of the solar concentrator as well. The following iteration will therefore be done for a wall temperature of the heat exchanger of $T_{wall} = 2349\,\mathrm{K}$, the melting temperature of boron.

To distinguish the different components more clearly, the following colouring scheme is used:

- Blue Cavity
- Orange TES container
- Green TES liner
- Red TES material
- Purple Heat exchanger (including piping)
- Brown Insulation
- Pink Nozzle

Using these colours results in the sketch of the system as shown in Figure 5.27.

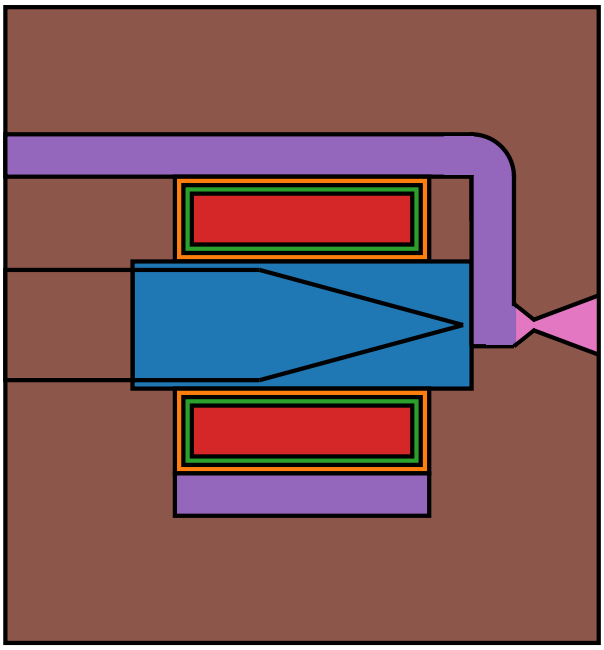

Figure 5.27: A coloured sketch of the preliminary design to distinguish between the components

A model of the spiral runner concept, including a section view, is shown in Figure 5.28. The insulation is transparent in the model.

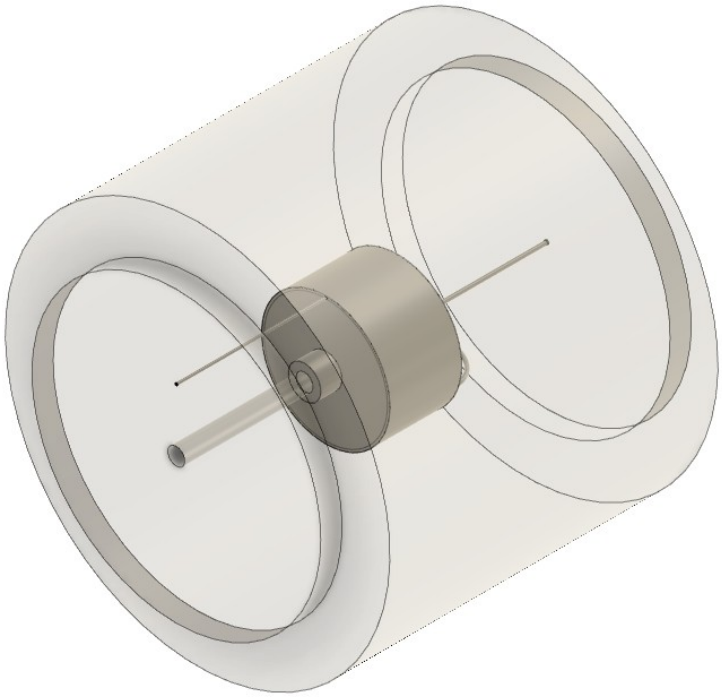

(a) An isometric view

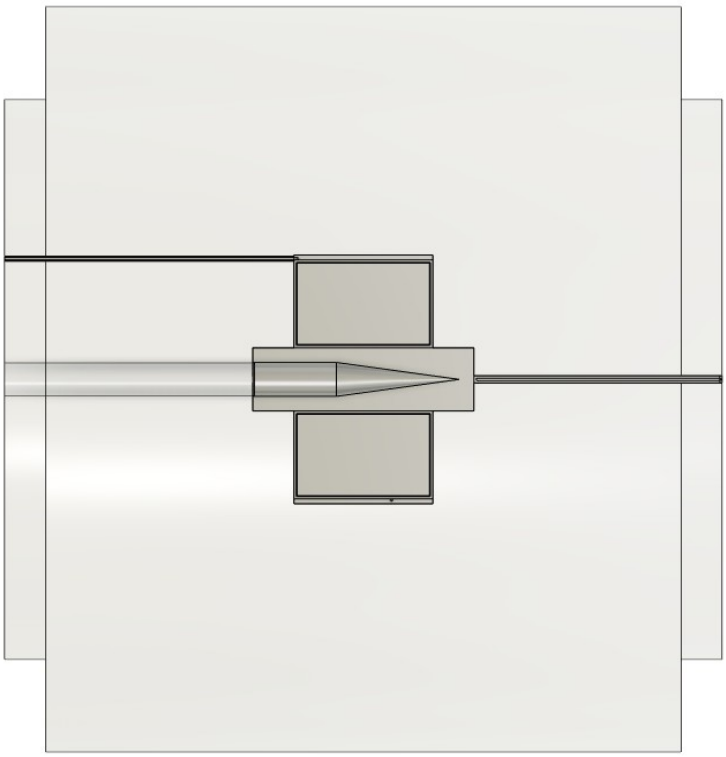

(b) A section view

Figure 5.28: A model of the preliminary design for the spiral runner concept

A model of the multiple channels concept, including a section view, is shown in Figure 5.29. The insulation is transparent in the model.

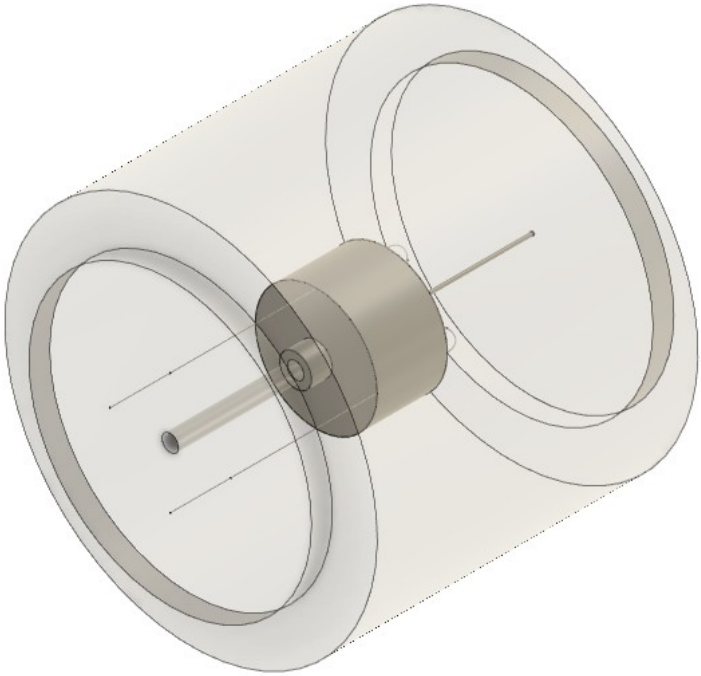

(a) An isometric view

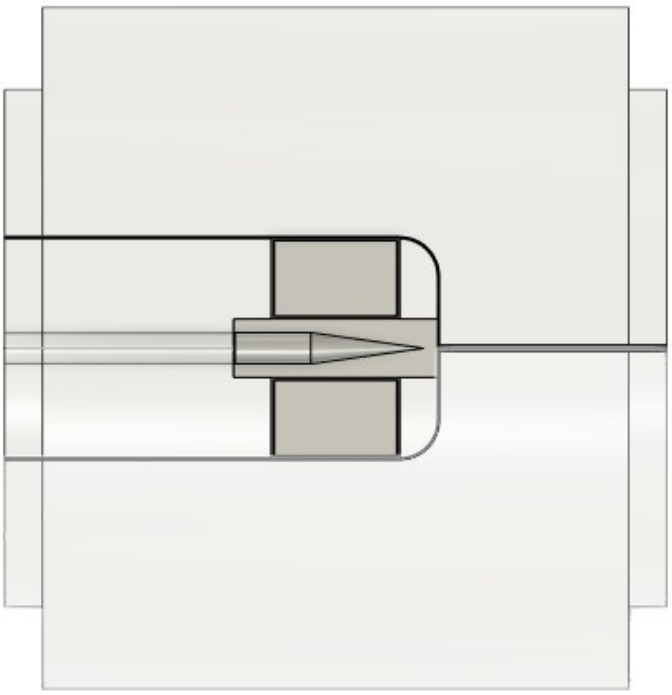

(b) A section view

Figure 5.29: A model of the preliminary design for the multiple channels concept

6

Mathematical Model

This chapter describes the mathematical model of the system that will be used for the simulations. To create the mathematical model of the system, three differential control elements will be used. One is a control volume with no bulk motion, one is a control volume with bulk motion, and one is a control surface.

6.1. Conduction

The control volume will be defined without a coordinate system. One surface of the control volume will be positioned at position vector $\vec{r}$, and the opposite surface in direction $\vec{n}$ at $\vec{r} + d\ell\vec{n}$. The heat rates at these surfaces are respectively $\vec{q}(\vec{r})$ and $\vec{q}(\vec{r} + d\ell\vec{n})$. The heat rates in a cylindrical coordinate system are shown in Figure 6.1.

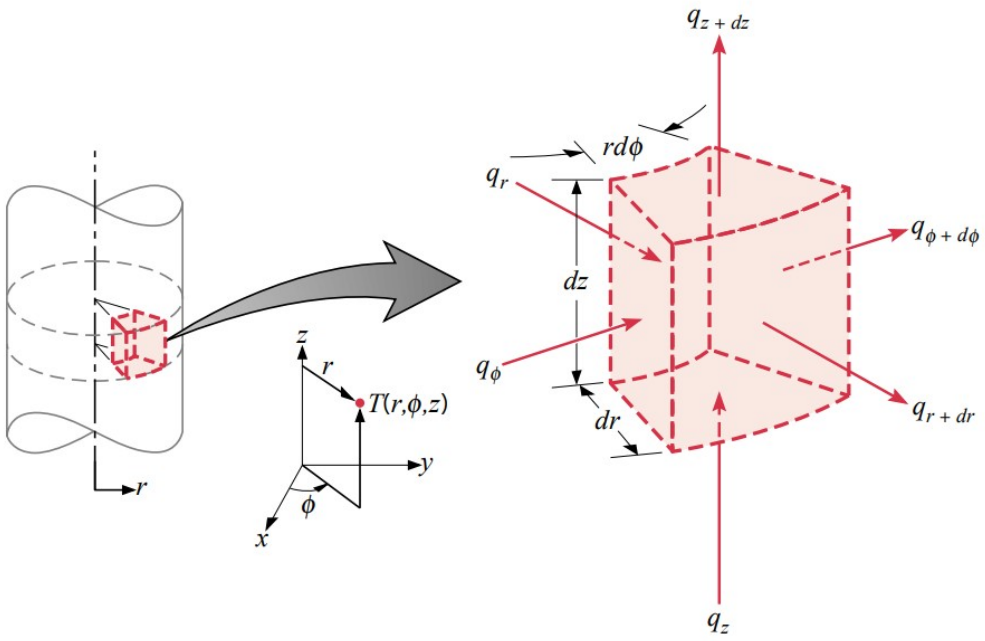

Figure 6.1: The heat rates of a differential control volume in a cylindrical coordinate system [32]

A first-order Taylor series approximation of the heat rate $\vec{q}(\vec{r} + d\ell\vec{n})$ is:

$$\vec{q}(\vec{r} + d\ell\,\vec{n}) = \vec{q}(\vec{r}) + d\ell\,(\nabla\vec{q}) \cdot \vec{n} \tag{6.1}$$

The heat flux over the boundary ∂V of control volume V is the net thermal power into the control element. The net thermal power is given by the following equation:

$$\dot{Q}_{cond} = -\int_{\partial V} \vec{q}'' \cdot \vec{n}\, dA \tag{6.2}$$

The negative sign is added before the integral because the outward normal is positively defined for the surface integral. When using the Divergence theorem to transform the surface integral, the net thermal power becomes:

$$\int_{\partial V} \vec{q}'' \cdot \vec{n}\, dA = \int_V \nabla \cdot \vec{q}''\, dV \tag{6.3}$$

$$\dot{Q}_{cond} = -\nabla \cdot \vec{q}''\, dV \tag{6.4}$$

The sensible energy storage of the medium is defined as:

$$\dot{Q}_{sens} = \rho\, c_p \frac{\partial T}{\partial t}\, dV \tag{6.5}$$

The latent energy storage of the medium is defined as:

$$\dot{Q}_{lat} = \rho L \frac{d\alpha}{dt}\, dV \tag{6.6}$$

The rate version of the conservation of energy equation becomes:

$$\dot{Q}_{cond} = \dot{Q}_{sens} + \dot{Q}_{lat} \tag{6.7}$$

$$-\nabla \cdot \vec{q}''\, dV = \rho\, c_p \frac{\partial T}{\partial t}\, dV + \rho L \frac{d\alpha}{dt}\, dV \tag{6.8}$$

The control volume can be divided out of the equation, resulting in:

$$-\nabla \cdot \vec{q}'' = \rho\, c_p \frac{\partial T}{\partial t} + \rho L \frac{d\alpha}{dt} \tag{6.9}$$

Using Fourier's law, the conduction heat rate in this equation is given by:

$$\vec{q}'' = -k\nabla T \tag{6.10}$$

Substituting results in:

$$\nabla \cdot (k\nabla T) = \rho\, c_p \frac{\partial T}{\partial t} + \rho L \frac{d\alpha}{dt} \tag{6.11}$$

$$\nabla \cdot (k\nabla T) = \rho \left(c_p \frac{\partial T}{\partial t} + L \frac{d\alpha}{dt} \right) \tag{6.12}$$

In cylindrical coordinates, this becomes:

$$\frac{1}{r}\frac{\partial}{\partial r}\left(k\, r\, \frac{\partial T}{\partial r}\right) + \frac{1}{r^2}\frac{\partial}{\partial \phi}\left(k\, \frac{\partial T}{\partial \phi}\right) + \frac{\partial}{\partial z}\left(k\, \frac{\partial T}{\partial z}\right) = \rho\, c_p\, \frac{\partial T}{\partial t} + \rho\, L\, \frac{d\alpha}{dt} \tag{6.13}$$

6.2. Convection

Convection transfers energy by conduction within the fluid, and by advection due to the bulk motion of the fluid. The total heat flux vector in this case consists of the conductive flux and the advective flux.

The control volume is bounded by the surface ∂V and the enclosing volume V. Let $\vec{v}$ be the velocity field of the fluid, and $\rho c_p T$ the specific enthalpy per unit volume. The advective transport of energy across the surface is given by:

$$\dot{Q}_{adv} = -\int_{\partial V} \rho\, c_p T\, \vec{v} \cdot \vec{n}\, dA \tag{6.14}$$

When using the Divergence theorem to transform the surface integral, the net thermal power becomes:

$$\int_{\partial V} \rho\, c_p T\, \vec{v} \cdot \vec{n}\, dA = \dot{Q}_{adv} = \int_V \nabla \cdot (\rho\, c_p T\, \vec{v})\, dV \tag{6.15}$$

$$\dot{Q}_{adv} = -\int_V \nabla \cdot (\rho\, c_p T\, \vec{v})\, dV \tag{6.16}$$

As the propellant does not undergo any phase changes, the total energy rate includes conductive, advective, and sensible energy terms:

$$\dot{Q}_{cond} + \dot{Q}_{adv} = \dot{Q}_{sens} \tag{6.17}$$

$$-\nabla \cdot \vec{q}''\, dV - \nabla \cdot (\rho\, c_p T\, \vec{v})\, dV = \rho\, c_p \frac{\partial T}{\partial t}\, dV \tag{6.18}$$

The control volume can be divided out of the equation, resulting in:

$$-\nabla \cdot \vec{q}'' - \nabla \cdot (\rho\, c_p T\, \vec{v}) = \rho\, c_p \frac{\partial T}{\partial t} \tag{6.19}$$

This can be rearranged into:

$$\nabla \cdot (k \nabla T) = \rho\, c_p \left(\frac{\partial T}{\partial t} + \vec{v} \cdot \nabla T \right) \tag{6.20}$$

In cylindrical coordinates, this becomes:

$$\frac{1}{r}\frac{\partial}{\partial r}\left(k\, r\, \frac{\partial T}{\partial r}\right) + \frac{1}{r^2}\frac{\partial}{\partial \phi}\left(k\, \frac{\partial T}{\partial \phi}\right) + \frac{\partial}{\partial z}\left(k\, \frac{\partial T}{\partial z}\right) = \rho\, c_p \left(\frac{\partial T}{\partial t} + v_r \frac{\partial T}{\partial r} + \frac{v_\phi}{r}\frac{\partial T}{\partial \phi} + v_z \frac{\partial T}{\partial z} \right) \tag{6.21}$$

6.3. Surface Energy Balance

At a differential control surface, energy transfers via conduction into the solid, and via convection and radiation from the surface into the surroundings. Because the control surface cannot store thermal energy, the resulting energy rate balance is:

$$q''_{cond} = q''_{conv} + q''_{rad} \tag{6.22}$$

where:

- $q''_{cond} = -k\ \frac{\partial T}{\partial n}\big|_{surface}$ is the conductive heat flux entering the surface from the solid direction,

- $q''_{conv} = h\left(T_s - T_\infty\right)$ is the convective heat flux transferred to the fluid,
- $q''_{rad} = \varepsilon\sigma\left(T_s^4 - T_\infty^4\right)$ is the net radiative heat exchange with the surroundings.

Combining these, the surface becomes:

$$-k\left.\frac{\partial T}{\partial n}\right|_{surface} = h\left(T_s - T_\infty\right) + \varepsilon\sigma\left(T_s^4 - T_\infty^4\right) \tag{6.23}$$

This expression can serve as a boundary condition to solve the conduction or convection energy rate balance equation.

7

Simulations

This chapter will discuss the simulations of the mathematical model described in chapter 6. The simulation results are based on the stable state of the system. Due to the complexity of modelling the velocity field in Equation 6.21, especially for turbulent flow, the convection will be simulated separately. The convection is first simulated to perform a trade-off between the spiral runner and the multiple channels concept. Then the selected heat exchanger will be included in the conduction and radiation simulation. Due to the difference of order of magnitude between the system dimensions with or without insulation, a layer with a $90\,\%$ smaller thickness and a $90\,\%$ lower thermal conductivity is used for the simulated preliminary design. This insulation layer will have the same thermal resistance as shown by Equation 5.79, but more nodes will be assigned to the other components of the system. This helps validate the estimated thickness and thermal losses, as this is based on a thin-walled assumption. For the final design, the correct thickness will be applied to ensure that the surface areas are accurate.

7.1. Convection

The goal of the convection simulation is to verify if the estimated chamber temperature T_c and chamber pressure p_c are reached. With those results, a heat exchanger concept can be selected. For the spiral runner, the complete TES system and heat exchanger will be modelled, as there is no rotational symmetry. For the multiple channels concept, only an eighth of the system has to be simulated due to rotational symmetry.

7.1.1. Boundary Conditions

To determine the required length of the channels, it was assumed that the wall temperature is constant. To get more realistic results, a boundary condition for the simulation will be that the surface temperature of the TES material is constant, as during the phase change. This allows the heat exchanger wall temperature T_{wall} to cool down due to the cooler propellant. A more accurate chamber temperature T_c can thus be determined.

At the inlet of the channels, a boundary condition for the temperature $T_{in} = 273.15\,\mathrm{K}$, the pressure $p_{in} = 5.000\,\mathrm{MPa}$, and the mass flow $\dot{m}$ is imposed. The outlet is specified as having unknown conditions. This then forces the wanted propellant flow while giving the solver the freedom to determine the pressure drop over the channels and the gained energy. The actual mass flow, however, depends on the outlet pressure, which itself depends on the mass flow. The ambient pressure cannot be set as the outlet pressure, because the pressure changes between the nozzle exit and the heat exchanger exit. It is of interest to know the change in enthalpy of the ideal mass flow, as this is used to determine the required TES material, but the determination of the actual mass flow will be a recommendation. For the multiple channels concept, at the symmetry planes, a symmetry/slip plane boundary condition is added as well.

7.1.2. Initial Conditions

To help the results converge better and more quickly, initial conditions are added. All components except the propellant are given an initial temperature equal to the estimated constant wall temperature T_{wall}, and thus not only the TES material. These materials then do not need to be heated up by the solver first.

7.1.3. Results

The results for the preliminary design of the spiral runner concept are shown in Figure 7.1.

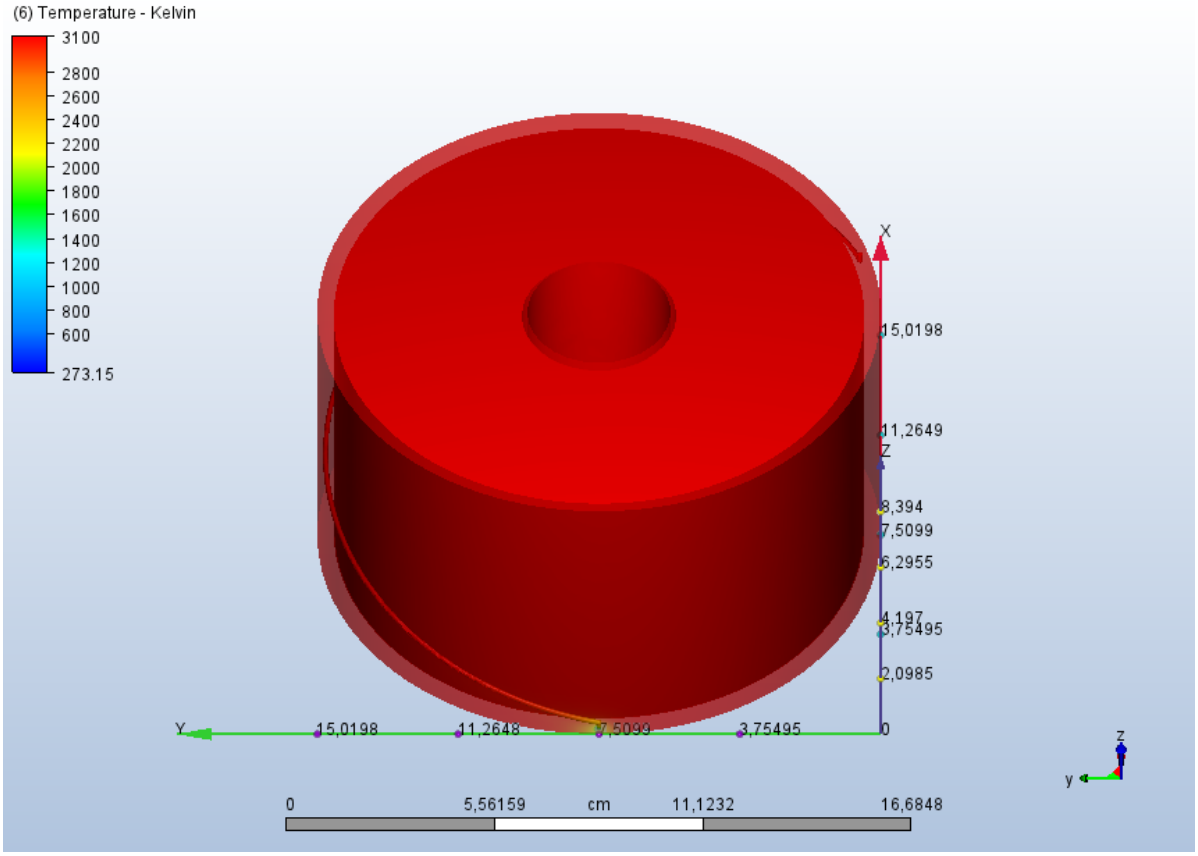

(a) The temperature results

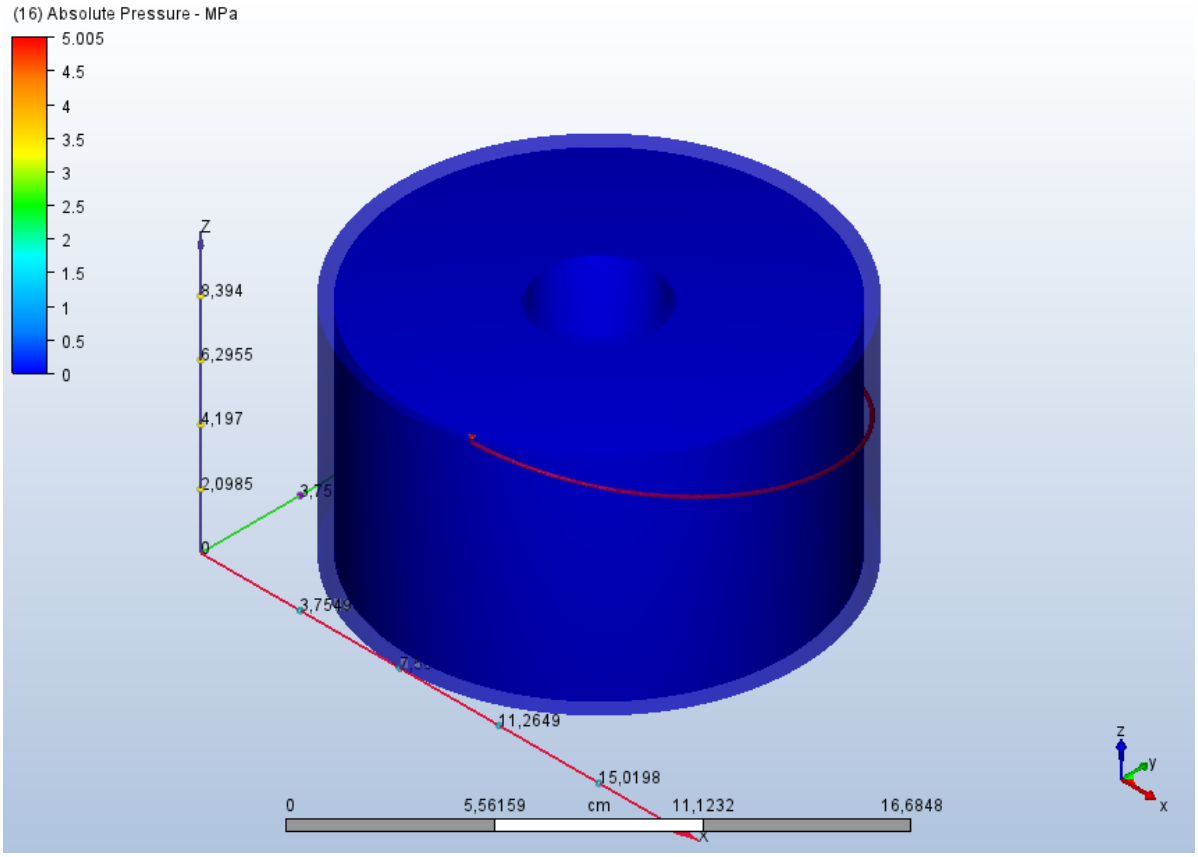

(b) The pressure results

Figure 7.1: The CFD results for the spiral runner concept

Due to the small channel size compared to the TES container, the difference in colour for the temperature and pressure within the model is small. This is because the change in temperature and pressure in the TES container is small, and it confirms a uniform distribution that does not induce additional stresses. Only within the channel do these conditions change significantly.

The results of interest are the conditions calculated within the model at the outlet. For the spiral runner concept, at the outlet, an average chamber temperature of $T_c = 3100\,\mathrm{K}$, and an average chamber pressure of $p_c = 4.998\,\mathrm{MPa}$ were found. The results for the multiple channels concept are shown in Figure 7.2.

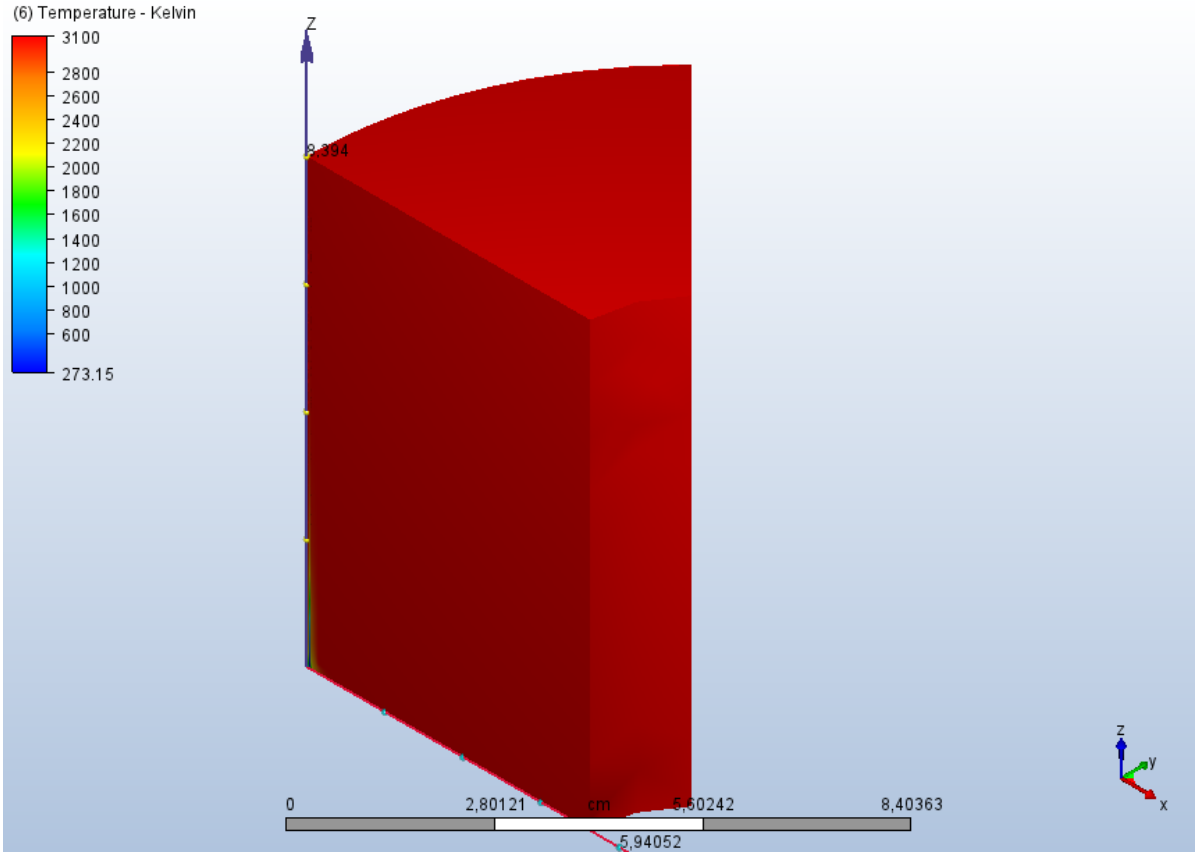

(a) The temperature results

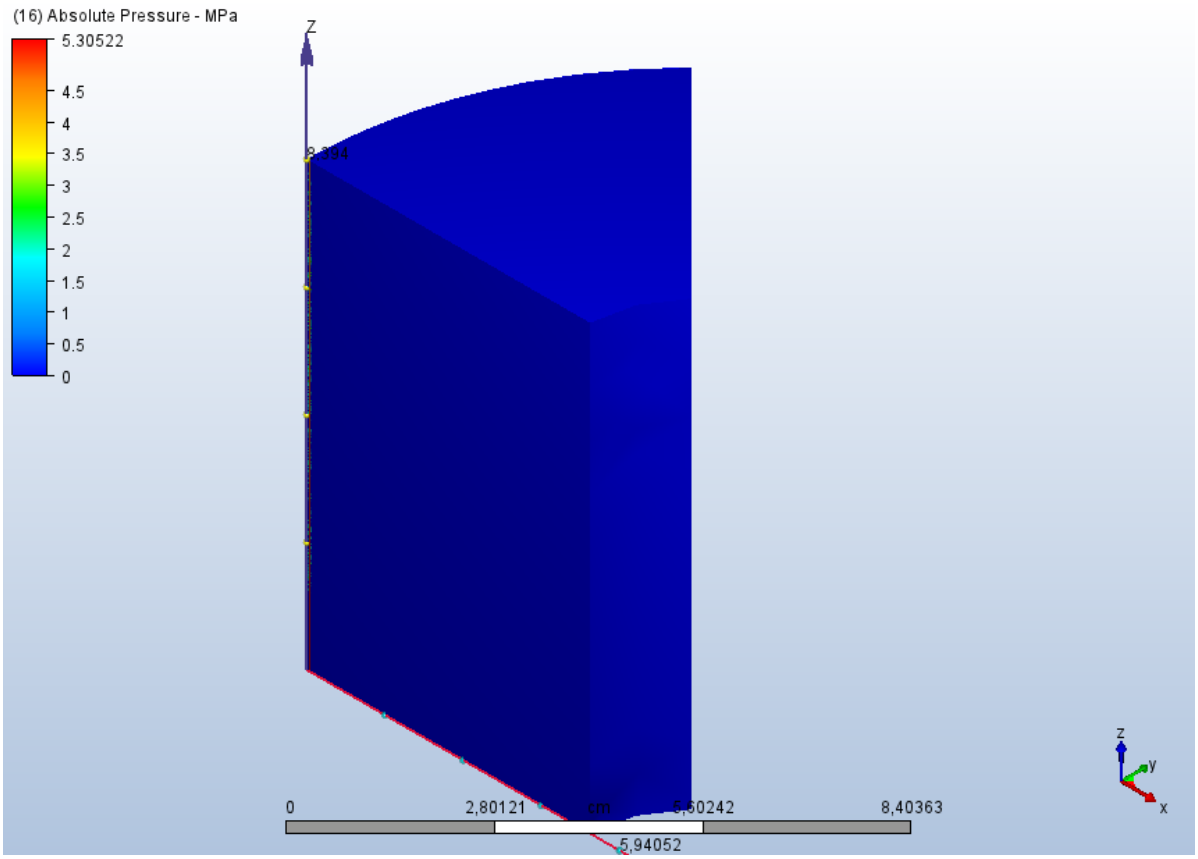

(b) The pressure results

Figure 7.2: The CFD results for the multiple channels concept

For the multiple channels concept, at the outlet, an average chamber temperature of $T_c = 3099\,\mathrm{K}$, and an average chamber pressure of $p_c = 4.489\,\mathrm{MPa}$ were found.

The spiral runner concept resulted in a higher achieved chamber temperature T_c and a higher chamber pressure p_c. However, for both concepts, it can be seen that there is a local static pressure that is higher than the inlet pressure. The large temperature difference causes a local compression of the flow. Due to this compression, the static conditions at the outlet are higher than estimated. Note that the static temperature at the outlet is also higher than estimated for both concepts because the channel lengths were larger than required.

When comparing the wall temperature T_{wall} at the inlet for both concepts, it can be seen that the outer wall of the multiple channels concept has cooled down more than the spiral runner concept, due to the smaller wall thickness t_{wall}. The wall temperatures T_{wall} for the spiral runner concepts and the multiple channels concept are shown in Figure 7.3.

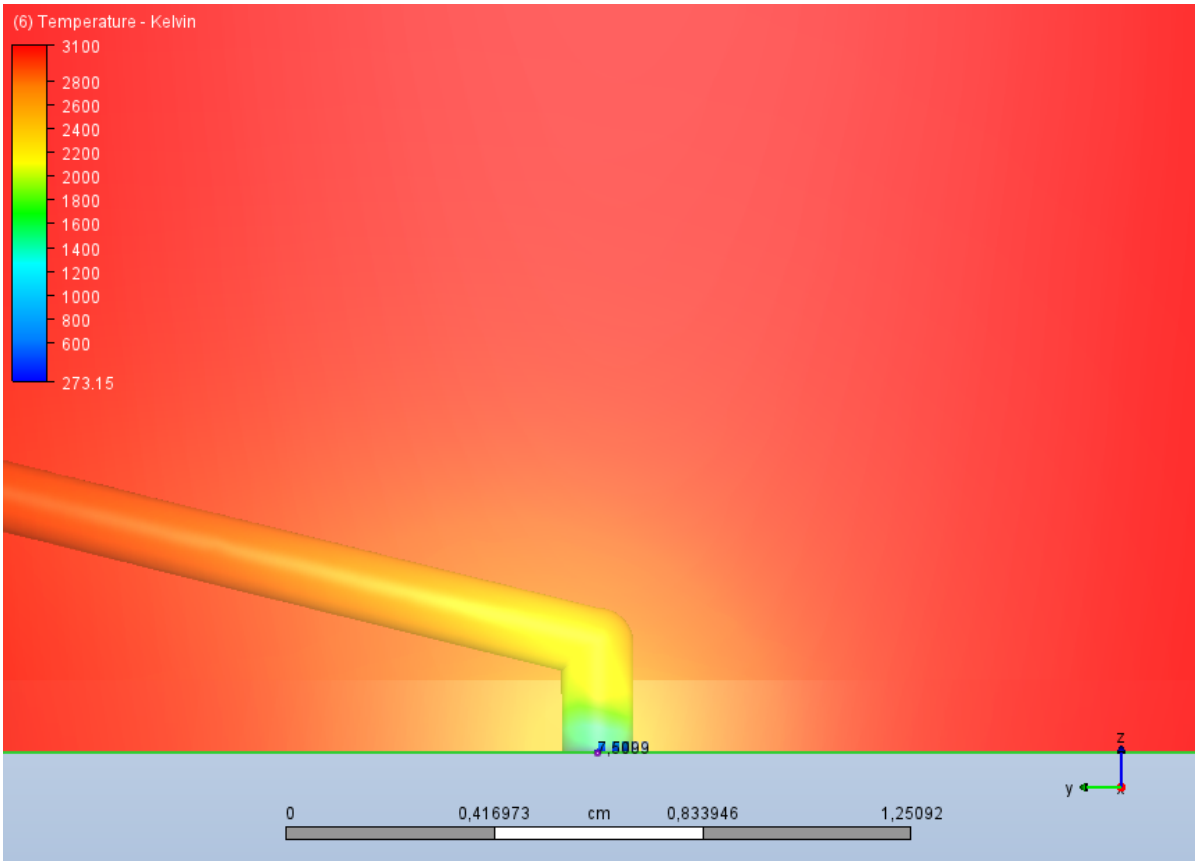

(a) The wall temperature of the spiral runner concept

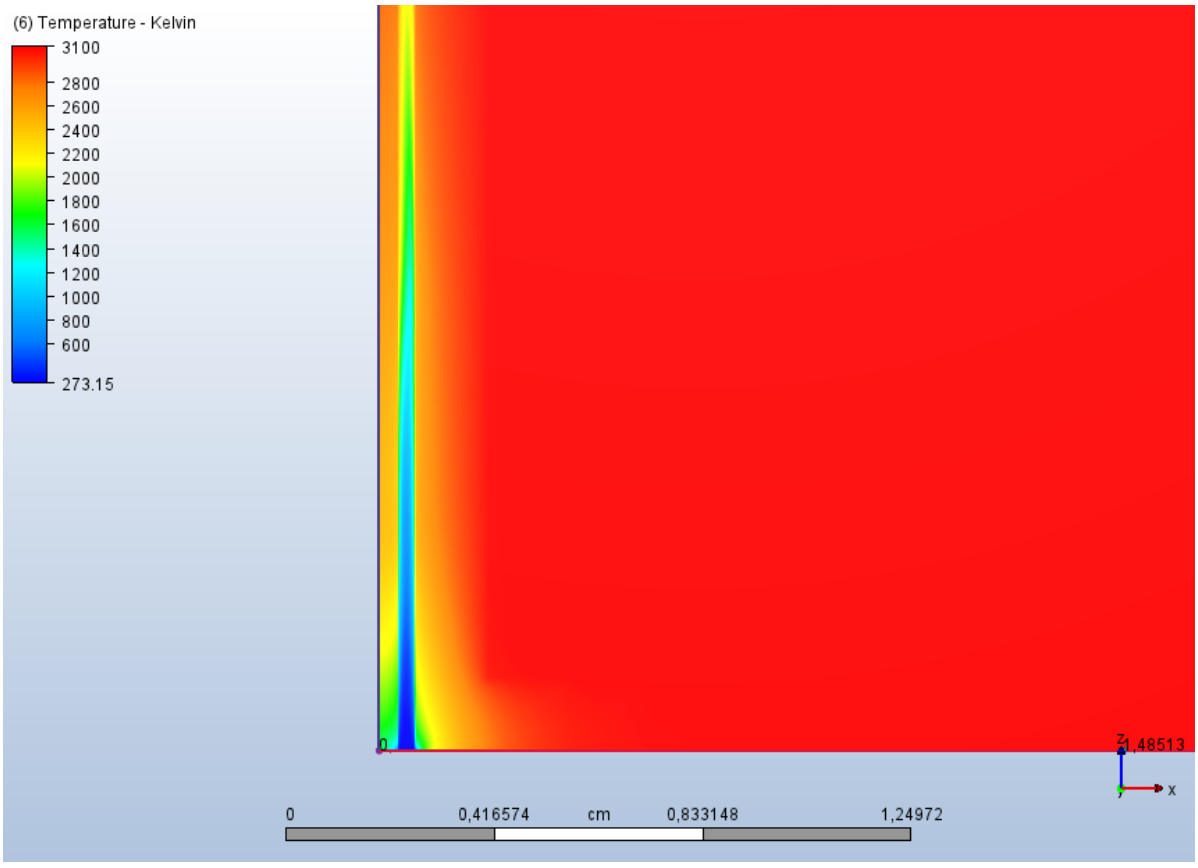

(b) The wall temperature of the multiple channels concept

Figure 7.3: The wall temperature at the inlet for the spiral runner concept and the multiple channels concept

To select a heat exchanger concept, a trade-off will be performed. The selected criteria are the chamber temperature T_c, the chamber pressure p_c, and the size. Both systems have the length of the TES container, but the diameter and required wall thickness t_{wall} vary. The result of the trade-off is shown in Table 7.1.

Table 7.1: Heat exchanger concept trade-off

Concept \ Criteria	Chamber Temperature	Chamber Pressure	Size	Score
Spiral Runner	$3100\,\mathrm{K}$	$4.998\,\mathrm{MPa}$	Largest	4.7
Multiple Channels	$3099\,\mathrm{K}$	$4.489\,\mathrm{MPa}$	Smallest	4.3

The concepts are comparable, and there is especially little difference in the temperature gained. But the required additional channel length scales inversely with the mean temperature difference, thus the closer the chamber temperature T_c is to the wall temperature T_{wall}, the more significant these small differences become. For the lowered wall temperature $T_{wall} = 2349\,\mathrm{K}$, less local compression will occur. This better performance of the spiral runner with respect to the outlet conditions is thus chosen at the cost of a larger heat exchanger.

7.2. Conduction and Radiation

The Python simulation will be used to model the absorber, thus including the cavity, TES system, heat exchanger, and insulation. To have the same coordinates as the ray tracing simulation for the cavity, the origin is placed at the centre of the aperture.

7.2.1. Nodes

When not taking into account the channels for the propellant, the system has rotational symmetry. Due to this, the system can be modelled by a 2D representation. For each component, a polygon is defined, with hollow components being modelled hollow to prevent overlap of the polygons. The resulting polygons for the preliminary design are shown in Figure 7.4.

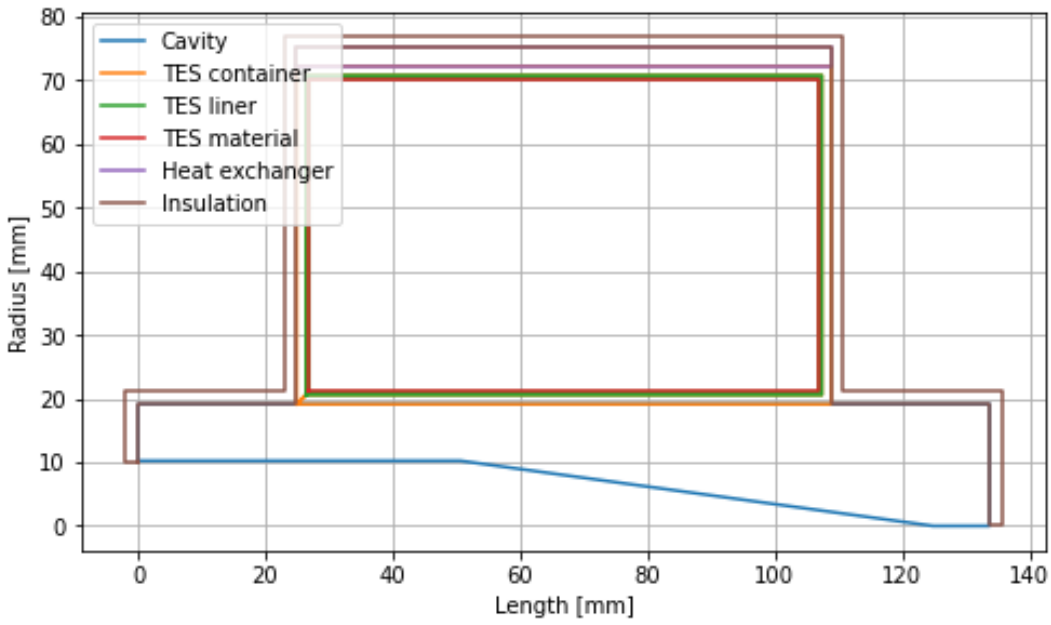

Figure 7.4: The polygons of the preliminary design used for the simulation

Then, based on the number of nodes per radial and axial direction, a mesh is created. The coordinates of each node are compared with the coordinates of the polygons to determine to which component

they belong. Nodes that do not lie within the polygon of a component are part of the environment surrounding the system. The verification results for random points being inside or outside the TES polygon are shown in Figure 7.5.

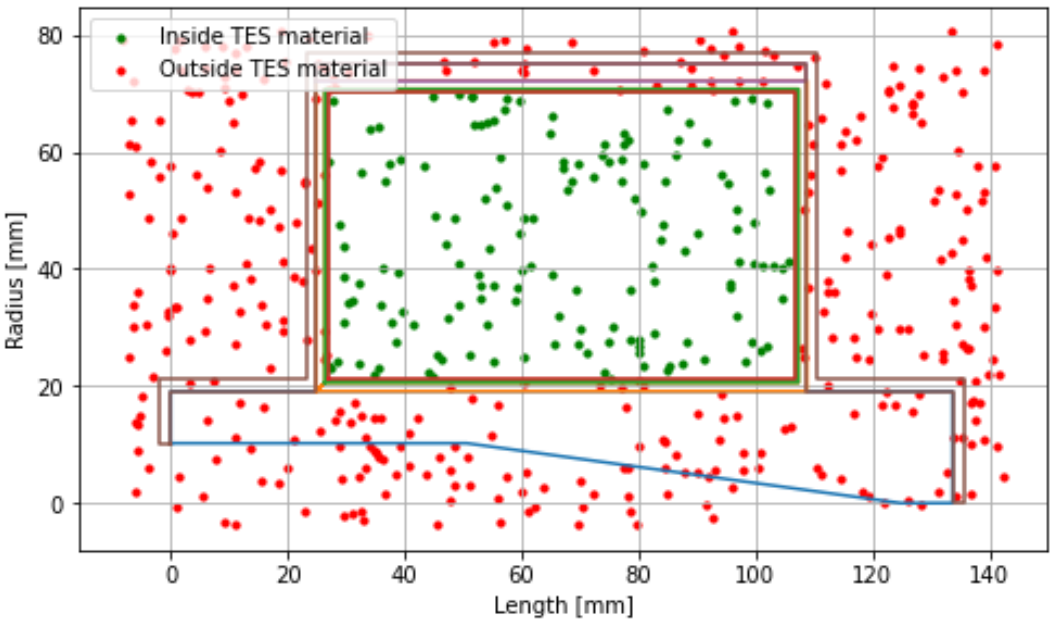

Figure 7.5: The verification results for random points being inside or outside the TES material polygon

By using domain classification, different properties can be assigned to different nodes. Each domain has its own material properties such as thermal conductivity k, emissivity ε, density ρ, and specific heat c_p. Combining for all domains, a material property results in an array that can be used for generalised equations instead of requiring a set of equations for each component. For the TES material domain, the temperature of a node at a time step determines if the heat is used for sensible or latent heat storage. The domain classifications of the nodes are shown in Figure 7.6.

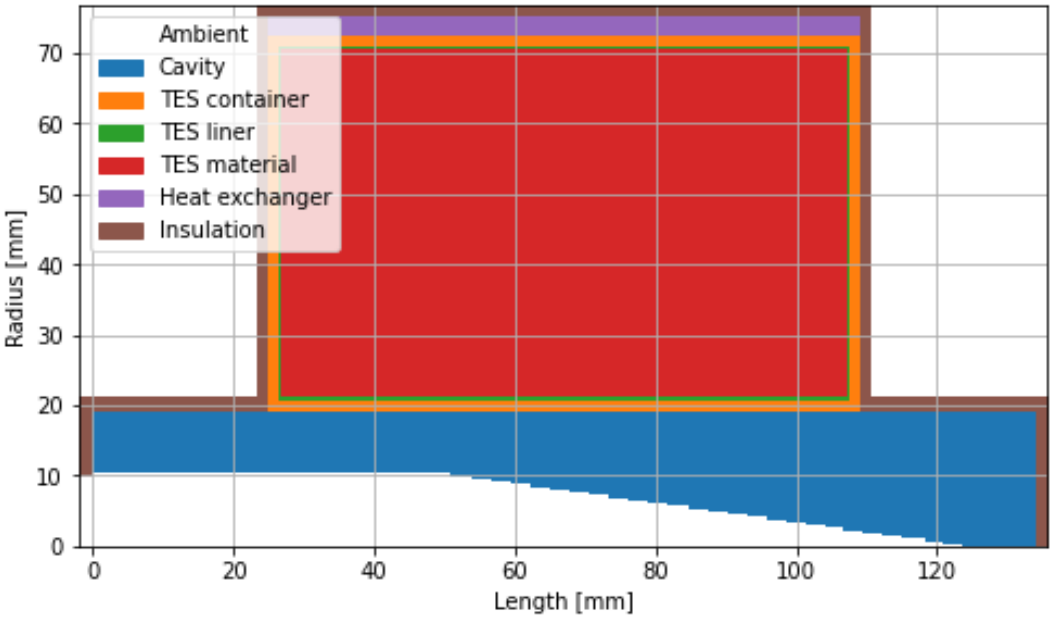

Figure 7.6: The domain classifications of the nodes

7.2.2. Boundary Conditions

These arrays are also used to apply boundary conditions. As convection is not modelled, the remaining boundary conditions are for the radiation. The percentage of the radiation received for each wall segment in section 5.2 is assigned to the nearest node to have a more accurate heat distribution than when applying the received radiation perfectly uniformly. The verification results of the radiation being applied to the correct nodes are shown in Figure 7.7.

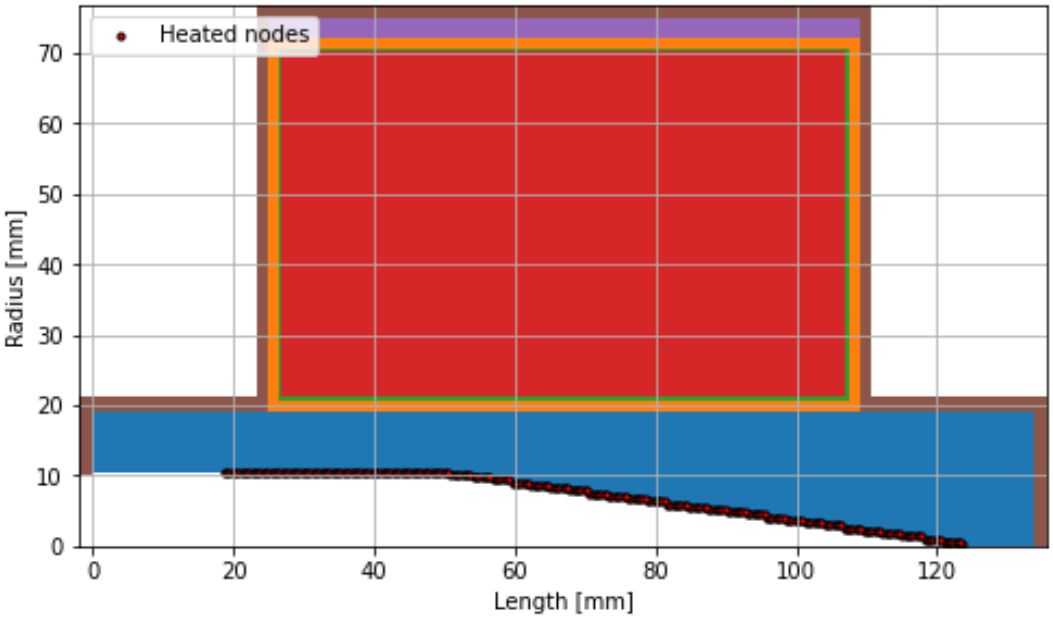

Figure 7.7: The domain verification results of the heated nodes

A node also emits radiation in the direction of a neighbouring node that is part of the environment. Because the system is stationary, it is possible to determine for each node beforehand in which direction the environmental nodes are. This prevents checking for each node at each time step, which domain the neighbouring nodes are part of. To simplify the simulation, the path of the emitted radiation is not modelled. However, for the cavity, a significant part of the emitted radiation is absorbed again. To incorporate this effect, the estimated emitted radiation by Equation 5.75 is used for this region. The combination of arrays then results in whether a node radiates due to neighbouring environmental nodes, and what the net radiation is.

7.2.3. Solver

Due to the rotational symmetry, the heat conduction equation Equation 6.13 simplifies to:

$$\rho c_p \frac{\partial T}{\partial t} + \rho\, L\, \frac{d\alpha}{dt} = \frac{1}{r}\frac{\partial}{\partial r}\left(kr\frac{\partial T}{\partial r}\right) + \frac{\partial}{\partial z}\left(k\frac{\partial T}{\partial z}\right) \tag{7.1}$$

Because the conductivity k varies between domains, a single value is needed for the shared face. If each node uses its own conductivity, the transferred flux between the nodes would be direction-dependent. The harmonic mean is therefore used:

$$k_{i+\frac{1}{2},j} = \frac{2\,k_{i,j}\,k_{i+1,j}}{k_{i,j}+k_{i+1,j}}, \quad k_{i,j+\frac{1}{2}} = \frac{2\,k_{i,j}\,k_{i,j+1}}{k_{i,j}+k_{i,j+1}} \tag{7.2}$$

To approximate the derivatives, the central difference method is used. The radial flux at the faces of the node becomes:

$$\frac{1}{r}\frac{\partial}{\partial r}\left(kr\frac{\partial T}{\partial r}\right) \approx \frac{1}{r_i \Delta r}\left[\left(kr\frac{\partial T}{\partial r}\right)_{i+\frac{1}{2},j} - \left(kr\frac{\partial T}{\partial r}\right)_{i-\frac{1}{2},j}\right] \tag{7.3}$$

The heat flux at each radial face is approximated as:

$$\left(kr\frac{\partial T}{\partial r}\right)_{i+\frac{1}{2},j} \approx k_{i+\frac{1}{2},j}\, r_{i+\frac{1}{2}} \frac{T_{i+1,j} - T_{i,j}}{\Delta r}, \quad \left(kr\frac{\partial T}{\partial r}\right)_{i-\frac{1}{2},j} \approx k_{i-\frac{1}{2},j}\, r_{i-\frac{1}{2}} \frac{T_{i,j} - T_{i-1,j}}{\Delta r} \tag{7.4}$$

For the axial direction, the heat flux difference is:

$$\frac{\partial}{\partial z}\left(k\frac{\partial T}{\partial z}\right) \approx \frac{1}{\Delta z}\left[\left(k\frac{\partial T}{\partial z}\right)_{i,j+\frac{1}{2}} - \left(k\frac{\partial T}{\partial z}\right)_{i,j-\frac{1}{2}}\right] \tag{7.5}$$

The heat flux at each axial face is approximated as:

$$\left(k\frac{\partial T}{\partial z}\right)_{i,j+\frac{1}{2}} \approx k_{i,j+\frac{1}{2}} \frac{T_{i,j+1} - T_{i,j}}{\Delta z}, \quad \left(k\frac{\partial T}{\partial z}\right)_{i,j-\frac{1}{2}} \approx k_{i,j-\frac{1}{2}} \frac{T_{i,j} - T_{i,j-1}}{\Delta z} \tag{7.6}$$

The heat equation at point (i, j) thus becomes:

$$\begin{aligned} \rho c_p \frac{dT_{i,j}}{dt} + \rho\, L\, \frac{d\alpha}{dt} \approx \frac{1}{r_i \Delta r^2}\left[k_{i+\frac{1}{2},j} r_{i+\frac{1}{2}} (T_{i+1,j} - T_{i,j}) - k_{i-\frac{1}{2},j} r_{i-\frac{1}{2}} (T_{i,j} - T_{i-1,j})\right] \\ + \frac{1}{\Delta z^2}\left[k_{i,j+\frac{1}{2}} (T_{i,j+1} - T_{i,j}) - k_{i,j-\frac{1}{2}} (T_{i,j} - T_{i,j-1})\right] \end{aligned} \tag{7.7}$$

This equation is then solved for each node to determine the temperature of each node for the next time step. This process is repeated until for each node the absolute change in temperature between a time step falls below a threshold or a specific condition is reached. The complete script for the radiation and conductivity simulation is shown in Listing B.

7.2.4. Results

The Python script can be run for the preliminary design to verify if the estimations and assumptions were correct. The converged result for the preliminary design is shown in Figure 7.8. The system without the insulation layer is also visualised to better show the temperature difference within the other components.

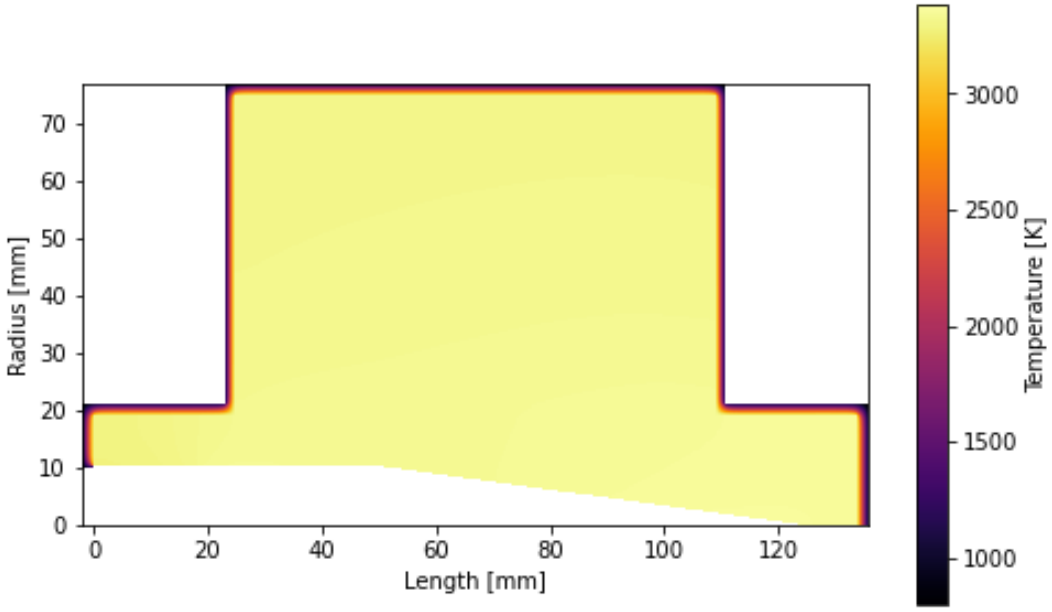

(a) With insulation

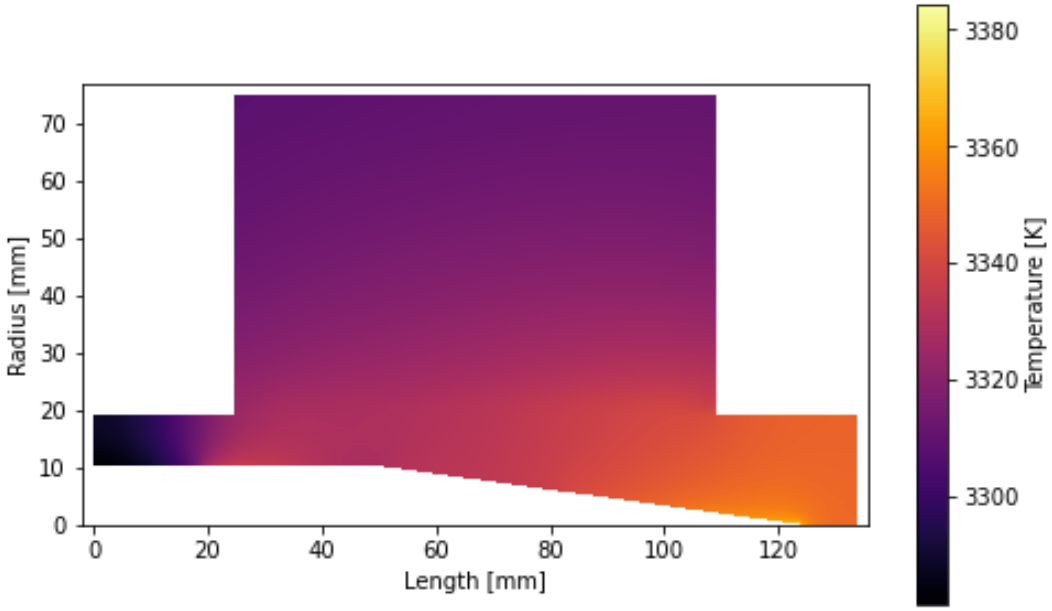

(b) Without insulation

Figure 7.8: The result thermal distribution for the preliminary design

The maximum temperature in the cavity is $T_{cav} = 3384\,\mathrm{K}$ and the maximum temperature in the heat exchanger is $T_{wall} = 3311\,\mathrm{K}$. There is thus good conduction between the cavity and the heat exchanger, as the temperature difference is only $2.205\,\%$. This resulted in a lower cavity temperature and a higher heat exchanger temperature. The required input power was thus overestimated because the thermal losses of the cavity are lower. Less power is also needed for the heat exchanger to reach the desired temperature as more thermal power flows from the cavity to the heat exchanger.

8

Iterating

This chapter describes the iteration process that incorporates the findings from chapter 5 and chapter 6. It will be discussed how the design process is adjusted to improve the accuracy, and how the findings change the design choices. The iterations will be performed for the lowered wall temperature $T_{wall} = 2349\,\mathrm{K}$.

8.1. Heat Exchanger

To determine the required diameter to keep the flow turbulent, the Reynolds number is calculated at the chamber temperature T_c and chamber pressure p_c found with the convection simulation as described in section 7.1. For this diameter, the required length is then estimated with the segment-based solver as described in section 5.1. section 7.1 showed that for this length a higher chamber temperature T_c is reached than estimated. The simulated temperature will be used for propellant-related calculations. The yield strength $\sigma_{y0.2}$ of the channel wall will be based on the maximum simulated temperature in the heat exchanger.

Due to the lowered temperature, the estimated wall temperature is $T_{wall} = 2349\,\mathrm{K}$, and the goal of the chamber temperature at the end of the spiral runner for the segment-based solver is set to $T_c = 2239\,\mathrm{K}$. For the first iteration, this temperature is used to determine the diameter, as this design has not yet been simulated.

8.2. Cavity

The optimisation of the cavity shape was done for a set cavity area ratio with respect to the aperture area $\frac{A_{cav}}{A_{ap}}$. This ratio was chosen such that the estimated absorptivity of the cavity was $99.5\,\%$. The results showed, however, that the optimised shape had a larger absorptivity than estimated. To find the minimum area for which no rays leave the cavity, the same ray tracing method is used. Before optimising for the uniformity of received radiation, the cavity will be optimised for the minimum area while maintaining the maximum possible absorptivity. Then, for the found minimum area, the cavity will be optimised for uniformity while maintaining the maximum absorptivity. This is done because a reduction in the size of the cavity also decreases the size of the surrounding components. If, during the area reduction process, rays leave the cavity for a converged shape, the area ratio needs to be increased. However, if during the optimisation process a shape is found for which no rays leave the cavity, the area ratio can be further reduced. Due to this step-like behaviour, the bisection method will be used to find the smallest area ratio.

The thickness of the cavity material was based on a maximum allowable stress of $6.9\,\mathrm{MPa}$ at the estimated cavity temperature $T_{cav} = 3410\,\mathrm{K}$. This estimation was based on the assumptions that the cavity temperature T_{cav} is $10\,\%$ higher than the wall temperature T_{wall}. subsection 7.2.4 however shows that for the preliminary design, the cavity temperature T_{cav} is only $2.205\,\%$ higher than the wall temperature T_{wall}. For the new lower wall temperature $T_{wall} = 2349\,\mathrm{K}$, this results in a cavity temperature

$T_{cav} = 2401\,\mathrm{K}$. To account for the reduced strength at lower temperatures, a maximum allowable stress of $21\,\mathrm{MPa}$ is chosen based on Figure 5.22 to prevent cracks.

8.3. Thermal Energy Storage

For the required TES material mass, the preliminary estimation did not include the thermal power losses $\dot{Q}_{loss}$. Based on the same method in section 5.5 but for the temperature $T_{wall} = 2349\,\mathrm{K}$, an estimation of the losses $\dot{Q}_{loss} = 815.0\,\mathrm{W}$ is found. With these estimated losses, the TES material mass can be determined for the first iteration. For the following iterations, the simulated losses will be used at the input power P_{in} where the minimum temperature of the TES material is $2349\,\mathrm{K}$ and the maximum insulation temperature is $1202\,\mathrm{K}$. The boron is then fully melted, and the low-emissivity coating has the maximum allowable temperature.

During an eclipse, the TES material stays at a temperature of $T_{wall} = 2349\,\mathrm{K}$, and no solar irradiation is received. The real losses will thus be lower during an eclipse, because the cavity will have a lower temperature. The real losses will also be lower because the estimated losses are based on the hottest simulated temperature in a component, and the colder regions of a component will thus radiate less.

TES-01 assumes the worst case scenario where at least one thruster is burning the whole eclipse, thus in this scenario the burn time during eclipse $t_{b,ec} = 900.0\,\mathrm{s}$ is equal to half the eclipse time $t_{ec} = 1800\,\mathrm{s}$. To solve Equation 5.50 and determine the required TES material mass, the required power to heat the propellant $\dot{Q}_{p,req}$ is taken from the heat exchanger calculation. For the lowered chamber temperature of $T_c = 2239\,\mathrm{K}$ and the mass flow $\dot{m} = 2.039 \times 10^{-4}\,\mathrm{kg\,s^{-1}}$, the required power is $\dot{Q}_{p,req} = 6275\,\mathrm{W}$

The sizing of the TES container will now be done to minimise the system's uninsulated outer surface area instead of the surface area of the TES container. The cavity area is not influenced by the dimensions of the TES container and will thus be excluded. However, the effect of the surface area of the material for the heat exchanger will now be included. Also, the effect of the thickness of the TES container on the available volume will be taken into account. Based on the cavity being either shorter or longer than the TES system, two sets of equations can be made. One set of equations is for the case where the cavity is shorter than the TES system, and one set of equations is for the case where the cavity is longer than the TES system. Because during the iteration process, both the cavity dimensions and the required TES material can change, the correct set of equations will be selected for each iteration.

If the cavity length L_{cav} is shorter than L_{TES}, the volume removed in the TES container by the cavity material is a cylinder with length L_{cav} and radius R_{cav}. The surface area to be minimised is the outer cylindrical face, one circular face, and one circular face with a hole. The volume of the TES material is thus the total volume minus the container material and the cavity volume:

$$V_{TES,mat} = \underbrace{\pi \left(R_{TES} - t_{TES}\right)^2 \left(L_{TES} - 2t_{TES}\right)}_{\text{outer cylinder volume}} - \underbrace{\pi \left(R_{cav} + t_{TES}\right)^2 L_{cav}}_{\text{inner cavity volume}} \tag{8.1}$$

The outer surface area of the container with the heat exchanger around it is to be minimised to minimise radiation losses:

$$A_{sur} = \underbrace{2\,\pi \left(R_{TES} + D + t_{wall}\right) L_{TES}}_{\text{cylindrical face}} + \underbrace{\pi \left(R_{TES} + D + t_{wall}\right)^2}_{\text{circular face}} + \underbrace{\pi \left(\left(R_{TES} + D + t_{wall}\right)^2 - R_{cav}^2\right)}_{\text{annular circular face}} \tag{8.2}$$

Equation 8.1 can be rewritten to substitute for L_{TES} in Equation 8.2:

$$L_{TES} = \frac{V_{TES,mat} + \pi (R_{cav} + t_{TES})^2 L_{cav}}{\pi (R_{TES} - t_{TES})^2} + 2t_{TES} \tag{8.3}$$

$$A_{sur} = 2\pi(R_{TES} + D + t_{wall}) \left(\frac{V_{TES,mat} + \pi(R_{cav} + t_{TES})^2 L_{cav}}{\pi(R_{TES} - t_{TES})^2} + 2t_{TES} \right) + 2\pi(R_{TES} + D + t_{wall})^2 - \pi R_{cav}^2 \tag{8.4}$$

The only unknown in this equation is the TES container radius R_{TES}. Equation 8.4 can be differentiated to find the minimum:

$$\begin{aligned} \frac{dA_{sur}}{dR_{TES}} &= \frac{d}{dR_{TES}} \left(2\pi(R_{TES} + D + t_{wall}) \left(\frac{V_{TES,mat} + \pi(R_{cav} + t_{TES})^2 L_{cav}}{\pi(R_{TES} - t_{TES})^2} + 2t_{TES} \right) \right) \\ &\quad + \frac{d}{dR_{TES}} \left(2\pi(R_{TES} + D + t_{wall})^2 - \pi R_{cav}^2 \right) \\ &= 2\pi \left(\frac{V_{TES,mat} + \pi(R_{cav} + t_{TES})^2 L_{cav}}{\pi(R_{TES} - t_{TES})^2} + 2t_{TES} \right) \\ &\quad - \frac{4(R_{TES} + D + t_{wall}) \left(V_{TES,mat} + \pi(R_{cav} + t_{TES})^2 L_{cav} \right)}{(R_{TES} - t_{TES})^3} \\ &\quad + 4\pi(R_{TES} + D + t_{wall}) = 0 \end{aligned} \tag{8.5}$$

Setting the derivative equal to $\frac{dA}{dR_{TES}} = 0$ results in an equation that needs to be solved numerically to determine the TES container radius R_{TES}:

$$\frac{dA_{sur}}{dR_{TES}} = 0 \quad \Longrightarrow$$

$$\begin{aligned} &2\pi \left(\frac{V_{TES,mat} + \pi(R_{cav} + t_{TES})^2 L_{cav}}{\pi(R_{TES} - t_{TES})^2} + 2t_{TES} \right) \\ &- \frac{4 \left(R_{TES} + D + t_{wall} \right) \left(V_{TES,mat} + \pi(R_{cav} + t_{TES})^2 L_{cav} \right)}{(R_{TES} - t_{TES})^3} \\ &+ 4\pi(R_{TES} + D + t_{wall}) = 0 \end{aligned} \tag{8.6}$$

Substituting the result in Equation 8.3 results in the TES container length L_{TES}.

When L_{cav} is longer than L_{TES}, the volume removed in the centre of the cylinder has the TES container length L_{TES} instead of the cavity length L_{cav}. The surface area to be minimised changes as well. It now also includes the cylindrical face of the cavity material that extends beyond the TES container, with radius R_{cav} and length $L_{cav} - L_{TES}$. The volume of the TES material is thus the total volume minus the container material and the cavity volume:

$$V_{TES,mat} = \underbrace{\pi(R_{TES} - t_{TES})^2 \left(L_{TES} - 2t_{TES} \right)}_{\text{outer material volume of TES container}} - \underbrace{\pi(R_{cav} + t_{TES})^2 \, L_{TES}}_{\text{cavity volume inside TES}} \tag{8.7}$$

The outer surface area that is to be minimised is defined as:

$$A_{sur} = \underbrace{2\pi(R_{TES} + D + t_{wall}) \, L_{TES}}_{\text{cylindrical side of TES + heat exchanger}} + \underbrace{2\pi \left((R_{TES} + D + t_{wall})^2 - R_{cav}^2 \right)}_{\text{top and bottom circular faces}} + \underbrace{2\pi R_{cav} \left(L_{cav} - L_{TES} \right)}_{\text{inner cavity side}} \tag{8.8}$$

Equation 8.7 can be rewritten to substitute for L_{TES} in Equation 8.8:

$$L_{TES} = \frac{V_{TES,mat} + 2\pi(R_{TES} - t_{TES})^2 t_{TES}}{\pi\left((R_{TES} - t_{TES})^2 - (R_{cav} + t_{TES})^2\right)} \tag{8.9}$$

$$\begin{aligned} A_{sur} = {} & 2\pi(R_{TES} + D + t_{wall}) \left(\frac{V_{TES,mat} + 2\pi(R_{TES} - t_{TES})^2 t_{TES}}{\pi\left((R_{TES} - t_{TES})^2 - (R_{cav} + t_{TES})^2\right)} \right) \\ & + 2\pi \left((R_{TES} + D + t_{wall})^2 - R_{cav}^2 \right) \\ & + 2\pi R_{cav} L_{cav} - 2\pi R_{cav} \left(\frac{V_{TES,mat} + 2\pi(R_{TES} - t_{TES})^2 t_{TES}}{\pi\left((R_{TES} - t_{TES})^2 - (R_{cav} + t_{TES})^2\right)} \right) \end{aligned} \tag{8.10}$$

The only unknown in this equation is the TES container radius R_{TES}. Differentiating Equation 8.10 with respect to R_{TES} results in:

$$\begin{aligned} \frac{dA_{sur}}{dR_{TES}} = {} & \frac{d}{dR_{TES}} \left(2\pi(R_{TES} + D + t_{wall}) \frac{V_{TES,mat} + 2\pi(R_{TES} - t_{TES})^2 t_{TES}}{\pi\left((R_{TES} - t_{TES})^2 - (R_{cav} + t_{TES})^2\right)} \right) \\ & + \frac{d}{dR_{TES}} \left(2\pi \left((R_{TES} + D + t_{wall})^2 - R_{cav}^2 \right) \right) \\ & + \frac{d}{dR_{TES}} \left(2\pi R_{cav} L_{cav} \right) \\ & - \frac{d}{dR_{TES}} \left(2\pi R_{cav} \frac{V_{TES,mat} + 2\pi(R_{TES} - t_{TES})^2 t_{TES}}{\pi\left((R_{TES} - t_{TES})^2 - (R_{cav} + t_{TES})^2\right)} \right) \\ = {} & 2\, \frac{V_{TES,mat} + 2\pi(R_{TES} - t_{TES})^2 t_{TES}}{(R_{TES} - t_{TES})^2 - (R_{cav} + t_{TES})^2} \\ & - 4\left(R_{TES} + D + t_{wall} - R_{cav}\right) \frac{(R_{TES} - t_{TES}) \left(V_{TES,mat} + 2\pi t_{TES} (R_{cav} + t_{TES})^2 \right)}{\left((R_{TES} - t_{TES})^2 - (R_{cav} + t_{TES})^2\right)^2} \\ & + 4\pi(R_{TES} + D + t_{wall}) \end{aligned} \tag{8.11}$$

Setting the derivative equal to $\frac{dA}{dR_{TES}} = 0$ results in an equation that needs to be solved numerically to determine the TES container radius R_{TES}:

$$\begin{aligned} & \frac{dA_{sur}}{dR_{TES}} = 0 \quad \Longrightarrow \\ & 2\, \frac{V_{TES,mat} + 2\pi(R_{TES} - t_{TES})^2 t_{TES}}{(R_{TES} - t_{TES})^2 - (R_{cav} + t_{TES})^2} \\ & - 4\left(R_{TES} + D + t_{wall} - R_{cav}\right) \frac{(R_{TES} - t_{TES}) \left(V_{TES,mat} + 2\pi t_{TES} (R_{cav} + t_{TES})^2 \right)}{\left((R_{TES} - t_{TES})^2 - (R_{cav} + t_{TES})^2\right)^2} \\ & + 4\pi(R_{TES} + D + t_{wall}) = 0 \end{aligned} \tag{8.12}$$

Substituting the result in Equation 8.9 results in the TES container length L_{TES}.

8.4. Nozzle

The nozzle will be used during the iterations to adjust the mass flow $\dot{m}$ for the simulated chamber temperature T_c and chamber pressure p_c, such that the thrust becomes $F = 1\,\mathrm{N}$. To determine the thrust F, Equation 5.66 will be used.

This also requires the pressure ratio $\frac{p_e}{p_c}$, which is determined with Equation 5.67, and a set expansion ratio of $\frac{A_e}{A_t} = 100$. With the pressure ratio $\frac{p_e}{p_c}$ known, the exhaust velocity V_e can be determined with Equation 2.3.

The last missing variable to solve Equation 5.66 is the exit area A_e. This can be determined with the determined expansion ratio $\frac{A_e}{A_t} = 100$, and the throat area A_t from Equation 5.65. The mass flow is needed for this equation as well, thus the mass flow $\dot{m}$ influences both the momentum and pressure thrust. This set of equations will thus be solved during the iteration process to update the mass flow $\dot{m}$.

8.5. Insulation

For the insulation, the same properties of the insulation material as in section 5.5 will be used, but now including the effect of the insulation thickness and heat exchanger on the surface area. With the thin-walled assumptions not being valid, the one-dimensional thermal conductivity also becomes invalid. Due to the complex geometry, the insulation thickness will thus be adjusted based on the thermal conduction and radiation simulation such that the maximum temperature of the insulation outer surface becomes $1202\,\mathrm{K}$. If a higher temperature is simulated, the insulation thickness is increased, and if a lower temperature is simulated, the insulation thickness is decreased.

The following sets of equations will be used for the initial estimation of the required insulation thickness. Based on the cavity being shorter or longer than the TES system, two sets of equations can be made. One set of equations is for the case where the cavity is shorter than the TES system, and one set of equations is for the case where the cavity is longer than the TES system.

The heat exchanger will be included in the surface area of the TES system as it is part of its outer wall. If the cavity becomes shorter than the TES container, the insulated surface area of the cavity $A_{cav,ins}$ becomes:

$$A_{cav,ins} = \underbrace{\pi \left(R_{cav}^2 - R_{ap}^2\right)}_{\text{insulated area of the cavity opening}} \tag{8.13}$$

The insulated surface area of the TES container then becomes:

$$\begin{aligned} A_{TES,ins} = &\underbrace{\pi \left((R_{TES} + D + t_{wall} + t_{ins,TES})^2 - R_{cav}^2\right)}_{\text{annular circular face}} \\ &+ \underbrace{\pi \left(R_{TES} + D + t_{wall} + t_{ins,TES}\right)^2}_{\text{circular face}} \\ &+ \underbrace{2\pi \left(R_{TES} + D + t_{wall} + t_{ins,TES}\right)\left(L_{TES} + 2\,t_{ins,TES}\right)}_{\text{cylindrical face}} \end{aligned} \tag{8.14}$$

If the cavity is longer than the TES container, the insulated surface area of the cavity $A_{cav,ins}$ becomes:

$$\begin{aligned} A_{cav,ins} = &\underbrace{\pi \left((R_{cav} + t_{ins,cav})^2 - R_{ap}^2\right)}_{\text{annular circular face}} \\ &+ \underbrace{\pi \left(R_{cav} + t_{ins,cav}\right)^2}_{\text{circular face}} \\ &+ \underbrace{2\pi \left(R_{cav} + t_{ins,cav}\right)\left(\left(L_{cav} + 2\,t_{ins,cav}\right) - \left(L_{TES} + 2\,t_{ins,TES}\right)\right)}_{\text{cylindrical face}} \end{aligned} \tag{8.15}$$

The insulated surface area of the TES container then becomes:

$$\begin{aligned} A_{TES,ins} = &\underbrace{2\pi \left((R_{TES} + D + t_{wall} + t_{ins,TES})^2 - (R_{cav} + t_{ins,cav})^2\right)}_{\text{annular circular face}} \\ &+ \underbrace{2\pi \left(R_{TES} + D + t_{wall} + t_{ins,TES}\right)\left(L_{TES} + 2\,t_{ins,TES}\right)}_{\text{cylindrical face}} \end{aligned} \tag{8.16}$$

8.6. Dependencies

For the design, multiple parameters are chosen, but many variables have to be determined. Based on the inputs and outputs used for the iteration process, the dependencies between the components and simulations can be determined. These dependencies are shown in Figure 8.1.

Heat Exchanger		Channel diameter Wall thickness	Channel diameter Wall thickness	Channel diameter Wall thickness	Channel diameter Wall thickness Channel length	
	Cavity	Cavity radius Cavity length	Cavity radius Cavity length	Cavity radius Cavity length Solar distribution	Cavity radius Cavity length	
		TES System	TES radius TES length	TES radius TES length	TES radius TES length	
			Insulation	Insulation thickness		
Wall temperature	Cavity temperature	Thermal losses	Insulation temperature	Conduction & Radiation Simulation		
					Convection Simulation	Chamber temperature Chamber pressure
Mass flow		Mass flow		Mass flow		Nozzle

Figure 8.1: N^2 Diagram of the system components

This diagram shows that for the first complete iteration, the mass flow $\dot{m}$ and the cavity temperature T_{cav} have to be estimated. Based on this, the sizing of the components except the nozzle can be done. For the first iteration, an iteration cycle between the TES system and insulation has to be performed to incorporate the estimated thermal losses $\dot{Q}_{loss}$ into the TES material mass. When the TES system and insulation results have converged, the system without the nozzle can be simulated. Based on the convection simulation results, the mass flow for the nozzle can be determined that results in the desired thrust. Based on the temperatures of the components determined with the radiation and conduction simulation, the components can be adjusted during the next iteration. During the conduction and radiation simulation, the input power is adjusted until the minimum temperature of the TES material is its melting temperature. For the next iteration, the new mass flow can be used to update the sizing of the components as well.

The calculations for the components and simulations are performed in the same order as the rows in Figure 8.1. However, the TES System and insulation are updated after running the conduction and radiation simulation until the temperatures converge before continuing with the convection simulation. The insulation thickness is updated until the maximum temperature of the outer surface of the insulation is $T_{ins} = 1202\,\mathrm{K}$. The TES material mass and input power are updated until the minimum temperature of the TES material is $T_{TES} = 2349\,\mathrm{K}$. The flow of the order in which everything is updated is shown in Figure 8.2.

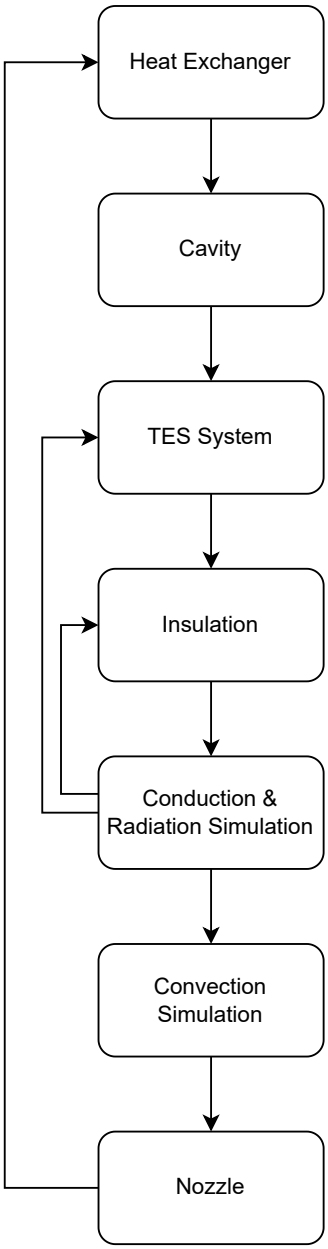

Figure 8.2: The flow of the order in which the components and simulations are updated

8.7. Results

This section will discuss the outcome of the iteration process and findings during the process. Because the change in component sizes resulted in a different layout, a new coloured sketch is shown in Figure 8.3 to distinguish the components more clearly.

- Blue Cavity
- Orange TES container
- Green TES liner
- Red TES material

- Purple Heat exchanger (including piping)
- Brown Insulation
- Pink Nozzle

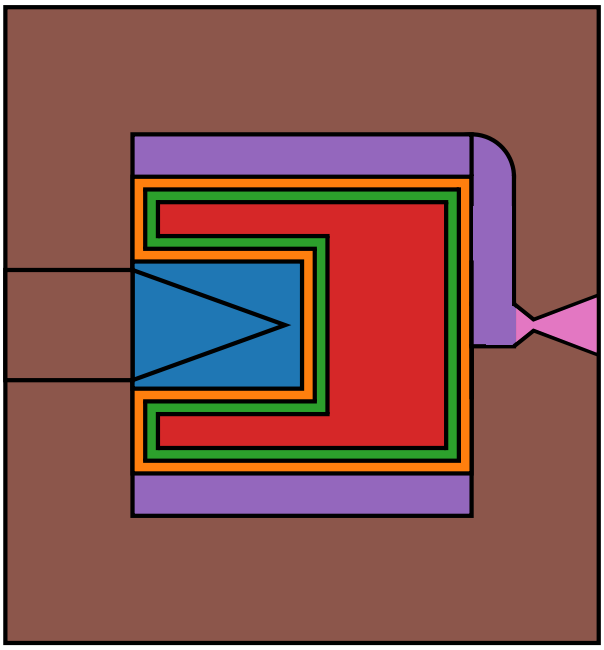

Figure 8.3: A coloured sketch of the iterated design to distinguish between the components

8.7.1. Parameters

The cavity shape with the minimum area but the maximum absorptivity found is a cavity that consists only of the second cone. The first cone and the cylindrical part are thus not needed for the optimised solution with the minimum area. The dimensions of the cavity are shown in Table 8.1.

Table 8.1: Cavity parameters

Parameter	Value
Cavity length, L_{cav}	$34.14\,\mathrm{mm}$
Cavity radius, R_{cav}	$12.86\,\mathrm{mm}$
Cavity wall thickness, t_{cav}	$2.857\,\mathrm{mm}$
Aperture radius, R_{ap}	$10.0\,\mathrm{mm}$
Right cone half-angle, θ_2	17.73°

The resulting ray tracing for this cavity shape is shown in Figure 8.4.

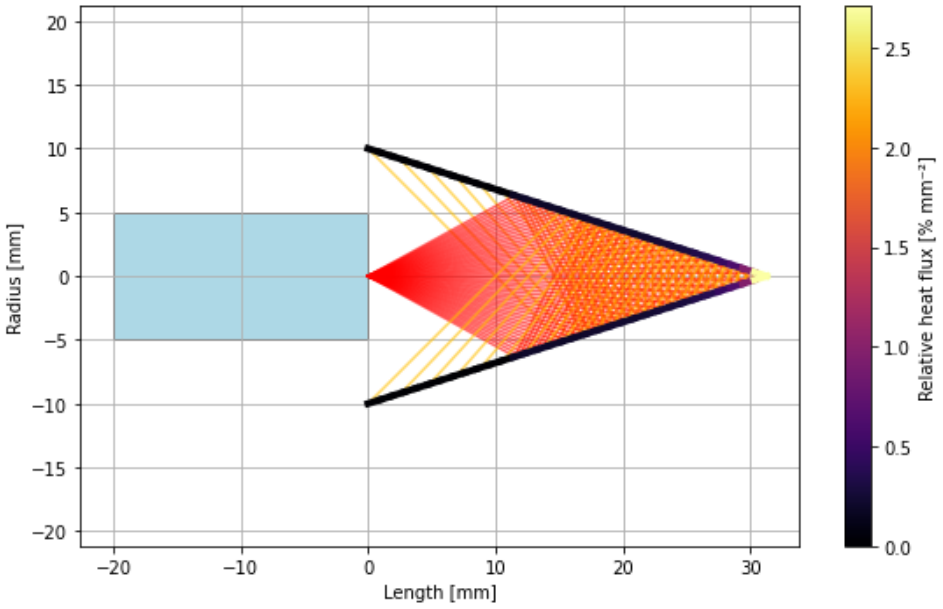

Figure 8.4: The ray tracing for the optimised cavity shape

Around the cavity, the TES system is placed with the dimensions shown in Table 8.2.

Table 8.2: Thermal Energy Storage system parameters

Parameter	Value
TES system radius, R_{TES}	$52.95\,\mathrm{mm}$
TES system length, L_{TES}	$103.8\,\mathrm{mm}$
TES system thickness, t_{TES}	$0.60\,\mathrm{mm}$
TES material mass, m_{TES}	$1.618\,\mathrm{kg}$
TES material volume, V_{TES}	$8.641 \times 10^{5}\,\mathrm{mm}^3$

Around the TES system, the spiral channel is placed, but with a longer length than estimated. Due to an insignificant pressure drop, a spiral with one revolution around the container is chosen to have a better thermal distribution. If the spiral runner was only spiralling around half the container, this side would cool down more than the other side and induce additional thermal stress. The lowered wall temperature $T_{wall} = 2349\,\mathrm{K}$ lowered the local compression, resulting in a maximum pressure of $5.007\,\mathrm{MPa}$, and the chamber temperature $T_c = 2349\,\mathrm{K}$ was equal to the wall temperature again Based on the maximum temperature of the heat exchanger walls, a minimum required wall thickness of $5.834 \times 10^{-2}\,\mathrm{mm}$ was found. For improved reliability, a wall thickness of $1.000 \times 10^{-1}\,\mathrm{mm}$ is used. The dimensions of the heat exchanger channel are shown in Table 8.3.

Table 8.3: Heat exchanger parameters

Parameter	Value
Wall thickness, t_{wall}	$1.000 \times 10^{-1}\,\mathrm{mm}$
Channel, D	$1.017\,\mathrm{mm}$
Channel cross-sectional area, A_c	$8.122 \times 10^{-1}\,\mathrm{mm}^2$
Channel length, L_{total}	$352.6\,\mathrm{mm}$
Chamber temperature, T_c	$2349\,\mathrm{K}$
Chamber pressure, p_c	$4.996\,\mathrm{K}$

Due to the larger expansion ratio, the mass flow could be halved, resulting in less power needed to

heat the propellant and decreasing the overall system size and mass. The nozzle dimensions and performance parameters are shown in Table 8.4.

Table 8.4: Nozzle geometry and performance parameters

Parameter	Value
Throat area, A_t	$1.093 \times 10^{-1}\,\mathrm{mm}^2$
Exit area, A_e	$10.93\,\mathrm{mm}^2$
Throat diameter, D_t	$3.730 \times 10^{-1}\,\mathrm{mm}$
Exit diameter, D_e	$3.730\,\mathrm{mm}$
Nozzle length, L	$6.264\,\mathrm{mm}$
Convergence half-angle, θ	$30°$
Divergence half-angle, θ	$15°$
Exit velocity, V_e	$8340\,\mathrm{m\,s}^{-1}$
Exit pressure, P_e	$2.002 \times 10^{-3}\,\mathrm{MPa}$

Because the TES container became longer than the cavity length, only a small part of the cavity has to be insulated. The required input power $\dot{Q}_{in}$ is lower when the cavity insulation thickness is the same as the TES system. Because only a small part of the cavity needs to be insulated, a thin part of the insulation would stick out. The thin part sticking out negatively contributed to the surface area, increasing the thermal losses. The insulation thickness of the TES system was large enough to also handle the thermal energy of the cavity. The found insulation thickness was lower than the estimated thickness, because the one-dimensional estimation overestimates the required thickness for the cylindrical faces. Because the circular faces do not have an infinite radius, their insulation thickness could also be reduced, as heat could also flow towards the insulation of the edges of the cylinder. The insulation parameters are shown in Table 8.5.

Table 8.5: Insulation and material properties

Parameter	Value
Cavity insulation thickness, $t_{ins,cav}$	$70.0\,\mathrm{mm}$
TES insulation thickness, $t_{ins,TES}$	$70.0\,\mathrm{mm}$
Porosity, ϕ	0.99

The general propulsion performance parameters of the complete system are shown in Table 8.6.

Table 8.6: Propulsion performance parameters

Parameter	Value
Solar irradiation, $\dot{Q}_{in}$	$1292\,\mathrm{W}$
Mass flow rate, $\dot{m}$	$1.173 \times 10^{-4}\,\mathrm{kg\,s}^{-1}$
Thrust, F	$1.000\,\mathrm{N}$
Specific impulse, I_{sp}	$869.5\,\mathrm{s}$

8.7.2. Simulations

The simulation of the converged results of the iteration process is shown in this subsection.

The results of the convection simulation of the iterated design are shown in Figure 8.5. This figure shows the temperature and pressure within the system.

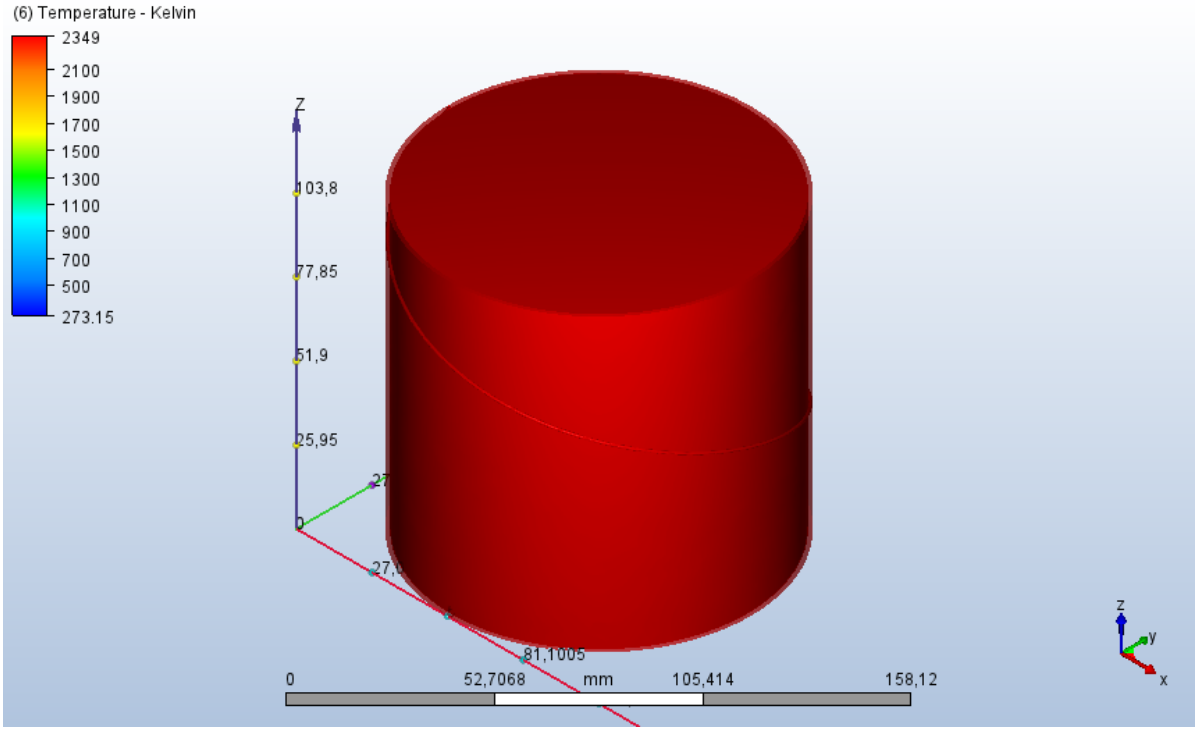

(a) The temperature results

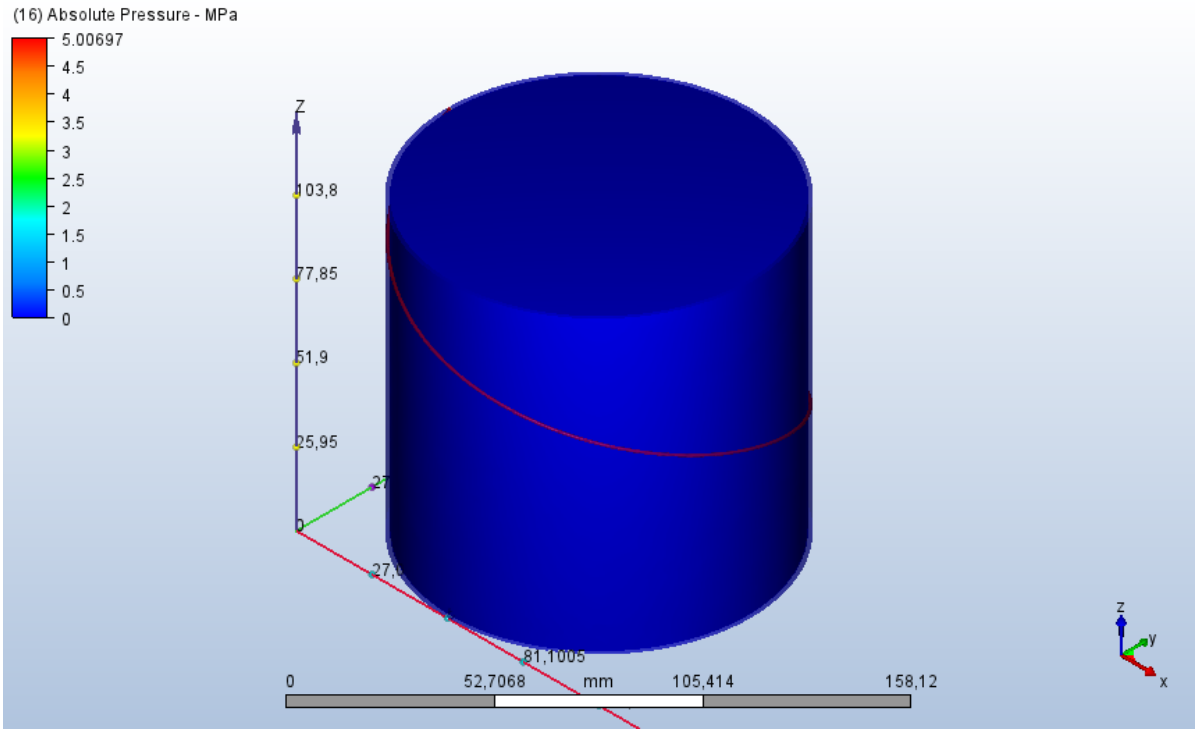

(b) The pressure results

Figure 8.5: The CFD results for the iterated design

The conduction and radiation simulation resulted in the thermal distribution shown in Figure 8.6.

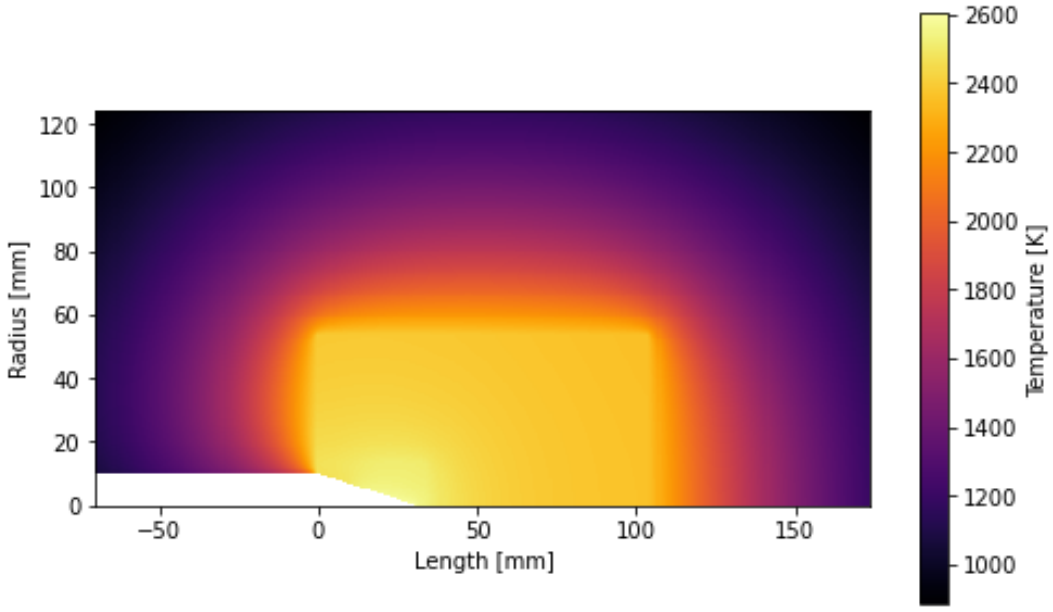

(a) The system with insulation

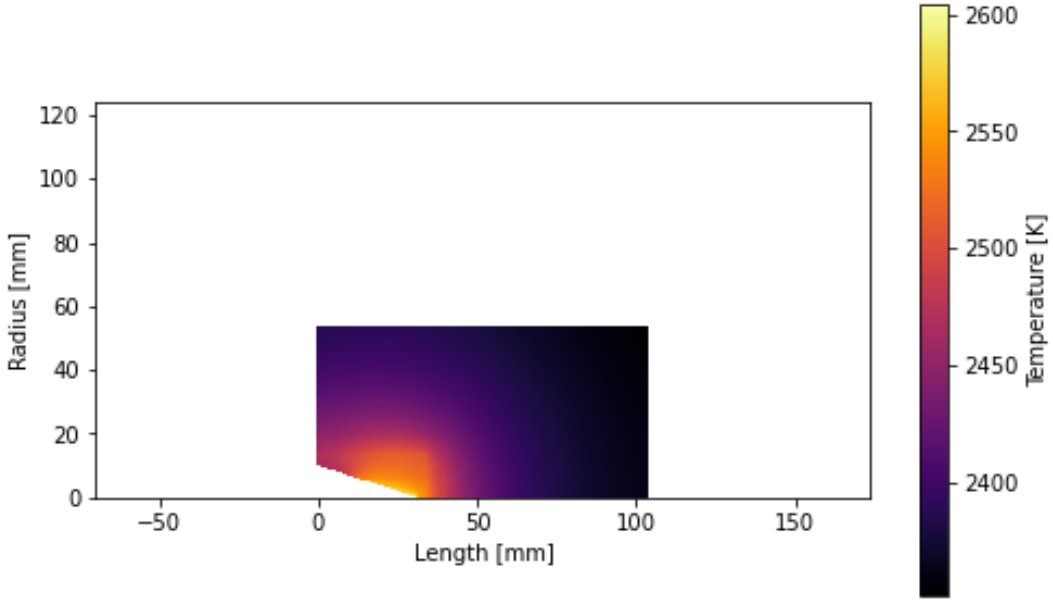

(b) The system without insulation

Figure 8.6: The resulting thermal distribution for the iterated design

A model of the iterated design, including a section view, is shown in Figure 8.7. The insulation is transparent in the model.

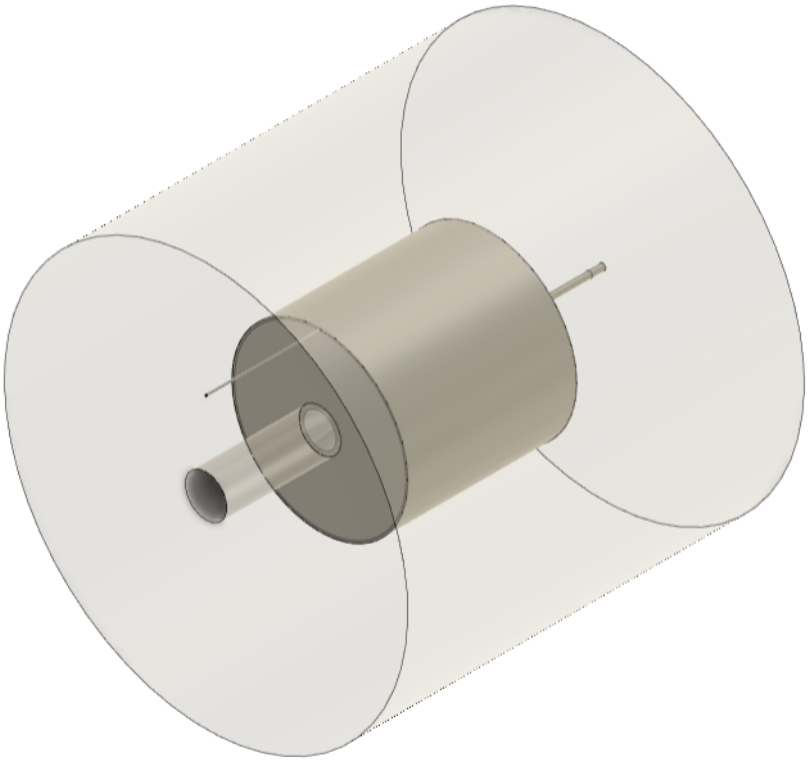

(a) An isometric view

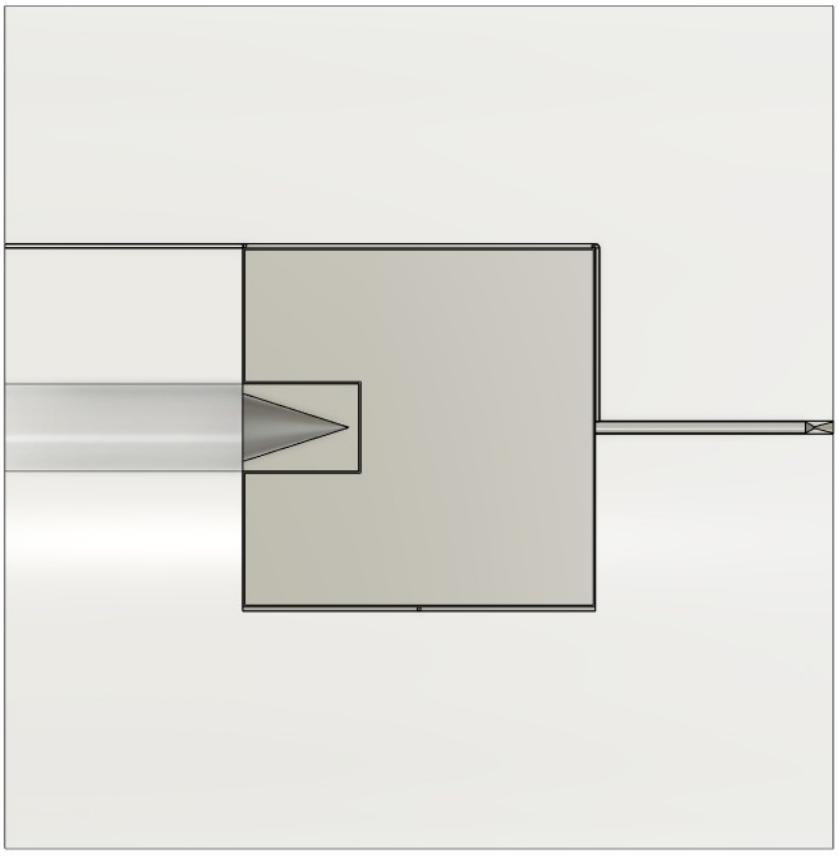

(b) A section view

Figure 8.7: A model of the iterated design

9

Optimisation

This chapter will discuss a further optimisation of the design and the resulting final design. First, the optimisation goals are discussed, followed by the results. To iterate and optimise the design to get to the final design, the following research questions are identified:

7. *What tools are the most suitable to analyse the design?*
   - 7.1 *What are the best ways to model the design?*
   - 7.2 *How can the models be used to optimise the design?*

9.1. Goals

During the iteration process, simulations were used to analyse the system at its stable state. For this, the conservative estimation was made that the thermal losses while receiving sunlight are equal to the thermal losses during an eclipse. Part of the system, however, cools down during an eclipse. This results in less radiation. The thermal losses can be determined when the TES material is solidifying by simulating the transient behaviour of the iterated design while it is not receiving solar irradiation. More accurate thermal losses can then be determined, allowing further reduction of the required TES material mass.

After the lower thermal losses during the eclipse are determined, the required input power can be increased again to heat the system and update the components according to the iteration process, but with the lower thermal losses. Because the size of the TES system decreased, the outer surface area of the system also decreased, reducing the thermal losses further. This causes a so-called snowball effect that reduces the TES material mass again. The optimisation goal will thus be to optimise the required TES material mass with the analysis of the transient state.

9.2. Optimized Results

The optimisation process based on the analysis of the transient behaviour of the system reduced the TES system mass, insulation thickness, and input power. An overview of the changed parameters is shown in Table 9.1. Based on the singular revolution of the spiral channel, the channel length was also reduced. Because the input power decreased, the required concentrator area did as well:

$$\begin{aligned} A_{conc} &= \frac{\dot{Q}_{in}}{\eta_{opt}\, G} \\ &= \frac{1267\,\mathrm{W}}{0.575 \times 1361\,\mathrm{W\,m^{-2}}} = 1.619\,\mathrm{m^2} \end{aligned}$$

Table 9.1: Updated parameters of the optimised design

Parameter	Value
TES system radius, R_{TES}	$51.97\,\mathrm{mm}$
TES system length, L_{TES}	$101.8\,\mathrm{mm}$
TES system thickness, t_{TES}	$0.60\,\mathrm{mm}$
TES material mass, m_{TES}	$1.539\,\mathrm{kg}$
TES material volume, V_{TES}	$8.219 \times 10^5\,\mathrm{mm}^3$
Channel length, L_{total}	$345.8\,\mathrm{mm}$
Solar irradiation, $\dot{Q}_{in}$	$1267\,\mathrm{W}$
Concentrator area, A_{conc}	$1.619\,\mathrm{m}^2$
Insulation thickness, t_{ins}	$69.0\,\mathrm{mm}$
Specific impulse, I_{sp}	$869.5\,\mathrm{s}$

The optimised design is thus a more accurate estimation of the required TES material mass and not the absolute minimum TES material mass. This analysis determined the higher thermal losses during an eclipse, but the system actually cools down further when part of the TES material has solidified. An even more accurate estimation can be made by incorporating the heat flow to the propellant in the simulation, and determining the overall thermal energy lost during the eclipse.

The coloured system model is shown in Figure 9.1.

- Blue Cavity
- Orange TES container
- Green TES liner
- Red TES material
- Purple Heat exchanger (including piping)
- Brown Insulation
- Pink Nozzle

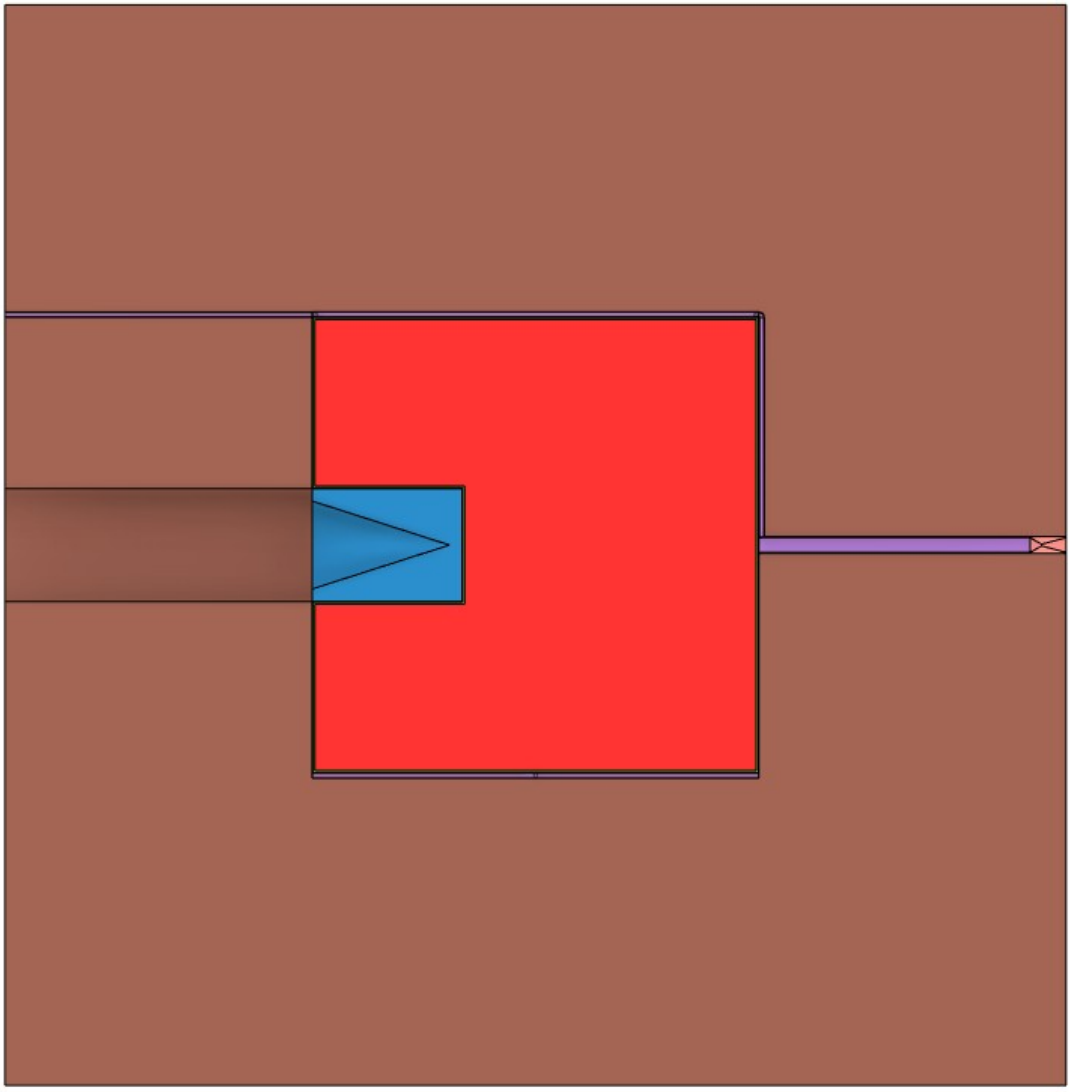

Figure 9.1: A coloured model of the system to distinguish between the components

9.2.1. Simulations

The main reduction in thermal losses is due to the cooling of the cavity. Because the size of the system changed, the convection has also been simulated to verify if changes to the chamber conditions occurred. Because the chamber temperature T_c and the chamber pressure p_c did not change, the mass flow did not have to be updated. The results of the simulated flow in the heat exchanger are shown in Figure 9.2.

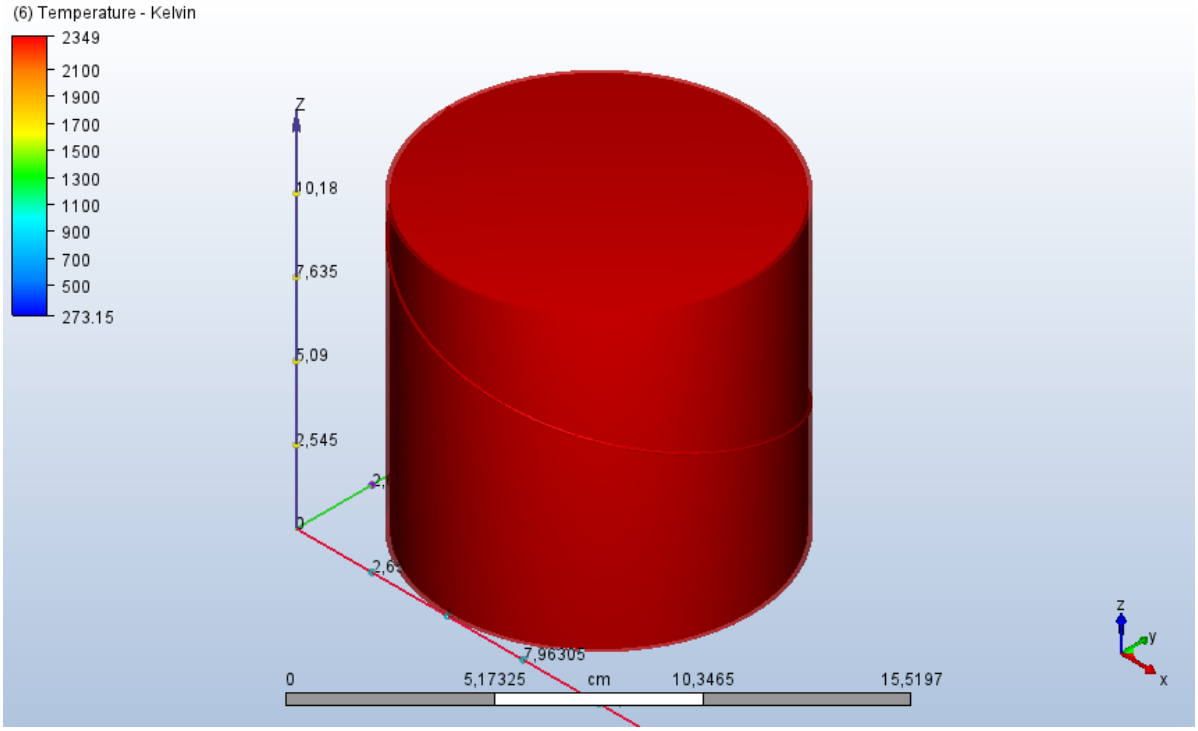

(a) The temperature results

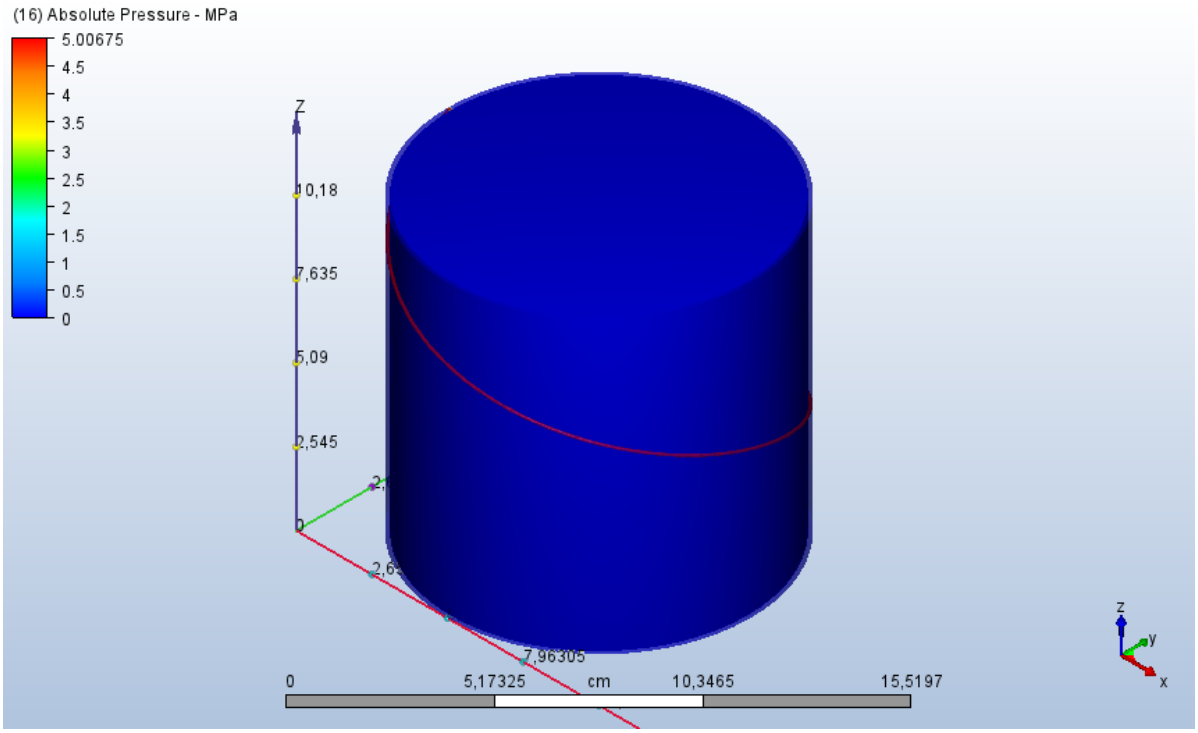

(b) The pressure results

Figure 9.2: The CFD results for the optimised design

The simulated thermal distribution of the system while receiving radiation is shown in Figure 9.3.

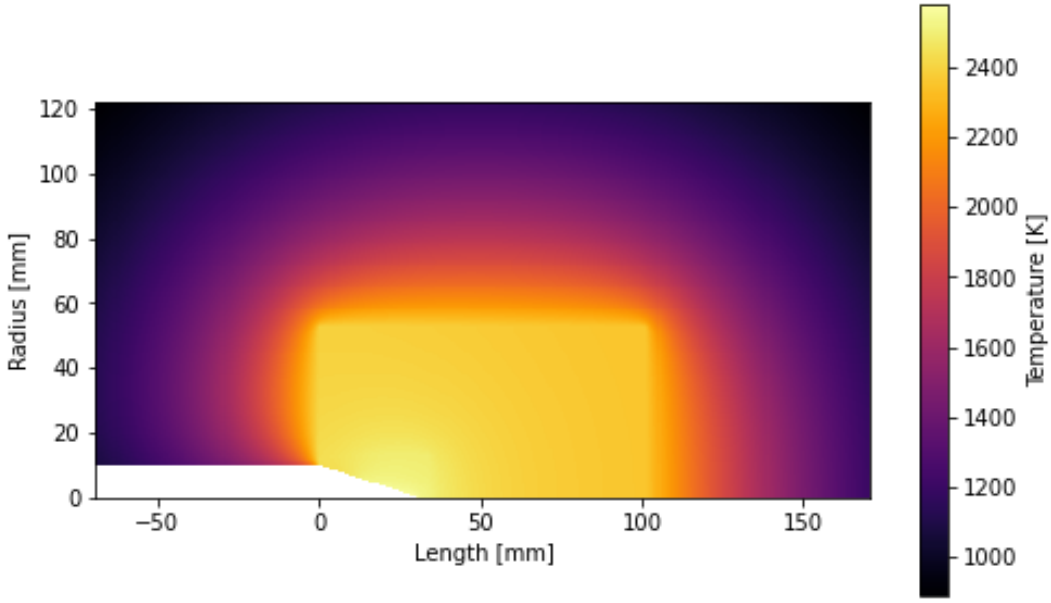

(a) The system with insulation

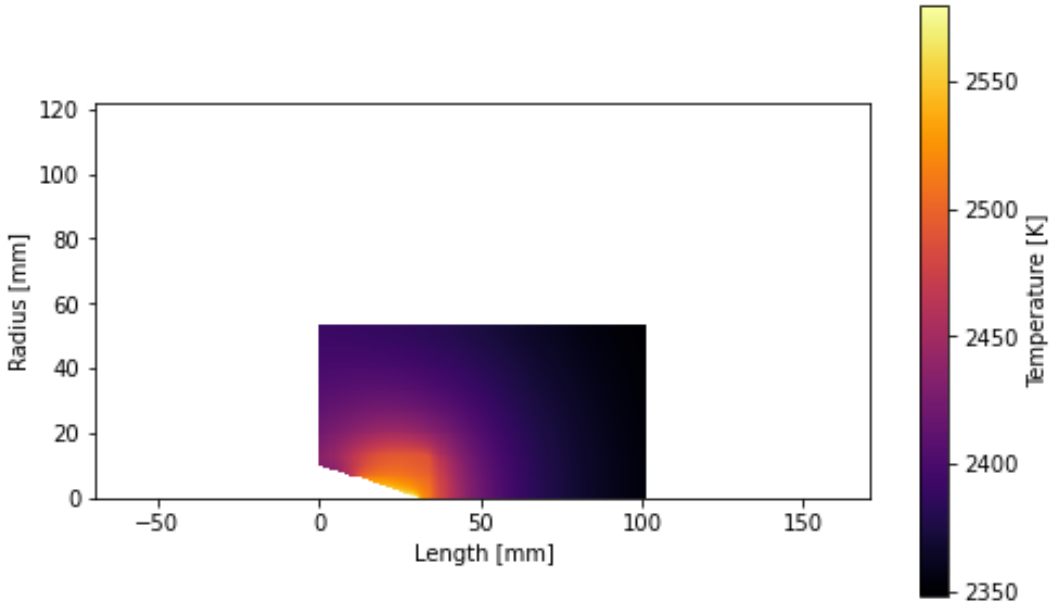

(b) The system without insulation

Figure 9.3: The resulting thermal distribution for the optimised design

9.2.2. Render

A render of the optimised design with the selected materials, including a section view, is shown in Figure 9.4. This figure shows a realistic appearance of the system.

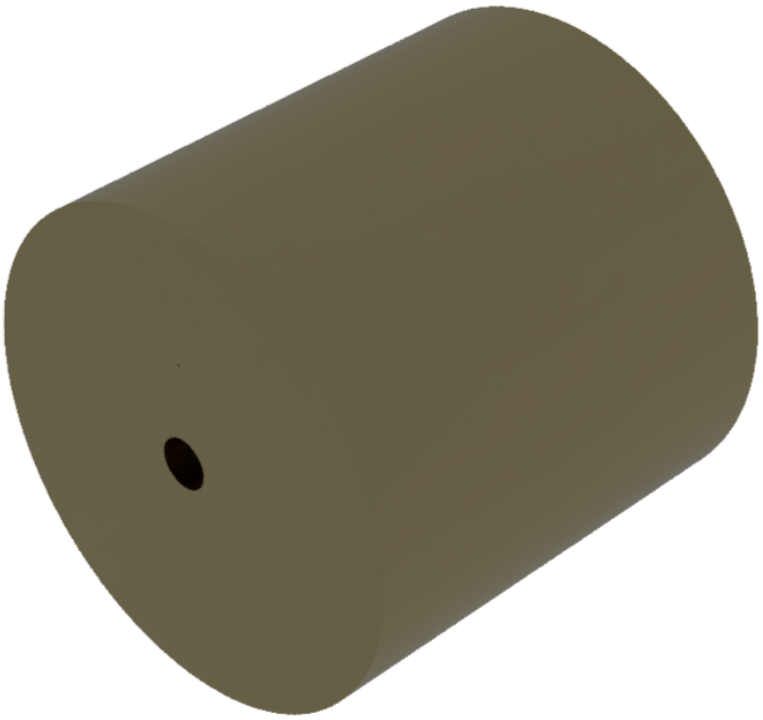

(a) An isometric view

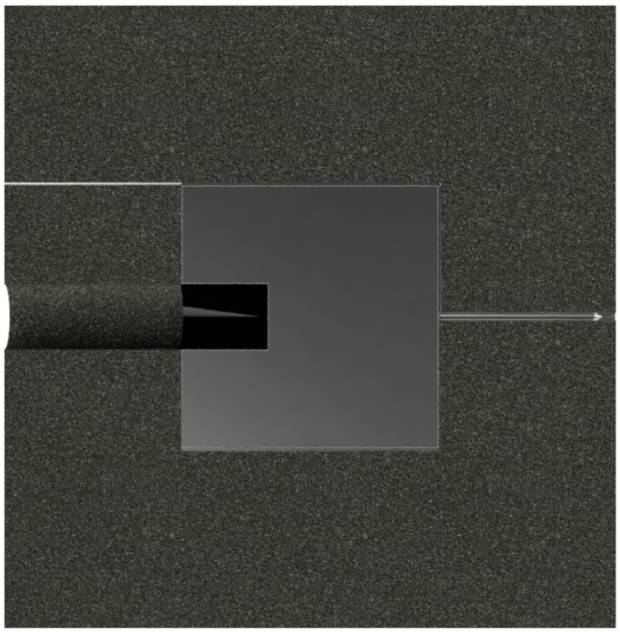

(b) A section view

Figure 9.4: A render of the optimised design

The thruster is large compared to the required cavity and the heat exchanger. Mostly, the insulation contributes to the size of the system, but the TES system contributes significantly as well. This is due to the high temperature of the system, which gives it a high specific impulse. The high specific impulse means that a low mass flow is required to reach the desired thrust. The high temperature of the system, however, also results in large thermal losses. To maintain the high temperature during an eclipse and to compensate for the large thermal losses, a lot of TES material is needed. A lower heat exchanger temperature would reduce the size of the system, at the cost of requiring more propellant.

If the required burn time for the complete mission duration is known, the propellant can be determined as well. It could be possible that reducing the heat exchanger temperature, reduces the thruster size more than it increases the volume or mass of the propellant due to the increased mass flow. In a later stage of the design process for the Green SWaP mission, this should be considered to optimise for either the overall system mass or volume. A different latent heat material should then be selected with a lower melting temperature that it close to the new heat exchanger temperature.

9.3. Experimental Validation

This chapter discussed the required experimental validation of the system. This experimental validation is based on the following research questions:

8. *What are the goals of the experimental testing?*
    - 8.1 *What are the goals of testing the materials?*
    - 8.2 *What are the goals of testing the performance?*

First, the testing of the selected materials is discussed. Then, the experimental validation of the performance of the system is discussed, including the considerations for the high temperature of the hydrogen. The chapter discusses the data to be collected, but not the detailed testing plan. The testing has to be done for different categories: the testing of the individual materials, the testing of the components, and the testing of the system.

9.4. High Temperature

To ensure that the system performs as required, the selected materials and the components need to be experimentally tested at elevated temperatures. In the simulations, material properties such as the thermal conductivity were assumed to be constant. However, they actually decrease with temperature. This means that the real thermal distribution within the system can differ from the simulated values. Components that become hotter than expected could fail, while lower temperatures influence the heat transfer negatively, reducing overall performance.

9.4.1. Materials

First, the thermal and mechanical properties of the individual materials have to be tested. For an accurate estimation of the thermal distribution within the system, the thermal conductivity and specific heat have to be determined at temperatures across the operational range. This ensures that while the system cools down or heats up, the thermal distribution does not differ catastrophically from what is estimated. The mechanical strength of the materials must be verified at the relevant temperatures. If the strength decreases more than assumed, the system could become structurally unstable, leading to failure of critical components.

First, the thermal and mechanical properties of the individual materials have to be tested. To improve the accuracy of the simulated thermal distribution within the system, the thermal conductivity and specific heat at different elevated temperatures need to be determined. It is important to know these properties over the range of operating temperatures to ensure no issues occur while the system cools down or heats up. The strength of the materials at elevated temperatures is also crucial to know. If the materials behave more weakly than expected, the whole system could fail.

The cavity is responsible for absorbing the concentrated solar irradiation. Both the overall absorption efficiency and the uniformity of the absorption need to be tested. Lower absorption than expected would reduce the thermal power going to the heat exchanger, requiring changes in cavity shape or size.

Non-uniform absorption could lead to local overheating and material degradation, even if the average temperature is acceptable.

When the TES material melts, its heat transfer behaviour changes. The phase change and the void for expansion of the material influence the effective thermal conductivity. It should be determined how these effects influence the thermal distribution during heating and cooling cycles, and whether complete melting is achieved. Furthermore, the reliability of the TES container should be validated. It must be verified that the protective boron nitride layer prevents the boron from reacting with the rhenium container. If insufficiently protected, the thickness or vapour pressure must be adjusted accordingly.

For the heat exchanger and the nozzle, experimental testing is required to analyse the effects of repeated thermal and pressure cycling. The components are exposed to large variations in temperature and pressure due to the presence or absence of propellant flow. This can induce fatigue over many cycles. Creep at high temperature must also be considered, as channel walls and the nozzle contour may deform. Such deformation could lead to failure of the channel walls and would change the nozzle geometry and affect the propulsion performance.

The effectiveness of the insulation of the system depends on the estimated thermal conductivity due to the porous nature of the material. It should be verified what the actual effect of the porosity on the thermal properties or the insulation are. On a system level, the maximum temperature of the insulation on the outside has to be determined to ensure the low-emissivity layer does not melt.

Finally, the insulation needs to be validated. Its thermal resistance depends on the porous structure, which determines the actual thermal conductivity. The assumed values must therefore be confirmed experimentally. On a system level, it is also important to determine the maximum external temperature of the insulation to verify that the low-emissivity layer does not melt during operation.

9.4.2. Hydrogen

In addition to the effects of the high temperatures on the system materials themselves, the interaction with hydrogen at elevated temperatures requires experimental validation. Even though rhenium showed great resistance against reactions with hydrogen or hydrogen embrittlement, this must be confirmed at high operating temperature and pressure. Degradation of the components could lead to undesired leaks and a decrease in performance.

If degradation of the throat occurs, the throat area could increase gradually. This would affect the flow conditions in the nozzle, potentially preventing the propellant from reaching critical conditions. This would decrease the performance of the system unacceptably. Within the heat exchanger, degradation due to hydrogen could weaken the channel walls and eventually lead to leaks within the system. The relevant components should thus be exposed to hydrogen at a high temperature and pressure to ensure system reliability.

The properties of hydrogen itself at high temperatures also need to be tested. The behaviour of the propellant flow changes with temperature, as changes in specific heat capacity and viscosity affect flow and heat transfer characteristics. Since these properties are uncertain in the high-temperature range, they should be experimentally verified. Without this data, the behaviour of the system is more unpredictable. Deviations between estimated and actual performance are better understood when the characteristics of the propellant are known accurately.

9.5. Performance

To determine if and why the actual performance of the system differs from the estimated performance, the quality factors have to be experimentally determined. These factors help determine where losses occur and form the basis for adjusting the system accordingly.

A reduction in the cross-sectional areas of the system due to friction forces could reduce the mass flow of the system. By measuring the actual mass flow, the discharge coefficient can be determined with Equation 2.15.

Equation 2.4 shows that based on the measured chamber pressure, throat area and mass flow, the real characteristic velocity can be determined. Equation 2.5 can then be used to determine the real

characteristic velocity with the chamber temperature and specific heat ratio. The heating quality can then be determined with Equation 2.16 to see if the difference in performance occurs due to significant energy losses.

Similarly, the real thrust coefficient can be determined with the measured chamber pressure, measured thrust, and the throat area by using Equation 2.7. Then this can be compared with the ideal thrust coefficient, determined with the specific heat ratio, the chamber and exit pressure, and the expansion ratio, by using Equation 2.8. Comparing the two by using Equation 2.17 shows how well the energy is changed into momentum.

9.5.1. Specific Impulse Dependencies

Combining Equation 2.2 and Equation 2.3 with Equation 5.66, results in the following equation:

$$I_{sp} = \frac{v_e}{g_0} + \frac{(p_e - p_a)A_e}{\dot{m} \cdot g_0} \tag{9.1}$$

Substituting v_e for Equation 2.3 results in the following equation:

$$I_{sp} = \sqrt{\frac{2\gamma}{\gamma - 1} \cdot \frac{R_A}{M} \cdot \frac{T_c}{g_0^2} \cdot \left(1 - \left(\frac{p_e}{p_c}\right)^{\left(\frac{\gamma-1}{\gamma}\right)}\right)} + \frac{(p_e - p_a)A_e}{\dot{m} \cdot g_0} \tag{9.2}$$

This equation shows that the momentum thrust contribution to the specific impulse increases with the square root of the chamber temperature. When the nozzle does not expand the propellant ideally, the momentum thrust decreases, but the pressure thrust increases. However, the change in momentum thrust is more significant, making a low exit pressure preferred. The exit pressure and thus the pressure ratio are dependent on the expansion ratio of the nozzle.

If the nozzle throat erodes, the expansion ratio decreases due to the smaller difference between the throat and the exit. Equation 5.67 shows that a reduced expansion ratio results in a lower pressure ratio as well. This decrease in the pressure ratio means that for a set chamber pressure, the exit pressure thus reduces. Equation 5.65 shows that if the throat area increases too much, the flow will not reach sonic conditions in the throat, leading to a subsonic flow in the divergent part of the nozzle.

Equation 5.65 shows that an increase in chamber temperature also leads to an increase in the critical throat area. On the other hand, if the chamber pressure increases, a smaller critical throat area is required. In the case of propellant contamination, a smaller critical throat area is required as well, because the heavier-than-hydrogen particles increase the average molar weight. An increased average molar weight also lowers the momentum thrust and thus specific impulse. When a different propellant is used, the same effect of an increased molar weight occurs. If the throat area is smaller than the critical throat area, the flow becomes choked before the throat, but the flow still becomes supersonic after the throat.

10

Conclusions & Recommendations

To conclude on the findings of this report, there will be a reflection on the research questions. Further, recommendations for future work will be discussed as well.

10.1. Research Questions

The goal of this report is to design the secondary propulsion system for the Green SWaP mission. To do this, three main research questions were defined:

1. *What is the most suitable STP system for the Green SWaP mission?*

This research question will be answered by using the information found during the literature review and creating different design options. Then, based on what is required for the propulsion system, the most suitable options are selected.

After creating a design, it has to be optimised for the Green SWaP mission, resulting in the following research question:

2. *How can the STP system be optimised for the Green SWaP mission?*

The optimisation goal will be defined, together with the optimisation process itself.

Finally, the design will have to be validated to ensure the reliability of the system and that it meets the requirements. This results in the following research question:

3. *How can the STP system be experimentally validated?*

To answer these research questions, additional questions are used that will be discussed. The dedicated research questions for the requirements of the thruster were:

1. *What performance characteristics are required for the thruster?*
    1.1 *What is the required thrust of the thruster?*
    1.2 *What is the required minimum specific impulse of the thruster?*

2. *What functionalities are required for the thruster?*

These questions were answered by the imposed requirements of the Green SWaP mission. The mission required a thrust of $1.000\,\mathrm{N}$, a minimum specific impulse of $500\,\mathrm{s}$ and a burn time of $15\,\mathrm{min}$ during an eclipse. These requirements formed the basis for the design of the system.

Then, to support the concept selection, the following research questions were used:

3. *What type of absorber is the most suitable for the mission?*
    3.1 *What type of heating is the most suitable for the mission?*

3.2 *What type of thermal energy storage is the most suitable for the mission?*

4. *What nozzle is the most suitable for the mission?*

4.1 *What nozzle shape is the most suitable for the mission?*

4.2 *What protection against hydrogen is the most suitable for the mission?*

Based on the required thrust and specific impulse of the system, it was determined that indirect heating methods were the best option. Due to their relatively simple design, they have a higher reliability than direct heating methods. Direct heating methods can achieve better performance, but at the cost of the complexity of the system. Because the possible performance with an indirect heating method was sufficient for the mission, this method was the most suitable. More specifically, the windowless cavity concept was selected due to the better reliability and performance than the windowed cavity concept.

It was determined that for lower Reynolds numbers and small nozzles, a conical nozzle is the most suitable. With friction effects being more significant for small nozzles, the determination of the right bell curve becomes more difficult. This can make conical nozzles outperform bell nozzles. This makes the conical nozzle, even though its simple design, the best nozzle for this mission. To ensure the reliability of the nozzle throughout its lifetime, a coating to protect against hydrogen or a hydrogen-resistant structural material is needed.

To guide the preliminary design phase, the following research questions were used:

5. *What materials are the best option for the thruster?*

5.1 *What material is the best option for the cavity?*

5.2 *What material is the best option for the heat exchanger?*

5.3 *What material is the best option for the nozzle?*

5.4 *What material is the best option for the insulation?*

6. *What are the key parameters of the design?*

The trade-off for the cavity material showed that graphite, even though it has brittle behaviour, is the best option due to its high absorptivity and thermal resistance. The cavity is the hottest part of the thruster, and a high absorptivity results in a smaller area required to absorb the solar irradiation. The highest temperature of the system results in a smaller required area, significantly reducing the thermal radiation losses. For the heat exchanger, rhenium was identified as the best option due to its ductile behaviour at high temperatures and its great resistance to hydrogen. Due to these characteristics, this material is also the best option for the nozzle material. The hydrogen resistance is not relevant for the insulation material, but the reliability at elevated temperatures makes it the best option for this component as well. For the coating of the insulation to lower the emissivity, polished gold was identified as the best option. This material balances between a high melting temperature and a low emissivity.

The design during the preliminary phase showed that the most important key parameters were the achieved chamber temperature and pressure by the heat exchanger, the required input power, and the thermal losses of the system. The conditions at the end of the heat exchanger influence how much mass flow is required for the desired thrust. The required input power and thermal losses tell how efficiently the system uses the solar radiation to heat the propellant.

To iterate and optimise the design to get to the final design, the following research questions were identified:

7. *What tools are the most suitable to analyse the design?*

7.1 *What are the best ways to model the design?*

7.2 *How can the models be used to optimise the design?*

Due to the complexity of convective heat transfer, especially for turbulent flow. CFD was identified as the best option to determine the effectiveness of the heat exchanger. To model the conduction and radiation of the system, a simulation was created to apply the most realistic boundary conditions. The results of the ray tracing of the solar irradiation were directly applied in this simulation to get the most accurate predicted thermal distribution within the system. With the temperature of the materials

affecting the sizing of the components, accurate estimations were important. This made a node-based program to solve the thermal distribution within the solids the best option. Based on the determined temperatures, the insulation thickness and input power could be minimised, lowering the system size.

The models could also be used to determine how the losses of the system change during the heating and cooling of the system. Based on this analysis, the required thermal energy to be stored during an eclipse could be determined more accurately. This analysis helped minimise the size of the TES system, resulting in a lower outer surface temperature and thus the thermal losses. This snowball effect helped decrease the system size and mass, while not influencing the concentrator negatively. Indirectly, the required input power also reduced as it was easier for the smaller system to melt all the TES material.

To validate the design, an experimental validation was proposed. This experimental validation is based on the following research questions:

8. *What are the goals of the experimental testing?*
    - 8.1 *What are the goals of testing the materials?*
    - 8.2 *What are the goals of testing the performance?*

The proposed experimental validation focuses on the effects of high temperature and pressure, and the interaction with hydrogen on the different components. By analysing the thermal and mechanical properties of the materials at the operating conditions, the design can be adjusted if necessary to ensure reliability. Also, the properties of the propellant at high temperature and pressure need to be analysed, as this directly influences the heat transfer in the heat exchanger.

Based on the specific heat ratio, mass flow, thrust, chamber and exit conditions, combined with the nozzle geometry, the performance characteristic can be determined. By comparing the ideal and real mass flow, characteristic velocity and thrust coefficient, it can be determined where the losses of the system occur. This helps improve the system where necessary to ensure the performance is as required for the mission.

10.2. Recommendations

The simulations of the modelled design have been used to optimise the design, based on more accurate operating conditions than what was conservatively estimated. However, a few parameters were set to be constant. For future work, it is therefore recommended to analyse the effect of a smaller or larger cavity on the overall system efficiency. A larger cavity could potentially lower the required input power if the limiting factor for the input power is the distance between the cavity and the coldest point of the TES material. A smaller cavity could potentially lower the required input power if a smaller radiating surface decreases the thermal losses more than the decreased absorptivity increases the required input power.

The cavity was optimised based on a set of identified shapes during the literature review. However, it is recommended to study cavity shapes with a lower area but the same surface area and a better uniformity score by having a variable half-angle along the shape. More complex cavity shapes could potentially improve the system efficiency.

Another design parameter that can be analysed is the insulation outer temperature or thickness. A larger system outer surface increases the radiating area, but a lower surface temperature decreases the thermal radiation. If the thermal losses decrease, less TES material is required to store energy, leading to a decrease in system size. It is recommended to analyse the balancing of these effects to optimise the system further.

To improve the accuracy of the conduction and radiation simulation, it is recommended to determine the actual radiation and reabsorption of the radiation. The current simulation uses estimated radiation losses based on the area ratio, without simulating the reabsorption of radiation. This would improve the uniformity of the cavity temperature, because the hotter nodes can distribute their heat over colder nodes via radiation as well and not only via conduction. The thermal losses of the system would also be more accurately determined.

References

[1] Salil Rabade et al. “The Case for Solar Thermal Steam Propulsion System for Interplanetary Travel: Enabling Simplified ISRU Utilizing NEOs and Small Bodies”. In: Sept. 2016.

[2] Krafft A. Ehricke. *The solar-powered space ship*. American Rocket Society, June 1956.

[3] B. Wilner, L. Hays, and R. Buhler. *Research and development studies to determine feasibility of a solar LH2 rocket propulsion system*. 6593d Test Group, Rocket Propulsion Laboratory, Air Force Research & Technology Divison, Edwards Air Force Base, 1963.

[4] C. C. Selph. *The place of solar thermal rockets in space*. AF Rocket Propulsion Loboratory, 1981.

[5] C C Selph. *Place of solar thermal rockets in space*. Tech. rep. Air Force Rocket Propulsion Lab., Edwards AFB, CA (USA), May 1981. URL: https://www.osti.gov/biblio/6536738.

[6] F. G. Etheridge. *Solar rocket system concept analysis*. AF Rocket Propulsion Loboratory, Nov. 1979.

[7] J. M. Shoji. “Solar rocket component study”. In: *Final Report, AFRPL TR-84-057* (1985).

[8] Patrick E. Frye and James M. Shoji. *Innovative applications of solar thermal propulsion*. Rocketdyne, July 1992. DOI: 10.2514/6.1992-3081.

[9] Robert M. Zubrin et al. *The integrated power and propulsion stage: a mission driven solution utilizing thermionic technology*. 1992. DOI: 10.1063/1.41747.

[10] Patrick Frye. *Integrated solar upper stage (ISUS) space demonstration design*. 1997. DOI: 10.1063/1.52033.

[11] Jesse F. Stewart and James A. Martin. *Dual fuel solar thermal propulsion for LEO to GEO transfer: Ideal rocket analysis*. 1995. DOI: 10.2514/6.1995-2840.

[12] R.E. Freeland and G. Bilyeu. “In-step inflatable antenna experiment”. In: *Acta Astronautica* 30 (1993), pp. 29–40. ISSN: 0094-5765. DOI: https://doi.org/10.1016/0094-5765(93)90098-H. URL: https://www.sciencedirect.com/science/article/pii/009457659390098H.

[13] Alan M. Adams. *Solar thermal upper stage: economic advantage and development status*. NASA George C. Marshall Space Flight Center, 1996.

[14] Michael Tinker. *Passively adaptive inflatable structure for the Shooting Star Experiment*. Apr. 1998. DOI: 10.2514/6.1998-1986.

[15] Stephen Tucker and Pat Salvail. *Solar-thermal engine testing*. 2002. DOI: 10.1063/1.1449764.

[16] F. G. Kennedy and P. L. Palmer. *Preliminary design of a micro-scale solar thermal propulsion system*. 2002. DOI: 10.2514/6.2002-3928.

[17] Morio Shimizu et al. *50mm cavity diameter solar thermal thruster made of single crystal molybdenum*. 2001. DOI: 10.2514/6.2001-3733.

[18] Hironori Sahara. *Opposed-cavity solar thermal thruster made of single crystal tungsten*. 2001. URL: https://www.researchgate.net/publication/228738354.

[19] RG Clinton Jr et al. “Integrated High Payoff Rocket Propulsion Technologies Program Material Development Plan”. In: *Proceedings of the 4th Conference on Aerospace Materials, Processes, and Environmental Technology*. 2001.

[20] Steven R. Wassom et al. *Solar thermal propulsion IHPRPT demonstration program status*. 2001. DOI: 10.2514/6.2001-3735.

[21] Fred Kennedy, Phil Palmer, and Malcolm Paul. *Results of a Microscale Solar Thermal Engine Ground Test Campaign at the Surrey Space Centre*. July 2004. DOI: 10.2514/6.2004-4137.

[22] Paul Henshall and Phil Palmer. *Solar thermal propulsion augmented with fiber optics: technology development*. 2006. DOI: 10.2514/6.2006-4874.

[23] Takashi Nakamura et al. *Solar thermal propulsion for small spacecraft*. American Institute of Aeronautics and Astronautics, June 2005.

[24] Yuuki Iwaki, Tsuyoshi Totani, and Harunori Nagata. *Thermal Design of a Solar Thermal Thruster for Piggyback Satellites*. Hokkaido University, 2009.

[25] David B Scharfe and Andrew D Ketsdever. *A Review of High Thrust, High Delta-V Options for Microsatellite Missions*. 2009.

[26] Matthew R Gilpin. *High temperature latent heat thermal energy storage to augment solar thermal propulsion for microsatellites*. 2015.

[27] Salil Rabade et al. *The case for solar thermal steam propulsion system for interplanetary travel: enabling simplified ISRU utilizing NEOs and small bodies*. 2016.

[28] Baoyu Xing et al. "High efficient configuration design and simulation of platelet heat exchanger in solar thermal thruster". In: *Journal of Thermal Science* 23 (3 2014), pp. 246–252. ISSN: 10032169. DOI: 10.1007/s11630-014-0702-x.

[29] Minchao Huang et al. *Solar Thermal Thruster*. 2025.

[30] Geroge P. Sutton and Oscar Biblarz. *Rocket propulsion elements*. 9th ed. John Wiley & Sons, 2017.

[31] Ran Zhou et al. "Design and analysis of a compact solar concentrator tracking via the refraction of the rotating prism". In: *Energy* 251 (July 2022). ISSN: 03605442. DOI: 10.1016/j.energy.2022.123800.

[32] Frank P. Incropera et al. *Fundamentals of heat and mass transfer*. John Wiley & Sons, 2006.

[33] Fangzhou Song et al. "Feasibility analysis of solar thermal propulsion system with thermal energy storage". In: *Advances in Space Research* 71 (5 Mar. 2023), pp. 2493–2508. ISSN: 18791948. DOI: 10.1016/j.asr.2022.10.061.

[34] Stephen B. Pope. *Turbulent Flows*. Cambridge University Press, 2000.

[35] Shivang Khare and Ujjwal K Saha. "Rocket nozzles: 75 years of research and development". In: (2021). DOI: 10.1007/s12046-021-01584-6S. URL: https://doi.org/10.1007/s12046-021-01584-6S.

[36] Margaret V Whalen. *Low Reynolds number nozzle flow study*. 1987.

[37] A. Ashkan Davani and Paul D. Ronney. "Optimal design of nozzles for microsatellite propulsion". In: American Institute of Aeronautics and Astronautics Inc, AIAA, 2021, pp. 1–7. ISBN: 9781624106095. DOI: 10.2514/6.2021-0992.

[38] J Boise Pearson, D Brian Landrum, and Clark W Hawk. *Parametric Study of Solar Thermal Rocket Nozzle Performance*. 1994.

[39] Nikhil Khobragade et al. "Control of Flow Separation in a Rocket Nozzle Using Microjets". In: *New Space* 7.1 (2019), pp. 31–42. DOI: 10.1089/space.2018.0037. eprint: https://doi.org/10.1089/space.2018.0037. URL: https://doi.org/10.1089/space.2018.0037.

[40] J. Shoji. "Performance potential of advanced solar thermal propulsion". In: American Institute of Aeronautics and Astronautics, June 1983. DOI: 10.2514/6.1983-1307. URL: https://arc.aiaa.org/doi/10.2514/6.1983-1307.

[41] H-J Chen et al. "Characteristics of fluid flow and heat transfer in a rotating helical rectangle duct". In: *Zhejiang Daxue Xuebao(Gongxue Ban)/Journal of Zhejiang University(Engineering Science)* 37 (4 2003), pp. 445–449.

[42] Robert L. Sackheim. "Overview of United States Rocket Propulsion Technology and Associated Space Transportation Systems". In: *Journal of Propulsion and Power* 22 (6 Nov. 2006), pp. 1310–1332. ISSN: 0748-4658. DOI: 10.2514/1.23257.

[43] Gianpiero Colonna et al. "Model for ammonia solar thermal thruster". In: *Journal of Thermophysics and Heat Transfer* 20 (4 2006), pp. 772–779. ISSN: 15336808. DOI: 10.2514/1.18380.

[44] Jonathan A Lee and Stephen Woods. *Hydrogen embrittlement*. Tech. rep. NASA, 2016.

[45] David L Edwards et al. “Overview of the natural space environment and ESA, JAXA, and NASA materials flight experiments”. In: *MRS bulletin* 35.1 (2010), pp. 25–34.

[46] T Spilker and ; J Lunine. *A Shallow Entry Probe Mission to Saturn*. 2012, pp. 2012–3172.

[47] Barry Miles and John Kerr. “Coatings for high temperature graphite thermal energy storage in the Integrated Solar Upper Stage”. In: American Institute of Aeronautics and Astronautics, July 1996. DOI: 10.2514/6.1996-3047.

[48] F K Leverone. “Bi-modal solar thermal propulsion and power system Modelling and optimisation for the next-generation of small satellites”. Delft University of Technology, 2021. DOI: 10.4233/uuid:faf85ca4-9020-469f-a79f-f1c7d6719337. URL: https://doi.org/10.4233/uuid:faf85ca4-9020-469f-a79f-f1c7d6719337.

[49] Jagmit Singh et al. “Effect of nozzle geometry on critical-subcritical flow transitions”. In: *Heliyon* 5 (2 Feb. 2019), e01273. ISSN: 24058440. DOI: 10.1016/j.heliyon.2019.e01273.

[50] James Biaglow. “High temperature rhenium material properties”. In: *34th AIAA/ASME/SAE/ASEE Joint Propulsion Conference and Exhibit*. 1998, p. 3354.

[51] Ian H. Bell et al. “Pure and Pseudo-pure Fluid Thermophysical Property Evaluation and the Open-Source Thermophysical Property Library CoolProp”. In: *Industrial & Engineering Chemistry Research* 53.6 (2014), pp. 2498–2508. DOI: 10.1021/ie4033999. eprint: http://pubs.acs.org/doi/pdf/10.1021/ie4033999. URL: http://pubs.acs.org/doi/abs/10.1021/ie4033999.

[52] Thomas C Hales. “An overview of the Kepler conjecture”. In: *arXiv preprint math/9811071* (1998).

[53] Peter Stephan. “B1 Fundamentals of Heat Transfer”. In: *VDI Heat Atlas*. Berlin, Heidelberg: Springer Berlin Heidelberg, 2010, pp. 15–30. ISBN: 978-3-540-77877-6. DOI: 10.1007/978-3-540-77877-6_115. URL: https://doi.org/10.1007/978-3-540-77877-6_115.

[54] Frank L Pedrotti, Leno M Pedrotti, and Leno S Pedrotti. *Introduction to optics*. Cambridge university press, 2017.

[55] C. E. Shannon. “A mathematical theory of communication”. In: *The Bell System Technical Journal* 27.3 (1948), pp. 379–423. DOI: 10.1002/j.1538-7305.1948.tb01338.x.

[56] C. Malmstrom, R. Keen, and L. Green. “Some Mechanical Properties of Graphite at Elevated Temperatures”. In: *Journal of Applied Physics* 22 (5 May 1951), pp. 593–600. ISSN: 0021-8979. DOI: 10.1063/1.1700013.

[57] DL Hildenbrand and WF Hall. “The vaporization behavior of boron nitride and aluminum NITRIDE1”. In: *The Journal of Physical Chemistry* 67.4 (1963), pp. 888–893.

A

Component Scripts

This appendix contains the scripts used for the components of the propulsion system. The filled-in parameters are the values of the final design.

Listing A shows the script for the required channel length of the heat exchanger.

```python
# ============================================================
# Imports
# ============================================================

import CoolProp.CoolProp as CP  # Thermophysical properties
import numpy as np
from scipy.optimize import brentq, root_scalar  # Root-finding
import matplotlib.pyplot as plt  # Plotting

# ============================================================
# Parameters
# ============================================================

N = 1
m_dot = 0.1173-3 / N       # Mass flow rate [kg/s]
T_in = 273.15               # Inlet temperature [K]
T_c = 2249                  # Channel temperature [K]
T_wall = 2349               # Wall temperature [K]
n = 1000                    # Number of temperature steps
dT = (T_c - T_in) / n       # Temperature increment [K]
P_in = 50e5                 # Inlet pressure [Pa]

R = 8.314                   # Gas constant [J/mol·K]
M_H2 = 2.016e-3             # Molar mass H2 [kg/mol]

epsilon = 1 - np.pi / (3 * np.sqrt(2))  # Porosity factor
d_p = 1.548e-3               # Particle diameter [m]
a_s = 2.860e3                # Specific surface area [m²/m³]

# ============================================================
# CoolProp Property Functions
# ============================================================

def dynamic_viscosity(T, P):
    """Return dynamic viscosity [Pa·s]"""
    return CP.PropsSI('VISCOSITY', 'T', T, 'P', P, 'Hydrogen')

def prandtl_number(T, P):
    """Return Prandtl number [-]"""
    return CP.PropsSI('PRANDTL', 'T', T, 'P', P, 'Hydrogen')

def enthalpy(T, P):
    """Return specific enthalpy [J/kg]"""
    return CP.PropsSI('H', 'T', T, 'P', P, 'Hydrogen')
```

```

def density(T, P):
    """Return density [kg/m³]"""
    return CP.PropsSI('D', 'T', T, 'P', P, 'Hydrogen')

def specific_heat_ratio(T, P):
    """Return Cp/Cv ratio [-]"""
    cp = CP.PropsSI('CPMASS', 'T', T, 'P', P, 'Hydrogen')
    cv = CP.PropsSI('CVMASS', 'T', T, 'P', P, 'Hydrogen')
    return cp / cv

# ============================================================
# Heat Transfer Calculations
# ============================================================

def required_heating_power(T, P):
    """Compute required power to heat gas over dT [W]"""
    h1 = enthalpy(T, P)
    h2 = enthalpy(T + dT, P)
    return m_dot * (h2 - h1)

def lmtd(T):
    """Logarithmic mean temperature difference [K]"""
    return dT / np.log((T_wall - T) / (T_wall - (T + dT)))

def heat_transfer_coefficient(T, P, Nu, L_c):
    """Convective heat transfer coefficient [W/m²·K]"""
    k = CP.PropsSI('L', 'T', T, 'P', P, 'Hydrogen')
    return Nu * k / L_c

def heat_transfer_coefficient_porous(T, P, Nu):
    """Porous media heat transfer [W/m³·K]"""
    h = heat_transfer_coefficient(T, P, Nu, d_p)
    return a_s * h

def transferred_heating_power(T, P, Nu, D, L):
    """Compute heating power transferred through smooth channel [W]"""
    h = heat_transfer_coefficient(T, P, Nu, D)
    return h * np.pi * D * L * lmtd(T)

def transferred_heating_power_porous(T, P, Nu, A_c, L):
    """Compute heating power in porous channel [W]"""
    h_v = heat_transfer_coefficient_porous(T, P, Nu)
    return h_v * A_c * L * lmtd(T)

# ============================================================
# Flow Calculations
# ============================================================

def reynolds_number(D, mu):
    """Reynolds number for smooth tube"""
    return (4 * m_dot) / (np.pi * D * mu)

def reynolds_number_porous(A_c, mu):
    """Reynolds number for porous media"""
    return (m_dot * d_p) / (epsilon * A_c * mu)

def friction_factor_t(Re):
    """Turbulent friction factor"""
    return (0.790 * np.log(Re) - 1.64)**-2

def nusselt_number_t(f, Re, Pr):
    """Turbulent Nusselt number"""
    numerator = (f / 8) * (Re - 1000) * Pr
    denominator = 1 + 12.7 * (f / 8)**0.5 * (Pr**(2/3) - 1)
    return numerator / denominator

def friction_factor_l(Re):
    """Laminar friction factor"""
    return 64 / Re

```

```
def nusselt_number_l(D, x, Re, Pr):
    """Laminar Nusselt number (entry region)"""
    term = (D / x) * Re * Pr
    numerator = 0.0668 * 0.04 * (2 / 3) * term**(5/3)
    denominator = (1 + 0.04 * term**(2/3))**2
    return 3.66 + numerator / denominator

def nusselt_number_porous(Re, Pr):
    """Nusselt number for porous media"""
    Nul = 0.664 * Pr**(1/3) * Re**0.5
    Nut = (0.037 * Re**0.8 * Pr) / (1 + 2.443 * Re**-0.1 * (Pr**(2/3) - 1))
    return 2 + np.sqrt(Nul**2 + Nut**2)

# ============================================================
# Pressure Drop
# ============================================================

def pressure_drop(T, P, f, L, D):
    """Pressure drop in smooth tube [Pa]"""
    rho = density(T, P)
    A = np.pi * D**2 / 4
    v = m_dot / (rho * A)
    return f * (L / D) * 0.5 * rho * v**2

def pressure_drop_porous(T, P, mu, L, A_c):
    """Pressure drop in porous media [Pa]"""
    rho = density(T, P)
    v_s = m_dot / (rho * A_c)
    term_viscous = (150 * (1 - epsilon)**2 * mu * v_s) / (epsilon**3 * d_p**2)
    term_inertial = (1.75 * (1 - epsilon) * rho * v_s**2) / (epsilon**3 * d_p)
    return (term_viscous + term_inertial) * L

# ============================================================
# Channel Length Calculations
# ============================================================

def channel_length(D, tol=1e-16, max_iter=100000):
    """Compute channel length and flow regimes for smooth tube"""
    L_total = 0
    P_total = P_in
    laminar_total = 0
    turbulent_total = 0
    transition_total = 0

    for T in np.linspace(T_in, T_c - dT, n):
        L_estimate, P_estimate = 0.1, 1e3
        for _ in range(max_iter):
            x = L_total + 0.5 * L_estimate
            P = P_total - 0.5 * P_estimate
            Q_dot_r = required_heating_power(T, P)
            mu = dynamic_viscosity(T + dT/2, P)
            Pr = prandtl_number(T + dT/2, P)
            Re = reynolds_number(D, mu)

            # Select flow regime
            if Re >= 3000:
                f = friction_factor_t(Re)
                Nu = nusselt_number_t(f, Re, Pr)
            elif Re <= 2300:
                f = friction_factor_l(Re)
                Nu = nusselt_number_l(D, x, Re, Pr)
            else:  # Transition
                f_lam = friction_factor_l(Re)
                f_turb = friction_factor_t(Re)
                Nu_lam = nusselt_number_l(D, x, Re, Pr)
                Nu_turb = nusselt_number_t(f_turb, Re, Pr)
                weight = (Re - 2300)/(3000 - 2300)
                f = (1 - weight)*f_lam + weight*f_turb
                Nu = (1 - weight)*Nu_lam + weight*Nu_turb

            # Solve for local length
```

```
            def find_L(L):
                return Q_dot_r - transferred_heating_power(T, P, Nu, D, L)
            L_solution = brentq(find_L, 1e-10, 10)
            P_solution = pressure_drop(T + dT/2, P, f, L_solution, D)

            # Convergence check
            if abs(L_solution - L_estimate) < tol and abs(P_solution - P_estimate) < 1e-6:
                break
            L_estimate, P_estimate = L_solution, P_solution

        L_total += L_solution
        if Re >= 4000: turbulent_total += L_solution
        elif Re <= 2300: laminar_total += L_solution
        else: transition_total += L_solution
        P_total -= P_solution

    rho = density(T + dT, P)
    A = np.pi * D**2 / 4
    v = m_dot / (rho * A)
    M = v / CP.PropsSI('A', 'T', T + dT, 'P', P, 'Hydrogen')  # Mach number
    return L_total, laminar_total/L_total, turbulent_total/L_total, transition_total/L_total,
         P_total, M

def channel_length_porous(A_c, tol=1e-16, max_iter=100000):
    """Compute channel length and flow regimes for porous medium"""
    L_total = 0
    P_total = P_in
    laminar_total = 0
    turbulent_total = 0
    transition_total = 0
    for T in np.linspace(T_in, T_c - dT, n):
        L_estimate, P_estimate = 0.1, 1e3
        for _ in range(max_iter):
            P = P_total - 0.5 * P_estimate
            mu = dynamic_viscosity(T + dT/2, P)
            Pr = prandtl_number(T + dT/2, P)
            Q_dot_r = required_heating_power(T, P)
            Re = reynolds_number_porous(A_c, mu)
            Nu = nusselt_number_porous(Re, Pr)

            def find_L(L):
                return Q_dot_r - transferred_heating_power_porous(T, P, Nu, A_c, L)
            L_solution = brentq(find_L, 1e-10, 10)
            P_solution = pressure_drop_porous(T + dT, P, mu, L_solution, A_c)

            if abs(L_solution - L_estimate) < tol and abs(P_solution - P_estimate) < 1e-6:
                break
            L_estimate, P_estimate = L_solution, P_solution

        L_total += L_solution
        if Re >= 4000: turbulent_total += L_solution
        elif Re <= 2300: laminar_total += L_solution
        else: transition_total += L_solution
        P_total -= P_solution

    rho = density(T + dT, P)
    v = m_dot / (rho * A_c * epsilon)
    M = v / CP.PropsSI('A', 'T', T + dT, 'P', P, 'Hydrogen')
    return L_total, laminar_total/L_total, turbulent_total/L_total, transition_total/L_total,
         P_total, M
```

Listing A shows the script for the cavity design.

```
# ============================================================
# Imports
# ============================================================

import numpy as np
import matplotlib.pyplot as plt
import matplotlib.cm as cm
from scipy.optimize import differential_evolution
```

```python
from scipy.optimize import root_scalar
from matplotlib.patches import Rectangle

# ============================================================
# Parameters
# ============================================================

numerical_aperture = 0.48           # NA determines maximum acceptance angle for rays
num_rays = 1000                     # Total number of rays to trace
num_rays_to_plot = 50               # Number of rays to plot for visualization
absorptivity = 0.84                 # Fraction of energy absorbed per wall hit
segment_length_const = 1.0          # Fixed segment length for wall discretization
max_bounces = 4                     # Maximum number of ray reflections
bin_width = 1                       # Bin width for histogram analysis (if used)
aperture_radius = 10                # Radius of the input aperture
area_ratio = 3.284                  # Ratio of total cavity surface to aperture area

first_cone = True                   # Boolean flag indicating if left cone exists

emission_angle_deg = np.degrees(np.arcsin(numerical_aperture))  # Maximum emission angle [deg]
max_absorption = 1-(1-absorptivity)**max_bounces  # Maximum achievable absorption after all bounces

# ============================================================
# Geometry and Surface Area Functions
# ============================================================

def total_surface_area(rc, theta1_deg, theta2_deg, cylinder_length_ratio):
    """Compute total internal surface area for a cavity (cones + cylinder)"""
    theta1 = np.radians(theta1_deg)
    theta2 = np.radians(theta2_deg)

    if first_cone:
        L1 = (rc - aperture_radius) / np.tan(theta1)  # Axial length of left cone
        l1 = np.sqrt((rc - aperture_radius)**2 + L1**2)  # Slant height of left cone
        S_cone1 = np.pi * (aperture_radius + rc) * l1   # Surface area of left cone
    else:
        L1 = 0
        S_cone1 = 0

    L2 = rc / np.tan(theta2)           # Axial length of right cone
    l2 = np.sqrt(rc**2 + L2**2)        # Slant height of right cone
    S_cone2 = np.pi * rc * l2          # Surface area of right cone

    Lc = cylinder_length_ratio * rc    # Cylinder axial length
    S_cyl = 2 * np.pi * rc * Lc        # Surface area of cylinder

    return S_cone1 + S_cyl + S_cone2   # Total surface area

def find_rc_for_target_surface(theta1_deg, theta2_deg, cylinder_length_ratio):
    """Find cavity radius that meets target surface area based on area_ratio"""
    aperture_area = np.pi * aperture_radius**2
    target_area = area_ratio * aperture_area

    def func(rc):
        return total_surface_area(rc, theta1_deg, theta2_deg, cylinder_length_ratio) -
            target_area

    rc_guess_min = aperture_radius * 1.0001
    rc_guess_max = aperture_radius * 100

    try:
        sol = root_scalar(func, bracket=[rc_guess_min, rc_guess_max], method='brentq')
        if sol.converged:
            return sol.root
    except (ValueError, RuntimeError):
        return None

    return None

```

```
77 def geometry(theta1_deg, theta2_deg, cylinder_length_ratio):
78     """Compute cavity wall coordinates and total length"""
79     if not first_cone:
80         rc = aperture_radius  # Fixed radius if left cone is not present
81         aperture_area = np.pi * aperture_radius**2
82         target_area = area_ratio * aperture_area
83 
84         # Solve theta2 that meets target area
85         def func(theta2_rad):
86             L2 = rc / np.tan(theta2_rad)
87             l2 = np.sqrt(rc**2 + L2**2)
88             S_cone2 = np.pi * rc * l2
89             Lc = cylinder_length_ratio * rc
90             S_cyl = 2 * np.pi * rc * Lc
91             return (S_cyl + S_cone2) - target_area  # Exclude left cone
92 
93         try:
94             sol = root_scalar(func, bracket=[np.radians(0.0001), np.radians(89.9)], method='
                brentq')
95             if not sol.converged:
96                 return None, None, None, None
97             theta2_rad = sol.root
98         except (ValueError, RuntimeError):
99             return None, None, None, None
100 
101     else:
102         rc = find_rc_for_target_surface(theta1_deg, theta2_deg, cylinder_length_ratio)
103         if rc is None:
104             return None, None, None, None
105         theta2_rad = np.radians(theta2_deg)
106 
107     # Compute axial lengths
108     theta1_rad = np.radians(theta1_deg)
109     L1 = (rc - aperture_radius) / np.tan(theta1_rad) if first_cone else 0
110     L2 = rc / np.tan(theta2_rad)
111     Lc = cylinder_length_ratio * rc
112 
113     total_length = L1 + Lc + L2
114     print(total_length)
115 
116     # Compute wall coordinates
117     x0 = 0.0
118     x1 = x0 + L1
119     x2 = x1 + Lc
120     x3 = x2 + L2
121 
122     walls = []
123     if first_cone:
124         walls += [
125             [(x0, aperture_radius), (x1, rc)],        # Left top cone
126             [(x0, -aperture_radius), (x1, -rc)],      # Left bottom cone
127         ]
128 
129     walls += [
130         [(x1, rc), (x2, rc)],        # Cylinder top
131         [(x1, -rc), (x2, -rc)],      # Cylinder bottom
132         [(x2, rc), (x3, 0.0)],       # Right top cone
133         [(x2, -rc), (x3, 0.0)],      # Right bottom cone
134     ]
135 
136     vertical_wall = [(0, -rc), (0, rc)]  # Central vertical wall for ray termination
137 
138     return walls, rc, total_length, vertical_wall
139 
140 # ============================================================
141 # Ray Tracing Functions
142 # ============================================================
143 
144 def ray_segment_intersection(ray_origin, ray_dir, p1, p2):
145     """Compute intersection point of ray with line segment"""
146     p1, p2 = np.array(p1), np.array(p2)
```

```
    v1 = ray_origin - p1
    v2 = p2 - p1
    v3 = np.array([-ray_dir[1], ray_dir[0]])
    dot = np.dot(v2, v3)
    if abs(dot) < 1e-10:
        return None, None
    t1 = np.cross(v2, v1) / dot
    t2 = np.dot(v1, v3) / dot
    if t1 > 1e-10 and 0 <= t2 <= 1:
        return ray_origin + t1*ray_dir, (p1, p2)
    return None, None

def reflect(ray_dir, normal):
    """Reflect ray about surface normal"""
    return ray_dir - 2*np.dot(ray_dir, normal)*normal

def wall_normal(p1, p2):
    """Compute normal vector for a wall segment"""
    vec = np.array(p2) - np.array(p1)
    n = np.array([-vec[1], vec[0]])
    return n / np.linalg.norm(n)

# ============================================================
# Simulation Core
# ============================================================

def simulate(theta1_deg, theta2_deg, cylinder_length_ratio, plot_density=False):
    """Simulate ray tracing and wall energy deposition"""
    walls, rc, total_length, vertical_wall = geometry(theta1_deg, theta2_deg,
        cylinder_length_ratio)

    if walls is None or rc is None:
        print("Invalid geometry - skipping simulation.")
        return 0.0, None, 0.0, None

    if not first_cone:
        theta2_deg = np.degrees(np.arctan(rc / (total_length - cylinder_length_ratio * rc)))
        print(f"Simulating | 2 = {theta2_deg:.5f}°, L_cyl/r_cyl = {cylinder_length_ratio:.5f
            }")
    else:
        print(f"Simulating | 1 = {theta1_deg:.2f}°, 2 = {theta2_deg:.2f}°, L_cyl/r_cyl = {
            cylinder_length_ratio:.2f}")

    # ----------------- Initialize Wall Segments -----------------
    wall_lengths = [np.linalg.norm(np.array(p2) - np.array(p1)) for p1, p2 in walls]
    segments_per_wall = [max(1, int(np.ceil(L / segment_length_const))) for L in wall_lengths
        ]
    wall_energy = [np.zeros(n) for n in segments_per_wall]

    # ----------------- Initialize Rays -----------------
    ray_origin = np.array([0.0, 0.0])
    theta_max = np.arcsin(numerical_aperture)
    u = np.linspace(0, 1, num_rays)
    theta = np.arcsin(np.sin(theta_max) * (2 * u - 1))
    ray_dirs = np.stack([np.cos(theta), np.sin(theta)], axis=1)

    total_initial_energy = 100.0

    if plot_density:
        plt.figure(figsize=(8, 5))
        plot_indices = set(np.linspace(0, num_rays - 1, num_rays_to_plot, dtype=int))

    # ----------------- Trace Rays -----------------
    for i, ray_dir in enumerate(ray_dirs):
        energy = total_initial_energy / num_rays
        ray_pos = ray_origin.copy()

        for bounce in range(max_bounces):
            closest_pt, hit_idx = None, -1
            min_dist = np.inf

```

```
            for idx, wall in enumerate(walls):
                hit, _ = ray_segment_intersection(ray_pos, ray_dir, *wall)
                if hit is not None:
                    d = np.linalg.norm(hit - ray_pos)
                    if d < min_dist:
                        min_dist = d
                        closest_pt = hit
                        hit_idx = idx

            if vertical_wall is not None:
                hit_v, _ = ray_segment_intersection(ray_pos, ray_dir, *vertical_wall)
                if hit_v is not None:
                    d_v = np.linalg.norm(hit_v - ray_pos)
                    if d_v < min_dist:
                        if plot_density and i in plot_indices:
                            cmap = cm.get_cmap("autumn")
                            color = cmap(bounce / max_bounces)
                            plt.plot([ray_pos[0], hit_v[0]], [ray_pos[1], hit_v[1]], color=
                                color, alpha=0.6)
                        break

            if closest_pt is None:
                break

            if plot_density and i in plot_indices:
                cmap = cm.get_cmap("autumn")
                color = cmap(bounce / max_bounces)
                plt.plot([ray_pos[0], closest_pt[0]], [ray_pos[1], closest_pt[1]], color=
                    color, alpha=0.6)

            p1, p2 = walls[hit_idx]
            seg_vec = np.array(p2) - np.array(p1)
            rel = np.dot(closest_pt - p1, seg_vec) / (np.linalg.norm(seg_vec) ** 2)
            seg_idx = min(max(int(rel * segments_per_wall[hit_idx]), 0), segments_per_wall[
                hit_idx] - 1)

            absorbed = energy * absorptivity
            wall_energy[hit_idx][seg_idx] += absorbed
            energy -= absorbed

            normal = wall_normal(*walls[hit_idx])
            ray_dir = reflect(ray_dir, normal)
            ray_pos = closest_pt

    # ----------------- Normalize by 3D Area ------------------
    segment_areas = []
    for (p1, p2), n in zip(walls, segments_per_wall):
        seg_vec = np.array(p2) - np.array(p1)
        for s in range(n):
            start = np.array(p1) + (s / n) * seg_vec
            end = np.array(p1) + ((s + 1) / n) * seg_vec
            y_avg = (abs(start[1]) + abs(end[1])) / 2
            seg_length = np.linalg.norm(end - start)
            area = np.pi * y_avg * seg_length
            segment_areas.append(area)

    all_energy_density = []
    top_half_energy_data = []

    for i in range(len(walls)):
        p1, p2 = walls[i]
        seg_vec = np.array(p2) - np.array(p1)
        n_segments = segments_per_wall[i]

        for j in range(n_segments):
            idx_flat = sum(segments_per_wall[:i]) + j
            start = np.array(p1) + (j / n_segments) * seg_vec
            end = np.array(p1) + ((j + 1) / n_segments) * seg_vec
            center = (start + end) / 2

            energy_density = wall_energy[i][j] / segment_areas[idx_flat]
```

```
            all_energy_density.append(energy_density)

            if center[1] > 0:
                top_half_energy_data.append([center[0], center[1], 2*wall_energy[i][j]])

    all_energy_density = np.array(all_energy_density)
    top_half_energy_data = np.array(top_half_energy_data)

    # ----------------- Compute Uniformity Score -----------------
    total_energy = all_energy_density.sum()
    if total_energy > 0:
        p_raw = all_energy_density / total_energy
        entropy = -np.sum(p_raw[p_raw > 0] * np.log(p_raw[p_raw > 0]))
        max_entropy = np.log(len(p_raw))
        uniformity_score = entropy / max_entropy
    else:
        uniformity_score = 1.0

    total_absorbed_energy = sum(all_energy_density[i] * segment_areas[i] for i in range(len(
        segment_areas)))
    print(f"Uniformity Score: {uniformity_score:.4f}")
    print(f"Absorbed Power (%): {total_absorbed_energy:.4f}%")

    # ----------------- Optional Plot -----------------
    if plot_density:
        wall_density = []
        for i in range(len(walls)):
            densities_i = []
            for s in range(segments_per_wall[i]):
                idx_flat = sum(segments_per_wall[:i]) + s
                densities_i.append(wall_energy[i][s] / segment_areas[idx_flat])
            wall_density.append(np.array(densities_i))
        all_nd = np.concatenate(wall_density)
        norm = plt.Normalize(vmin=0, vmax=all_nd.max() if all_nd.max() > 0 else 1)
        cmap = cm.get_cmap("inferno")

        for idx, wall in enumerate(walls):
            p1, p2 = np.array(wall[0]), np.array(wall[1])
            seg_vec = p2 - p1
            for s in range(segments_per_wall[idx]):
                start = p1 + (s / segments_per_wall[idx]) * seg_vec
                end = p1 + ((s + 1) / segments_per_wall[idx]) * seg_vec
                plt.plot([start[0], end[0]], [start[1], end[1]],
                         color=cmap(norm(wall_density[idx][s])), linewidth=4)

        # Add representation of input cylinder
        block_x = -20
        block_width = 20
        block_height = 10
        block_bottom = -5

        block = Rectangle(
            (block_x, block_bottom),
            block_width,
            block_height,
            facecolor="lightblue",
            edgecolor="black",
            linewidth=1
        )
        plt.gca().add_patch(block)

        sm = cm.ScalarMappable(norm=norm, cmap=cmap)
        sm.set_array([])
        plt.colorbar(sm, label="Relative heat flux [% mm²]")
        plt.axis('equal')
        plt.xlabel("Length [mm]")
        plt.ylabel("Radius [mm]")
        plt.grid(True)
        plt.tight_layout()
        plt.show()

```

```
    absorption_ratio = (total_absorbed_energy / 100) / max_absorption

    return uniformity_score, top_half_energy_data, absorption_ratio, theta2_deg

# ============================================================
# Optimization Functions
# ============================================================

def optimize_geometry():
    """Optimize cavity geometry using differential evolution"""
    def objective(params):
        if first_cone:
            theta1, theta2, cyl_len_ratio = params
        else:
            cyl_len_ratio, = params
            theta1 = 1e-5  # placeholder
            theta2 = 1e-5  # solved inside geometry

        score, _, _, _ = simulate(theta1, theta2, cyl_len_ratio, plot_density=False)
        return -score if score is not None else 1e6  # penalize invalid

    if first_cone:
        bounds = [
            (0.00001, 89.9999),  # θ1
            (0.00001, 89.9999),  # θ2
            (0.00001, 10.0),     # L_cyl/R_cyl
        ]
    else:
        bounds = [
            (0.00001, 10.0),     # L_cyl/R_cyl only
        ]

    result = differential_evolution(
        objective,
        bounds,
        strategy='best1bin',
        popsize=20,
        tol=1e-4,
        seed=42,
        updating='deferred',
    )

    if first_cone:
        best_theta1, best_theta2, best_length_ratio = result.x
    else:
        best_length_ratio, = result.x
        best_theta1 = 1e-5
        best_theta2 = 1e-5

    best_score = -result.fun
    print("Best configuration found:")
    if first_cone:
        print(f"  θ1 = {best_theta1:.2f}°")
    print(f"  θ2 = {best_theta2:.2f}°")
    print(f"  L_cyl/R_cyl  = {best_length_ratio:.2f}")
    print(f"  Score = {best_score:.4f}")

    _, _, _, best_theta2 = simulate(best_theta1, best_theta2, best_length_ratio, plot_density
        =True)

def min_area(area_min=1.0, area_max=18, tol=1e-5, target_absorption=0.99999):
    """Lowest cavity area with maximum absorption"""
    global area_ratio

    class TargetReached(Exception):
        pass

    best_config = None
    best_area = None
    low, high = area_min, area_max

```

```
    while high - low > tol:
        mid = (low + high) / 2
        area_ratio = mid
        print(f"\nTesting area_ratio = {mid:.6f}")

        best_found = {"absorption": -float('inf'), "params": None}

        if first_cone:
            bounds = [
                (0.00001, 89.9999),  # 1
                (0.00001, 89.9999),  # 2
                (0.00001, 10.0),    # L_cyl/R_cyl
            ]
        else:
            bounds = [
                (0.00001, 10.0),    # L_cyl/R_cyl only
            ]

        def objective(params):
            if first_cone:
                theta1, theta2, cyl_len_ratio = params
            else:
                cyl_len_ratio, = params
                theta1 = 1e-5
                theta2 = 1e-5

            _, _, absorption_ratio, _ = simulate(theta1, theta2, cyl_len_ratio, plot_density=
                False)

            if absorption_ratio is None:
                return 1e6  # invalid geometry

            if absorption_ratio > best_found["absorption"]:
                best_found["absorption"] = absorption_ratio
                best_found["params"] = params

            if absorption_ratio >= target_absorption:
                raise TargetReached

            return -absorption_ratio

        try:
            differential_evolution(
                objective,
                bounds,
                seed=42,
                popsize=20,
                tol=1e-4,
                updating='deferred',
                polish=False,
            )
        except TargetReached:
            high = mid
            best_area = mid
            best_config = (*best_found["params"], best_found["absorption"])
            print(f"Absorption = 1 reached at area_ratio = {mid:.6f}")
            continue

        low = mid
        print(f"Absorption = {best_found['absorption']:.4f} at area_ratio = {mid:.6f}")

    print("\nMinimal area_ratio found:")

    if best_config:
        if first_cone:
            best_theta1 = best_config[0]
            best_theta2 = best_config[1]
            best_length_ratio = best_config[2]
            best_absorption = best_config[3]
        else:
            best_length_ratio = best_config[0]   # optimized L_cyl/R_cyl
```

```
            # Get theta2 from simulate()
            _, _, best_absorption, best_theta2 = simulate(1e-5, 1e-5, best_length_ratio,
                plot_density=False)

        print("\nBest␣configuration␣found␣for␣minimal␣area:")
        print(f"␣␣area_ratio␣=␣{best_area:.6f}")
        if first_cone:
            print(f"␣␣␣1␣=␣{best_theta1:.2f}°")
        print(f"␣␣␣2␣=␣{best_theta2:.2f}°")
        print(f"␣␣L_cyl/R_cyl␣=␣{best_length_ratio:.2f}")
        print(f"␣␣Absorption␣ratio␣=␣{best_absorption:.4f}")

        # Run simulation with density plot
        _, _, _, _ = simulate(
            best_theta1 if first_cone else 1e-5,
            best_theta2,
            best_length_ratio,
            plot_density=True
        )
        return best_config
    else:
        print("No␣configuration␣found␣achieving␣absorption␣ratio␣=␣1")
        return None

np.savetxt("energy_data.csv", export, delimiter=",", header="z,r,energy_percent", comments=''
    )
```

B

System Scripts

This appendix contains the scripts used for the complete propulsion system. The filled-in parameters are the values of the final design.

Listing B shows the script for the radiation and conduction simulation.

```
# ============================================================
# Imports
# ============================================================

import numpy as np
import matplotlib.pyplot as plt
from matplotlib.path import Path
import matplotlib.colors as mcolors
import random
from numba import njit, prange
import matplotlib.patches as mpatches

# ============================================================
# Input files
# ============================================================
energy_data = np.loadtxt("energy_data.csv", delimiter=",", skiprows=1)
T_final = np.load("T_final.npy")

# ==========================
# === 1) GLOBAL CONSTANTS
# ==========================

sigma = 5.67e-8     # Stefan-Boltzmann constant [W/ m²K]

# --- Geometry constants (all in mm; we will convert to meters later) ---
t_cav      = 2.857           # cavity wall thickness [mm]
R_cav      = 10.0 + t_cav       # max inner cavity radius [mm]
aperture_r = 10.0          # -smallend tip radius at entrance [mm]
theta1_deg = 0       # left cone -halfangle [deg]
theta2_deg = 17.73       # right cone -halfangle [deg]
L_cav      = 31.28 + t_cav       # total inner cavity length [mm]

alpha = 0.84
area_ratio=3.284

t_wall = 0.10 # [mm]
D = 1.017 # [mm]


R_TES = 51.97            # [mm]
L_TES = 101.84              # [mm]
t_liner         = 0.5 # [mm]
t_TES           = t_wall+t_liner#       # TES layer thickness [mm]
container_start = 0      # -zstart of TES cylinder [mm]
```

```
45
46 t_ins_cav = 69.0  # [mm]
47 t_ins_TES = 69.0 # [mm]
48
49 k_s_TES = 29.1        # solid
50 k_v_TES = 0.0         # void (air)
51 phi_TES = 0.2
52
53 k_s_ins = 48.6        # solid
54 k_v_ins = 0.0         # void (air)
55 phi_ins = 0.99
56
57 def effective_conductivity(k_s, k_v, phi):
58     numerator = 2 * k_s + k_v - 2 * phi * (k_s - k_v)
59     denominator = 2 * k_s + k_v + phi * (k_s - k_v)
60     k_eff = k_s * (numerator / denominator)
61
62     return k_eff
63
64 # --- Material properties (SI units) ---
65 material_props = {
66     0: {"k": 0.0,  "epsilon": 1.0,  "rho": 0.0,  "cp": 0.0},     # void
67     1: {"k": 168.0,  "epsilon": 0.81,  "rho": 2260.0,  "cp": 717.0},   # cavity shell
68     2: {"k": k_s_ins,  "epsilon": 1.0,  "rho": 21020.0,  "cp": 140.0},   # TES container (
           example values)
69     3: {"k": 751,  "epsilon": 1.0,  "rho": 21000.0,  "cp": 720.0},  # TES liner
70     4: {"k": effective_conductivity(k_s_TES, k_v_TES, phi_TES),  "epsilon": 1.0,  "rho":
           2450.0*(1-phi_TES),  "cp": 960.0*(1-phi_TES)},   # TES material (example values)
71     5: {"k": k_s_ins,  "epsilon": 1.0,  "rho": 21020.0,  "cp": 140.0},   # heat exchanger
72     6: {"k": effective_conductivity(k_s_ins, k_v_ins, phi_ins),  "epsilon": 0.03,  "rho":
           21020.0*(1-phi_ins),  "cp": 140.0*(1-phi_ins)},   # Insulation
73 }
74
75 # Define latent heat only for TES material (mask == 2)
76 latent_heat_value = 4.644e6  # J/kg for TES
77 melt_temp_value   = 234  # K midpoint of melting transition
78 delta_T_melt      = 1.0  # melting range [K]
79
80 # --- Power input on inner cavity [W] ---
81 P_in_total = 1267  # total constant power delivered to the inner cavity surface
82
83 # --- Ambient temperature (K) ---
84 T_ambient = 0.0
85 T_start = 2000
86 initial_temperatures = {
87     0: T_ambient,    # void
88     1: 2349*1.1,     # cavity shell (example)
89     2: 2349,         # TES container (example)
90     3: 2349,         # TES liner (example)
91     4: 2349,         # TES material
92     5: 2349,         # Heat exchanger
93     6: (1202+2349)/2 # Insulation
94 }
95
96 Nr = 200      # number of radial nodes
97 Nz = 350      # number of axial (z) nodes
98
99 dt = 0.94e-4   # [s] - reduce if unstable
100 t_total = 100.0  # [s]
101 Nt = round(t_total/dt)   # number of time steps
102
103 rad_escape = 1 / (1 + alpha*area_ratio)
104
105 tol = 1.0e-5  # tolerance for convergence (adjust as needed)
106
107 # ============================
108 # === 2) SHAPE DEFINITIONS (in mm)
109 # ============================
110
111 def cavity_polygon():
112     t = t_cav  # wall thickness
```

```
113
114     1 = np.radians(theta1_deg)
115     2 = np.radians(theta2_deg)
116
117     # Cone lengths
118     # L1 = (R_cav - t - aperture_r) / np.tan(1)
119     L1 = 0
120     L2 = (R_cav - t) / np.tan(2)
121
122     # Cylinder length
123     Lc = L_cav - (L1 + L2 + t)
124     if Lc < 0:
125         raise ValueError("L_cav too short for given angles and radii.")
126
127     # Axial positions
128     z0 = 0.0
129     z1 = z0 + L1
130     z2 = z1 + Lc
131     z3 = z2 + L2
132     z4 = L_cav
133
134
135     # Inner cavity profile
136     z_in = np.array([z0, z1, z2, z3])
137     r_in = np.array([aperture_r, R_cav-t, R_cav-t, 0.0])
138
139     # Outer shell: straight back wall, up radially, forward to aperture
140     z_out = np.array([z4, z4, z0])
141     r_out = np.array([0.0, R_cav, R_cav])
142
143     # Combine to form full polygon
144     Z = np.concatenate((z_in, z_out, [z0]))
145     R = np.concatenate((r_in, r_out, [aperture_r]))
146
147     return Z, R
148
149
150 def TES_material_polygon():
151     z0 = container_start + t_TES
152     z1 = container_start + L_TES - t_TES
153     z2 = L_cav + t_TES
154
155     r0 = R_cav + t_TES
156     r1 = R_TES - t_TES
157     r2 = 0
158
159     # Rectangle (closed loop)
160     # Z = np.array([z0, z1, z1, z0, z0])
161     # R = np.array([r0, r0, r1, r1, r0])
162     Z = np.array([z0, z2, z2, z1, z1, z1, z0, z0])
163     R = np.array([r0, r0, r2, r2, r1, r1, r1, r0])
164     return Z, R
165
166
167 def TES_container_polygon():
168     z0 = container_start
169     z1 = container_start + L_TES
170     z2 = L_cav
171
172     r0 = R_cav
173     r1 = R_TES
174     r2 = 0
175
176     t  = t_TES - t_liner
177
178     # Outer loop (counter-clockwise)
179     # z_outer = np.array([z0, z1, z1, z0, z0])
180     # r_outer = np.array([r0, r0, r1, r1, r0])
181     z_outer = np.array([z1, z1, z0, z0, z2, z2])
182     r_outer = np.array([r2, r1, r1, r0, r0, r2])
183
```

```
    # Inner loop (clockwise)
    # z_inner = np.array([z0+t, z0+t, z1-t, z1-t, z0+t])
    # r_inner = np.array([r0+t, r1-t, r1-t, r0+t, r0+t])

    z_inner = np.array([z2+t, z2+t, z0+t, z0+t, z1-t, z1-t])
    r_inner = np.array([r2, r0+t, r0+t, r1-t, r1-t, r2])

    # Combine into one polygon: outer CCW, then inner reversed (CW)
    Z = np.concatenate((z_outer, z_inner, [z_outer[0]]))
    R = np.concatenate((r_outer, r_inner, [r_outer[0]]))
    return Z, R

def TES_liner_polygon():
    z0 = container_start + t_TES - t_liner
    z1 = container_start + L_TES - t_TES + t_liner
    z2 = L_cav + t_TES - t_liner

    r0 = R_cav + t_TES - t_liner
    r1 = R_TES - t_TES + t_liner
    r2 = 0

    t  = t_liner

    # Outer loop (counter-clockwise)
    # z_outer = np.array([z0, z1, z1, z0, z0])
    # r_outer = np.array([r0, r0, r1, r1, r0])
    z_outer = np.array([z1, z1, z0, z0, z2, z2])
    r_outer = np.array([r2, r1, r1, r0, r0, r2])

    # Inner loop (clockwise)
    # z_inner = np.array([z0+t, z0+t, z1-t, z1-t, z0+t])
    # r_inner = np.array([r0+t, r1-t, r1-t, r0+t, r0+t])

    z_inner = np.array([z2+t, z2+t, z0+t, z0+t, z1-t, z1-t])
    r_inner = np.array([r2, r0+t, r0+t, r1-t, r1-t, r2])

    # Combine into one polygon: outer CCW, then inner reversed (CW)
    Z = np.concatenate((z_outer, z_inner, [z_outer[0]]))
    R = np.concatenate((r_outer, r_inner, [r_outer[0]]))
    return Z, R

def insulation_polygon():
    t1 = t_ins_cav
    t2 = t_ins_TES

    z0 = 0.0
    z1 = container_start
    z2 = container_start + L_TES
    z3 = L_cav

    r0 = 0.0
    r1 = aperture_r
    r2 = R_cav
    r3 = R_TES+D+t_wall

    # Outer loop
    # z_outer = np.array([z3+t1, z3+t1, z2+t2, z2+t2, z1-t2, z1-t2, z0-t1, z0-t1])
    # r_outer = np.array([r0, r2+t1, r2+t1, r3+t2, r3+t2, r2+t1, r2+t1, r1])

    z_outer = np.array([z2+t2, z2+t2, z0-t1, z0-t1, z0-t1, z0-t1])
    r_outer = np.array([r0, r3+t2, r3+t2, r2, r2, r1])


    # Inner loop
    # z_inner = np.array([z0, z0, z1, z1, z2, z2, z3, z3])
    # r_inner = np.array([r1, r2, r2, r3, r3, r2, r2, r0])

    z_inner = np.array([z0, z0, z0, z0, z2, z2])
    r_inner = np.array([r1, r2, r2, r3, r3, r0])

    # Combine into one polygon: outer CCW, then inner reversed (CW)
```

```
    Z = np.concatenate((z_inner, z_outer, [z_inner[0]]))
    R = np.concatenate((r_inner, r_outer, [r_inner[0]]))
    return Z, R

def heat_exchanger_polygon():
    z0 = container_start
    z1 = container_start + L_TES

    r0 = R_TES
    r1 = R_TES + D + t_wall

    # Rectangle (closed loop)
    Z = np.array([z0, z1, z1, z0, z0])
    R = np.array([r0, r0, r1, r1, r0])
    return Z, R


# === Convert all polygons from mm → m ===
scale = 1e-3
Z_cav2d, R_cav2d = cavity_polygon()
Z_cav2d *= scale;  R_cav2d *= scale

Z_mat2d, R_mat2d = TES_material_polygon()
Z_mat2d *= scale; R_mat2d *= scale

Z_cont2d, R_cont2d = TES_container_polygon()
Z_cont2d *= scale; R_cont2d *= scale

Z_liner2d, R_liner2d = TES_liner_polygon()
Z_liner2d *= scale; R_liner2d *= scale

Z_ins2d, R_ins2d = insulation_polygon()
Z_ins2d *= scale; R_ins2d *= scale

Z_heat2d, R_heat2d = heat_exchanger_polygon()
Z_heat2d *= scale; R_heat2d *= scale

# Build Path objects for --pointinpolygon tests
cav_path = Path(np.vstack((Z_cav2d, R_cav2d)).T)
mat_path = Path(np.vstack((Z_mat2d, R_mat2d)).T)
cont_path = Path(np.vstack((Z_cont2d, R_cont2d)).T)
liner_path = Path(np.vstack((Z_liner2d, R_liner2d)).T)
ins_path = Path(np.vstack((Z_ins2d, R_ins2d)).T)
heat_path = Path(np.vstack((Z_heat2d, R_heat2d)).T)

#================================
# === 3) GENERATE FINITE-DIFF GRID
# ================================

# 3.1) DOMAIN EXTENTS (all in meters now)
r_max = (R_TES + D + t_wall + t_ins_TES) * scale  # outermost radius in meters

z_min = (-t_ins_cav) * scale
z_max = (L_TES + t_ins_TES) * scale

# 3.2) DISCRETIZATION
dr = r_max / Nr
dz = (z_max-z_min) / Nz
print(dr*1000)
print(dz*1000)
# 3.3) BUILD (r, z) MESH
r_vals = np.linspace(dr/2, r_max - dr/2, Nr)   # radial coordinates [m]
z_vals = np.linspace(z_min+dz/2, z_max - dz/2, Nz)   # axial coordinates [m]
R_mesh, Z_mesh = np.meshgrid(r_vals, z_vals, indexing='ij')

# 3.4) MASK ARRAY (0=void, 1=cavity shell, 2=TES material, 3=TES container shell)
mask = np.zeros((Nr, Nz), dtype=int)

# 3.5) INITIALIZE TEMPERATURE FIELD
T = np.zeros((Nr, Nz), dtype=float)

```

```
# 3.6) VECTORIZE --POINTINPOLYGON TESTS
# Build a (Nr*Nz, 2) array of points in meters (to match cav_path, mat_path, cont_path)
points = np.vstack((Z_mesh.ravel(), R_mesh.ravel())).T  # shape = (Nr*Nz, 2), in meters

# Flatten mask for assignment
mask_flat = np.zeros(points.shape[0], dtype=int)

# Use vectorized contains_points (all in meters now!)
mask_flat[cav_path.contains_points(points)] = 1
mask_flat[cont_path.contains_points(points)] = 2
mask_flat[liner_path.contains_points(points)] = 3
mask_flat[mat_path.contains_points(points)] = 4
mask_flat[heat_path.contains_points(points)] = 5
mask_flat[ins_path.contains_points(points)] = 6

# Reshape back to (Nr, Nz)
mask = mask_flat.reshape(Nr, Nz)

r_phalf_vals = np.zeros(Nr)   # radius at r+½ face of cell i
r_mhalf_vals = np.zeros(Nr)   # radius at -r½ face of cell i

area_array_r_plus  = np.zeros(Nr)
area_array_r_minus = np.zeros(Nr)
area_array_z       = np.zeros(Nr)

volume_array = np.zeros(Nr)
for i in range(Nr):
    r_i = r_vals[i]
    r_phalf_vals[i] = r_i + 0.5 * dr  # radius at i+1/2 face
    r_mhalf_vals[i] = max(r_i - 0.5*dr, 0.0)  # radius at i-1/2 face

    area_array_r_plus[i]  = 2.0 * np.pi * r_phalf_vals[i] * dz
    area_array_r_minus[i] = 2.0 * np.pi * r_mhalf_vals[i] * dz

    area_array_z[i] = 2.0 * np.pi * r_vals[i] * dr

    volume_array[i] = 2.0 * np.pi * r_i * dr * dz

rad_loss_array = np.zeros((Nr, Nz))
rad_input_array = np.zeros((Nr, Nz))
energy_change_array = np.zeros((Nr, Nz))

for region in np.unique(mask):
    T[mask == region] = initial_temperatures[region]

k_array   = np.zeros_like(mask, dtype=float)
epsilon_array = np.zeros_like(mask, dtype=float)
rho_array = np.zeros_like(mask, dtype=float)
cp_array  = np.zeros_like(mask, dtype=float)

for region in np.unique(mask):
    region_mask = (mask == region)
    k_array[region_mask] = 1.0*material_props[region]["k"]
    epsilon_array[region_mask] = material_props[region]["epsilon"]
    rho_array[region_mask] = material_props[region]["rho"]
    cp_array[region_mask] = material_props[region]["cp"]

void_r_minus = np.zeros((Nr, Nz), dtype=bool)
void_r_plus  = np.zeros((Nr, Nz), dtype=bool)
void_z_minus = np.zeros((Nr, Nz), dtype=bool)
void_z_plus  = np.zeros((Nr, Nz), dtype=bool)

# Check r-1 (radial inward)
void_r_minus[1:, :] = (mask[:-1, :] == 0)

# Check r+1 (radial outward)
void_r_plus[:-1, :] = (mask[1:, :] == 0)

# Check z-1 (axial down)
void_z_minus[:, 1:] = (mask[:, :-1] == 0)

```

```
# Check z+1 (axial up)
void_z_plus[:, :-1] = (mask[:, 1:] == 0)

# At lowest r (i=0), no void inward (outside domain)
void_r_minus[0, :] = 0  # or False

# At highest r (i=Nr-1), outside domain => void present
void_r_plus[-1, :] = 1  # or True

# At lowest z (j=0), outside domain => void present
void_z_minus[:, 0] = 1  # or True

# At highest z (j=Nz-1), outside domain => void present
void_z_plus[:, -1] = 1  # or True

k_array_r_minus = np.zeros_like(k_array)
k_array_r_plus = np.zeros_like(k_array)
k_array_z_minus = np.zeros_like(k_array)
k_array_z_plus = np.zeros_like(k_array)

for i in range(Nr):
    for j in range(Nz):
        k_ij = k_array[i, j]

        # Radial minus (i-1, j)
        if i > 0 and not void_r_minus[i, j]:
            k_nbr = k_array[i - 1, j]
            denom = k_ij + k_nbr
            k_array_r_minus[i, j] = 2 * k_ij * k_nbr / denom
        else:
            # At lowest r (or void), use k_ij
            k_array_r_minus[i, j] = k_ij

        # Radial plus (i+1, j)
        if i + 1 < Nr and not void_r_plus[i, j]:
            k_nbr = k_array[i + 1, j]
            denom = k_ij + k_nbr
            k_array_r_plus[i, j] = 2 * k_ij * k_nbr / denom
        else:
            # At highest r (or void), use k_ij
            k_array_r_plus[i, j] = k_ij

        # Axial minus (i, j-1)
        if j > 0 and not void_z_minus[i, j]:
            k_nbr = k_array[i, j - 1]
            denom = k_ij + k_nbr
            k_array_z_minus[i, j] = 2 * k_ij * k_nbr / denom
        else:
            # At lowest z (or void), use k_ij
            k_array_z_minus[i, j] = k_ij

        # Axial plus (i, j+1)
        if j + 1 < Nz and not void_z_plus[i, j]:
            k_nbr = k_array[i, j + 1]
            denom = k_ij + k_nbr
            k_array_z_plus[i, j] = 2 * k_ij * k_nbr / denom
        else:
            # At highest z (or void), use k_ij
            k_array_z_plus[i, j] = k_ij

latent_heat_array = np.zeros_like(mask, dtype=float)  # J/kg
melt_temp_array   = np.zeros_like(mask, dtype=float)  # K
latent_heat_array[mask == 4] = latent_heat_value
melt_temp_array[mask == 4]   = melt_temp_value


# ====================================
# === 4) BOUNDARY CONDITIONS SETUP
# ====================================

# …(previous geometry code …unchanged)
```

```
468
469 # 4.0) … [same as before: compute L1,L2,Lc; z_in, r_in; etc.] …
470
471 # Initialize -zeroflux map
472 q_flux_plus_r = np.zeros((Nr, Nz))
473 q_flux_minus_r = np.zeros((Nr, Nz))
474 q_flux_z = np.zeros((Nr, Nz))
475
476
477 # Build list of all -cavitywall cells (mask == 1)
478 cavity_nodes = []
479 cavity_coords = []
480 for i in range(Nr):
481     for j in range(Nz):
482         if mask[i, j] == 1:
483             if (void_r_minus[i, j] or
484                 void_r_plus[i, j] or
485                 void_z_minus[i, j] or
486                 void_z_plus[i, j]):
487
488                 cavity_nodes.append((i, j))
489                 cavity_coords.append((z_vals[j], r_vals[i]))
490
491 epsilon_orig = epsilon_array.copy()
492
493 for row in energy_data:
494     z_pt_mm, r_pt_mm, flux_val = row    # mm, mm, W
495     z_pt = z_pt_mm * scale               # convert to meters
496     r_pt = r_pt_mm * scale               # convert to meters
497
498     # Find closest (z, r) cell center
499     distances = [np.hypot(z_pt - zc, r_pt - rc) for (zc, rc) in cavity_coords]
500     closest_idx = np.argmin(distances)
501
502     i, j = cavity_nodes[closest_idx]
503
504     area_r_plus  = area_array_r_plus[i]
505     area_r_minus = area_array_r_minus[i]
506     area_z       = area_array_z[i]
507
508     # --- Apply epsilon scaling only once ---
509     if (void_r_minus[i, j] or void_r_plus[i, j] or
510         void_z_minus[i, j] or void_z_plus[i, j]) and epsilon_array[i, j] == epsilon_orig[i, j
            ]:
511             epsilon_array[i, j] *= rad_escape
512
513     exposed_area = (
514         void_r_minus[i, j] * area_r_minus + void_r_plus[i, j] * area_r_plus +
515         (void_z_minus[i, j] + void_z_plus[i, j]) * area_z
516     )
517
518     assigned_flux = flux_val / 100 * P_in_total / exposed_area
519     q_flux_plus_r[i, j] += assigned_flux*void_r_plus[i, j]
520     q_flux_minus_r[i, j] += assigned_flux*void_r_minus[i, j]
521     q_flux_z[i, j] += assigned_flux*(void_z_minus[i, j] + void_z_plus[i, j])
522
523
524 print(f"␣␣Assigned␣-raytraced␣flux␣to␣{len(energy_data)}␣-wallcells.")
525
526
527 # ============================
528 # === 5) -TIMESTEPPING LOOP (Explicit Euler)
529 # ============================
530
531 @njit(parallel=True)
532 def time_step_explicit_euler(
533     T, T_new, mask, q_flux_plus_r, q_flux_minus_r, q_flux_z, r_vals,
534     k_array_r_plus, k_array_r_minus, k_array_z_plus, k_array_z_minus,
535     epsilon_array, rho_array, cp_array,
536     T_ambient, dr, dz, dt, Nr, Nz,
537     latent_heat_array, melt_temp_array, delta_T_melt,
```

```
    void_r_minus, void_r_plus, void_z_minus, void_z_plus,
    sigma,
    rad_loss_array, rad_input_array, energy_change_array,
    r_phalf_vals, r_mhalf_vals, area_array_r_plus, area_array_r_minus, area_array_z,
        volume_array
):
    T_ambient_2 = T_ambient * T_ambient
    T_ambient_4 = T_ambient_2 * T_ambient_2

    inv_dr = 1.0 / dr
    inv_dz = 1.0 / dz

    for i in prange(Nr):
        r_i = r_vals[i]
        r_iphalf = r_phalf_vals[i]
        r_imhalf = r_mhalf_vals[i]

        area_r_plus = area_array_r_plus[i]
        area_r_minus = area_array_r_minus[i]
        area_z = area_array_z[i]
        volume = volume_array[i]

        inv_r = 1.0 / r_i if r_i > 0.0 else 0.0

        for j in range(Nz):
            if mask[i, j] == 0:
                T_new[i, j] = T_ambient
                continue

            T_ij = T[i, j]
            T_ij_2 = T_ij * T_ij
            T_ij_4 = T_ij_2 * T_ij_2

            qij_r_plus = q_flux_plus_r[i, j]
            qij_r_minus = q_flux_minus_r[i, j]
            qij_z = q_flux_z[i, j]

            rho_ij = rho_array[i, j]
            cp_ij = cp_array[i, j]
            epsilon_ij = epsilon_array[i, j]

            k_r_plus = k_array_r_plus[i, j]
            k_r_minus = k_array_r_minus[i, j]
            k_z_plus = k_array_z_plus[i, j]
            k_z_minus = k_array_z_minus[i, j]

            # latent heat tweak
            if latent_heat_array[i, j] > 0.0:
                melt_T = melt_temp_array[i, j]
                if abs(T_ij - melt_T) <= 0.5 * delta_T_melt:
                    cp_ij += latent_heat_array[i, j] / delta_T_melt

            q_rad = epsilon_ij * sigma * (T_ij_4 - T_ambient_4)

            #Net radiative loss at each face (W)
            rad_loss_array[i, j] = (
                void_r_minus[i, j] * q_rad * area_r_minus +
                void_r_plus[i, j] * q_rad * area_r_plus +
                void_z_minus[i, j] * q_rad * area_z +
                void_z_plus[i, j] * q_rad * area_z
            )

            rad_input_array[i, j] = (
                void_r_minus[i, j] * qij_r_minus * area_r_minus +
                void_r_plus[i, j] * qij_r_plus * area_r_plus +
                void_z_minus[i, j] * qij_z * area_z +
                void_z_plus[i, j] * qij_z * area_z
            )


            Ts_r = T_ij
```

```
            Ts_z = T_ij

            # Radial minus face
            T_int = T[i-1, j] if i > 0 and not void_r_minus[i, j] else T_ij
            T_r_minus = (1.0 - void_r_minus[i, j]) * T_int + void_r_minus[i, j] * Ts_r
            q_cond_r_minus = k_r_minus * (T_ij - T_r_minus) * inv_dr
            q_surf_r_minus = (q_rad - qij_r_minus) * void_r_minus[i, j]
            q_r_minus = q_cond_r_minus + q_surf_r_minus

            # Radial plus face
            T_int = T[i+1, j] if (i + 1 < Nr and not void_r_plus[i, j]) else T_ij
            T_r_plus = (1.0 - void_r_plus[i, j]) * T_int + void_r_plus[i, j] * Ts_r
            q_cond_r_plus = k_r_plus * (T_r_plus - T_ij) * inv_dr
            q_surf_r_plus = (q_rad - qij_r_plus) * void_r_plus[i, j]
            q_r_plus = q_cond_r_plus - q_surf_r_plus

            # Axial minus face
            T_int = T[i, j-1] if (j > 0 and not void_z_minus[i, j]) else T_ij
            T_z_minus = (1.0 - void_z_minus[i, j]) * T_int + void_z_minus[i, j] * Ts_z
            q_cond_z_minus = k_z_minus * (T_ij - T_z_minus) * inv_dz
            q_surf_z_minus = (q_rad - qij_z) * void_z_minus[i, j]
            q_z_minus = q_cond_z_minus + q_surf_z_minus

            # Axial plus face
            T_int = T[i, j+1] if (j + 1 < Nz and not void_z_plus[i, j]) else T_ij
            T_z_plus = (1.0 - void_z_plus[i, j]) * T_int + void_z_plus[i, j] * Ts_z
            q_cond_z_plus = k_z_plus * (T_z_plus - T_ij) * inv_dz
            q_surf_z_plus = (q_rad - qij_z) * void_z_plus[i, j]
            q_z_plus = q_cond_z_plus - q_surf_z_plus

            # Finite differences
            radial_div = (r_iphalf * q_r_plus - r_imhalf * q_r_minus) * inv_r * inv_dr
            axial_div = (q_z_plus - q_z_minus) * inv_dz

            dT_dt = (radial_div + axial_div) / (rho_ij * cp_ij)
            T_new[i, j] = T_ij + dt * dT_dt

            C_node = rho_ij * cp_ij * volume   # [J/K]
            energy_change_array[i, j] = dT_dt * C_node     # [W]  (rate of change of internal
                energy)

def run_until_convergence():
    T_local = T_final.copy()
    T_new = T_local.copy()
    T_local += -0.00
    E_internal_old = np.sum(rho_array * cp_array * T_local * volume_array[:, None])

    for step in range(Nt):
        # zero per-step arrays
        rad_loss_array.fill(0.0)
        rad_input_array.fill(0.0)
        energy_change_array.fill(0.0)
        time_step_explicit_euler(
            T_local, T_new, mask, q_flux_plus_r, q_flux_minus_r, q_flux_z, r_vals,
            k_array_r_plus, k_array_r_minus, k_array_z_plus, k_array_z_minus,
            epsilon_array, rho_array, cp_array,
            T_ambient, dr, dz, dt, Nr, Nz,
            latent_heat_array, melt_temp_array, delta_T_melt,
            void_r_minus, void_r_plus, void_z_minus, void_z_plus,
            sigma,
            rad_loss_array, rad_input_array, energy_change_array,
            r_phalf_vals, r_mhalf_vals, area_array_r_plus, area_array_r_minus, area_array_z,
                volume_array
        )

        max_diff = np.max(np.abs(T_new - T_local))/dt

        T_local, T_new = T_new, T_local

        E_internal_new = np.sum(rho_array * cp_array * T_local * volume_array[:, None])
        dE_dt = (E_internal_new - E_internal_old) / dt
```

```
        E_internal_old = E_internal_new

        if step % 1000 == 0:
            T_TES = np.ma.masked_where((mask != 4), T_local)
            print(np.min(T_TES)/2349.545378820166)
            total_rad_loss = np.sum(rad_loss_array)      # W
            total_rad_input = np.sum(rad_input_array)    # W
            total_dE_nodes = np.sum(energy_change_array) # W (should equal dE_dt within
                numerical noise)
            print(f"Time = {step * dt:.3f} s, max_diff = {max_diff:.5e} K/s")
            print(f"Radiation loss = {total_rad_loss:.4f} W, Radiation input = {
                total_rad_input:.4f} W")
            print(f"Energy residual = {total_rad_input - total_rad_loss - dE_dt:.4f} W")
            print(f"dE/dt (global) = {dE_dt:.4f} W, sum nodes energy change = {total_dE_nodes
                :.4f} W")

        if max_diff < tol:
            print(f"Converged after {step} steps with max_diff = {max_diff:.5e}")
            break

    return T_local

T = run_until_convergence()
```